Value of Flow Measurement Accuracy in Hydropower Plants with Short Converging Intakes

A Dissertation Presented for the
Doctor of Philosophy
Degree
The University of Tennessee, Knoxville

Mark Herbert Christian
August 2017

ACKNOWLEDGEMENTS

It is impossible to fully acknowledge my gratitude to the large the number of individuals that have helped me realize the development of my Ph.D. research. In my small attempt to do so I wish to first thank my family for all of their love and support throughout the years. I have always considered myself fortunate to grow up in a household where I was actively encouraged to experience new concepts and cultures. This exposure acted as my primary impetus to try to make the world a better place and I will be eternally grateful. My father taught me the importance of flexibility and good humor when challenges arise and my mother taught me to embrace these challenges, making them into opportunities. My older brother has always represented strength to me and helped me from a young age to not shy away from adversity, and rather face it head one and overcome it.

In addition to the support from my family I wanted to take this opportunity to thank the many mentors I have had over the course of my work. This naturally begins with my major advisor, Brennan Smith, who provided me with the initial opportunity work in his lab group. He guided and encouraged me as a young researcher while providing me with the freedom to establish my own research process. I would also like to thank the other staff members of the Energy-Water Resources Group at Oak Ridge National Laboratory, namely Boualem Hadjerioua who provided me with the opportunity to work on several impactful projects concurrently with my thesis work. I cannot begin to express how invaluable my experience at Oak Ridge National Laboratory has been to me. In addition to this I would like to thank Paul Wolff and Jim Walsh who are experts within the hydropower industry. Their support and advice on both technical and practical matters has enabled me to side step many obstacles and focus my work on impactful areas.

I would to also take this opportunity to thank the many industries that supported my research. This includes the U.S. Army Corps of Engineers who was willing to provide information critical for the realization of the benefits of this work. In addition I would like to thank Ott Hydromet, Valeport, Rittmeyer Brugg, and ADS Environmental Services. They represent key manufactures of the sensors investigated in my research, and I very much appreciate their continued contact and wiliness to actively engage with me. Furthermore I would like to thank the support staff of Star-CCM+, the CFD software used in my research. Their positive and timely feedback enabled me to rapidly climb the steep learning curve associated with the actual application of CFD.

Outside of this I would like to acknowledge the support of the Hydro Research Foundation. This fellowship organization not only provided financial support for the initial phase of my research it also took pains to ensure that I was able to

actively integrate with the hydropower industry itself. The connections I made as a part of the HRF were critical to the success of my research and have demonstrability changed the path of my career. I would like to thank Brenna Vaughn, the director of the HRF, for her forward looking approach to the recruitment and retainment of the next generation of the hydropower industry.

Most of all I want to express my sincerest appreciation to the love of my life, Guinevere. Your unwavering love and motivation have pushed me to be both a better scientist and man. I am proud of everything that we have been through together, from our late night working sessions around the kitchen table to our glorious, lazy afternoons. As this chapter of our lives begins to close I look on it with fondness but without sorrow or fear because I know that you will be with me in the next phase of the adventure that is our lives.

Finally I wish to thank you, the reader of this document, for your time and attention. The following represents the culmination of more hours, cups of coffee and lines of code than I would care to count but I truly believe this effort to be worth its cost. With that I hope that you will indulge me with my favorite quote:

“Amongst men of good will, science and democracy together offer an ever-richer life and ever-larger satisfaction to the individual. With this change in our moral climate and our rediscovered ability to improve our economic order, we have set our feet upon the road of enduring progress. …If I know aught of the spirit and purpose of our Nation, we will not listen to Comfort, Opportunism, and Timidity. We will carry on.”

-President Franklin D. Roosevelt

Second Inaugural Address
Wednesday, January 20th, 1937

ABSTRACT

This report documents research undertaken to determine the value of flow measurement accuracy in hydropower plants with short converging intakes. The motivation was to provide a suite of tools and best practices to streamline flow measurement sensor modeling in any type of hydropower plant. The Lower Granite Lock and Dam hydroplant was leveraged in development of the analysis tool. Computational fluid dynamics (CFD) models of Lower Granite Unit 4 provided necessary information about the hydraulic structures distribution through the unit. Two different CFD models were created. The first was done using the as-built plans; the second was created through modifications of the as-built plans. The two models were necessary to understand the hydraulic characteristics of the intake and the subsequent financial sensitivities. The CFD information was used in the development of a post processing tool that enables the user to simulate any number of the two types of flow sensors traditionally used in short converging intakes (current meters and acoustic time-of-flight transducers). The simulation of five different types of current meters and three different applications of the acoustic time-of-flight transducers are embedded within the code. The economic research component utilized historic plant generation and electrical cost data in concert with the sensor simulation results to determine the impact of flow measurement accuracy on water management. The incremental avoided-opportunity cost due to the error in flow measurement was then compared with the cost of the sensors to determine the incremental cost-benefit ratio, which acts as the primary indicator of sensor value. The investigation into Lower Granite revealed that the opportunity cost associated with suboptimal unit operation ranges from 2.47% to 0.09% of hydroplant revenue, depending on the type and number of sensors used. When the opportunity cost was compared with the cost of the flow sensors, the optimal numbers of instruments in the as-built model were found to be 10, 11, and 15 acoustic paths, transiting current meters, and static current meters. In the case of the modified as-built simulation, the optimal numbers were found to be 11, 15, and 15 acoustic paths, transiting current meters, and static current meters, respectively.

TABLE OF CONTENTS

Chapter One Motivation 1
Chapter Two Background and Literature Review 4
Types of Hydropower Projects 4
Unit Efficiency and Flow Measurement 5
Unit Flow Measurement 6
Computational Fluid Dynamic Modeling 14
Value of Flow Measurement 17
Lower Granite Research 24
Reservoir Drawdown Study 25
Stay Vane and Wicket Gate Modification Study 27
Lower Granite Site Performance Testing 28
Lower Granite Historical Market Data 29
Chapter Three Computational Fluid Dynamics Theory 32
Chapter Four Methods 43
Statement of Assumptions 43
Computational Fluid Dynamics 43
Sensor Simulation 46
Economic Evaluation 48
Computational Fluid Dynamics Modeling 51
Physical Domain 52
Computational Domain 56
Preliminary Investigation 61
Boundary Conditions 63
Mesh Development 71
Bay Flow Recirculation Reproduction 73
CFD Result Validation 77
Flow Sensor Modeling 79
Local Velocity Characteristic Calculations 80
Current Meter Simulation 81
Acoustic Time of Flight Simulation 96
Indicated Unit Characteristic Curve 100
Value Establishment 101
Optimal Plant Dispatch Curve 102
Determination of Operational Opportunity Cost 103
Value of Flow Measurement Accuracy 104
Chapter Five Results 107
Computational Fluid Dynamics Modeling 107
Boundary Condition and Turbulence Model Preliminary Investigation 107
Mesh Resolution Study 109
Residual Analysis 110
As-Built Recirculation Investigation 111
As-Build Modification Recirculation Investigation 112
Model Validation 113

Flow Meter Simulation....114
Current Meter Simulation....115
Acoustic Time of Flight Simulation....119
Value Analysis....122
Optimized Hydroplant Dispatch....122
Opportunity Cost Analysis....123
Value Analysis....125
Chapter Six Summary, Conclusions and Recommendations....128
Summary and Conclusions....128
Recommendations....134
Works Cited....136
Appendices....147
Appendix 1: Mesh Independence Study Code....148
Appendix 2: Current Meter Simulation Code....159
Appendix 3: Acoustic Time of Flight Simulation Code....181
Appendix 4: Opportunity Cost Code....190
Appendix 5: Chapter 1 Figures and Tables....194
Appendix 6: Chapter 2 Figures and Tables....196
Appendix 7: Chapter 3 Figures and Tables....210
Appendix 8: Chapter 4 Figures and Tables....215
Appendix 9: Chapter 5 Figures and Tables....241
Appendix 10: Residual Threshold Values....288
Appendix 11: Assessed Performance Curves....294
As-Built Static Current Meter Application Analysis....294
As-Built Dynamic Current Meter Application Analysis....296
As-Built Acoustic Time of Flight Application Analysis....299
Modified As-Built Static Current Meter Application Analysis....300
Modified As-Built Dynamic Current Meter Application Analysis....301
Modified As-Built Acoustic Time of Flight Application Analysis....303
Vita....305

LIST OF TABLES

Table 3.1. Front Facing Step Preliminary Investigation Specifications ..... Appendix 214
Table 4.1. Preliminary Investigation Specifications ..... Appendix 235
Table 4.2. Preliminary Investigation Details ..... Appendix 235
Table 4.3. Turbine Head Loss Details ..... Appendix 235
Table 4.4. Turbine Efficiency Coefficients ..... Appendix 236
Table 4.5. Generator Efficiency Coefficients ..... Appendix 236
Table 4.6. Intake Headloss Coefficients ..... Appendix 236
Table 4.7. Unit 4 Cumulative Head Loss Calculations ..... Appendix 237
Table 4.8.Computational Domain Outlet Pressure Characteristics .. Appendix 237
Table 4.9.Mesh Quality Results ..... Appendix 237
Table 4.10. Recirculation Zone Study As-Built and Surface Roughness Modifications ..... Appendix 238
Table 4.11. Backwards Facing Step Velocity Polynomial Coefficients ..... Appendix 238
Table 4.12.Computational Domain Outlet Pressure Characteristics ..... Appendix 238
Table 4.13.Computational Domain Outlet Pressure Characteristics ..... Appendix 239
Table 4.14. Axial Pulsation Correction Factor Coefficients ..... Appendix 239
Table 4.15. Individual Drag Coefficient Calculation Results ..... Appendix 239
Table 4.16. Transverse Drag Coefficient Factor Coefficients ..... Appendix 240
Table 4.17. Transverse Turbulent Response Correction Factor Coefficients ..... Appendix 240
Table 5.1. Preliminary Investigation Bay Flow Distribution Flow Distribution Percent Distribution ..... Appendix 271
Table 5.2. Preliminary Investigation Bay Flow Distribution Accuracy ..... Appendix 271
Table 5.3. Preliminary Investigation Bay Flow Distribution Model ANOVA Analysis ..... Appendix 272
Table 5.4. Preliminary Investigation Bay Flow Distribution Prototype ANOVA Analysis ..... Appendix 272
Table 5.5. Mesh Resolution Goodness of Fit Study ..... Appendix 272
Table 5.6. Recirculation Zone Description ..... Appendix 273
Table 5.7. Acoustic Time of Flight Velocities resulting from the Modified As-Built CFD ..... Appendix 274
Table 5.8. Acoustic Time of Flight Velocities resulting from the Modified As-Built CFD Percent Difference from Field Data ..... Appendix 275
Table 5.9. Bay Flow Distribution Accuracy ..... Appendix 275
Table 5.10. Acoustic Time of Flight Validation F Test ..... Appendix 275
Table 5.11. Acoustic Time of Flight Validation Average Percent Accuracy ..... Appendix 276
Table 5.12. Acoustic Time of Flight Validation Standard Deviation... Appendix 276

Table 5.13. Interpolation Numerical Method Investigation Results ... Appendix 276
Table 5.14. Average Percent of Operational Flow Rate Recorded As-Built: General Current Meter ..... Appendix 277
Table 5.15. Average Percent of Operational Flow Rate Recorded As-Built: Ott C31-1(Plastic) Current Meter ..... Appendix 277
Table 5.16. Average Percent of Operational Flow Rate Recorded As-Built: Ott C31-1(Metal) Current Meter ..... Appendix 277
Table 5.17. Average Percent of Operational Flow Rate Recorded As-Built: Ott C31-A Current Meter ..... Appendix 278
Table 5.18. Average Percent of Operational Flow Rate Recorded As-Built: Ott C31-R Current Meter ..... Appendix 278
Table 5.19. Standard Deviation in Percent of Operational Flow Rate Recorded over all Flow Rates As-Built: General Current Meter ..... Appendix 278
Table 5.20. Standard Deviation in Percent of Operational Flow Rate Recorded over all Flow Rates As-Built: Ott C31-1(Plastic) Current Meter..... Appendix 279
Table 5.21. Standard Deviation in Percent of Operational Flow Rate Recorded over all Flow Rates As-Built: Ott C31-1(Metal) Current Meter ..... Appendix 279
Table 5.22. Standard Deviation in Percent of Operational Flow Rate Recorded over all Flow Rates As-Built: Ott C31-A Current Meter ..... Appendix 279
Table 5.23. Standard Deviation in Percent of Operational Flow Rate Recorded over all Flow Rates As-Built: Ott C31-R Current Meter ..... Appendix 280
Table 5.24. Average Percent of Operational Flow Rate Recorded Modified As-Built: General Current Meter ..... Appendix 280
Table 5.25. Average Percent of Operational Flow Rate Recorded Modified As-Built: Ott C31-1 (Plastic) ..... Appendix 280
Table 5.26. Average Percent of Operational Flow Rate Recorded Modified As-Built: Ott C31-Type A Current Meter ..... Appendix 281
Table 5.27. Standard Deviation in Percent of Operational Flow Rate Recorded over all Flow Rates Modified As-Built: General Current Meter ..... Appendix 281
Table 5.28. Standard Deviation in Percent of Operational Flow Rate Recorded over all Flow Rates Modified As-Built: Ott C31-1 (Plastic) Current Meter ..... Appendix 281
Table 5.29. Standard Deviation in Percent of Operational Flow Rate Recorded over all Flow Rates Modified As-Built: Ott C31-Type A Current Meter ..... Appendix 282
Table 5.30. Incremental Annual Benefit Cost Ratio for As-Built Static Current Meter Application..... Appendix 282
Table 5.31. Incremental Annual Benefit Cost Ratio for

As-Built Dynamic Current Meter Application ..... Appendix 282
Table 5.32. Years to Achieve a Benefit Cost Ratio of 1 for
As-Built Static Current Meter Application ..... Appendix 283
Table 5.33. Years to Achieve a Benefit Cost Ratio of 1 for
As-Built Dynamic Current Meter Application ..... Appendix 283
Table 5.34. Incremental Annual Benefit-Cost Ratio for the
As-Built Acoustic Time of Flight Application ..... Appendix 283
Table 5.35. Incremental Annual Benefit Cost Ratio for Modified
As-Built Static Current Meter Application ..... Appendix 284
Table 5.36. Incremental Annual Benefit Cost Ratio for
Modified As-Built Dynamic Current Meter Application ..... Appendix 284
Table 5.37. Years to Achieve a Benefit Cost Ratio of 1 for
Modified As-Built Static Current Meter Application ..... Appendix 284
Table 5.38. Years to Achieve a Benefit Cost Ratio of 1 for
Modified As-Built Dynamic Current Meter Application ..... Appendix 284
Table 5.39. Incremental Annual Benefit-Cost Ratio for the
Modified As-Built Acoustic Time of Flight Application ..... Appendix 285
Table 5.40. Reduction in Suboptimally Assigned Water per
incremental investment in Static Current Meters As-Built
Application ..... Appendix 285
Table 5.41. Reduction in Suboptimally Assigned Water per
incremental investment in Transient Current Meters As-Built
Application ..... Appendix 285
Table 5.42. Reduction in Suboptimally Assigned Water per
incremental investment in Acoustic Time of Flight Paths As-Built
Application ..... Appendix 286
Table 5.43. Reduction in Suboptimally Assigned Water per
incremental investment in Static Current Meters Modified As-Built
Application ..... Appendix 286
Table 5.44. Reduction in Suboptimally Assigned Water per
incremental investment in Transient Current Meters Modified
As-Built Application ..... Appendix 286
Table 5.45. Reduction in Suboptimally Assigned Water per
incremental investment in Acoustic Time of Flight Paths Modified
As-Built Application ..... Appendix 287

LIST OF FIGURES

Figure 1.1: Hill Diagram ..... Appendix 194
Figure 1.2: Unit Characteristic Curve ..... Appendix 194
Figure 1.3: Research Work Structure ..... Appendix 195
Figure 2.1: Storage Hydroplant ..... Appendix 196
Figure 2.2: Mainstem Hydroplant ..... Appendix 196
Figure 2.3: Current Meter ..... Appendix 197
Figure 2.4: Current Meter Transverse Flow Response ..... Appendix 197
Figure 2.5: Turbulent Flow Scotch Yoke ..... Appendix 198
Figure 2.6: Current Meter Static Mounting ..... Appendix 198
Figure 2.7: Dynamic Current Meter Mounting ..... Appendix 199
Figure 2.8: Dynamic Current Meter Operation ..... Appendix 199
Figure 2.9: Dynamic Current Meter Resulting Vertical and Horizontal Resolution ..... Appendix 200
Figure 2.10: Current Meter Layout and Dimensions ..... Appendix 200
Figure 2.11: Acoustic Time of Flight Transducer ..... Appendix 201
Figure 2.12: Dual Path Acoustic Time of Flight Layout ..... Appendix 201
Figure 2.13: Unit Efficiency Curves ..... Appendix 202
Figure 2.14: Optimized Unit Dispatch ..... Appendix 202
Figure 2.15: Optimum Plant Efficiency ..... Appendix 203
Figure 2.16: Lower Granite Lock and Dam ..... Appendix 203
Figure 2.17: Lower Granite Fish Bypass System Overview ..... Appendix 204
Figure 2.18: Lower Granite Fish Bypass Screen and Application Points ..... Appendix 205
Figure 2.19: Lower Granite Bladeless Turbine Model Test Data ..... Appendix 206
Figure 2.20 Lower Granite Modified Geometry Performance Test Data ..... Appendix 207
Figure 2.21: Installation of Acoustic Time of Flight Transducers ..... Appendix 208
Figure 2.22a: Lower Granite 2016 Hourly Generation Chart ..... Appendix 208
Figure 2.22b: Lower Granite 2015 Hourly Generation Chart ..... Appendix 209
Figure 2.23: Mid-Columbia Electric Clearing Price in 2016 ..... Appendix 209
Figure 3.1: Wall Region Discretization and Treatment ..... Appendix 210
Figure 3.2: Forward Facing Step Velocity Contours and Comparison Transect Locations ..... Appendix 210
Figure 3.3: Transect 1 Freestream Velocity Profile ..... Appendix 211
Figure 3.4: Transect 2 Near Wall Velocity Profile..... Appendix 211
Figure 3.5: Transect 8 Near Wall Velocity Profile ..... Appendix 212
Figure 3.6: NASA Langley Near Wall Velocity Distribution ..... Appendix 212
Figure 3.7: Star-CCM+ Near Wall Velocity Distribution at an Average Y+ of 0.2 ..... Appendix 213
Figure 3.8: Near Wall Velocity Distribution Associated with Different Near Wall Mesh Resolutions at a Downstream Distance of 1 meter ..... Appendix 213

Figure 3.9: Near Wall Velocity Distribution Associated with Different Near Wall Mesh Resolutions at a Downstream Distance of 2 meter ..... Appendix 214

Figure 4.1: Subdomains of the Unit 4 Flow Path ..... Appendix 215
Figure 4.2a: Trashrack Engineering Drawing (Front View) ..... Appendix 216
Figure 4.2b: Trashrack Engineering Drawing (Side View) ..... Appendix 216
Figure 4.3: Intake Engineering Drawing (Plan View) ..... Appendix 217
Figure 4.4: Intake Engineering Drawing (Top View) ..... Appendix 217
Figure 4.5a: Scroll Case Engineering Drawing (Top View) ..... Appendix 218
Figure 4.5b: Scroll Case Engineering Drawing (Transect Dimensions) ..... Appendix 218
Figure 4.6a: Stay Ring Engineering Drawing (Top View)..... Appendix 219
Figure 4.6b: Stay Vane Engineering Drawing (Transect Dimensions)..... Appendix 219
Figure 4.7: Turbine Engineering Drawing (Transect Dimensions) .... Appendix 220
Figure 4.8: Turbine Blade Drawing (Transect Dimensions) ..... Appendix 220
Figure 4.9: Draft Tube Engineering Drawing (Transect Dimensions) Appendix 221
Figure 4.10: Subdomains of the Computational Domain ..... Appendix 222
Figure 4.11: Computational Domain Trashracks ..... Appendix 223
Figure 4.12a: Computational Turbine Model ..... Appendix 224
Figure 4.12b: Turbine Hub Subdomain of the Computational Domain ..... Appendix 224
Figure 4.12c: Aggregated Blade Subdomain of the Computational Domain ..... Appendix 225
Figure 4.13: Simplified Turbine Blade Geometry ..... Appendix 225
Figure 4.14: Simplified Turbine Blade Geometry ..... Appendix 226
Figure 4.15: Forebay Boundary Labels ..... Appendix 226
Figure 4.16: Turbine Pressure Drop over Flow Range of Unit 4 ..... Appendix 227
Figure 4.17: Prism Layer Resolution ..... Appendix 227
Figure 4.18: Thin Layer Resolution ..... Appendix 228
Figure 4.19: Enhanced Mesh Resolution ..... Appendix 228
Figure 4.20: As-Build Angled Obstruction Modification..... Appendix 229
Figure 4.21: As-Build Straight Obstruction Modification ..... Appendix 230
Figure 4.22: Acoustic Transducer Distances ..... Appendix 231
Figure 4.23: Current Meter Geometry ..... Appendix 232
Figure 4.24: Least Squares Fit of Turbulent Transverse Drag Coefficient ..... Appendix 232
Figure 4.25: Acoustic Time of Flight Diagram ..... Appendix 233
Figure 4.26: Flow Measurement Accuracy Opportunity Cost ..... Appendix 233
Figure 4.27 Performance of Unit Combinations ..... Appendix 234
Figure 4.28: Optimal Dispatch of Units from General Static Current Meter Application ..... Appendix 224

Figure 5.1: Upstream Model Preliminary Investigation Velocity Distribution ..... Appendix 241
Figure 5.2: Downstream Model Preliminary Investigation Velocity Distribution ..... Appendix 241
Figure 5.3: Bay C Acoustic Time of Flight Recorded Velocity Distribution..... Appendix 242
Figure 5.4a: Bay A-U Velocity Comparison ..... Appendix 215
Figure 5.4b: Bay A-V Velocity Comparison ..... Appendix 243
Figure 5.4c: Bay A-W Velocity Comparison..... Appendix 243
Figure 5.4d: Bay A-TKE Comparison ..... Appendix 244
Figure 5.5a: Bay B-U Velocity Comparison ..... Appendix 244
Figure 5.5b: Bay B-V Velocity Comparison ..... Appendix 245
Figure 5.5c: Bay B-W Velocity Comparison ..... Appendix 245
Figure 5.5d: Bay B-TKE Comparison ..... Appendix 246
Figure 5.6a: Bay C-U Velocity Comparison ..... Appendix 247
Figure 5.6b: Bay B-V Velocity Comparison ..... Appendix 247
Figure 5.6c: Bay C-W Velocity Comparison ..... Appendix 247
Figure 5.6d: Bay C-TKE Comparison ..... Appendix 248
Figure 5.7: Bay A-Nearest Neighbor Histogram ..... Appendix 248
Figure 5.8: Bay B-Nearest Neighbor Histogram ..... Appendix 249
Figure 5.9: Bay C-Nearest Neighbor Histogram ..... Appendix 249
Figure 5.10: CFD Residual Plot ..... Appendix 250
Figure 5.11a: Local U-Velocity Residual Histogram ..... Appendix 250
Figure 5.11b: Local V-Velocity Residual Histogram ..... Appendix 251
Figure 5.11c: Local W-Velocity Residual Histogram ..... Appendix 251
Figure 5.11d: Local TKE Residual Histogram ..... Appendix 252
Figure 5.11e: Local Continuity Residual Histogram ..... Appendix 252
Figure 5.11f: Local TDR Residual Histogram ..... Appendix 253
Figure 5.12: Diagram of Flow Recirculation Characteristics ..... Appendix 253
Figure 5.13: Pressure Distribution at the Recirculation Site ..... Appendix 254
Figure 5.14: Bay A Velocity Distribution Resulting From As-Built Modifications ..... Appendix 254
Figure 5.15: Bay A Validation at 634 m3sec-1 ..... Appendix 255
Figure 5.16: Bay B Validation at 634 m3sec-1 ..... Appendix 255
Figure 5.17: Bay C Validation at 634 m3sec-1 ..... Appendix 256
Figure 5.18: Number of Points of Influence Histogram ..... Appendix 256
Figure 5.19: As-Built Static Current Meter Accuracy Differential ..... Appendix 257
Figure 5.20 As-Built Dynamic Current Meter Accuracy Differential .. Appendix 257
Figure 5.21: Modified As-Built Static Current Meter Accuracy Differential ..... Appendix 258
Figure 5.22 Modified As-Built Dynamic Current Meter Accuracy Differential ..... Appendix 258
Figure 5.23: Dual Path Recorded Flow Rate Accuracy ..... Appendix 259

Figure 5.24: Differential between the Maximum and Minimum Percent Recorded Flow Rate ..... Appendix 259
Figure 5.25: Differential in Flow Rates Predicted by Single Acoustic Paths in each direction as a function of the overall Flow Rate ..... Appendix 260
Figure 5.26: Recorded Unit Characteristic Curve as a Function of the Number of Applied Dual Acoustic Paths ..... Appendix 260
Figure 5.27: Differential in Flow Rates Predicted by Single Acoustic Paths in each direction as a function of the overall Flow Rate ..... Appendix 261
Figure 5.28: Differential in Flow Rates Predicted by Single Acoustic Paths in each direction as a function of the overall Flow Rate ..... Appendix 261
Figure 5.29: Differential in Flow Rates Predicted by Single Acoustic Paths in each direction as a function of the overall Flow Rate ..... Appendix 262
Figure 5.30: Performance of Increasing Number of Units using the Operational Efficiency of the Unit 4 ..... Appendix 263
Figure 5.31: Optimal Performance of the Plant informed by Operational Efficiency of the Unit as well as Static Mounted General Current Meter Measured Efficiency ..... Appendix 263
Figure 5.32: Optimal Performance of the Plant informed by Operational Efficiency of the Unit as well as Dynamic Mounted General Current Meter Measured Efficiency ..... Appendix 264
Figure 5.33: Optimal Performance of the Plant informed by Operational Efficiency of the Unit as well as Dual Acoustic Time of Flight Measured Efficiency ..... Appendix 264
Figure 5.34: Optimal Performance of the Plant informed by Operational Efficiency of the Unit and the lowest levels of investigated Current Meters and Acoustic Paths ..... Appendix 265
Figure 5.35: Optimal Performance of the Plant informed by Operational Efficiency of the Unit and the highest levels of investigated Current Meters and Acoustic Paths ..... Appendix 265
Figure 5.36: As-Built Static Current Meter Opportunity Cost as a Ratio of Annual Plant Revenue ..... Appendix 266
Figure 5.37: As-Built Dynamic Current Meter Opportunity Cost as a Ratio of Annual Plant Revenue ..... Appendix 266
Figure 5.38: As-Built Acoustic Time of Flight Opportunity Cost as a Ratio of Annual Plant Revenue ..... Appendix 267
Figure 5.39: As-Built Static and Transiting Current Meter Incremental Opportunity Cost as a Ratio of Annual Plant Revenue ..... Appendix 267
Figure 5.40: As-Built Acoustic Time of Flight Incremental Opportunity Cost as a Ratio of Annual Plant Revenue ..... Appendix 268

Figure 5.41 Modified As-Built Static Current Meter Opportunity Cost as a Ratio of Annual Plant Revenue ..... Appendix 268
Figure 5.42: Modified As-Built Dynamic Current Meter Opportunity Cost as a Ratio of Annual Plant Revenue ..... Appendix 269
Figure 5.43: Modified As-Built Acoustic Time of Flight Opportunity Cost as a Ratio of Annual Plant Revenue ..... Appendix 269
Figure 5.44: Modified As-Built Static and Transiting Current Meter Incremental Opportunity Cost as a Ratio of Annual Plant Revenue ..... Appendix 270
Figure 5.45: Modified As-Built Acoustic Time of Flight Incremental Opportunity Cost as a Ratio of Annual Plant Revenue ..... Appendix 270

Figure A10.1: Continuity Residual of 290 m3sec-1 ..... Appendix 288
Figure A10.2: Y Momentum Residual of 290 m3sec-1 ..... Appendix 289
Figure A10.3: X Momentum Residual of 290 m3sec-1 ..... Appendix 290
Figure A10.4: Z Momentum Residual of 290 m3sec-1 ..... Appendix 291
Figure A10.5: Turbulent Kinetic Energy Residual of 290 m3sec-1 ... Appendix 292
Figure A10.6: Specific Dissipation Rate Residual of 290 m3sec-1 .. Appendix 293
Figure A11.1: Recorded Unit Characteristic Curve as a Function of the Number of Static General Current Meters ..... Appendix 294
Figure A11.2: Recorded Unit Characteristic Curve as a Function of the Number of Static Ott C31-1(Plastic) Current Meters ..... Appendix 294
Figure A11.3: Recorded Unit Characteristic Curve as a Function of the Number of Static Ott C31-1(Metal) Current Meters ..... Appendix 295
Figure A11.4: Recorded Unit Characteristic Curve as a Function of the Number of Static Ott C31-A Current Meters..... Appendix 295
Figure A11.5: Recorded Unit Characteristic Curve as a Function of the Number of Static Ott C31-R Current Meters ..... Appendix 296
Figure A11.6: Recorded Unit Characteristic Curve as a Function of the Number of Dynamic Applied General Current Meters ..... Appendix 296
Figure A11.7: Recorded Unit Characteristic Curve as a Function of the Number of Dynamic Ott C31-1(Plastic) Current Meters ..... Appendix 297
Figure A11.8: Recorded Unit Characteristic Curve as a Function of the Number of Dynamic Ott C31-1(Metal) Current Meters ..... Appendix 297
Figure A11.9: Recorded Unit Characteristic Curve as a Function of the Number of Dynamic Ott C31-A Current Meters ..... Appendix 298
Figure A11.10: Recorded Unit Characteristic Curve as a Function of the Number of Dynamic Ott C31-R Current Meters ..... Appendix 298
Figure A11.11: Recorded Unit Characteristic Curve as a Function of the Number of Applied Single Acoustic Paths (Right to Left) ..... Appendix 299
Figure A11.12: Recorded Unit Characteristic Curve as a Function of the Number of Applied Single Acoustic Paths (Left to Right) ..... Appendix 299

Figure A11.13: Recorded Unit Characteristic Curve as a Function of the Number of Static General Current Meters ..... Appendix 300
Figure A11.14: Recorded Unit Characteristic Curve as a Function of the Number of Static Ott C31-1(Plastic) Current Meter ..... Appendix 300
Figure A11.15: Recorded Unit Characteristic Curve as a Function of the Number of Static Ott C31 Type A Current Meters ..... Appendix 301
Figure A11.16: Recorded Unit Characteristic Curve as a Function of the Number of Transiting General Current Meters ..... Appendix 301
Figure A11.17: Recorded Unit Characteristic Curve as a Function of the Number of Transiting Ott C31-1(Plastic) Current Meters ..... Appendix 302
Figure A11.18: Recorded Unit Characteristic Curve as a Function of the Number of Transiting Ott C31 Type A Current Meters ..... Appendix 302
Figure A11.19: Recorded Unit Characteristic Curve as a Function of the Number of Applied Single Acoustic Paths (Right to Left) ..... Appendix 303
Figure A11.20: Recorded Unit Characteristic Curve as a Function of the Number of Applied Single Acoustic Paths (Left to Right) ..... Appendix 304

LIST OF SYMBOLS

a_{blade}	Current meter blade characteristic 1
A_{blade}	Current meter blade area
$a_{c\text{-}face}$	Area of a cell face
A_{BFSn}	Backwards Facing Step Velocity Distribution “nth” coefficent
A_p	Axial pulsation correction factor
A_{pn}	Axial pulsation
A_{CS}	Flow path cross sectional area
b_{blade}	Current meter blade characteristic 2
b_{cal}	Intercept of the current meter calibration curve
$C_{friction}$	Coefficient of friction between the current meter hub and propeller
C_{mdrag}	Mean transverse drag coefficient of the current meter blade
C_{mdrag}	Mean transverse drag coefficient of the current meter blade
$C_{\varepsilon 1}$	Turbulent closure Coefficient
$C_{\varepsilon 2}$	Turbulent closure Coefficient
$C_{\varepsilon 3}$	Turbulent closure Coefficient
d_{prop}	Diameter of the current meter propeller
D_{HCi}	Distance of the “ith” current meters from the horizontal centerline
D_{VCi}	Distance of the “ith” current meters from the vertical centerline
F	F Statistic value
f	Turbulent shedding frequency
g	Acceleration due to Gravity
GC_n	Generator efficiency equation coefficients
H	Hydroplant net head
h_i	Height of the “ith” acoustic path
HC_n	Intake head loss equation coefficients
H_{DT}	Draft tube head loss
H_I	Intake head loss
H_{Losses}	Total head loss along a streamline
H_T	Turbine head loss
H_C	Conduit height at the measurement cross section
H_{CS}	Cross section height at the acoustic time of flight measurement Section
H_{Step}	Backwards Facing Step Height
I_{prop}	The moment of inertia of the current meter propeller
i_{ROI}	Point “i” within the radius of influence

i_V	Number of the “ith” vertical current meter
i_H	Number of the “ith” horizontal current meter
i_{ap}	Number of the “ith” sampling point along the acoustic path
k	Turbulent kinetic energy
K	Current meter propeller pitch
K_{DT}	Draft Tube Loss Coefficient
K_α	Porous Internal Resistance
K_β	Porous Viscous Resistance
L	Current meter cord length over which values are averaged
l_{bev1}	Current meter blade beveling length 1
l_{bev2}	Current meter blade beveling length 2
l_{blade}	Current meter blade length at radius r_{blade}
l_{Rh}	Current meter blade length blade hub
m	Current meter wall effect coefficient
$\dot{m}$	Total mass flow rate
m_{cal}	Slope of the current meter calibration curve
$\dot{m}_{c\text{-}face}$	Mass flow rate through a cell face
n_{AP}	Number of acoustic paths
N_{ap}	Number of sampling points along the acoustic path
n_{bins}	Number of data discrete data sources
N_{Blades}	Number of blades on the current meter propeller
$n_{population}$	Number of data points in the entire dataset
n_{sample}	Number of data point from each data source
N_{ROI}	Number of points within the radius of influence
N_{CM}	Number of current meters
N_V	Current meter horizontal resolution
N_H	Current meter vertical resolution
P	Local Pressure
p_a	Axial turbulence fluctuation frequency
P_{AP}	Length of the acoustic pulse path
p_t	Transverse turbulence fluctuation frequency
P_{ROI}	Power used in the radius of influence method
P_{Gen}	Power Generated
P_{Blade}	Current meter propeller blade pitch
P_1	Pressure at streamline point 1
P_2	Pressure at streamline point 2
P_{Load}	Plant load
Q	Volumetric Flow Rate

Q_{mes}	Measured volumetric Flow Rate
Q_i	Volumetric flow rate through the “ith” unit
Q_{imax}	Maximum volumetric flow rate through the “ith” unit
Q_{imin}	Minimum volumetric flow rate through the “ith” unit
r_1	Current meter blade angle at beginning of bevel 1
r_2	Current meter blade angle at beginning of bevel 2
r_{blade}	Propeller blade radius
R_{Mblade}	Radius from the current meter axis to the propeller blade midpoint
R_h	Hub radius of current meter blade
R_t	Tip radius of current meter blade
s	non-Cartesian distance value
St	Strouhal number
S	Shear rate source term
t	Time
t_u	Time for an acoustic path to travel upstream
t_d	Time for an acoustic path to travel downstream
T_{axial}	Axial torque
$T_{friction}$	Friction torque
T_{P1}	Transducer Location 1
T_{P2}	Transducer Location 2
$T_{transverse}$	Transverse torque
TC_n	Turbine efficiency equation coefficients
u_{apa}	Average velocity in the x direction over the acoustic pulse path
u_{apl_iap}	Velocity in the x direction at the “ith” sampling point on the acoustic path
U_{BFS}	Backwards Facing Step Velocity Distribution
u_i	Instantaneous fluid velocity in the x direction
u_j	Instantaneous fluid velocity in the y direction
u_k	Instantaneous fluid velocity in the z direction
u_i'	Transient fluid velocity fluctuation in the x direction
u_j'	Transient fluid velocity fluctuation in the y direction
u_k'	Transient fluid velocity fluctuation in the z direction
U_i	Mean fluid velocity in the x direction
U_j	Mean fluid velocity in the y direction
U_k	Mean fluid velocity in the z direction
U_{Path}	Acoustic Path Average Velocity
V	Local velocity magnitude along a streamline
V_{a_mean}	Mean axial velocity along acoustic path
V_{t_mean}	Mean transverse velocity along the acoustic path

v_{apa}	Average velocity in the y direction over the acoustic pulse path
v_{apl_iap}	Y velocity at the “ith” sampling point on the acoustic path
V_{axial}	Velocity parallel to the axis of the current meter
V_{avg}	Average velocity in the measurement cross section
V_{AM}	Measured acoustic time of flight velocity over acoustic pulse path
$V_{mesaxial}$	Velocity measured by the instrument based on the calibration
V_{maxial}	Mean velocity parallel to the axis of the current meter
V_{meter}	Rotational velocity of the current meter propeller
V_n	Velocity normal to a surface
$V_{population}$	Velocity data from the entire dataset
V_{sample}	Velocity data from each data source
V_{Trans}	Velocity transverse to the axis of the current meter
V_{mtrans}	Mean velocity transverse to the axis of the current meter
V_1	Velocity at streamline point 1
V_2	Velocity at streamline point 2
w_{apa}	Average velocity in the z direction over the acoustic pulse path
w_{apl_iap}	Velocity in the z direction at the “ith” sampling point on the acoustic path
w_i	Legendre-Gauss quadrature weight of the “ith” acoustic path
W_{out}	Power Extracted by the Unit
W_C	Conduit width at the measurement cross section
W_{CS}	Cross section width at the acoustic time of flight measurement section
x_1	Location 1 along the x axis
x_2	Location 2 along the x axis
x_{api}	Location of the “ith” acoustic path sampling point on the x axis
x_{apb}	Location of the beginning of the acoustic path on the x axis
x_{ape}	Location of the end of the acoustic path on the x axis
x_i	Cartesian point location in the x direction
x_j	Cartesian point location in the y direction
x_k	Cartesian point location in the z direction
x_{step}	Downstream distance from backwards facing step
y	Distance from a wall
y_1	Location 1 along the y axis
y_2	Location 2 along the y axis
y_{api}	Location of the “ith” acoustic path sampling point on the y axis
y_{apb}	Location of the beginning of the acoustic path on the y axis
y_{ape}	Location of the end of the acoustic path on the y axis
y_{step}	Distance from the wall
z	Distance in line with the gravitational force

z_1	Elevation at point 1
z_2	Elevation at point 2
z_{api}	Location of the “ith” acoustic path sampling point on the z axis
z_{apb}	Location of the beginning of the acoustic path on the z axis
z_{ape}	Location of the end of the acoustic path on the z axis
α_{SST}	Turbulent closure Coefficient
α_1	Turbulent closure Coefficient
β	Turbulent closure Coefficient
β^*	Turbulent closure Coefficient
γ	Specific Weight
Δp	Pressure differential
Δl	Distance between current meter measurement points
$\delta \forall$	Nominal Volume
ε	Dissipation per unit mass
η	Unit efficiency
$\eta_{Generator}$	Generator efficiency
η_i	Efficiency of the “ith” unit
η_{mes}	Measured turbine efficiency
$\eta_{Turbine}$	Turbine efficiency
θ_{apx}	Acoustic path angle in the x direction
θ_{apy}	Acoustic path angle in the y direction
θ_{apz}	Acoustic path angle in the z direction
θ_B	Current meter propeller sweep angle
θ_{Blade}	Mean angle of current meter propeller blade
$\theta_{Streamline}$	Angle between gravitational direction and streamline normal
θ_{AP}	Angle of the acoustic path
λ_a	Axial turbulent intensity
λ_t	Transverse turbulent intensity
μ	Dynamic Viscosity
μ_T	Eddy Viscosity
ν	Kinematic viscosity
ρ	Density
ρ_{prop}	Density of the material comprising the current meter propeller
σ_ε	Turbulent closure Coefficient
$\sigma_{\omega 2}$	Turbulent closure Coefficient
Φ	Transient scalar value in a turbulent flow
ϕ	Intransient mean scalar value in a turbulent flow
ϕ'	Transient turbulent fluctuation of a scalar quantity
φ_s	Hydraulic characteristic calculated in the radius of influence study
Ψ	Distance between points in the radius of influence study
ω	Specific dissipation rate
$\hbar\upsilon$	Known hydraulic characteristics

CHAPTER ONE
MOTIVATION

Hydroelectric power provides approximately 6% of total domestic energy generation.[101] Hydropower plants include one or more turbine-generator units, with each turbine-generator unit having a unique relationship between flow rate, head differential, and power output. Of these, the unit flow rate is the most difficult of the values to accurately measure. This relation is typically represented in a Hill Diagram (Figure 1.1) or a characteristic curve diagram (Figure 1.2) which depicts the performance of the unit across the range of variables and at a specific head differential respectively.[27][76]

The primary economic drivers for accurate unit characteristics are: optimizing how each unit is allocated to meet the plant's power demand (known as the Unit Commitment), and ensuring contractual performance requirements are met. Optimal Unit Commitment allows the plant operator to maximize the amount of power produced by the plant by selecting the unit, or combination of units, which is able to meet electric demand most effectively. Contractual performance requirements refer to the agreement between vendors and plant operators for the minimum acceptable characteristics resulting from a product or service rendered; measured by the differential in unit characteristics before and after the service.

Over the lifetime of a unit, small changes in unit efficiency have significant value. For example, a one percent decrease in the unit efficiency of a 42 MW unit represents a loss of 4.6 million dollars over its lifetime (50% capacity factor; electricity price of 50 USD/MWh; unit lifespan of 50 years).[17][29] Because of the level of influence of flow measurement on unit performance tests, test standards were developed by the American Society Mechanical Engineers (ASME) and the International Electrotechnical Commission (IEC) in an effort to ensure uniformity of measurement accuracy.[6][37] The application of flow measurement methods

that conform to these standards should achieve measurement errors of less than two percent; however, the flow must have a fully developed turbulent velocity profile to ensure this. A fully developed velocity profile is a predictable velocity distribution within the conduit caused by viscous stress between the fluid and the wall, however a sufficient “development length” of conduit is required for the viscous stresses to overcome velocity distribution at the conduit entrance. Plants with short converging intakes do not have sufficiently long or uniform conduits to produce this profile and, because of this, the plants are unable to measure flow rates or monitor unit efficiency with confidence using the prescribed numbers of flow measurement instrumentation. Considering this, the objective of this thesis is to answer the following: [1] what is the relationship between the number of applied flow measurement instrumentation and flow measurement accuracy? and [2] what is the economic viability of applying each sensor quantity given the cost of flow measurement and its relation to plant revenue? To answer these questions the author will perform the work structure outlined in Figure 1.3.

The research outlined below contributes serval novel components over the process of answering the research questions above. These will be discussed below and can be best discretized into the three primary areas of research that were performed. The first novel contribution addressed in the development of the computational fluid dynamic model is that the simulations represent the first published investigation into the dependence of the velocity distribution in short converging hydropower intakes on the inlet boundary conditions as well as the closure model employed. The investigation has several implications on subsequent research because it will provide guidance as to the sensitivity of the velocity distribution to both the direction of the flow in the intake and it demonstrates the extent of the computational resources that should be invested into modeling the intakes. In addition the research investigates the presence of a recirculation zone found within the intake, which has implications on both the value of flow measurement accuracy and the structural health of the plant. A final

component of the computational fluid dynamic work that was developed as a part of this investigation is that the application of CFD methods to flow measurement has not achieved full acceptance and the work performed acts to demonstrate the extent to which CFD measurements can be leveraged to inform flow measurement. The section of the research focused on developing the simulation of sensor response also produced several novel contributes. The first is the synthesis of historical experimental results along with an understanding of the fundamental operating characteristics of current meters to develop a generalized equation which has the capabilities to demonstrate the response of propeller current meters to non-ideal flow conditions. The research also contributes significantly to the modeling of sensors within flow paths overall because the techniques developed below are done in a highly modular fashion, thereby enabling their rapid application to a wide range of other intakes as well as flows in other closed conduits. The value analysis section of the research presents an established methodology which converts the changes in measured unit efficiency into the monetary benefit that could be obtained through increased flow measurement accuracy. The method builds previous advances discussed in the background section and not only demonstrates how the rate of return on investment in flow sensors changes, it also identifies the point at which it is no longer economically viable for further sensors to be applied. The efforts performed over the course of the dissertation have two overarching contributions with the first being the insights gains regarding the investigation into Lower Granite. The results specific to the plant naturally provide information for local best practices, however these results can also be leveraged to provide insight into sensor economics of other hydroplants with short converging intakes. In addition to this the entire methodology has been developed in such a way that it can be readily applied to a wide range of hydroplants given the requisite information, thereby providing site specific insight into the value of flow measurement accuracy.

CHAPTER TWO
BACKGROUND AND LITERATURE REVIEW

The five sections presented discuss: [1] hydropower plant types in terms of configuration and hydraulics; [2] calculation of efficiency and flow measurement; [3] application of computational fluid dynamics modeling to intake flow fields; [4] calculation of the value of flow measurement and [5] Previous relevant research performed at Lower Granite Lock and Dam.

Types of Hydropower Projects

One way to classify hydropower projects is through their storage capacity, which broadly discretizes plants into storage and mainstem projects. Storage projects (Figure 2.1) have significant retention capacity and a long penstock to convey water from the reservoir to the plant.[84] The length of the penstock allows the velocity profile to become fully developed and therefore flow measurement in conventional projects is covered by the existing test codes.[83] The design of Mainstem projects (Figure 2.2) is a result of the minimization of project development costs.[104] One of the primary ways that this is done is through the integration of the powerhouse (where the turbines are located) into the dam structure itself.[45][106] The relevant implication of this is that the water is conveyed to the turbine via a shaped entrance in the dam. This entrance is known as a short converging intake and because of its minimal length the flow is not fully developed; therefore, flow measurement in mainstem projects is not addressed in the test codes. Within the classification of short converging intake types, it is important for the reader to note that there are several subcategories whose unique geometrical characteristics have the capability to affect the flow field within the intake and therefore the overall flow measurement accuracy. The desire to investigate how the value of flow measurement changes over the range of different subcategories is the rationale for the development of the subsequent analytical methods and codes in a broadly applicable manor. There are four primary types of mainstem hydroplants. The first of these has a symmetrical

constriction of the walls of the intake leading to the turbine and has vertical trashracks. The second type also has vertical trashracks but has an asymmetrical constriction of the flow path. The third type also contains an asymmetrical flow constriction but rather than vertical trashracks, the structure has inclined trashracks. The last type of short converging intake possesses a slightly elongated, non-linear intake flow path and inclined trashracks. An analysis of the Tennessee Valley Authority's fleet of hydroplants has demonstrated the following percent distribution of their plants with short converging intakes amongst the types listed above respectively: 15%, 69% 8%, and 8%.[49] The plant studied in the following thesis is a type three short converging intake, though it should be noted that even within the subcategories of plants there are variations which reflect the nonstandard nature of hydroplant construction that has the capability to impact overall flow measurement accuracy.

Unit Efficiency and Flow Measurement

Unit efficiency is the ratio of the power produced by the unit to the amount present in the water passing through the dam as demonstrated in Equation 1 below. Determination of both the acceleration of gravity and water density is straight forward and therefore will not be addressed in this report. Quantification of both the net head and power produced is achieved using a well-established, relatively inexpensive method described in detail in the relevant test codes and therefore will also not be discussed. In contrast with these, the flow rate is difficult and relatively expensive to accurately measure because it must be inferred from field measurements taken by sensors which are costly to purchase and install.[81] In order to determine the efficiency of the unit over its production range, multiple, discrete, efficiency tests at varying flow rates are performed and then interpolated across the power production range of the unit.[56]

$$\eta = \frac{P_{Gen}}{g\rho QH}$$

Equation 2.1

Unit Flow Measurement

Current meter and acoustic time of flight systems are two of the most commonly applied types of flow measurement in all types of hydroelectric plants and due to a combination of technical and practical constraints flow measurement in short converging intakes almost always precludes the use of any other techniques.[1] [4][24][68]

Current Meters

Current meters (Figure 2.3) are mechanical devices which record the local fluid velocity by measuring the rate of rotation of the propeller at the end of the device.[99] The ideal hydraulic condition for current meters is steady laminar axial flow which is what is used to calibrate the instrument. The calibration process records the rotation rate of the current meter propeller when exposed to axial flow over a series of flow rates. A linear fit is then developed to quantify this relationship, allowing for unknown flow rates to be assessed using the rotation rate of the meter (Equation 2.2).[39] The response curves are unique to each class of turbine, therefore requiring that they are tested prior to use. Several of such tests relevant to this research have been provided to the author.[61] [32]

$$V_{maxial} = m_{cal}\overline{V_{meter}} + b_{cal}$$

Equation 2.2

Outside of these conditions the user must take several characteristics of the instrumentation into account. The first is the response of the current meter to transverse flow. Ideally when exposed to transverse flow the current meter should only record the component of fluid velocity in line with the shaft of the current meter; however, field measurements have demonstrated that this is not

the case.[47] Each specific subtype of current meter has a unique response to this, and given the tendency naturally occurring flows to have transverse fluid components several investigations have been performed. The most comprehensive version of this was developed by Fulford et al. who exposed 14 different types of current meters to flows at different angles of incidence. The rotation rate incurred at each angle was then used to determine what flow rate would be predicted given the calibration curve developed using strictly axial flow conditions. The results of this demonstrated a general trend for all horizontal axis current meters (the only type used in the subsequent research). At small angles of incident (+/- 20 degrees) performance represented the ideal current meter fairly well, however beyond this angle performance began to vary significantly. The study was limited to +/- 70 degrees because significant error was uncovered outside of this. This effect as can be seen in Figure 2.4 demonstrated below. In addition to studying the effect of non-axial flow, the study also investigated the effect of fluid velocity on current meter response to transverse flow components. The study was performed at 10 and 30 degrees (thereby within and without the well-behaved response region) and found that the current meters had nominal variations in response because of flow rate. The one exception to this was the Valeport Model 001 current meter, which experienced a significant variation at the highest velocity tested, this current meter was not investigated in the following study.[32] While the research by Fulford et al, does not represent all of the research done in this area, it is the most comprehensive. A similar study was performed by Kolupaila which demonstrated a general compliance with the results from Fulford, however the types of current meters were not specified thereby limiting the use of this study to the research developed in this thesis.[47] In addition to this other studies were developed to investigate the effect transverse flow however, in many cases, these were performed in a limited way or on current meters that are no longer under production.[2][28]

Turbulent effects must also be addressed when investigating the use of current meters because they are impacted by the turbulent fluctuations to the mean flow. This was first demonstrated in 1852 by Yarnell et al who placed current meters downstream of bluff bodies in a testing channel and observed the effect that turbulent fluid structures shedding off of the bodies had on current meter responses. Unfortunately, techniques had not yet been developed at that time to assess turbulence levels and therefore responses were recorded as a function of the type of body placed in the flow.[112] Subsequent research into current meter response to turbulent pulsations was primarily done by mounting a current meter on an oscillatory device and placing it in a steady stream of water. The current meter was then made to move back and forth, in a steady motion and the rotation rate of the current meter propeller was then recorded to determine the effect. The natural drawback of this is that only one frequency was studied in the test, however this method enabled an understanding of the effect of turbulence of current meter registration. This was done over several studies, each with varying types of current meters and hydraulic conditions.[13][28][31] [34][43] Of these studies the work performed by Jepson as well as Fulford stand out because it was performed over a wide range of current meter types, thereby demonstrating the sensitives of the current meters. One of the primary variations between these studies is the frequency of current meter oscillation with Fulford and Jepson having a range of 0.03-0.914 and 2.62-10.5 cycles per second respectfully. The combination of these studies demonstrates that at higher frequencies of axial pulsation the flow rate is over predicted whereas at lower frequencies the flow rate is underpredicted. In addition to this the studies demonstrated that as the magnitude of the variations increased there was a corresponding increase in over-estimation of the fluid velocity.[31][43] The other variation that was observed is that Jepson also studied the effect of transverse turbulence on current meter performance. This was done by turning the oscillating device (in this case a scotch yoke see Figure 2.5) sideways such that the mean flow was still axial to the propeller and the velocity pulsations were constrained to the transverse

direction.[43] It will be noted that the investigation by Fulford was performed on a range of currently available current meters (Ott C-31 variants, and Valeport models 001 and 002) whereas Jepson studied turbulent effects on an earlier version of the Ott C-2 current meters. The primary variation between these two types is the diameter of the current meter, with the C-2 modeling being roughly half of the size of the other models.[31][43]

The appropriate use of current meters to measure the flow rate is dictated by these industry codes: [1] ISO's Standard 3354, [2] ASME's Performance Test Code (PTC) 18 and [3] IEC's International Standard 41.[6][37][40] PTC 18 and IEC 41 primarily focus on using the flow rate informed by the use of current meters to determine the characteristic curve of the plant and refer the reader to ISO 3354 for the specific use of the current meters to determine the flow rate. If hydraulic conditions are fully developed a minimum of 25 measurement points are required. However, if the flow is suspected to be irregular the minimum number of points is specified by Equation 2.3 with more measurement points to be added at the user's discretion.[37]

$$24\sqrt[3]{A_{CS}} < N_{CM} < 36\sqrt[3]{A_{CS}}$$

Equation 2.3

The standards further address the positioning of current meters and the conversion of the measured velocities into a flow rate. Current meters are applied either statically or dynamically. The traditional application of current meters is to a static support grid constructed within the flow path (Figure 2.6).[77] However, this is rarely used due to expense and logistical conflicts. The dynamic method involves mounting the meters horizontally on a trolley which is incrementally lowered in the intake of the plant as shown in Figure 2.7.[33] This is far more common because it costs less, requires fewer current meters, and is easier to implement. A key advantage of the dynamic method is that it does not require the unit to be dewatered.[40] An area of note is that ISO 3354 does not specify the

requisite vertical and horizontal resolution of meters. This has significant implications because the required number of measurement locations can be achieved with a minimal number of current meters by simply increasing the number vertical stops of the trolley. The result of this practice is extremely high horizontal resolution with minimal vertical resolution which can potentially lower flow measurement accuracy as demonstrated by the author in the appropriate citation.[16] Code approved spacing of the measurement locations is specified by Equations 2.4 and 2.5 which describe the appropriate locations as a function of distance from the center of both the horizontal and vertical accesses, respectively. During the test, the instruments are exposed to the flow for a minimum of two minutes at each location and the recorded velocities at each point are averaged to mitigate the effect of velocity fluctuations.

$$D_{HC_i} = \frac{W_C}{2}\sqrt{\frac{i_H}{N_H/_2 - 1}}$$

Equation 2.4

$$D_{VC_i} = \frac{H_C}{2}\sqrt{\frac{i_V}{N_v/_2 - 1}}$$

Equation 2.5

The velocities measured by individual current meters are converted into an average velocity along the horizontal transect using Equation 2.6. This is a weighted averaging technique which is comprised of several different constituent equations. The average velocity between meters is typically determined using the influence of the four nearest current meters using Equation 2.7. In the case of the exterior points (Δl_1 and Δl_5 in Figure 2.10) and exterior adjacent points (Δl_2 and Δl_4 in Figure 15), an alternative equation must be used (Equation 2.8 and 2.9 respectively) because there are an insufficient number of adjacent measurement

points. This process is performed on all the horizontal transects, producing a series of average velocities along the vertical centerline. Equation 2.6 is then reapplied to these values to determine the average fluid velocity; which is then converted to the flow rate by multiplying it by the cross-sectional area of the conduit.[40]

$$V_{avg} = \frac{1}{L}\left[V_1\left(\frac{m\,\Delta l_1}{m+1} + \frac{{\Delta l_2}^2}{12m\Delta l_1} + \frac{7\Delta l_2}{12} - \frac{\Delta l_3}{12}\right) + V_2\left(\frac{\Delta l_2}{2} + \frac{7\Delta l_3}{12} - \frac{\Delta l_4}{12}\right) + \sum_{j=3}^{n-2} V_j\left(\frac{7\Delta l_j}{12} + \frac{7\Delta l_{j+1}}{12} - \frac{\Delta l_{j+2}}{12} - \frac{\Delta l_{j-1}}{12}\right) + V_{n-1}\left(\frac{\Delta l_n}{2} + \frac{7\Delta l_{n-1}}{12} - \frac{\Delta l_{n-2}}{12}\right) + V_n\left(\frac{m\Delta l_{n+1}}{m+1} + \frac{{\Delta l_n}^2}{12m\Delta l_{n+1}} + \frac{7\Delta l_n}{12} - \frac{\Delta l_{n-1}}{12}\right)\right]$$

Equation 2.6

$$V_{avg_{CM_{Edge}+1 \rightarrow CM_{Edge}+1}} = \frac{7V_i}{12} + \frac{7V_{i-1}}{12} - \frac{V_{i-2}}{12} - \frac{V_{i+1}}{12}$$

Equation 2.7

$$V_{avg_{CM_{Edge}+1 \rightarrow CM_{Edge}+2}} = \frac{6V_i}{12} + \frac{7V_{i-1}}{12} - \frac{V_{i+1}}{12}$$

Equation 2.8

$$V_{avg_{CM_{Edge} \rightarrow CM_{Edge}+1}} = V_i\left[\frac{m}{m+1} + \frac{1}{12m}\left[\frac{\Delta l_{i+1}}{\Delta l_i}\right]^2\right]$$

Equation 2.9

Acoustic Time of Flight Meters

The acoustic time of flight technique uses a pair of acoustic transducers (Figure 16) mounted on opposing sides of the conduit (Figure 2.11) to determine the

average fluid velocity across the acoustic path formed between the sensors. [14][71] In the first step of the process, an acoustic pulse is directed from the upstream transducer to the downstream transducer. In the second step, the downstream transducer directs another acoustic pulse towards the upstream one. The transit periods of the two steps are recorded and the differential is used to predict the average fluid velocity along the acoustic path. In the first step the pulse is sped up by the motion of the water and in the second the pulse is slowed down causing the differential transit time. Because an acoustic time of flight pair records a single acoustic transect, additional instrumentation is required to fully capture the flow distribution. Unlike the current meter method, the measurement resolution is strictly a function of the number of acoustic modules applied in the vertical direction.[14] [16]

The ideal hydraulic condition for the use of acoustic time of flight is purely axial flow however, because this is not present in short converging intakes the effect of transverse flow must be addressed.[109] Its presence alters the transit time of the acoustic pulse similarly to axial flow because a component of the transverse flow is aligned with the acoustic path and therefore speeds up or slows down the acoustic pulse as well. Because of this, the measured axial flow rate taken in the presence of both transverse and axial flow is incorrect unless compensated for accordingly.[6] This is done by applying an additional transducer pair with the opposite orientation as shown in Figure 13.[14] The mean velocity recorded by each acoustic path is averaged thereby removing the influence of the oblique flow because in one case the pulse is sped up and in the other the pulse is slowed.[6][37]

While transverse flow is the most commonly addressed concerned with the application of the acoustic time of flight method there are three other points which have the potential to affect the accuracy of the applied method. The first is that the acoustic time of flight technique captures the variations in fluid velocity

resulting from turbulent fluctuations. Due to the discrepancy between the speed of sound in water and the fluid velocity the acoustic pulse fully captures the effect of individual turbulent pulsations within the flow (albeit in an aggregated fashion).[109] This effect was studied by Strunz et al. who uncovered a linear relation between the standard deviation of the error caused by turbulent fluctuations and the fluid velocity. As a result of this study it became apparent that as fluid velocity increases, it is critical to increase the number fluid velocity samples to ensure the mean flow velocity is accurately recorded.[80] To mitigate this concern it is common practice within industry for measurements to be taken at a high frequency for an extended period of time (5-7 minutes or greater) to ensure that the full range of turbulent fluctuations are captured thereby providing an accurate mean.[107]

The other two points of concerns attributed to the application of acoustic time of flight are attributed to the presence of the acoustic time of flight instrumentation within the flow path itself. The effect of this is twofold with the first resulting from the fact that the acoustic time of flight path does not start from the wall instead, there is a small offset equivalent to the height of the transducer. The resulting shorter acoustic path length results in an over-prediction of the flow rate. The second effect of this is that flow stagnates upstream of the acoustic time of flight transducer. This causes a reduction in local velocity and therefore a reduction in the measured fluid velocity overall. The effects of these are thought to generally cancel out under the provision that the height of the transducer is less than 0.25% of the acoustic path length.[6] The height of the transducers studied in this research represents a value slightly less than this enabling the author to follow the code base correction factor for the presence of transducers within the flow.[72][88] While guidance is not provided acoustic path lengths at the scale of those investigated the author was able to leverage guidance for the largest conduit which states that a flow rate correction factor of an additional 0.05% should be applied.[6]

PTC 18 and IEC 41 recommend the application of 4 dual path time of flight meters at a location with a minimum of 10 straight diameters upstream and 3 downstream. If these conditions are not available, it is recommended by the PTC 18 code that 9 dual paths should be applied. The conversion of the time differentials between the up and downstream travel time to the average axial velocity along the acoustic path is described in Equation 2.10. The location of the acoustic paths and their use to predict the flow rate is governed by the Gauss-Legendre Quadrature numerical method. Quadrature is a technique that allows the user to integrate over a length by selecting the values from appropriate points along the length; weighting them and summing them (Equation 2.11). The measurement locations are determined by solving for the zeros of the polynomial created by Equation 2.12 and the weights for each of the locations are established by Equation 2.13.[53]

$$V_{a_mean} = V_{t_mean}\tan(\theta_{AP}) + \frac{P_{AP}}{2\cos(\theta_{AP})}\left(\frac{1}{t_d} - \frac{1}{t_u}\right)$$

Equation 2.10

$$Q_{mes} = \frac{H_{CS}W_{CS}}{2}\sum_{i=1}^{n_{AP}} w_i V_{AM}$$

Equation 2.11

$$0 = \frac{1}{2^{n_{AP}} n_{AP}!}\frac{d^{n_{AP}}}{dH_{CS}{}^{n_{AP}}}\left(H_{CS}{}^2 - 1\right)^{n_{AP}}$$

Equation 2.12

$$w_i = \frac{2}{(1 - h_i{}^2)\frac{d}{dh_i}\left(\frac{1}{2^{n_{AP}} n_{AP}!\frac{d^{n_{AP}}}{dh_i{}^{n_{AP}}}\left(h_i{}^2 - 1\right)^{n_{AP}}}\right)}$$

Equation 2.13

Computational Fluid Dynamic Modeling

The use of CFD in hydropower has traditionally been limited to the design of turbines because of the cost and complex nature of simulation specific coding.

However, due to recent advances in computational power and the development of commercial software which rapidly allows the user to produce a model, the use of CFD in hydropower has become increasingly viable. The principle of CFD is that the equations which describe the conservation of energy, mass, and momentum within a fluid flow can be solved by discretizing the computational domain and solving iteratively. One technique to do this is the Finite Volume Method, a process which separates the domain into a series of contiguous volumes. The conservation equations are integrated over each of the control volumes; producing a series of coupled algebraic equations describing the flux of the equations between the volumes. These equations are then placed in a matrix and solved iteratively. The user-defined boundary conditions which drive the solution include inflow; outflow, pressure and turbulence characteristics. The finite volume method is used in a majority of commercial codes because of its robust nature and ability to solve over an unstructured grid, making it more applicable than the finite difference method many CFD models. There are two significant areas which influence the solution of the CFD model; the first is the resolution of the calculation points (known as mesh), and the equations which are used to describe the fluid flow.

Mesh resolution is important because it impacts both the resolution of the results and their accuracy. Because appropriate mesh density is case specific, it is common practice within industry to perform a mesh resolution study. The appropriate mesh density is determined by incrementally increasing its resolution and comparing the results of the completed simulation to those produced by lower resolution simulations.[78] A review of applicable studies demonstrated that a typical mesh for a short converging intake contains between 1 and 10 million nodes.[9][46][58][79][81]

Another important aspect is the selection of the appropriate turbulence model. The difficulty with the solution of the Navier-Stokes equations is that they cannot

be directly solved for because the Reynolds Stress tensors within the time-averaged equations introduce more unknowns than there are equations. This discrepancy is known as the closure problem of turbulence. There are a variety of methods to determine an approximate solution for the closure problem, representing the fundamental differences between the different turbulence models. Prior CFD simulations performed on short converging intakes have all used two equation models to introduce additional information, specifically the k-ε, k-ω and Shear Stress Transport models. These models assume different equations for the balance between the production and dispersion of turbulent energy within the flow. The k-ε method models the balance between the transport of turbulent energy and the dissipation of turbulent kinetic energy. It performs well when modeling external flows and computational memory requirements are reduced because it uses wall functions. A consequence of this is that the model performs poorly when simulating adverse pressures and flow separation. The k-ω technique models the balance between the turbulent kinetic energy and the dissipation per unit kinetic energy. Wall functions are also used, however, the structure of the equation allows for a much more accurate representation of internal flows because it tracks vorticity within the flow. The k-ω method is significantly more sensitive to freestream conditions than the k-ε method and therefore a k-ε model is typically produced first and used as the initial conditions for the model. The SST model actually is a combination of the k-ε and k-ω models, where the k-ε is used in the freestream and the k-ω is used in lieu of wall functions. Given the lack of wall functions this model gives the most accurate estimation of the flow field of the presented methods, however convergence rate concerns typically necessitate that the results of one of the other models is used as the initial condition estimation (similar to the relation between the k-ε and k-ω methods).[20][78][111]

A majority of CFD simulations of hydropower intakes have selected the SST method for their final model. The author was unable to find published literature

that utilized a more advanced method (such as LES or DES).The SST model was found to produce acceptable representations of the flow field when compared to field measurements.[9][11][46][50][69][79][81] One exception to this was when the plant trashracks were not included in the model, resulting in the predicted turbulent kinetic energy being approximately half of that which was measured within the actual intake.[50] The other exception to this is in the case of Almquist, Taylor, and Walsh where the results of the CFD had poor correlation with the velocities measured in the field.[3] This was assumed to be a function of inaccurate upstream boundary condition selection, highlighting its importance. Because determining the precise boundary conditions is extremely difficult, all the prior studies included an upstream section that was felt sufficiently large enough to naturally produce the appropriate distribution at the intake. Nicolle and Proulx performed an experiment which was designed to investigate the impact of varying angles of intake flow on the downstream velocity distribution of a short converging intake. This investigation found that varying intake velocity angles resulted in an average pressure variation of 3% within the scroll case of the unit.[58] No specific information was provided about the velocity variation that occurred in the intake of the unit.

Value of Flow Measurement

Accurate hydroplant flow measurement plays an integral component in the effective operation of a hydroelectric system. It should be noted however that due to its fundamental nature, it is difficult to completely quantify the value of flow measurement accuracy in hydroplants. The following section is designed to provide the reader with insight into both the breath of the effect of accurate flow measurement and the complex nature of measuring flow into and out of the reservoir system. The latter of these is critical to a discussion regarding flow measurement because it enables hydroplant operators to better understand and predict the availability of water in the plant reservoir. Effective reservoir management (which is enabled by accurate flow measurement) allows plant

operators to maximize plant revenue while also meeting the complex range of reservoir/plant operational constraints.

For the purposes of this discussion flow measurement accuracy manifests itself in three primary ways, with the first of which being the confirmation of unit performance. The unit performance is determined by assessing the efficiency by which the unit can produce power using Equation 2.1 across the range of potential unit power production. An accurate measurement of this enables plant operators to document the deterioration of system performance throughout the year because of system operation; and determine the appropriate threshold for the implementation of repair or maintenance. Unit performance is then used in this process as well because a determination of system efficiency before and after a plant upgrade or maintenance enables both the operator and service provider to determine if contractual performance requirements have been met. Unfortunately, given the sensitive nature of these contractual agreements, there has not been any published information associated with the benefit of the confirmation of unit performance. The only work available was presented by the author at a conference in the summer of 2015. This research analyzed field measured data to produce an approximate velocity distribution at the gate slot of a short converging intake. This was then used to investigate the evolution of flow measurement accuracy achieved by increasing numbers of current meters. The results found that even at the highest level of simulated instrumentation, unit performance was overestimated an average of 0.82 percent.[16] As the investigated unit was rated to 40 MW it can be estimated that this inaccuracy has an opportunity cost of 3.6 million dollars over a 50 year period (assuming a capacity factor of 50% and a price of electricity of 50USD/MWh). This is particularly relevant given the increasing age of the domestic hydropower fleet which will require increasing levels of maintenance. [100]

Another way in which accurate unit flow measurement is critical to the operation of hydropower plants is the method in which it acts to demonstrate the amount of

water passing through the dam. Knowledge of the amount of water entrained in the reservoir affects many attributes of the plant from both a technical and regulatory standpoint. In the case of the latter, many plants have a minimum flow requirement to ensure that the plant is in legal compliance for passage of water downstream. [38][42] The flow rate that must be passed is a result of site-specific ecological and social requirements for passage of water through the system. The Federal Energy Regulatory Commission is tasked with ensuring that these flow rates are maintained. [26] Outside of this, there are also regulations regarding the height of the reservoir as this also has social and ecological implications as well. In addition, the height of the reservoir also affects the operation of the dam from a technical and operations perspective. For the purposes of this research this is largely observed by the fact that the height of the reservoir affects the amount of energy contained within the fluid, and therefore the amount of energy that can be produced by water within the reservoir. On the opposite end of the spectrum, a minimum water elevation must be maintained to ensure proper operation of the units. If the water level is drawn down excessively, not only does the energy contained within the water correspondingly lower there is the possibility that air from the surface will be drawn into the hydroplant. The entrainment of air in the flow entering the plant is extremely hazardous to the operation of the plant and therefore significant effort is placed on ensuring that the minimum water level is maintained. [5] To mitigate this it is recommended that a minimum intake submergence depth of 1.5 times the height of the intake itself is maintained.[67] Given the demonstrated importance of reservoir height, there are several mechanisms by which this is evaluated and controlled. The primary mechanism by which this is measured a sensor (physical or acoustic) which directly recorded reservoir height and this is able to recorded to a high level of accuracy.[6] Despite this level of accuracy in reservoir height there is not a mechanism by which the volumetric flow of water into and out of the reservoir is recorded to a similar level of accuracy. Rather, the flow into and out of the dam is assessed using the sum of two gages on the rivers upstream of the reservoir (for the inflow) and

calibration curves for the water released by the spillway, units and lock systems for the outflow.[94] As such any inaccuracies in the recorded inflow and outflow mechanisms, which the subsequent research demonstrates is on the order of 18.5 m^3sec^{-1}, will take an extended period of time to manifest themselves on the reservoir height measurement given the significant surface area of most reservoirs. In Lower Granite, the surface area is 36 km^2, and therefore at the nominal rate quoted above a month of such variation would result in only 1.3 meters of surface height variation.[95] The following dissertation addresses the accuracy to which flow through the units can be recorded however it is important to briefly explore the flow measurement accuracy in the other aspects of the reservoir flow path. The first of these is the spillway system within lower granite which is comprised of eight 15.24 by 18.44-meter radial gates.[95] Radial gates are curved, solid surfaces located in the path of the spillway which can be rotated vertically to produce a gap between the top of the concrete spillway surface and the bottom of the gate allowing water to pass through. The equations which assess the flow rate though the gates have been demonstrated to under predict the flow rate and have an uncertainty ranging between 3 to 5 percent.[98] An analysis of the historic flow passing through Lower Granite demonstrated that 15.67 percent of reservoir outflows travel through the spillway, though it is operated incrementally throughout the year. A majority of the spillway flow occurs between April and September.[94] The other primary outlet outside of the turbines and the spillway is the navigation locks at Lower Granite. While there has not been an appreciable amount of research performed into the accuracy of navigation lock flow rates, it is assumed to be reasonably accurate as it represents an isolated volume which is incrementally filled and lowered between known heights. Furthermore, if Lower Granite is assumed to have the same annual number of lock cycles as Lower Monumental, another dam on the Snake River, the volume passes through the lock represents 0.89 percent of the total flow through the reservoir.[65][94][96][98] The measurement of flow into the reservoir itself is also subject to uncertainty and therefore also can obscure the effect of

flow measurement inaccuracy though the units. This was demonstrated by Herschy to be approximately five percent of the flow rate measured under ideal conditions.[36] Given the confluence of uncertainty associated with the flow into and out of the reservoir it can be observed that inaccuracy associated with flow measurement through the unit might be misassigned to one of the other flow structures. This would then lead the opportunity cost associate with sub-optimization of power production to be perpetuated significantly.

The final role of flow measurement accuracy on hydropower plants is its use to optimize unit dispatch. Optimized plant dispatch refers to the process of using the unit, or combination of units which is able to use the minimum amount of water to meet load demand. Water conservation allows the plant to produce additional electricity and therefore additional revenue. Optimum unit dispatch represents a constrained optimization problem whose objective function (Equation 2.14) is subject to inequality constraints (Equation 2.15) and an equality constraint (Equation 2.16) at each plant load level. From this calculation process, it is apparent that an accurate function for the unit efficiency over the production range of each unit is imperative because it specifies the amount of produced energy in Equation 19. The results of this optimization process on a two-unit plant can be seen in Figures 2.13 through 2.15. The first of these displays the efficiencies of the units over their production range, demonstrating the difference between the two. These are then used to inform the optimization process which displays how power production is most effectively divided between the units (Figure 20). The overall plant efficiency corresponding to this unit power allocation is displayed in Figure 2.15.[15]

$$minimize\ [\sum_{i=1}^{N_U} Q_i]$$

Equation 2.14

$$Q_{imin} \leq Q_i \leq Q_{imax}$$

Equation 2.15

$$P_{Load} = g\rho H\left[\sum_{i=1}^{N} Q_i \eta_i(Q_i)\right]$$

Equation 2.16

The Tennessee Valley Authority (TVA), a federally owned hydropower operator, is one of several utilities which implements optimized unit dispatch. Optimized unit dispatch is implemented with WaterView. The optimization algorithm in WaterView also implements constraints that include discharge requirements, cavitation avoidance zones, and constraints to reduce the frequency of unit starts and stops. While fleet-wide information about the impact of WaterView is unavailable, a single plant was reported to have increased efficiency by over 4 percent through optimization.[51] Outside of this, there have been several case studies in which unit optimization has been investigated and employed, leading to plant efficiency increases between 1 and 4.4 percent. The relation between increased electrical production and increased revenue is specific to the production of the facility however, one case study found that optimization had the potential to produce an additional 9,704 MWhs boosting revenue nearly half a million dollars annually.[18] The anecdotal rule for the benefit associated with the implementation of an optimization scheme is that the increase in plant efficiency is roughly equivalent to the maximum variation in unit efficiency divided by the number of units.[17]

The Hydropower Advancement Project (HAP) by the Department of Energy at Oak Ridge National Laboratory also explored the effect of system optimization. This investigation was comprised of case studies on 5 separate facilities to determine the differential between the: installed; current and potential production capacity. Installed capacity refers to the potential electrical production that was available when the plant was new. The current capacity is the existing (typically

reduced) production availability of the facility resulting from the extended operation. The potential production level specifies the capacity of the plant if various upgrades were applied. One of the potential upgrades investigated was unit optimization. For the two publicly released reports, system optimization alone was found to result in a mean efficiency increase of 3.5% and 2.2%.[59][60] The potential benefit associated with plant optimization quantified in the HAP research lead to the development of the Hydro Performance Calculator (HPC) a tool to assess the value of optimization. The HPC uses unit characteristics and plant loading profiles provided by the user to determine opportunity costs incurred through suboptimal operation of the plant.[52]

An expanded investigation was recently performed by the Electric Power Research Institute (EPRI) which simulated the change in optimization for plants with varying numbers of units (2, 3, 5 and 7) with unit performance differentials of 1, 2.5 and 5% across the units. In addition to this, three different plant loadings were simulated along with different levels of system optimization to determine the impact of the performance differentials. This study found that the performance differential between equally loaded units and optimally loaded units ranged between 2 and 6 percent. Most interestingly, the study determined the effect of improper unit characterization on plant dispatch optimization, finding that 1, 2.5 and 5% inaccuracies in unit characteristic curves caused corresponding inefficiencies of 0.205, 0.482 and 0.96% respectively. The findings of this paper roughly follow the same general trend of the rule of thumb presented by Cook and Walsh discussed above.[23]

From the abbreviated discussion above it should be evident to the reader that quantifying the value of flow measurement is extremely difficult as this process requires an accurate understanding of the value of water at a specific site. In addition to this it is important to understand that due to both the scale of water traveling through the system and the extremely long life of the effects of small percent efficiency losses are magnified. While the subsequent research will

largely focus on quantifying both the volume of water non-optimally assigned for power generation and the approximate value of the water it is important for the reader to understand that the scientific process of establishing the holistic value of water is still under development.

Lower Granite Research

The following section is designed to provide the reader with an understanding of the hydropower plant studied over the course of this research. As such background information of the plant is provided as well the historic plant operation data used in the research. The thesis focused on Unit 4 of Lower Granite Hydroelectric Plant (Figure 2.16), which is located on the Snake River in the Columbia River Basin. The plant is operated by the United States Army Corps of Engineers and the power produced by the plant is distributed by the Bonneville Power Administration. The generation facilities at Lower Granite are comprised of 6 Kaplan units, with a combined capacity of 810 MW and a rated head of 94 feet.[25][101] Outside of the generation capabilities, Lower Granite has several operational drivers outside of the basic generation of power which affect the operation and structure of the dam itself. The primary attribute of this pertinent to the research performed is the juvenile fish bypass system (Figure 2.17).[97] This system is designed to prevent juvenile fish (known as fry) from passing through the turbine on their way downstream. This is a concern due to the large number of migratory fish species in the northwest which travel upstream as adults to spawn and whose fry then subsequently travel downstream as adults. (U.S. Army Corps of Engineers) The upstream passage is achieved at the site through the use of a fish ladder and the downstream passage is performed with the use of a fish screen system in the intakes of the units. The submerged traveling screens are 20 by 20 foot structures which can be lowered into either the intake bulkhead slot or the fish screen slot of each intake bay. The angle of the screens is adjustable allowing for a modification of the local hydraulic

conditions to be optimized for fish passage. The screen location, as well as the structure itself, can be observed in Figure 2.18 below.[54] [89] [90]

Prior to discussion of pertinent work on Lower Granite, it is important to note that rationale behind modeling an existing project. This is critical for the success and applicability of the work because it allows for the use of realistic plant geometries; unit efficiencies and field measurements (which will facilitate validation of the CFD models of the unit). A single unit is analyzed rather than the entire plant because the development of a high-resolution CFD model of the plant is excessively computationally expensive. This truncation is supported by the fact that unit performance tests are usually limited to a single unit and performance is assumed to be identical between units. The following section will address the nature and results of four previous studies whose findings were leveraged in this work. In addition to this, the source and specification of historic site data are discussed.

Reservoir Drawdown Study

The first study performed at Lower Granite whose results were leveraged in the dissertation work was an investigation designed to evaluate options to mitigate the effect of dam operation on juvenile fish. This study was prompted as awareness of the existing dam structure's (which was completed in 1979) effect on the local ecology became better understood. As a result of this three options to modify the structure of Lower Granite were investigated in 1991 to determine the path which would reduce the effect of the dam on fish while minimizing the effect on dam operation. These options included: upgrading existing fish handling facilities and operating the dam to prioritize fish passage survivability, the construction of significant fish bypass infrastructure such as surface collectors and submerged bypass screens, and the breaching of the dam itself to remove the earthen embankment to allow the free passage of water around the side of the powerhouse and spillway structure. While the section option was selected for implementation the results of the third study provided critical information that was

used for the subsequent research and therefore the work and the pertinent results will be briefly discussed.[91][93]

To achieve the breaching of the Lower Granite embankment in a controlled fashion it was determined that the reservoir would need to be drawn down significantly prior to the removal of the embankment. A highly expedited draw-down of the reservoir was evaluated to put the structure of the embankment at risk of failure during the drawn process, and therefore the evacuation of the reservoir was limited to 0.6 meters of elevation per day. It was determined that performing the draw down using the spillway would introduce levels of dissolved gas into the river that would prove to be detrimental to downstream environmental health. Given this, along with a desire to minimize the cost of the operation, it was decided to achieve this by passing the water through the powerhouse of the dam. The plan to do this involved two discrete sections. The first phase involved the use three of the units in passing water through the plant to lower the reservoir level 6 to 12 meters. Such a reduction in reservoir height would place the units well outside of their operating envelope and therefore the remaining three units were modified to allow water to be drawn down even further. The modifications were required because the operation of the turbines under the low head conditions had the potential to significantly damage the unit. To mitigate the potential for this the researchers proposed physically cutting the blades off the Kaplan turbine. To confirm the effectiveness of this methodology model testing was performed on a 1:25 ratio model of the unit without its blades. This test investigated fluid velocities at a series of vertical transects within the center of Bays C and B. While this was performed over a range of flow rates the only publicly available dataset from this investigation was taken at a scaled flow rate of 283.2 m^3sec^{-1}. The results of this can be observed in Figure 2.19 below.[87]

Stay Vane and Wicket Gate Modification Study

The second study performed at Lower Granite which pertains to the research developed in this thesis is an investigation performed in 1995 into the effect of stay vane and wicket gate geometry on hydroplant performance. The overall objective was to determine if water quality and plant performance improvements could be achieved through minor modifications of the distributor assembly as had been attained in similar studies on similar dams (McNary and Bonneville hydoplants). The research into this was developed over with two discrete research thrusts: a computational fluid dynamic study and scale model investigation to compare the as-built geometry of the hydroplant and the modification which provided the highest performance improvement in the CFD study. The computational study leveraged the k-ε turbulence closure model and investigated four different stay vane and wicket gate geometries. They were: the as-built geometries, mild modifications to a subset of the geometry, mild modifications all of the structures, and significant modifications to all of the structures. This investigation indicated that the second variation provided the best performance improvements for the amount of effort that would need to be expended on flow path modification. Unfortunately, specific details of the CFD model (computational domain, boundary conditions, mesh density, etc.) were not published in the official report.[103]

The physical investigation to confirm these results was performed at the VA Tech facility on a 1:25th scale model of Lower Granite. As previously stated the second modification was compared to the original geometry, however, in addition to this, the study also investigated the effect of the fish screens and trash racks on system performance. The study was performed by evaluating the power produced given simulated head and flow rates through the model domain. The study simulated prototype flow rates ranging from 11,000 to 25,500 ft^3sec^{-1} at heads of 98.5 and 105 ft. Overall it was observed that significant operational improvements (0.5% and 0.7% with the modified wicket gate and stay vanes and

a modified turbine runner respectively) could be attained through the modification of the flow path. The results of this investigation can be observed in Figure 2.20 below.[103]

Lower Granite Site Performance Testing

One of the most important pieces of previous work used in this investigation were the results of the Lower Granite site performance tests. The site testing was performed in 2004 as a part of a larger research thrust by the American Society of Mechanical Engineers to evaluate the application of flow measurement techniques in hydroplants with short converging intakes. This specific study investigated the use of acoustic time of flights sensors within each of the intakes bays. There were 18 acoustic paths (9 dual paths) applied in both the vertical and horizontal orientation, resulting in a total of 108 applied acoustic paths between the bays. For feasibility reasons the acoustic paths were applied downstream of the bulkheads (Figure 2.21) in each bay as it limited the extent to which the unit had to be dewatered. The spacing of the paths in Bay A strictly followed the procedure outlined by the PTC 18, however because there were acoustic paths previously applied in Bays B and C (in the 4 dual path configuration) minor modifications were made in the numerical method to allow the investment in these acoustic paths to be leveraged for this study. This was necessary because as the number of acoustic paths changes the spacing of the paths correspondingly changes as seen in Equation 2.12. To determine the appropriate mean velocities to populate the numeric method, the velocities were interpolated over the height of the bay to create a continuous function for the mean velocity. The appropriate heights were then used as inputs to these equations, yielding the values leveraged in the flow measurement study.[108]

The acoustic time of flight flow meters were then leveraged in the development of the site performance test resulting in an evaluation of system performance at 490 individual instances. Half of these were performed with the fish screens

discussed above installed and half were done without the screens. Furthermore, measurements were performed 5 times with the same system controls and averaged, thereby increasing confidence in the results of the study (therefore 49 different control system characteristics were evaluated within and without the fish screens). The flow rate in the study ranged from 290.7 to 632.3 m^3sec^{-1} thereby capturing the entirety of the operational window of the unit. The power generated at each test case along with the measured velocities by each acoustic path was provided in the results. Interestingly the acoustic time of flight flow meters demonstrated a consistent recirculation zone at the top of the bay at the measurement section. In the case of the horizontal acoustic paths, this was manifested by a negative velocity along the top acoustic path, whereas in the case of the vertical acoustic paths significant distortions in the mean velocity were recorded.[92][108] This indicated that the recirculation region existed over the entire width of each of the intake bays. The results of this align with a prior investigation into the influence of significant flow recirculation on the acoustic time of flight results.

Lower Granite Historical Market Data

The final information from Lower Granite leveraged in this work is historical information regarding the generation of the plant and the price of power in the marketplace where electricity produced by the plant is sold. Information regarding the generation of the Lower Granite is publicly available and provides hour level resolution on the plant level generation. This data set can be observed in Figure 2.22 below for 2016 and 2015 (Figures a and b respectively). This data is available from 2006 to 2016 and largely follows the general trend indicated in the Figure below. Site generation peaks between March and June before falling to a yearly low from July to September.[94]

The second critical component of historical data used in this research is the local market price data to establish the historical cost of the energy produced by Lower

Granite. The energy created by Lower Granite, along with 30 other hydroelectric sites and one nuclear facility, is sold by the Bonneville Power Administration (BPA). The BPA acts as a wholesale utility and therefore sells its power to a range of utilities and industrial customers, but does not actually sell power to residential users.[8] Given this sales arrangement, the sale price of electricity varies not only between the customers served but also within the individual power markets of the individual consumers. A comprehensive investigation of the intricacies of the domestic power market are beyond the scope of this research effort, however, an important attribute of this is a value known as the locational marginal pricing of electrical power. This is the theoretical price that would be required for the development of one additional unit of electrical power in the electrical marketplace given the optimized dispatch of available generators.[30] The locational market price is established at a range of specific locations within the grid, known as nodes, allowing for an accurate understanding of the true value of electricity at a regional level. While market data was unavailable to identify the specific economics of the BPA system, the author could access historical market data from the Mid-Columbia regional day ahead market. This data is provided by the Intercontinental Exchange which is a venue in which a significant majority of domestic electric commodities are traded. The Mid-Columbia represents the primary trading house within the northwest of the United States and therefore provides reasonable resolution of the market value of electricity within the region. The cost information provides insight into the highest, lowest, and average price of electricity over the course of a day. Data was provided for nearly every day in 2016, with only 59 days missing from the dataset. The profile of electrical cost in the region can be observed in Figure 2.23. In this, the average price of electricity is 24.16, 21.17, 22.61 dollars per megawatt-hour ($/MWh) for the daily high, daily low and weighted average respectively. Beyond this, the electrical price follows a general seasonal trend with the price at the beginning of the year being nearly 30$/MWh, which falls as the spring progresses. In the summer the value of electricity spikes to a yearly

high which is, in one case was nearly triple the cost of electricity at the beginning of the year. The value of electricity then drops off in the fall and experiences a brief increase in price near December.[102]

CHAPTER THREE
COMPUTATIONAL FLUID DYNAMICS THEORY

The following section will provide the reader with an overview of fluid flow modeling to demonstrate the underlying principles of the CFD models used in this research and provide an explanation of why specific models were leveraged. The two subjects will be discussed in more depth than those found in the background section above and therefore an additional chapter was included in this work. The overall purpose of this section is to place the research in context and provide a rationale for model selection and assumptions. The primary difficulty in modeling turbulent flows is understanding the random, turbulent, pulsations which characterize the fluid flow in this regime. Due to the chaotic and multi-scale nature of the fluid flow, there is no comprehensive equation which can accurately capture the essence of the fluid flow. While significant progress has been made in the modeling of these flow, the primary mechanism by which these are simulated uses Reynolds Time Averaging. This is a process implemented to mitigate some of the complexity of turbulence equations and thereby extract actionable information, the generalized process is that turbulent characteristics can be effectively be represented by a mean and fluctuating term (Equation 3.1). If a time average is then taken of these quantities, turbulent effects are then eliminated and only the mean characteristics remain. The process assumes that the time scales which represent turbulent fluctuations are much lower than that which governs the larger flow.[82]

$$\Phi(s,t) = \phi(s) + \phi'(s,t)$$

Equation 3.1

Traditionally Reynolds Time Averaging is applied to the three equations (the conservation of mass, momentum, and energy) which represent the characteristics of incompressible fluid flow with constant properties in an effort to

derive actionable information. When considering the incompressible conservation of mass equation (Equation 3.2), Reynolds decomposition yields Equation 3.3 which naturally can be simplified into Equation 3.4 due to the time averaged nature of turbulence. When the process is applied to the intransient momentum equation (Equation 3.5) the result is as found in Equation 3.6 however this does not simplify as directly as the continuity equation because the time average of multiplied turbulent terms cannot be reduced to zero. As such it can be observed that the final terms are strictly a function of turbulent terms. These terms are known as Reynold's stresses.[12]

$$\frac{\partial u_i}{\partial x_i} = 0$$

Equation 3.2

$$\frac{\partial U_i}{\partial x_i} + \frac{\partial \overline{u'_\iota}}{\partial x_i} = 0$$

Equation 3.3

$$\frac{\partial U_i}{\partial x_i} = 0$$

Equation 3.4

$$u_i \frac{\partial u_i}{\partial x_i} + u_j \frac{\partial u_i}{\partial x_j} + u_k \frac{\partial u_i}{\partial x_k} = -\frac{1}{\rho}\frac{\partial p}{\partial x_i} + \mathrm{v}\left(\frac{\partial^2 u_i}{\partial {x_i}^2} + \frac{\partial^2 u_i}{\partial {x_j}^2} + \frac{\partial^2 u_i}{\partial {x_k}^2}\right) + \rho g$$

Equation 3.5

$$\begin{aligned} U_i \frac{\partial U_i}{\partial x_i} + U_j \frac{\partial U_i}{\partial x_j} + U_k \frac{\partial U_i}{\partial x_k} \\ = -\frac{1}{\rho}\frac{\partial P}{\partial x_i} + \mathrm{v}\left(\frac{\partial^2 U_i}{\partial {x_i}^2} + \frac{\partial^2 U_i}{\partial {x_j}^2} + \frac{\partial^2 U_i}{\partial {x_k}^2}\right) + \rho g \\ + \left(\frac{\partial \overline{{u'_\iota}^2}}{\partial x_i} + \frac{\partial \overline{u'_\iota u'_J}}{\partial x_j} + \frac{\partial \overline{u'_\iota u'_k}}{\partial x_k}\right) \end{aligned}$$

Equation 3.6

In this process it can be observed, while the equations have been simplified (though not shortened) in a generalized manner, the additional Reynolds stress terms impart additional terms to the equations which predict turbulent fluid flow leaving more unknown terms than equations to describe them. The differential between these two is known as the Closure Problem of Turbulence, and significant effort has been expended on the behalf of the scientific community on developing equations which act to provide the requisite information to solve these equations. These efforts can be broadly categorized by the number of equations which are used to provide this information. The most widely used methods leverage two equations to describe the flow and leverage the Boussinesq hypothesis. This hypothesis states that the viscous stresses at the end of Equation 3.6 can be modeled as viscous stresses multiplied by a hypothetical Eddy Viscosity term. The following research uses two such models to solve the closure problem, specifically the k-ε and shear stress transport k-ω methods which will be briefly explored below. It should be noted that because of the well-established nature of the terms and their implementation in the research via commercial software the following discussion will primarily focus on assumptions and associated implications of the models.[111]

The k-ε two equation model provides the requisite information as a function of the kinetic energy per unit mass of the turbulent fluctuations (k) and the dissipation per unit mass of the flow (ε). The generalized equation for kinetic energy (Equation 3.7) is comprised largely of 6 separate terms, with the first term on the left-hand side represents the kinetic energy rate of change and the second left term is the convective transport of energy. The first on the right-hand side demonstrating the specific kinetic energy that will be gained due to eddies within the flow. The second term on the right-hand side specifies the dissipation of this energy into heat at the lowest scales of turbulence, and the third displays the dissipation of the energy throughout the volume due to motion. The final term dictates the transportation of kinetic energy within the volume due to pressure

fluctuations. From the complexity of this equation, it can be observed that the kinetic energy equation must be coupled with another term to provide the requisite information to solve for the Reynolds Stresses.[12] From a dimensional perspective, this term must be introduced in such a way that the turbulent length scale can be assessed such that the Reynolds stresses can be assessed. It is important to note however that this is strictly based on a dimensional analysis of the stresses rather than on any fundamental physics. Given this, ε is introduced under the assumption that this value is roughly equivalent to the ratio of the turbulent kinetic energy and the turbulent length scale. For brevity, the author will not delve into its derivation of, as this is a lengthy process not strictly pertaining to the research and is well documented in a series of sources.[12][111] It is important to note however that a series of variations were produced in efforts to develop models which provide increasing levels of accuracy. The version that is used in this research is the Realizable k-ε model which proposes the dissipation equation found in Equation 3.9. This model was selected because has been shown to perform better in cases with recirculation and jets than others sub-models such as RNG k-ε and Standard k-ε.[7] In addition, it is important to note that in the commercial code used in the research wall functions were leveraged in the numerical solution of this model. Wall functions assume the velocity profile of the fluid flow near the wall to varying degrees based on the resolution of the mesh near the wall. The rationale behind the use of these is that the flow in this region is extremely complex due to cascading vortices resulting from shear between the fluid and the wall. In order for the numerical method to capture this vorticity, a high-resolution mesh must be employed which can be extremely computationally expensive. To do this the velocity profile nearest to the wall (known as the viscous sublayer) is assumed.[75]

$$\rho\frac{\partial k}{\partial t}+\rho\frac{\partial U_i k}{\partial x_i}=\mu_t\left(\frac{\partial u'_j}{\partial x_j}+\frac{\partial u'_i}{\partial x_i}\right)\frac{\partial U_i}{\partial s_j}-\mu\frac{\partial\overline{u'_\iota}}{\partial x_k}\frac{\partial\overline{u'_\iota}}{\partial x_k}$$
$$+\frac{\partial}{\partial x_k}\left(\mu\frac{\partial k}{\partial x_k}-\frac{1}{2}\rho\overline{u'_\iota u'_\iota u'_\jmath}-\overline{p'u'_\jmath}\right)$$

Equation 3.8

$$\rho\frac{\partial\varepsilon}{\partial t}+\rho\frac{\partial u_j\varepsilon}{\partial x_j}=\frac{\partial}{\partial x_j}\left[\left(\mu+\frac{\mu_t}{\sigma_\varepsilon}\right)\frac{\partial\varepsilon}{\partial x_j}\right]+\rho C_{\varepsilon 1}S\varepsilon-\rho C_{\varepsilon 2}\frac{\varepsilon^2}{k+\sqrt{\nu\varepsilon}}+C_{\varepsilon 3}\frac{\varepsilon}{k}$$

Equation 3.9

The other model used in this research was the shear stress transport variation of the k-ω initially proposed by Wilcox in 1988.[111] This was produced by Menter in 1994 and acts to combine the k-ω with the k-ε method. This model also leverages the Boussinesq hypothesis to determine an appropriate length scale to estimate the eddy viscosity of the fluid. The numerical method prescribed for this technique was determined through the substitution of the dissipation rate for the dissipation per unit mass terms found in Equation 3.9 above. While the numerics of this process are not developed in this thesis result of this process can be observed in Equation 3.10 below. In this, it can be observed that the resulting equation can be broadly seen as a three-term function resulting from the use of the separation function (F_1) embedded within the larger equation. In the region near the wall, this function is 1, thereby including the last term of the equation which produces an operational equation very similar to that produced by Weber. As the distance from the wall to the cell in questions grows the wall blending function then begins to reduce in magnitude to the point where the value approaches zero in the freestream region of the flow. At this point, the equation for the turbulent length scale in this region produces results similar to the traditional k-ε model.[55] This turbulence model has been widely accepted by industry (as discussed above) given its ability to achieve the benefits of both models. The primary concern that has been expressed in the use of this model is that the blending function is considered to be somewhat arbitrarily places and

that the Boussinesq theory is still relied on for the development of the model. Despite this the model has been shown to provide more accurate results than the strictly k-ε based models without the high sensitivity to initial boundary conditions observed in the application of the k-ω model.[7][55]

The other critical attribute of the SST however, is that wall functions are not traditionally employed to represent flow near the wall as one of the primary strengths of the approach is its ability to capture the turbulent dynamics specific to this region. To effectively achieve this, however, the initial cell near the wall must have a y+ value of one as this indicates that the viscous sublayer of the wall region has effectively been captured. The y+ value acts as a non-dimensional distance which demonstrates the ratio of turbulent influence to laminar influence. As such, the mesh resolution is required to be fine enough at the wall region to allow the numerical method to accurately capture the fluid dynamics. The implementation of this is somewhat challenging in large-scale computational domains as meeting this requirement can significantly increase the number of cells within the domain and therefore the computational expense of the simulation. To circumvent these concerns however, many commercial solvers have implemented techniques to allow for the application SST method in such applications. The code leveraged in the following research, Star-CCM+, employs a technique which evaluates local hydraulic conditions to assess if the local mesh will provide adequate resolution to capture the viscous sublayer. If inadequate mesh resolution is present to calculate the wall region without the use of wall functions Star-CCM+ implements the appropriate wall function to reflect the anticipated hydraulic characteristics that were not captured in cell nearest to the wall. Figure 3.1 demonstrates the three discrete regions in which wall functions can be employed to capture. The use of these functions enables the user to apply the SST method reliably to a mesh which does not achieve a y+ value of 1 uniformly across the computational domains.[75]

$$\frac{\partial \omega}{\partial t} + u_j \frac{\partial \omega}{\partial x_j} = \alpha_{sst} S^2 - \beta \omega^2 + \frac{\partial}{\partial x_j}\left[(\nu - \sigma_\omega \nu_T)\frac{\partial \omega}{\partial x_j}\right] + 2(1 - F_1)\sigma_{\omega 2}\frac{1}{\omega}\frac{\partial k}{\partial x_i}\frac{\partial \omega}{\partial x_i}$$

Equation 3.10

Where

$$F_1 = tanh\left\{\left\{min\left[max\left(\frac{\sqrt{k}}{\beta^* \omega y}, \frac{500\nu}{\omega y^2}\right), \frac{4\sigma_{\omega 2} k}{C_{CD} y^2}\right]\right\}^4\right\}$$

Equation 3.11

$$C_{CD} = max\left\{2\rho\sigma_{\omega 2}\frac{1}{\omega}\frac{\partial k}{\partial x_i}\frac{\partial \omega}{\partial x_i}, 10^{-10}\right\}$$

Equation 3.12

$$\nu_T = \frac{\alpha_1 k}{max\{\alpha_1 \omega, SF_2\}}$$

Equation 3.13

$$F_2 = tanh\left[max\left\{\frac{2\sqrt{k}}{\beta^* \omega y}, \frac{500\nu}{y^2 \omega}\right\}^2\right]$$

Equation 3.14

As a part of the research effort but before the investigation into flow measurement accuracy the author undertook a preliminary investigation into the effect of mesh resolution near the wall to ensure that the wall functions employed by Star-CCM+ would appropriately model the flow. The research investigated the flow profile over a two dimensional model of a forward facing step (see Figure 3.2) using four different mesh resolutions near the wall and the same mesh distribution in the freestream of the flow. This was achieved by imposing different numbers of prism layers (3, 7, 11, and 15 layers) near the wall within the same total area. The resulting average y+ values along the top of the step were 247.8, 25.07, 3.41, and 0.69 respectively. The shear stress transport k-ω turbulent closure model discussed above in the research was used because this method does not traditionally leverage wall functions and therefore it is important to assess the ability of the wall functions to reproduce the velocity distribution produced by the y+ values less than 1 as the industry best practices recommend.

Three aspects were compared between the models developed from the four different meshes, the first of which was the velocity distribution in the freestream above the step. Velocities were compared at 50 locations along 8 transects taken above the step as seen in Figure 3.2. The results this investigation demonstrated that there was a minimal variation between the models produced with average y+ values greater than 1 and the one produced with an average y+ layer less than one. This is demonstrated visually in Figure 3.3 which documents the velocities recorded at Transect 1, which was found to have the highest level of variation between the produced profiles. It should be noted that the figure does not include the velocity at the walls of the simulation because available velocities at the walls are taken from the near wall cell centroids. Because the height of the near wall cell changes between models the velocity naturally correspondingly changes despite not being indicated in the model. The average difference between the point velocities produced by the models with average y+ values greater than model with an average y+ of 0.69 is 0.45, 0.32, and 0.72 percent for the 247.8, 25.07, 3.41 models respectively. The next section investigated the reattachment length behind the forward facing step produced by each of the different models. This length was assessed as the distance between the front of the step and the furthest cell centroid with an instream velocity at, or below zero. The results of this investigation can be observed in Table 3.1 which demonstrates that the recirculation length is fairly consistent between the different models with a maximum percent difference of 3.2 percent produced by the model with a y+ value of 25.07. The finally study of this preliminary investigation was focused on the variation between the velocity profile in the wall region of the simulation. The reason for the focus on the wall region is naturally to allow an investigation into the applicability of the wall functions to predict the velocity distribution produced by the high resolution mesh. The velocity profiles were found to be similar with the largest variation in the velocity profile occurring immediately after the step (Transect 2). The velocity profile at this point can be seen in Figure 3.4 where it is demonstrated that the performance of the wall functions were observed to

produce a similar profile with the exception of the cell closest to the wall resulting from the mesh with the average y+ value of 247.8. At the cell nearest to the wall the difference between the velocity predicted by the y+ 247.8 mesh and the y+ 0.69 mesh was found to be 19.3 percent however at the next cell this variation was found to be mitigated with the difference being reduced to 2.6 percent. The nearest cell variation was found to improve corresponding to the distance downstream of the beginning of the forward facing step culminating with the near wall velocity profile found in Figure 3.5 which was extracted at Transect 8. This velocity profile demonstrates that the cell nearest to the wall in the y+ 247.8 mesh still experiences a mild variation however outside of this there is a nominal variation between the remaining calculated velocities.

The results of this investigations demonstrated several important attributes of the performance of the wall functions employed by Star-CCM+ when the shear stress transport k-ω turbulence closure model is used. The first is that that velocity in the freestream of the simulation does not significantly vary as a result of the wall resolution. The second is that the reattachment length predicted by the models also does not experience a significant variation resulting from the selection of near wall mesh resolution. The final aspect is the effect of wall functions in the near wall region which. The investigation into this found that at the lowest levels of mesh resolution the near wall cell demonstrated variability from the velocity distribution resulting from the prescribed mesh resolution. The variation was found to be highest nearest to the beginning of the recirculation zone and was fairly low after the flow had reattached. The meshes at higher levels of resolution however were found to demonstrate good agreement over the entirety of the studied domain. The results of this preliminary study support the assertion that the wall functions employed by Star-CCM+ can be effectively leveraged to model the near wall velocity distribution in the following research provided that the average wall y+ value is within a reasonable tolerance of the wall resolution prescribed for the closure model.

In addition to the internal validation to ensure that Star-CCM+ was able to reproduce velocity profiles based on varying wall y+ values, it was also felt important by the author to ensure that the modeling software appropriately represented physical flows. To ensure that this was the case the author elected for perform another study on the evolution of the boundary layer over a flat plate. The topic of the study was specifically selected because it allowed for a direct comparison to the validation files produced by Nasa Langley Research for this purpose. For the purpose of brevity the discussion on the physical domain will be limited to the fact that flow over a non-slip plate was investigated at local Reynolds numbers of 5 and 10 million. The model represented this region in 2 dimensions and the turbulent closure model used in the simulation was the k-omega shear stress transport. Further information regarding the specifics of the simulation can be observed on the appropriate citation. As with the previous investigation the author developed a range of meshes with which to investigate the flow over the step. The only variation between the meshes however, was the number of prism layers modeled within the boundary layer. The average near wall y+ values of the different meshes was: 0.2, 1.6, 37.7, 121.0 and 837.4. Figure 3.6 below demonstrates the near wall velocity profile provided by NASA Langley taken at two points along the length of the plate over which the boundary layer grew.[57] It will be noted by the reader that the NASA profile is extremely close to the anticipated velocity distribution as predicted by boundary layer theory (as found in Figure 3.1). The same equations which predict boundary layer theory were compared to the velocity profiles extracted from the CFD model produced using near wall average y+ value of 0.2 (Figure 3.7). A comparison of Figures 3.6 and 3.7 demonstrate that Star-CCM+ was able to simulate the evolution of the boundary layer to an adequate level using a highly resolved near wall mesh. Unfortunately in the subsequent research was unable to utilize such a refined mesh as it was found to be computationally expensive. To understand and quantify the potential effects of this on the accuracy of the near wall boundary layer in the research presented the author then compared the near wall

velocity profiles produced by the differing values of average near wall y+. The comparison was done at the same point two points as previously and the results of each can be found in Figures 3.8 and 3.9 below. The largest variation between the near wall meshes investigated at each comparison point was found to be associated with the average near wall y+ value of 1.6. The average difference between the u+ values provided by the 1.6 average near wall y+ mesh and the 0.2 averages near wall y+ mesh was 7.8 percent. Given the nominal level of variation between the near wall profiles in both this preliminary investigation and the investigation discussed previously the author is confident in the ability of Star-CCM+ to adequately represent the near wall region of the fluid flow at varying near wall mesh resolutions.

CHAPTER FOUR
METHODS

The following section is designed to address the methods used to investigate the value of flow measurement accuracy in hydropower plants with short converging intakes. The methodology section is discretized into the discrete parts: the development of the CFD models of the unit; the creation of numerical methods to replicate the response of the flow measurement instrumentation within the unit; and the effort to establish the value varying quantities of applied information.

Statement of Assumptions

The following represents a brief discussion of the model sensitivities inherent to the research along with rationales for the exploration or omission of exploration of the sensitivities of the results to the parameter in question. Unfortunately given the scope of the research the vast number of permutations precludes an investigation of all of the subtleties associated with the work performed. Despite this, the assumptions made in the research will be outlined along with the method that was used, or would be used, to study the model sensitivities. The assumptions will be discretized into the three primary research areas, computational fluid dynamic modeling, sensor simulation modeling, and economic evaluation.

Computational Fluid Dynamics

The development of computational fluid dynamic models inherently makes assumptions regarding the equations governing fluid flow. While discussed in depth in the previous chapter the most pertinent attributes will be discussed below along with their relevant implications. The first assumption in the CFD modeling is that the fluid flow can be effectively modeled using a steady state simulation. The decision to model the flow in this was arose primarily from the computational resources that would be required to resolve the range of transient hydraulic characteristics of the flow. The decision to do so is supported due to

the fact that the sensors are sampled over a long period of time in order to capture the effect of these transient characteristics. The effect of this assumption was not studied over the course of this research, however the author recommends in future work that additional computational resources be brought to bear and the hydraulic characteristics resulting from the steady state and transient simulations at points important for this research be compared to ensure that they are similar. Another assumption that was made in this research was that the Reynolds Averaged Navier Stokes turbulence modeling would appropriately calculate the flow through the plant. Inherent to these is the Boussinesq hypothesis which states that the Reynolds stresses can be modeled using the turbulent viscosity. The research employs both the k-epsilon and the Shear Stress Transport k-omega which calculate the turbulent viscosity in different ways as outlined in the Theory chapter of this dissertation. The results of these two closure models are compared to each other in a section of the research where the author investigates the selection of the model. Another assumption imbedded within the research is that the flow in the wall region is modeled appropriately. This can be achieved in two ways, through the creation of a highly resolved mesh in the wall region or through the use of wall functions. In the case of the research below an average wall region y+ value of 25 is employed. As a result of this a hybrid methodology was employed, where the first cell at the wall utilized the appropriate wall functions (see Figure 3.1). To ensure that this behaves appropriately the author performed an investigation into the ability of the commercial software to reproduce a physical velocity profile in the near wall region with a mesh which has a y+ value similar to that found in the modeling of the intake flows. Several additional assumptions were inherit in the modeling of the intake region which include: the distribution of the mass flow rate upstream of the intake; the turbulent characteristics of this flow and the homogeneity of the velocity distribution. These values are important because it has the potential to impact the ability of the computational model to accuracy reproduce the velocity distribution were the sensors are mounted and therefore

the accuracy of the calculated flow measurement accuracy. The effect of the flow directionality was investigated by the author in a preliminary study to determine the extent to which this affected the downstream velocity profile and what combination of mass flow directionality best reproduced the velocity profile present in the intake. The turbulent characteristics selected in this research were specified using data taken from similar hydroplants because field data was unavailable. To this end the author performed an investigation to document the decay of turbulent structures established at the inlet. In future work the author recommends an investigation involving the dependence of the hydraulic characteristics at the flow sensor region on the intake turbulence specifications. The velocity distribution was assumed to be uniform at the upstream computational domain boundaries because the author did not have specifications regard the velocity structure at these points. While this was assessed to be a reasonable assumption given the complexity of the research additional efforts could be developed to investigate its influence on the downstream velocity distribution. Such an investigation would involve heavily perturbing the velocity distribution (while maintain the total mass flow rate) and monitoring how the initial velocity profiles evolve as the flow accelerates into the intake. The final assumptions that were studied in the CFD section of the research apply to the recirculation zone observed in the intake region. As will be discussed below the presence caused the research to take on two separate paths. The first research path assumed that the as-built dimensions provided by the Army Corps of Engineers were accurate and the second assumed that an addition fish screen structure was present in the flow path. As a part of the former several permutations of the CFD model were developed in an attempt to reproduce the recirculation zone found in the unit testing. Unfortunately these were not able to able to create a recirculation of sufficient size to be detected by the flow meters. Despite this the author also investigated the value of flow measurement accuracy using the results of the developed CFD models as this also will provide valuable information to the hydropower industry because hydroplants are specifically

designed not to have recirculation zones develop in their intakes. In the latter investigation into the recirculation zone the author imposed a structure that was not found in the as-built drawings provided. This was assumed to be included as part of the fish screens that were installed after the initial construction was completed. Two dimensions for this structure were developed for this investigation, as will be discussed below, however these were designed specifically to reproduce the recirculation zone. As such, it was assumed that these structures are representative of the geometry within the intake.

Sensor Simulation

The simulation of flow meter responses also contains several assumptions which will be discussed below. The first is that the results of the computational fluid dynamic investigation, which are provided at specific locations within the computational domain, can be reliably converted to the hydraulic conditions at points required for the simulation of the sensors. This is important because it enables the appropriate fluid values to be used in the simulation of the sensors. The author investigated the effect of this by using a range of numerical techniques in the interpolation and then compared the results of each to each other. The simulation of the current meters also contained several underlying assumptions, the first of which being that the sensors could effectively modeled as point measurements. The current meters physically operate as a result of the aggregated fluid flow over the entirety of the propeller and future work will investigate this effect, however the research made the assumption that local hydraulics would be constant over the surface of the meter and therefore the sensor could be modeled as a point measurement. This is supported by the fact that the fluid exhibits internal shear which prevents excessive variation in velocity over a short distance (such as the propeller diameter of 0.1 meters). Another assumption that was made was that the rotation rate of the current meter propeller is a result of the sum of discrete torques that the current meter is subject to. In the physical operation this is not the case as the forces which turn

the propeller interact, particularly in the complex structure of the propeller itself. This is largely a result of the minimal information that was used to inform the calculated response of the current meters. These historical experiments isolated hydraulic characteristics that the current meters would be subject rather that investigate the cumulative effects of multiple characteristics. Future efforts in this area should use the current meter numerics to predict the results of exposure to several torques and follow up with physical experiments to determine the viability of the predictions. In an additional assumption was made regarding the use of historical experimental historical data to develop an equation for the current meter response. In the case of turbulent effects, the available data was not for the four specific current meters investigated in the research, rather the data was regarding the performance of older, smaller version of the sensors. As a result the author developed a generalized equation for the response of the sensors based on physical and hydraulic characteristics that were identified to be important. Naturally in future work the author would recommend physical experiments be performed to validate these effects. In regards to investigating the sensitivity of the torque equation the author would recommend in future work that the correction coefficients below are modified slightly (within the range of their respective R^2 values) to document the extent to which the variations propagate through the value analysis. The final assumption that was made in the modeling of the current meters was that turbulence levels were isotropic. Due to the steady state nature of the CFD simulation local turbulent intensities were calculated using local turbulent kenotic energy levels, unfortunately the kinetic energy is a result of the cumulative effect of turbulent intensities in all directions and therefore an assumption had to be made regarding the turbulent structure. Without insight provided from the field the author elected to assume that turbulent intensities were isotropic, as a future sensitivity study the author recommends that permutations on the ratio of turbulent intensity are investigated to quantify the extent of this impact on the value proposition. The final series of assumptions in sensor modeling naturally arise from the modeling of the acoustic

time of flight paths and several of these are a result of the fact that the author elected to model sensors conceptually rather than physically, the future actions that should be prescribed to model the physics of the sensor are discussed in the subsequent sections. Outside of this however there are several assumptions that were made in the modeling of the acoustic paths. The first of these is that the acoustic path was modeled in the research as series of points along the acoustic path. In the research 20 total points were used in the assessment however a preliminary assessment demonstrated that the addition of more sensor points had a nominal effect. When the number of points was tripled the variation in the average velocity record was less than 0.8 percent.

Economic Evaluation

As will be expressed below the economics associated with quantifying the value of flow measurement accuracy are extremely complex given that flow measurement plays an integral role in the effective operation of the plant and the availability of electrical power acts to impact the market price of electricity. Given this complexity a range of assumptions had to be made to ensure that the research was achievable within the scope of the thesis. The assumptions can be largely grouped into three different categories: assumptions in the conversion from flow measurement accuracy to power produced, assumptions in the conversion from power produced to power revenue, and assumptions in the cost of flow measurement.

The process in which flow measurement is converted to power produced is outlined in appropriate methods section below, however it is important to understand that the primary value of flow measurement assessed within this thesis is a function of the assignment of water to meet energy production requirements throughout the day. To this end the initial economic evaluation depends on the underlying assumption that the non-optimally assigned water within the analysis period (in this case an hour) is used within that same hour for

additional energy production at the efficiency corresponding to the operational characteristics of the unit given the additional generation. While in further research it will be recommended that temporal effects of optimal water use are investigated to do so now would be beyond the scope of the research. On a related note the Family-of-Units assumption will be leveraged in this research to approximate the performance of the other units located in Lower Granite. This assumption had to be made to allow the author to effectively model the generation within the plant and the corresponding generation efficiency across the production scale of the plant. While the performance of the other units within Lower Granite is unlikely to be completely in alignment with this assumption, this is a commonly used within the industry given the cost of unit performance testing. A full exploration of this would require that unit performance be performed over the range of units within a plant and the subsequent research process be employed to investigate the effect that different units within the plant have on flow measurement. It is hoped that the thesis work performed will facilitate such an investigation which will fully demonstrate and quantify the value of flow measurement in a plant. Embedded within the assumption of the plant generating with the non-optimally assigned water within the same hour the plant is operating in is that ramping rates for the plant are neglected. The effect of this is deemed to be relatively nominal because the variances in the measured performance of the units were found to be fairly independent of unit power level. The final assumption in this section is that the conversion of non-optimally assigned water to power it is important to understand that the authors assumption of a constant head level of 100 ft over the course of the research. The specific head was selected because this was the value present in the unit testing and the constant head decision was supported because unit head data was unavailable for the time period investigated as well as the fact that the mainstem style plants do not support significant storage of water.

The quantification of the cost of non-optimally assigned also have several assumptions that were required. The first of which is that the value of the power resulting from the non-optimally assigned water is a function of the difference between the maximum and minimum price of electricity during the day in which the power was generated. The result of this is that the resulting price of the non-optimally assigned water is at a maximum. In the future it is recommended that the investigation into transient generation takes the changing price of electricity into account. In addition to this the author made an assumption that the site is price taking from the Mid-Columbia power exchange. Due to the sales agreements regarding the power produced by Lower Granite from Bonneville Power Authority this is naturally not fully reflective of the price of electric by Lower Granite. Despite this, the Mid-Columbia Exchange provides reasonable insight into the local price of power over the course of the year thereby permitting an acceptable level of understanding in the research.

In the cost of flow measurement there are several assumptions that are broadly made, the first of which is that the sensors will be installed and that site testing will be performed during scheduled down periods for the plant. The result of the assumption is that the opportunity cost for site testing (revenue from generating electricity) does not have to be included in the cost of site testing. The assumption is appropriate because this is standard practice within the hydropower industry. The second assumption made is that the sensors were purchased rather than rented for the research and that sensors were purchased in such a way that flow measurement could be performed simultaneously in all bays. The final assumption within the research is that the cost of site testing as well as the mounting of sensors was not included in the research. The decision to do this was largely based on the significant variation in these costs as this is a result of site geometry as well as site access.

Computational Fluid Dynamics Modeling

The development of CFD models of Unit 4 represents a critical component of the research because they provide a holistic understanding of the hydraulic process present along the flow path through the unit. These hydraulic characteristics are significant because they dictate the operation of the flow measurement instrumentation, enabling an understanding of the effectiveness of the sensors within the unit. As such the author expended significant effort into the development of a model which best replicates the flow distribution in the intake itself. This work is represented in the subsequent section which will initially address the information available to the author regarding the physical domain. This will then be juxtaposed with the computational domain that was utilized in the simulations the rationale for variations between the two will be addressed. Furthermore the selection of the appropriate boundary types, boundary conditions and turbulence closure models will be discussed. In addition to this the development of computational mesh will be discussed as well as the methodology that was used to assess the validity of the results. It should be noted by the reader that the author used Star-CCM+, a finite-volume based commercial CFD software for the development of the computational models. The software not only allows for a myriad of multidisciplinary physical processes to be simulated, it also contains computer aided design and meshing suite. In addition to this, the reader should note that the author elected to constrain the simulation the steady state. The reason for this is twofold, the first is that due to the scale of the computational domain a transient simulation such a simulation would be excessively computationally expensive at the timescales required. Such a timescale would need to be on the order of 2 minutes at a minimum to capture the range of variability that could occur in the flow field.[6][37] The second rationale for the steady state simulation is that because industry performance test codes require an extended period of exposure to compensate for the potential variation in the flow field, the author judged that transient hydraulic structures would not significantly affect the findings and recommendations of the research.

Physical Domain

The physical domain represents the relevant characteristics of the flow path within the unit itself. These details effect on the hydraulic characteristics through incurring head losses, affecting turbulence levels as well impacting the flow profile through the conduit cross section. Given this relevance, the author has elected to discretize the domain into relevant sub-domains and discuss the important characteristics of each briefly in individual sections below. These subdomains are demonstrated in Figure 4.1 below along with the important elevation characteristics for each.

Forebay Subdomain

The forebay of the unit represents the volume of water upstream of the dam which is channeled through Unit 4 or one of the adjacent units within the plant. The geometrical characteristics of this volume are largely unknown by the author, despite bathometric studies that were performed in previous investigations of Lower Granite. The only geometrical information that was made available for this study was that of the face of the dam abutting the forebay as well as the elevation of the water in the forebay itself. For brevity, the figures depicting the upstream dam face are not included in this section. This is achievable given the relatively straight forward nature of the structure itself. The important characteristics are the slope of the dam face (1:6.5) and the forebay water elevation during testing (235.61 m). Unfortunately, the hydraulic characteristics such as turbulence levels and velocity measurements were not available for this site.

Trashrack Subdomain

The trashrack of the intake is the physical structure designed to filter out suspended debris within the water flowing into the unit which might damage or otherwise impact the operation of the dam. This filtering is achieved through the placement of a series of ridged metal bars at the front of the intake structure itself. In the case of Lower Granite the trashrack bars were mounted on a frame

which was lowered to the appropriate location and secured. Due to the size of the intake structure, it was unfeasible to develop one continuous frame and therefore six frames were mounted vertically to achieve the required coverage of each intake bay. An engineering drawing of the frame can be observed in Figure 4.2 below (it should be noted that the level of detail present within the figure has been reduced from its original level to strictly demonstrate characteristics relevant to the study being performed). In this, it should be noted that there are three primary components of the trashrack frame itself. The first are the bar stock components which comprise the outermost surface of the frame and act as the foundation of the structure. The second are a series of secondary support I-beams (three vertical and six horizontal) upon which the trashrack bars are directly attached. The trashracks themselves are represented by fifty thin vertical members, which are directly welded to the secondary supports.[86]

Inlet Subdomain

The inlet itself if is represented as the shaped conduit structure between the trashrack and the scroll case of the unit. The plain view of the Unit 4 intake is demonstrated in Figure 4.3 below. In this figure it can be observed that the intake slopes downward, with the bottom of the intake sloping in a linear fashion and the top in a generally rounded shape As with all short converging intakes this structure rapidly constricts over its flow path from the initial height of 24.59 meters to 14.13 meters over the path length of 30.54 meters along the centerline of the conduit. It should be noted that the intake itself is comprised of three bays (henceforth known as Bays A, B, and C – Labeled in Figure 4.4) with a constant width of 6.40 meters in each bay. In light of this it is possible to observe that the flow path cross section is initially 472.18 m^2 however this decreases to 271.33 m^2 over the course of the intakes. In addition to the multiple bays the intake has several interesting attributes that should be addressed, specifically along the top of the intake wall itself. These aspects are, in order of distance downstream, the Fish Screen Slot, the Bulkhead slot, and the Gate Slot. Little information is

available regarding the geometry of Fish Screen Structure, however the author was informed that the screen itself was not present during the testing performed on the unit.

Scroll Case Subdomain

The scroll case is the spiral shaped-structure designed to route water from the upstream intake bays around the distributor, facilitating the equal radial distribution of water to the turbine itself. The cross section of the scroll case varies radially with the largest area in front of and at the beginning of the scroll case. The cross section of the scroll case then iteratively decreases as flow path wraps around the distributor. This reduction in area is down to ensure that the local velocities remain constant, despite a reduction in overall flow rate due to withdrawals from the flow into the distribution. In the case of Lower Granite, the author was provided with the dimensions of twenty radial transects taken from the scroll case. These transects were taken at 18-degree increments (demonstrated in Figure 4.5a and 4.5b), thereby providing a holistic understanding of the structure overall.

Distributor Subdomain

The distributor is the region between the scroll case and the turbine and is designed to regulate flow into the turbine. This is achieved with two structures, the first of which is the stay vanes which are a series of equally radially distributed vertical members with a wing profiles designed to draw water into the turbine via a pressure differential. The effect of the stay vanes are then complimented by the use of the wicket gates. These structures are placed behind the stay vanes with a slight radial offset (9 degrees) and are also the shape of extruded wings however, they differ because the hydroplant operator is able to change the pitch of these structures. This aspect is vital to the operation of the plant because this establishes the flow rate through the plant overall by introducing a variable head loss. In Lower Granite there are nineteen stay vanes and twenty wicket gates however, it is important to notes that the end of the scroll

case impinges into the stay vane ring, providing a similar hydraulic effect. The distribution of the stay vanes along with the geometry of the cross section can be observed in Figure 4.6a and 4.6b.

Turbine Subdomain

The turbine represents the initial stage of the mechanical device which converts the energy contained within the flow of water to electrical energy. As previously stated the turbine present within Lower Granite is a Kaplan turbine, and therefore it can be thought of as propeller with articulating blades. The changing angle of the blade allows the turbine to harvest different amounts of torque from the water, thereby allowing for a higher level of unit efficiency when exposed to different flow rates. This specific turbine has six blades. Given the proprietary nature of hydropower turbine design, a complete understanding of the turbine geometry is unavailable. However, a reasonable amount of information regarding the hub of the propeller was provided to the author and a sufficient amount of information regarding the blade was derived from the drawings to develop a reasonable representation of the blades (as will be discussed in the next section). A cross section of the turbine is demonstrated in Figure 4.7 and an engineering drawing of one of the turbine blades is found in Figure 4.8.

Draft Tube Subdomain

The draft tube of a hydropower unit has two primary purposes, the first is that is acts as the conduit which returns the water diverted into the unit back to the downstream river. The second aspect of the draft tube is that it acts as a pressure recovery device for the unit. This pressure recovery is necessary because during generation local pressures in the turbine subdomain drop appreciably due to the amount of energy being extracted from the system. As such the leaving the turbine may have sub-atmospheric pressure levels. To increase this to levels that will not induce backward flow from the tailrace, the draft tube cross section expands over the flow path, thereby slowing the flow and increasing pressure levels. Unit 4 specifically has a two-bay draft tube with the

dimensions listed in Figures 4.9. Given these dimensions, it can be demonstrated that the velocity at the exit of the draft tube will be approximately 70 percent of that at the beginning.

Tailrace Subdomain

The tailrace of the unit represents the volume of water downstream of the dam which is delivered through Unit 4, one of the adjacent units within the plant, the spillway or the lock. The geometrical characteristics of this volume are largely unknown by the author, despite bathymetric studies that were performed in previous investigations of Lower Granite. The only geometrical information that was made available for this study was that of the face of the dam abutting the tailrace as well as elevation of the water. As with the forebay section, figures depicting the downstream dam face are not included in this section. This is achievable given the even more straightforward nature of the structure itself. The important characteristic is primarily the water elevation during testing (192.20m). Unfortunately, the hydraulic characteristics such as turbulence levels and velocity measurements were not available for this site.

Computational Domain

The following section will describe the computational domain leveraged to develop the CFD models of Lower Granite flow fields. The computational domain has been discretized into the same subdomains that were employed in the description of the physical domain (Figure 4.10). This will then be used to compare the two to demonstrate areas where the subdomains are the same and highlight areas where they differ. The rationales and implications behind any variations between the two will be addressed. It should be noted by the reader that the author developed the computational domain using the computer aided design software internal to Star-CCM+.

Forebay Subdomain

The following section will address the underlying rationale for the geometry that was used by the author to represent the forebay subdomain in the CFD model. The downstream surface of this subdomain is identical to the upstream face of the dam and therefore assumed to be appropriate. The geometry of this face was developed using the engineering drawings provided by the USACE. The sides of the domain were selected to extend 4 meters beyond the outermost edge of intake bays A and C. This distance was selected because it represents the distance between Unit 4 and the outermost edges of adjacent units. As such this distance allowed for the investigation of the impact of the adjacent units on the flow field present in Unit 4. The bottom and top surfaces of the forebay are at the appropriate distances to represent the river bed and the surface of the river respectively. Both surfaces were assumed to be level and while this is unlikely to be completely representative of the river bottom, it was felt an appropriate assumption on behalf of the author given the lack of other information. The distance between the upstream and downstream faces of the subdomain naturally varies due to the slope of the dam face, however the mean distance is 13.5 meters. This distance was selected for three primary reasons. The first of these is that the shorter upstream length would allow for a more rapid solution of the simulation given available computational power. The second is that the truncated distance has been shown to demonstrate acceptable levels of accuracy in previous simulations.[58][69] The third reason for this distance is that it was anticipated that the velocity distribution of the upstream boundary would have more effect on the accuracy of the simulation than the upstream distance modeled.

Trashrack Domain

The modeling of the trashrack within the simulation was done with several simplifications. Rather than model the entire structure discussed above the author elected to only model the horizontal secondary supports. The trashrack members themselves were not modeled by the author because it was felt that

they would require a prohibitively dense computational mesh to capture the effects. The vertical members were not included because the author felt that the effects of the much more numerous horizontal members (36 horizontal and 3 vertical) would dominate the effect of the trashrack on the downstream section where the sensors were simulated. Additionally, rather than model the horizontal members as I-beams the author elected to model them as bar stock equivalent to the maximum dimensions of the I-beam. This was done because the computational resolution required to capture the effect of the small I-beams was determined to be prohibitive, and the effects of this type of beam was determined to have a nominal effect on the downstream flow field characteristics when compared to the solid beam. The modeled trashracks can be observed in Figure 4.11 below.

Inlet Subdomain

The inlet subdomain was modeled using the available information from the USACE engineering drawings, which provided the author with sufficient information to model it without simplification.

Scroll Case Subdomain

The scroll case developed for the CFD model leveraged the radial transects geometric data described above and displayed in Figure 4.5b. Using this information the author employed the loft tool internal to the Star-CCM+ solids modeling suite to interpolate between the points. The numerical methods underlying this interpolation are proprietary; however, the technique results in a volume that showed good agreement with the available information.

Distributor subdomain

The distributor subdomain within the computational model is represented without the use of the wicket gates. While the stay vanes and underlying structure are represented as defined in the engineering plans, the wicket gates were not included two reasons. The first is that because the angle of the wicket gate is dynamic a new solids model and mesh would need to be developed for each flow

rate. The second reason for not including them within the model is their role in controlling the flow rate through the unit. As stated prior, in the operation of the physical unit the wicket gates act to introduce head loss and thereby control the flow through the unit, however to ensure accuracy the author has elected to establish the flow rate using an upstream boundary condition. While the lack of wicket gates may slightly change, the pressure drop through the turbine as well as the distribution of the flow rate between the bays it was felt by the author that this would have an acceptably minimal result. Furthermore, the latter impact was investigated over the course of model validation to ensure a reasonable result.

Turbine Domain

There were several assumptions that went into the modeling of the turbine in the computational domain. These assumptions were primarily based on the fundamental decision by the author that fluid-structure interaction would not be included in the scope of the project thesis. Thus, the turbine would not move as a result of the water flowing around it and in order to mitigate concerns regarding potential asymmetries that would be a result of static turbine the author elected to model the turbine blades as a lumped mass around the turbine hub (Figure 4.12a, 4.12ab and 4.12c). To achieve this, a generalized volume approximation for the turbine had to be developed based on the information available within the USACE database. Using this, the author the developed a simplified solid (Figure 4.13) do represent a single turbine. It is important to note that while the solid is crude, its primary role is to be used to establish a condensed volume and therefore it simply needs to be an accurate representation of the total hub to tip area along the length of the blade. Using this shape, the author determined that the total area of the central region of the blade (without the tapered edges) was 0.085 m^3. This was then combined with the mean blade angle over the testing period (35 degrees) to determine the vertical length over which the additional volume should be added to the turbine (1.51 m). Given the required total volume to represent the central regions of the turbines being modeled and the area over

which they could be applied an increase turbine hub radius of 0.76099 m was included into the model of the turbine. To include the tapered edge volumes of the blades the author simply drew down from the increased hub radius to the standard turbine hub width over blade angle adjusted lengths (0.28 m and 0.37 m for the leading and trailing edges respectively). The effect of this modeling is that the same level of flow acceleration occurs within the turbine region without the asymmetries in the flow that may have occurred. Given that the fluid structure interaction is not occurring, the author must still deal with the head loss caused by the turbine itself however that is addressed with the use of a porous boundary at the turbine (as will be discussed later).

Downstream subdomain

The most significant variation between the actual and computational geometry is in the downstream subdomain, which represents both the draft tube and tailrace subdomain. Rather than develop the draft tube and tailrace within the model the author actively decided to represent this region as an extended, cylindrical flow path. The reason for this variation is that, due to the diverging nature of the draft tube, flows in this region are highly complex and therefore achieving a physically representative solution is computationally expensive. This, combined with the fact that the region where the flow measurement instrumentation is modeled in this research is a significant distance upstream of the draft tube led the author to include the relevant effects of the draft tube on the upstream region through a manipulation of the outlet boundary condition rather than model the physical structure itself. The process behind this is addressed in the appropriate section of the boundary condition methods below. The downstream subdomain begins at the start of the draft tube liner (see Figure 4.14) and is represented by a 45-meter-long cylinder with a consistent diameter equivalent to the beginning of the draft tube liner (3.42 m). The extended length of the cylinder was selected to ensure that the simulation would be able to achieve acceptable levels of convergence given the swirling flow exiting the turbine subdomain. In addition, the interface of the turbine and downstream subdomain is the location where a

porous boundary condition is introduced to the computational domain. This boundary condition is used to simulate the effects of head loss due to the operation of the turbine and the nature and conditions of this boundary will be addressed in the section below.

Preliminary Investigation

As stated previously in the discussion of the forebay boundary, the nature of the flow into the dam was unknown to the author. Due to this, it was felt prudent to perform an investigation into the impact of upstream boundary condition on the ability of the simulation to accurately reproduce the velocity distribution that was measured in Unit 4 of Lower Granite. In addition to this the author felt if prudent to include turbulence closure models in this investigation as these play a critical role in the accuracy of CFD results. As a result, the author developed 8 separate preliminary CFD simulations of flow through Unit 4 to determine the appropriate closure model and upstream boundary condition to employ in the simulations. The specific nature of the boundary conditions are addressed in the section below Table 4.1 demonstrates the boundary conditions that were performed and Figure 4.15 shows the inlet boundary condition nomenclature. The Realizable K-Epsilon and SST K-Omega turbulence closure models discussed above were utilized in this investigation. The Realizable K-Epsilon closure model was selected for its robust convergence capability as well as its ability to address complex models better than standard K-Epsilon. The SST K-Omega method was selected due to its ability to model viscous regions while still reliability achieving convergence. In addition to this these models were selected because they have been demonstrated to be effective in prior simulations of hydroplants and the author wanted to document their ability to replicate a flow field to be used for the simulation of flow sensors. It should be noted by the reader that the flow rate for all the preliminary simulations was 290.36 m^3sec^{-1} and that the appropriate porous interface and outlet boundary conditions were employed for this simulation (addressed in the following section). The flow rate each of the

activated forebay faces was representative of their proportional contribution to the overall activated surface area.

Once all eight simulations were performed the author then compared the results to the measurements taken in the field to determine the appropriate upstream boundary condition and closure model to use in the subsequent computational models. Three distinct tests were performed by the author: comparison of percent flow rate in each intake bay; ability to replicate the acoustic time of flight data measured in the intake during performance testing of Unit 4; and the ability of the CFD models to replicate the velocity magnitude measurements that were recorded in the center of Bay C during the model testing that was discussed in the Background section above. The first two of these represent the validation that was performed on all the subsequent simulations that were performed to ensure acceptable levels of accuracy on the models and therefore the author directs the reader to this section for a thorough discussion of them. The last one was not however performed on the remainder of the simulations because model test data was only available at a flow rate of 283.17 m^3sec^{-1} (10,000 ft^3sec^{-1}). In the process, the author utilized the point interpolation software native to Star-CCM+ to identify the relevant hydraulic characteristics at each point where velocity data was available from the model test. The velocities from the model test were then calibrated to reflect the slight variation in flow rate through a basic ratio of velocities. Once this was performed the point velocities developed in the CFD models were compared to the adjusted point models from the model test using the Analysis of Variance (ANOVA) test (Equation 4.1) to develop the F-Statistic which acts to demonstrate the likeliness of variation between the data sets to be a result of the variability within the individual datasets as opposed to variation between the datasets. This was done at two locations within Bay C, thereby providing the author with a measure of the applicability of the preliminary model along the flow path of the unit. While the results of this preliminary investigation can be observed in the subsequent results section of this work, given its impact

on the subsequent research the author feels it prudent to state that the SST K-Omega model with flow from all directions in the forebay had the highest probability of being appropriate. As such this method was used to develop the computational models for the remaining flow rates used in the study.

$$F = \frac{\sum n_{sample}\left(\frac{\sum V_{sample}}{n_{sample}} - \frac{\sum V_{population}}{n_{population}}\right)^2 / (n_{bins} - 1)}{\sum\sum\left(V_{sample} - \frac{\sum V_{sample}}{n_{sample}}\right)^2 \Big/ \left(n_{population} - n_{bins}\right)}$$

Equation 4.1

Boundary Conditions

Selection of the appropriate boundary conditions for the CFD models represents an important attribute of this research as these are critical to achieving a velocity distribution at the sensor location that is representative of the actual flow field. The inlet boundary occurred in the forebay subdomain and included two types of boundary condition, the mass flow and the symmetry plane boundary conditions. The mass flow boundary condition at the inlet faces represents a section in which mass flux along with velocity is uniform along the surface where the mass flow into the surface of each cell face at the boundary is determined via Equation 4.2 under that assumption that density is constant. The pressure at the surface is extracted from adjacent cells which cascades through the domain from the outlet boundary condition discussed below.

$$\dot{m}_{c-face} = \dot{m}\frac{a_{c-face}}{\sum a_{c-face}}$$

Equation 4.2

Even though the symmetry plane boundary condition was not used in the primary research section, its inclusion in the preliminary investigation necessitates its inclusion in this section of the methods. Given this, the symmetry plane is represented by a surface without shear stress whose local velocity values are

determined using the velocity of adjacent cells. Similarly, the pressure at the face is also determined with the use of the adjacent cells and the heat flux at the face is assumed to be zero. The pressure boundary represents a surface at which a global pressure value is specified, and the local velocity characteristics are determined through adjacent cells which cascade through the computational domain.[75]

Inlet Boundary Conditions

The inlet boundary conditions to the computational model were briefly addressed previously, however, this section will establish the specific mass flow rates that were used for each face for the six flow rates that were investigated. The areas for the side and front of the forebay are 654.95 m^2 and 1,641.76 m^2 respectively and therefore the mass flow rates that were imposed on each face are demonstrated in Table 4.2. In addition to the incoming mass flow rates, further hydraulic characteristics must be specified at the upstream boundary condition to inform the CFD model, specifically the turbulent characteristics. These are the turbulent intensity and the turbulent viscosity ratio and they inform the solution of the turbulent closure models discussed above. The turbulent intensity is the ratio of the magnitude of the fluctuating turbulent velocity to the mean velocity and the turbulent viscosity ratio is the ratio between the turbulent viscosity and the actual viscosity of the water. The former value was set to 5% and the latter was established at 10. The turbulent intensity was set as such because this value was specified in the modeling of La Grande-1.[58] The turbulent viscosity was selected because this was the value used in the CFD modeling of Ice Harbor dam.[35] These specific values were utilized because the similar characteristics of both dams represented the most accurate approximation of the required hydraulic characteristics at Unit 4's intake.

Porous Boundary Conditions

An important repercussion of the turbine not being taken into account is that the head loss resulting from turbine operation will not be included in the simulation.

Given this, the author has elected to simulate this effect using a porous interface at the turbine location as discussed in the section above. The porous interface represents an infinitely thin porous surface through which fluid passes and experiences a pressure drop determined by the specifications of the interface. It is important to note however that the interface does not model the pores in the interface itself; rather it models the aggregate effect of the surface on the bulk flow itself. The equation which dictates the specific pressure drop is found below, where the requisite coefficients that must be determined can be observed (Equation 4.3).[75] The underlying principle of this pressure drop equation is Darcy's Law which demonstrates that the pressure differential of fluid flow through a surface is proportional to the fluid viscosity and a linear permeability function.[21]

$$\Delta p = -\rho\left[K_\alpha |V_n| + K_\beta\right]V_n$$

Equation 4.3

From Equation 4.3 it will be observed that to determine the appropriate coefficients to represent the turbine both the pressure drop and the velocity normal to the surface must be determined. The latter was assessed with a uniform velocity assumption whose values were calculated by dividing the established flow rate by the known cross section at the porous boundary location. While the assumption of a uniform, normal velocity does not occur at that location, it was assessed as a reasonable estimation given that the requisite pressure drop still transpires and the region of where the sensors were modeled occurred upstream of the porous boundary condition. The resultant normal velocity values are displayed in Table 4.3 below. The pressure drop caused by the turbine itself is represented by Equation 4.4.[56] It will be noted from this equation that the efficiency of the turbine, as well as the generator, is required to accurately convert the power produced by the unit, to the energy removed from the system to produce the electrical power. Given this, the author determined site-specific characteristics for the efficiency of both the turbine and the

generator. In the case of turbine efficiency the model test data was used rather than the acceptance testing performed at Unit 4 because model conditions allowed for holistic monitoring and control of the system (head and flow rate), and therefore it provided a more accurate approximation of the conversion efficiency.[103] It should be noted that the values provided were scaled up from the model test efficiency to prototype efficiency. In addition to this, the minimum flow rate performed in the model testing did not encompass the entirety of the operational envelope of the unit itself and therefore the performance of the Unit itself was used to inform the conversion of the minimum flow rate. The corresponding efficiency calculation is Equation 4.5 with the coefficients enumerated in Table 4.4. Is should be noted within this equation that the flow rate variable is in units of cubic meters per second. The efficiency characteristics of the provided by the manufacturer of the on-site generator were used in the pressure drop calculations because the characteristic efficiencies can be determined to a high level of accuracy because efficiency is measured as a function of power produced and this can be readily tested (Equation 4.6 and coefficients in Table 4.5). The corresponding efficiency curve and function describing the curve can be found below, and it should be noted that presented results are a function of generator output in kilowatts. Utilizing this information, it is possible to determine the total pressure loss resulting from the turbine and associated geometry (displayed in Table 4.3). The head loss resulting from the turbo-generator system, along with the mean normal velocities, was then used to assess the appropriate coefficients to populate Equation 4.3 above. This was done by using the least-squares technique with the known values over the range of flow rates modeled. The mean porous internal resistance and mean porous viscous resistance were found to be 0.35 and 21.19 respectively, however it should be noted that the least squares regression technique did not perfectly fit the data (R^2 of 0.97) and therefore a correction factor specific to the flow rate is necessary. The correction factor was determined by assessing the loss provided by the mean quantities in relations to the required quantities and adjusting the

viscous resistance accordingly (found in Table 4.3). It will be noted by the reader that the total pressure loss imposed by the turbine is relatively constant over the range of flow rates despite the varying amount of power produced at each flow rate. The consistent nature of the losses is explained through an examination of Equation 4.4 because the head loss along a streamline is determined by the power extracted divided by the flow rate. As such, even though the power extraction is increasing the flow rate is observed to have a corresponding increase. This level of consistency is then further supported by the turbo-generator efficiency, whose effect can be observed in Figure 4.16.

$$H_T = \frac{W_{out}}{Q\eta_{Turbine}\eta_{Generator}}$$

Equation 4.4

$$\eta_{Turbine} = TC_1Q^6 + TC_2Q^5 + TC_3Q^4 + TC_4Q^3 + TC_5Q^2 + TC_6Q + TC_7$$

Equation 4.5

$$\eta_{Generator} = GC_1{W_{out}}^4 + GC_2{W_{out}}^3 + GC_3Q{W_{out}}^2 + GC_4W_{out} + GC_5$$

Equation 4.6

Outlet Boundary Conditions

The outlet boundary of the CFD domain was selected to be a pressure type. This was selected to ensure the stability of the simulation and to attempt to produce physically representative results. Determining the appropriate pressure values for the simulations however required additional effort on behalf of the author because not only were field pressure measurements unavailable at the outlet of the physical domain but also the physical domain outlet conditions needed to be converted to hydraulically similar conditions for the outlet boundary of the computational model. Given this, the assessment of the appropriate pressure required a calculation of the former and then an assessment of the latter. To this end a one-dimensional hydraulic approximation (Equation 4.12) was employed. The function in question is known as the Bernoulli Equation, and is derived from the conservation of energy whose governing function along a streamline is

described in Equation 4.7. The first term of the equation describes gravitational effects, the second pressure and the final the net forces observed by a small fluid particle on the streamline. It will be noted in this equation that the viscous effect has been assumed to be negligible and the flow is assumed to be irrational furthermore the assumption of a streamline flow inherently includes the assumption that flow does not perform work or transfer heat. Using the assumptions found in Equations 4.8, 4.9 and 4.10 enables the initial energy equation to be rewritten and integrated as seen in Equation 4.11. It should be noted that the first term of this equation remains in the integral form as it is unknown how density changes as a function of pressure. If this is assumed to be a constant value it enables the equation to be written in its final form (Equation 4.12) which state that under the idealized conditions the interplay between the variables is constant along a streamline.[56] Incompressibility is considered a reasonable underlying assumption because of the nominal compressibility of water at the pressures anticipated in the intake.[44]

$$\delta\forall\left(-\gamma\sin(\theta_{streamline})-\frac{\partial p}{\partial s}\right)=\delta\forall\left(pV\frac{\partial V}{\partial s}\right)$$

Equation 4.7

$$\theta_{streamline}=\frac{dz}{ds}$$

Equation 4.8

$$\frac{\partial p}{\partial s}=\frac{dp}{ds}$$

Equation 4.9

$$V\frac{\partial V}{\partial s}=\frac{1}{2}\frac{d(V^2)}{ds}$$

Equation 4.10

$$\int\frac{1}{\rho}dp+\frac{1}{2}V^2+gz=Constant$$

Equation 4.11

$$p + \frac{1}{2}\rho V^2 + \gamma z = Constant$$

Equation 4.12

To compensate for the idealized nature of the underlying equation a series of head loss terms have been added to represent energy loss due to a variety of sources that occur from the beginning of the forebay to the end of the downstream subdomain (described using subscripts of 1 and 2 in Equation 4.13). In the case of the research that was performed these head loss components are discretized into the: intake, scroll case-distributor-turbine system, and draft tube. The intake losses are the summation of individual losses incurred by the trash racks, gate slots and the intake itself, and are traditionally addressed as separate components. Fortunately, the author was able to access the combined head loss values for the trash racks, intake and gate slot utilized over the course of the unit performance testing; thereby enabling an accurate estimation of the resulting pressure drop (Equation 4.15 with coefficients in Table 4.6). It should be noted that this equation is in imperial units; however, the author converted the results for the research. The head loss caused by the operation of the turbine itself is discussed in the section above and is directly leveraged for the assessment. The final flow path component whose head loss is included is the draft tube (Equation 4.16). The coefficient employed to represent this was developed using information from an investigation into draft tube losses as a function of subdomain dimensions performed by Prasad et al. in 2010.[66] The author linearly interpolated the results of the study to represent the geometry of Unit 4, developing a loss coefficient of 0.078. The results of this investigation were supported by an investigation by Idaho National Engineering Laboratory (INEL) which established that a draft tube loss coefficient of 0.28 was a typical value for such a factor.[19] The variation between the two values is largely explained by the fact that the INEL study was performed in imperial units; when converting the head loss resulting from these values to metric a 9.41 percent variation was uncovered. As such the author used the 0.078 value as it was customized to the

geometry of Lower Granite. It should be noted that the velocity value utilized in the equation is representative of the speed of the water entering the draft tube nozzle. Leveraging these functions along with the established flow rates and elevation differentials it is possible to calculate the pressure that would be present at the end of the draft tube at Lower Granite. The constituent head losses and result of the outlet pressure calculations using Equation 4.13 can be found in Table 4.7 below.

$$\frac{{V_1}^2}{2g} + \frac{P_1}{\rho g} + z_1 = \frac{{V_2}^2}{2g} + \frac{P_2}{\rho g} + z_2 + \sum H_{Losses}$$

Equation 4.13

Where

$$\sum H_{Losses} = H_I + H_T + H_{DT}$$

Equation 4.14

$$H_I = HC_1Q^5 + HC_2Q^4 + HC_3Q^3 + HC_4Q^2 + HC_5Q + HC_6$$

Equation 4.15

$$H_{DT} = K_{DT}\left[\frac{V^2}{2g}\right]$$

Equation 4.16

It will be noted, that the outlet pressure conditions found in Table 4.7 strictly reflect the calculated pressure values at the exit of the draft tube in the physical domain. To develop the requisite boundary conditions for the computational model, however the author had to convert the pressure values at the outlet of the physical domain using Equation 4.13. This equation was used because it conserves the distribution of energy within the system, allowing for the computational model to be developed in a hydraulics similar fashion. The requisite characteristics of both the physical and computational domains are

displayed in Table 4.8 along with the pressure values that were employed in the development of the CFD models.

Mesh Development

The mesh which used for the CFD modeling of Unit 4 of Lower Granite was comprised of 14.7 million individual cells and was developed using the mesh generation software internal to Star-CCM+. A polyhedral mesh with a target size of 0.2 meters was selected as this mesh density has been demonstrated in previous studies outlined in the background section above to provide sufficient resolution to accurately calculate the hydraulic characteristics in the computational domain. There were three primary means in which the base mesh was modified for this research however. The first was the inclusion of a prism layer at the edges of the walls of the computational domain, to ensure that the shear layer of the flow was accurately captured. The total prism layer thickness was 0.2 meters, with 14 layers within the cell structure. Given that the author selected a cell growth rate of 1.4 the initial cell had a height of 7.26E-4 meters which was assumed by the author to provide an acceptable wall resolution for the simulations. It should be noted that the prism layer mesh resulted in a y+ ranging between 1 and 50 in the domain (with the exception of the downstream sub-domain). Repeated attempts at further refinement of this region lead the model to diverge and while it is recognized to not be ideal for the application of several turbulence closure models it is not prohibited and therefore this mesh resolution was used in the subsequent research.

In addition, the author also employed a similar technique, the thin layer mesh, to ensure accurate resolution in the flow path as well. The thin layer mesh is a routine embedded within the meshing function in Star-CCM+ designed to recognize thin parts in the meshing domain and develop a prism volume mesh around the surface. The thin layer mesher was set to an appropriate value to ensure that the trashrack bars were captured, such that their effect on the flow

field was captured appropriately. To ensure cohesiveness of the mesh the author used the same total size, growth rate and number of cells that were used in the prism layer. In addition to these two factors, the author included a mesh refinement in the turbine and distributor subdomain. In the refined volume, the target cell size decreased to 0.1 meters. This refinement was done to accurately capture the complex hydraulic characteristics in this region, without increasing mesh resolution in other sections of the flow where the increased resolution was not required. The results of the three increased resolution techniques can be found in Figures 4.17, 4.18, and 4.19 which represent the results of the prism, thin layer, and resolved meshes respectively.

To ensure that the mesh that was developed for this research was valid, the author performed two investigations using the mesh diagnostic tool within Star-CCM+. These included the face validity and volume change. The face validity investigates the directionality of the cell faces, to ensure that they are oriented primarily outwards. A cell with a face validity of 1 represents a cell whose faces are completely normal with the cell centroid and any cell with less than this has some degree of concavity. As the name suggests the cell volume change determines the extent to which adjacent cell volumes vary. This confirms that the determination of flux between the cells can be accurately calculated by the software. A value of 1 represents equivalent cell sizes, which is ideal for calculation. The results of these investigations can be observed in Table 4.9.

In addition to this the author performed a preliminary mesh resolution study using a mesh developed at a larger base cell size (0.25 meters). The other values and modifications to the mesh, such as the thin mesher, remained the same when developing this mesh. A simulation was run at a flow rate 565 m^3sec^{-1} using each of the meshes, and the author then compared the hydraulic characteristics required to simulate sensors in the subsequent section of the research. This was done by determining these hydraulic characteristics (the Cartesian velocity

components and the local turbulent kinetic energy levels) at 8,000 points scattered within each intake bay over the region where the sensors were modeled. Given that the points were at identical locations it enabled the author to readily assess if the mesh had a significant impact on the computational solution. Hydraulic information at each location was determined using the nearest neighbor method outlined in the subsequent section, however once obtained the author used the Adjusted R^2 method to determine the level of similarity between the two datasets. While the specific results of this study are displayed in the results section of the research, the author feels it pertinent to state that the results were acceptably similar. The code used to develop this can be observed in Appendix 1 at the end of this document.

Bay Flow Recirculation Reproduction

As stated in the background section above, a recirculation zone was observed in each of the intake bays at the mounting location of the acoustic time of flight paths. In an effort to recreate the recirculation at the site, the author developed a series of four separate CFD model permutations to understand the influences on the recirculation zone formed at the gate slot of the intake. This location was specifically investigated because the recirculation that occurs at the gate slot represents the closest upstream continuity to the recirculation that was measured in the acoustic time of flight sub-domain. The distance between the end of the gate slot and the beginning of this domain is 3.8 meters. In this effort the author specifically studied the effect of wall material, inlet turbulent intensity, and the geometry of the local computational domain.

One of the characteristics that were investigated was the effect of wall surface roughness on the recirculation dimensions at the site. The wall roughness acts to alter the velocity profile because as the wall roughness increases the velocity gradient between the wall region and the freestream correspondingly decreases. To this end the author studies the effect of a “smooth” no-slip wall function and a

no slip wall function with roughness equivalent to riveted steel.[75][110] The modification of the turbulent intensity at the inlet, allowed the author to control the amount of turbulent kinetic energy contained within the flow thereby influencing the amount of energy at the gate slot itself. Increasing levels of turbulent kinetic energy were found to reduce the reattachment length of the recirculation zone.[22][41] To study the effect of this the author developed models with inlet intensity of 0.1 and 0.01. The modification of the local geometry allowed the author to explore the potential that the gate was located near the end of the gate slot rather than lifted a significant distance upwards. As such the permutations on the gate slot height included a distance of 0.31 meters under the assumption of the former and 4.98 meters under the assumption of the latter. This was included in the study because it was felt by the author that a variation in this distance may have an impact on the characteristics of the local recirculation zone that occurs. The four permutations were: [1] an inlet intensity of 0.01 with a surface roughness equivalent to riveted steel on the geometry with the extended gate slot, [2] an inlet intensity of 0.1 with a surface roughness equivalent to riveted steel on the geometry with the extended gate slot, [3] an inlet intensity of 0.1 with a smooth surface roughness on the geometry with the extended gate slot and [4] an inlet intensity of 0.1 with a smooth surface roughness on the geometry with the constrained gate slot. It should be noted that in all cases the flow rate investigated was 290 m^3sec^{-1} with flow coming from all inlet directions, the SST closure model was used in this process also. The dimensions of the recirculation zone resulting from each were then studied.

In addition to this effort to document the development of a recirculation zone downstream of the gate slot the author performed a secondary investigation to demonstrate the effect of this recirculation zone on both flow measurement accuracy and the subsequent economic evaluation. This investigation was found to be necessary because, despite the best efforts of the author, the recirculation zone recorded by the field measurements could not be fully reproduced using the

as build drawings of Lower Granite Lock and Dam. To this end the author imposed two different types of obstructions at the celling of the intake bays immediately behind the gate slot. The two types studied were an angled obstruction and a straight obstruction (Figures 4.20 and 4.21 respectively). The creation of the specifications for each of the obstructions will be discussed in the subsequent paragraph once the investigation method has been discussed. In addition to the effect of the obstructions the author also endeavored to document the effect of surface roughness on the development of the recirculation zone. As stated in the initial study to recreate the recirculation zone, surface roughness effects the distribution of fluid flow within a conduit. To this end the author increased the surface roughness of the floor of the intake bays while keeping the remainder of the surfaces at a constant roughness equivalent to steel. The floor roughness was increased in an effort to alter the distribution of the fluid velocity further toward the ceiling of the intake bays. In doing this, velocities near the floor of the bays found in the CFD will be more like the field data, and the corresponding increased fluid velocity near the ceiling was assumed to increase the size of the recirculation zone. Floor surface roughness equivalent to ten and twenty times that of riveted steel were investigated. [110] Given these two research interests the author developed nine additional CFD models at a flow rate of 290 m^3sec^{-1} corresponding to Table 4.10 below, these different combinations allowed the author to better document the relative importance as well and the cumulative effect each. Acoustic time of flight sensors were then simulated in each of the nine CFD simulations and compared to the field data to determine the specifications which produce a velocity distribution most similar to that found in Lower Granite. These specifications were then leveraged to develop an additional series of CFD models over a range of flow rates representative of the operational range of Unit 4 as was done with the previous study. These simulations where then used to develop a secondary investigation into the sensor accuracy evolution and corresponding economic study discussed in the subsequent section. It was felt to be important to include this section because it

will provide insight into the sensitivity of both flow measurement accuracy and its associated financial repercussions to the velocity distribution within the intake.

The specifications associated with the flow path obstructions were developed using the well explored theory behind the recirculation zone found behind a backward facing step. The use of this information enabled the author to calculate the required height of the obstruction to reproduce a recirculation zone sufficiently long to induce an appropriate negative velocity at the highest acoustic path. Experimental velocity profiles recorded at various distances behind a backward facing recorded by Saric et al. in 2005 were used to develop a two dimensional fourth order polynomial (Equation 4.17) which represented the velocity behind a step as a function of both the ratio of the distance behind the step to the step height and the ratio of the vertical distance above the floor to the step height.[73] The coefficients of this polynomial can be found in Table 4.11 below and represent the velocity distribution with an accuracy corresponding to an adjusted R^2 value of 0.988. The author then determined the distance between the transducers of the upper most acoustic path and the artificially imposed obstruction as these values also effected the extent of the recirculation impact. This was measured in two ways as the effect of the conduit convergence on the recirculation zone was unknown. The first was the horizontal distance between the obstruction and the acoustic paths, this was used in the development of the vertical obstruction. The second set of distances that was calculated assessed the distance between the obstructions along the angled surface of the converging conduit. The distances from this calculation were used in the assessment of the appropriate height of the angled obstruction. Naturally because the angle the second set of distances was longer. To assist in the visualization of the distances the author developed Figure 4.22 which displays them. The combination of generalized function for the velocity downstream of the step along with the acoustic paths distances then enabled the author to calculate the appropriate obstruction height by integrating the general function over the acoustic path

length using the desired average velocity along this distance (Equation 4.18). The integration of this function then enabled the author to algebraically assess the appropriate height for each step type. As a result of the analysis it was calculated that the appropriate heights are 1.33 and 2.43 meters for the straight and angled obstructions respectively.

$$U_{BFS} = A_{BFS1} + A_{BFS2}\frac{x_{step}}{H_{step}} + A_{BFS3}\frac{y_{step}}{H_{step}} + A_{BFS4}\left(\frac{x_{step}}{H_{step}}\right)^2 + A_{BFS5}\frac{x_{step}}{H_{step}}\frac{y_{step}}{H_{step}} + A_{BFS6}\left(\frac{y_{step}}{H_{step}}\right)^2 + A_{BFS7}\left(\frac{x_{step}}{H_{step}}\right)^3 + A_{BFS8}\left(\frac{x_{step}}{H_{step}}\right)^2\frac{y_{step}}{H_{step}} + A_{BFS9}\frac{x_{step}}{H_{step}}\left(\frac{y_{step}}{H_{step}}\right)^2 + A_{BFS10}\left(\frac{y_{step}}{H_{step}}\right)^3 + A_{BFS11}\left(\frac{x_{step}}{H_{step}}\right)^4 + A_{BFS12}\left(\frac{x_{step}}{H_{step}}\right)^3\frac{y_{step}}{H_{step}} + A_{BFS13}\left(\frac{x_{step}}{H_{step}}\right)^2\left(\frac{y_{step}}{H_{step}}\right)^2 + A_{BFS14}\frac{x_{step}}{H_{step}}\left(\frac{y_{step}}{H_{step}}\right)^3 + A_{BFS15}\left(\frac{y_{step}}{H_{step}}\right)^4$$

Equation 4.17

$$U_{Path} = \frac{1}{T_{P2} - T_{P1}}\int_{T_{P1}}^{T_{P2}} U_{BFS}\,dx$$

Equation 4.18

CFD Result Validation

The following section address the steps the author took over the course of the research to compare the results of the computational fluid dynamic model to the physical domain itself. This is an important process because it demonstrates the applicability of the subsequent analysis to Unit 4. In addition to this, the results of the validation process will enable a better understanding of the sensitivities involved in the modeling of short converging intakes. There were two primary methods in which this investigation was performed, based on the two primary sources of flow field information that was available to the author. It should be noted by the reader that both of these techniques were also employed in the preliminary investigation that the author undertook as addressed above. In

addition to this the author performed an investigation into both the global and local computational residuals and y+ values. These both play a pivotal role in the CFD process as the computational residuals indicate the ability of the model to converge to a singular value and the y+ value indicates the ability at each cell along the wall to fully capture the shear layer. These are done globally as well as locally because demonstrating the variation between the region where sensors were modeled and the overall characteristics acts to indicate more accurately the appropriateness of the CFD simulation that was used for sensor simulation. The results of both these attributes as well as the two validation studies performed below are displayed in the results section below.

Bay Flow Rate Distribution

The first validation study that was undertaken by the author is an investigation of the distribution of the fluid flow between the individual bays that comprise the intake. The flow rate within each bay was measured during site performance testing at Unit 4 and was given to the author by the USACE. While it is assumed that the specific flow rate provided is slightly inaccurate (hence the investigation into flow measurement accuracy in short converging intakes), it was felt that the percentage of recorded flow distribution between the bays would be acceptably representative. Given this, the author then investigated the distribution of flow rates in each of the developed computational models using a tool internal to the Star-CCM+. This flow rate report tool allowed the author to rapidly and reliably determine the flow rate within each bay. These subtotals were then aggraded to determine the total flow rate, and subsequently the percent total flow rate in each intake bay. These values were then compared to the measured field data and a percent difference was addressed and used to determine how closely the CFD model was able to replicate this category.

Acoustic Time of Flight Comparison

The second method that was employed in the validation studies that were performed on the developed CFD models of Lower Granite Unit 4 used the Acoustic Time of Flight Instrumentation that was used in the performance testing that was done on the Unit. This information was comprised of mean velocity information along acoustic paths formed between the transducers at a range of heights for all the flow rates that were investigated by the author. Given this the author leveraged the acoustic time of flight simulation tool developed for this research to document the response of acoustic time of flight sensors exposed to the hydraulic conditions simulated by the CFD models. Using this, the author could compare the average transect velocities at each point using an Analysis of Variance (ANOVA) test. These tests allowed the author determine the likelihood of differences in the two datasets to be a result of variation within each of the datasets as opposed to a result of variation between the datasets.

Flow Sensor Modeling

The following section addresses the methodology used by the author to determine the flow rates that would be measured differing amounts of current meters and acoustic time of flight transducers when exposed to the hydraulic conditions present in Unit 4. This technique enabled the calculation of how flow measurement accuracy scales in relation to the total number of applied sensors. The methodology below leverages the numeral techniques for sensor placement as well as the conversion of the detected velocity values to a flow rate established by the industry test codes. The section will initially address the mechanism by which data from the computational fluid dynamic model was used to assess the hydraulic characteristics at points within the domain necessary for sensor modeling. The use of this data to model the results of individual current meters and the conversion of the individual points to an overall flow rate will then be discussed. Finally this section will address how the hydraulic information for the CFD models will be leveraged to model individual acoustic time of flight

transducers and, subsequently how the average velocity recorded by the velocity will be converted to a flow rate.

Local Velocity Characteristic Calculations

The results of the CFD models produced by Star-CCM+ developed a high-resolution model of the computational domain, however the meshing algorithm employed by the commercial software does not allow for specific solution points to be established by the user. As a result the points where the hydraulic characteristics were determined by the solver do not coincide with the points where information is required for the modeling of the current meters or the acoustic path. To mitigate this differential the author then employed two techniques to determine the appropriate hydraulic characterizes using the information provided by the CFD model. The first of these is the nearest neighbor method, where the characteristics of the closest known location are assumed to be representative of the point where data is required. The other method used in this is the inverse distance weighting technique (IWD), which establishes a region of influence around the point of interest and uses the values from known points within this region along with the distance between the known point and point of interest to establish the hydraulic values. This method follows Equation 4.19 below where it can be observed that the primary factors which determine calculated characteristics are the region of influence as well as the weighting power.[74] As a part of the thesis work the author investigated the effect of both the radius and the power used in the radius of influence study. This was done by comparing the point velocities calculated using the nearest neighbor method and the IWD method with the following permutations: a radius equivalent to the base and half base size of the computational mesh; and a weighting power of 2 and 3. The research investigated the influence of the numeric method as well as the specifications entrained in the inverse distance weighting method by documenting the variation in predicted current meter flow rates in Bay A at a flow rate of 565 m^3sec^{-1} over a range of horizontal and vertical resolutions. The study

established the mean variation between the flow rates measured at each current meter resolution. The understanding of the mean variation was used to establish the numeric method which provided a central value as well as the variability caused by the technique. The study along with the full results can be found below, however the author established that the inverse distance weighting method (with a power of 3 and a radius of 0.2m) proved to be most effective, and therefore this method was used in the subsequent sections. In addition, this study determined the distribution of the number of points within the two difference radii studied.

$$\varphi_s = \frac{\sum_{i_{ROI}=1}^{N_{ROI}} \Psi_i \mho_i}{\sum_{i_{ROI}=1}^{N_{ROI}} \Psi_i}$$

Equation 4.19

where

$$\Psi_i = \frac{1}{\sqrt{(x_1 - x_2)^2 + (y_1 - y_2)^2 + (z_1 - z_2)^2}^{P_{ROI}}}$$

Equation 4.20

Current Meter Simulation

The simulation of current meter response will be performed on four different types of current meters because, due to their mechanical nature, the sensors respond differently based on the hydraulic conditions present. The study of the different types will provide insight into the sensitivities of both flow measurement accuracy and flow measurement value on the current meter design. The sensors that were the: Ott C31-1, Ott C31-1 (Plastic), Ott C31-A, and the Ott C31-R. Modeling of the current meters was performed by simulating the sensors as individual points within the flow, located at the gate slot of the computational domain. This section will initially address how the individual current meters were modeled and then how the individual measurements were combined to determine the overall flow rate measured by varying quantities of the sensors. It should be noted by the reader that due to the steady state nature of the CFD modeled developed, transient nature of turbulence could not be directly assessed

in this study. As such the magnitude of turbulent pulsations was calculated from the local turbulent kinetic energy values and the assumption of isotropic turbulence.

Individual Current Meter Response

The modeling of the velocity recorded by individual current meters when exposed to local hydraulic characteristics represents a critical tenant of the research as this will enable an understanding of flow measurement accuracy as a function of both the number and type current meter. As such it was decided by the author that the most effective method of modeling results would utilize the balance of torques which governs the turning rate of the current meters propeller thereby representing the physics. The general equation leveraged can be found below (Equation 4.21) and it should be noted that this expands upon prior research into this effect by including the impact of transverse flow on the rotation rate of the meters in addition to the effects of both friction and axial effects.

$$2\pi I_{Prop}\frac{dV_{meter}}{dt} - T_{axial} - T_{Transverse} + T_{Friction} = 0$$

Equation 4.21

The first term in the above equation describes the rotation rate of the current meter's propeller as a function of the inertia of the about the axis of the propeller. This information was determined using Equation 4.22 under the assumption of a constant blade angle for each of the investigated blades. While this does not yield a completely representative value, this was determined effective as corrective factors applied later in the research process were assumed to compensate for any variance in the calculated inertia. The integral component was determined for the three different shapes of current meters (with the Ott Metal and Plastic having the same shapes) using diagrams of the propellers provided by Ott (an exemplary layout is demonstrated in Figure 4.23, though it should be noted that specific dimensional values have been omitted to mitigate privacy concerns) to develop functions for the length of the propeller blade as a

function of propeller radius. Given, the integral requirements of Equation 4.22 the author then developed three equations which described length as a function of blade height. Three equations were utilized as the blade area can be discretized into three discrete subdomains, the initial region dominated by the upstream slope, a midway domain where either the front or back beveling occurs in conjunction with the upstream slope, and finally the outermost domain where beveling upstream and downstream section of the blade occurs. The blade subdomains are demonstrated in Figure 4.23 and the general equations which describe the domains can be observed below. As the domain is continuous the author solved the integral using the current meter subdomain equations, and the propeller inertia along with the solution to the integral values (as these are used in subsequent equation) and integrated length equations (which demonstrate the blade area, also used in the subsequent equations) are displayed in Table 4.12.

$$I_{Prop} = \frac{\rho_{prop} d_{prop} N_{Blades}}{cos(\theta_{blade})} \int_{R_h}^{R_t} l_{blade} {r_{blade}}^2 dr_{blade}$$

Equation 4.22

from r_{blalde}=R_h:r_1

$$l_{blade} = l_{Rh} - r_{blade} \tan(\emptyset_B)$$

Equation 4.23

from r_{blalde}=r_1:r_2

$$l_{blade} = l_{Rh} - r_{blade} \tan(\emptyset_B) - \left[l_{bev_1} - \sqrt{{l_{bev_1}}^2 - (r_{blade} - r_1)^2} \right]$$

Equation 4.24

from r_{blalde}=r_2:R_t

$$l_{blade} = l_{Rh} - r_1 \tan(\emptyset_B) - \left[l_{bev_1} - \sqrt{{l_{bev_1}}^2 - (r_{blade} - r_1)^2} \right] - \left[l_{bev_2} - \sqrt{{l_{bev_2}}^2 - (r_{blade} - r_2)^2} \right]$$

Equation 4.25

The torque produced by axial flow into the propeller is described in Equation 2.26 below which is was derived by Jepson in[43] under the assumption of constant blade angle and a small angle difference between the relative fluid velocity and the angle of the propeller blade. These assumptions were determined appropriate given that current meters used in this investigation have a relatively small pitch. Additionally, the steady state nature of this investigation and long exposure period of the meters in the field validate the latter assumption as the propeller should be relatively free running and responsive. It will be noted that the integration term found in the inertial equation solved for above is found in both supplemental terms for this equation and therefore the author was able to leverage the meter specifications provided to determine these values.

$$T_{axial} = \rho {d_{prop}}^3 {V_{axial}}^2 \left[a_{blade} + b_{blade} \frac{V_{meter} d_{prop}}{V_{axial}} \right]$$

Equation 4.26

Where

$$a_{blade} = \frac{2\pi^2 N_{Blade}}{P_{Blade} {d_{prop}}^3 \left[1 + \frac{2A_{Blade}}{(R_t - R_h)^2} \right]} \int_{R_h}^{R_t} l_{blade} {r_{blade}}^2 dr_{blade}$$

Equation 4.27

$$b_{blade} = \frac{-2\pi^2 N_{Blade}}{{d_{prop}}^4 \left[1 + \frac{2A_{Blade}}{(R_t - R_h)^2} \right]} \int_{R_h}^{R_t} l_{blade} {r_{blade}}^2 dr_{blade}$$

Equation 4.28

The effect of transverse flow is found in the third term of Equation 4.21 and is described in Equation 4.29 below. This equation is borrowed from modeling the response of cup anemometers as the blades of the propeller can be thought of as low profile anemometers when impacted by transverse flow. As such, the author modified the transient equation for torque imparted by anemometer cups put forth by Kondo et al. in 1971.[48] The primary variation employed by the author is that, rather than assessing the mean drag force imparted on the cup over a

rotation via integration, mean values for this are assumed. The rationale for this means of assessment is that there was not information for the drag coefficient of the propeller as a function of angle; however, there were a series of measurements performed investigating both the mean effect of steady and pulsating transverse flow on sensor response, thereby enabling the author to calculate this coefficient.

$$T_{Trans} = \frac{\rho N_{Blade} C_{mdrag} A_{Blade} R_{Mblade} {V_{Trans}}^2}{2}$$

Equation 4.29

The final component of the current meter response equation found above is the torque resulting from friction which acts to resist rotation of the propeller. While industry standards as well as operating instructions recommend that current meters are oiled and serviced prior to testing, there is still nominal resistance given the mechanical nature of the system.[37][40] [62][85][105] As such it is assumed by the author for this study that the resistive torque will be a linear function of the velocity as found in the equation below. This basic equation utilized by Ower is leveraged rather than the more complex form proposed by Ott due to both the relatively minimal impact of this torque and the fact that the coefficient was derived from performance testing data made available to the author and there was insufficient information to appropriately develop the more complex function.[63] [64]

$$T_{Friction} = C_{friction} V_{axial}$$

Equation 4.30

Given the completed governing equation the author then made the assumption that the instantiations axial and transverse velocities were the result of cyclical turbulent pulsations about a mean velocity value as found in Equations 4.31 and 4.32. The rationale behind this assumption is twofold, the first being that all testing into turbulent effects on current meter response made a similar such assumption and therefore effectively leveraging the results of these studies to

inform the modeling required a similar such assumption. The second reason behind such an assumption was that given the steady state nature of the CFD simulations there was no available information regarding the spectrum of turbulent fluctuation periods and therefore the primary value found by Reeb et. al. will be utilized.[70] This simplification then allowed the transient form of the general current meter response to take the form found in Equation 4.33, and from there to be simplified into Equation 4.38. This form of the equation cannot be mathematically taken further and therefore a simplification put forth by Ower is also employed. This assumes that the ratio of the turbulent intensity to the turbulent fluctuation period is nominal and therefore can be safely removed from the equation, allowing it to evolve to Equation 4.39. It is found that this assumption is appropriate given that the local turbulent intensity is 0.05 and the primary fluctuation frequency is 3 Hz (6π) therefore at its maximum the ratio is 0.003. This fluctuation value was determined through an analysis of turbulence levels behind a series of chains that were installed at the entrance of a hydroplant to simulate the effect of trashracks and is supported by an analysis of the Strouhal Number associated with the hydroplant trashracks.[70][86] This frequency is supported by an investigation by the Bureau of Indian Standards which determined that the Strouhal Number (Equation 4.41) behind a trashrack is equivalent to 0.155. Using the equation for the Strouhal number and the local fluid velocity and trashrack geometry the shedding frequency of the bars can be determined to be 1.33.[10]

If Equation 3.39 is discretized into its constituent components it demonstrates that there is fluctuating value in addition to an initial disturbance which attenuates over time. The author then makes the combined assumptions that a sufficient period has passed such that the initial disturbance has passed that a mean value had been assessed for the rotation rate of the propeller blade over a series of complete cycles. These assumptions allow the final equation dictating the

rotation rate to be assessed in Equation 4.40, and are determined appropriate due to the long exposure period prescribed in industry tests codes.

$$V_{axial} = V_{maxial}[1 + \lambda_a \sin(p_a t)]$$

Equation 4.31

$$V_{trans} = V_{mtrans}[1 + \lambda_t \sin(p_t t)]$$

Equation 4.32

$$\frac{dV_{meter}}{dt} + \text{Ą}[1 + \lambda_a \sin(p_a t)] = \text{Ɓ}[1 + \lambda_a \sin(p_a t)] + \text{Ć}\left[1 + 2\lambda_a \sin(p_a t) + {\lambda_a}^2 \sin^2(p_a t)\right] + \text{Đ}\left[1 + 2\lambda_t \sin(p_t t) + {\lambda_t}^2 \sin^2(p_t t)\right]$$

Equation 4.33

Where

$$\text{Ą} = \frac{-\rho {D_{prop}}^4 b_{blade} V_{maxial}}{2\pi I_{prop}}$$

Equation 4.34

$$\text{Ɓ} = \frac{-C_{friction} V_{maxial}}{2\pi I_{prop}}$$

Equation 4.35

$$\text{Ć} = \frac{\rho {D_{prop}}^3 a_{blade} {V_{maxial}}^2}{2\pi I_{prop}}$$

Equation 4.36

$$\text{Đ} = \frac{\rho N_{Blade} C_{mdrag} A_{Blade} R_{Mblade} {V_{mtrans}}^2}{2\pi I_{prop}}$$

Equation 4.37

$$V_{meter} e^{\text{Ą}\left[1 - \frac{\lambda_a}{p_a}\cos(p_a t)\right]} = \int \left[\text{Ɓ} + \text{Ć} + \text{Đ} + [\text{Ɓ} + 2\text{Ć}][\lambda_a \sin(p_a t)] + \text{Ć}{\lambda_a}^2 \sin^2(p_a t) + 2\text{Đ}\lambda_t \sin(p_t t) + \text{Đ}{\lambda_t}^2 \sin^2(p_t t)\right] e^{\text{Ą}\left[1 - \frac{\lambda_a}{p_a}\cos(p_a t)\right]} dt + \text{Ƕ}$$

Equation 4.38

$$V_{meter} = \frac{B + C + D}{A} + [B + 2C]\frac{Asin(p_a t) - p_a cos(p_a t)}{A^2 + {p_a}^2} + C{\lambda_a}^2 \frac{-A^2 cos(2p_a t) + A^2 - 2Ap_a sin(2p_a t) + 4{p_a}^4}{2[A^3 + 4Ap_a{}^2]} + 2D\frac{Asin(p_t t) - p_t cos(p_t t)}{A^2 + {p_t}^2} + D{\lambda_t}^2 \frac{-A^2 cos(2p_t t) + A^2 - 2Ap_t sin(2p_t t) + 4{p_t}^4}{2[A^3 + 4Ap_t{}^2]} + He^{-At}$$

Equation 4.39

$$\overline{V_{meter}} = \frac{C_{friction}}{\rho b_{blade}{D_{prop}}^4} - \frac{a_{blade}}{b_{blade}D_{prop}}V_{maxial} - \frac{a_{blade}{\lambda_a}^2}{2b_{blade}D_{prop}}V_{maxial} - \frac{N_{Blade}C_{mdrag}A_{Blade}R_{Mblade}}{2b_{blade}{D_{prop}}^4}\frac{{V_{mTrans}}^2}{V_{maxial}} - \frac{N_{Blade}C_{mdrag}A_{Blade}R_{Mblade}{\lambda_t}^2}{4b_{blade}{D_{prop}}^4}\frac{{V_{mTrans}}^2}{V_{maxial}}$$

Equation 4.40

$$St = \frac{fD_{bar}}{V_i}$$

Equation 4.41

It should be noted that the equation above is extremely similar to the calibration function prescribed to convert the rotation rate of the propeller to the mean flow axial to the meter. The first two terms are what is evaluated during the calibration itself and the effects of the remaining terms are not observed due to the constraints of the testing parameters.[39] Using this information it is then possible to assess the velocity measured by the current meter when informed by the calibration values under idealized conditions.

$$\overline{V_{mesaxial}} = \frac{C_{friction}}{\rho a_{blade}{D_{prop}}^3} - \frac{b_{blade}D_{prop}}{a_{blade}}\overline{V_{meter}}$$

Equation 4.42

The calibration equations for all four of the current meters investigated can be observed in Equation 2.2 above in the Literature Review Section. However the implication of this is that using Equations 4.40 and 4.42 it is possible to assess

the flow rate recorded by the current meters if the variables in Equation 4.40 can be accurately determined. However, to do this each of the three terms (axial turbulent pulsation, mean transverse flow, and transverse turbulent pulsation) not explicitly determined via the calibration were compared to experiments specifically investigating these effects. When necessary a corrective factor was included to better represent the physical operation of the current meters.

Axial Pulsations

Embedding the impact of axial pulsations on the registration of axial represents one of the critical elements in the development of an accurate numerical simulation of current meter registration. In this it is important to leverage experimental studies into this as it captures the important nuances of the fluid structure interaction that are not taken into account Equation 4.42. Given this the author used the results of the study by Jepson discussed above to inform the numeric model. It is important to note that Jepson did not use the C31 current meters that are being simulated, rather he used an early variant of the C2 meter also developed by Ott. As such the author developed the subsequent modeling framework using the data from the Ott 2-7858/2-3 variation (as this had the most information), and then tested the model on different meter types for which data was available to determine the effectiveness of the numeric model. In the experiments by Jepson the current meters were only exposed to mean and transverse axial flow, and the results of this study were presented as error in measurement as a function of mean velocity, pulsation frequency, and turbulent intensity.[43] Given this raw information, in combination with the fact that the generalized equation reduces to Equation 4.43 under strictly axial conditions, the author proceeded to calculate the propeller rotation rate strictly using the current meter characteristics and Equation 4.42. The calculated rotation values were then compared to the ones determined experimentally to determine the difference between the two. This difference was observed to overwhelmingly be a function of turbulence intensity and pulsation frequency rather than flow rate,

and as such the author proceeded to employ a two-dimensional least squares fit to the differential between the calculated and experimental propeller rotation rate. This was done using at 4th, 3rd, 2nd, and 1st order regression, to ensure an effective data fit. Higher level regressions were performed by the author however significant evidence of Runge's Phenomenon was detected and therefore the results of this were not included in the research. This regression was performed using a post-processing code developed by the author, designed to allow the user to generate the coefficients of any order two-dimensional regression. As this work was done in support of the author's Hydro Research Foundation Fellowship a further explanation as well as the raw code is available in the documentation of the tool.[14] While the all the regressions provided reasonable results, the 4th order demonstrated the best fit of the data (R^2 of 0.99004). As such the modified rotation equation prescribed by this investigation can be found in Equation 4.44 with the appropriate coefficients for the equation found in Table 4.14. To ensure the validity of the revised equation for the rotational speed induced by axially pulsating flow the author then calculated the anticipated rotation rate of the Ott-2-7858/3 when exposed to axial pulsations using the same revised equation derived using the characteristics from the Ott-2-7858/2-3. This equation was found to replicate the experimental response of the Ott-2-7858/3 to a high degree of accuracy, with an average differential of only 2.45% between the measured and calculated rotation rate of the current meter.

$$\overline{V_{meter}} = \frac{C_{friction}}{\rho b_{blade} {D_{prop}}^4} - \frac{a_{blade}}{b_{blade} D_{prop}} V_{maxial} - \frac{a_{blade} {\lambda_a}^2}{2 b_{blade} D_{prop}} V_{maxial}$$

Equation 4.43

$$\overline{V_{meter}} = \frac{C_{friction}}{\rho b_{blade} {D_{prop}}^4} - \frac{a_{blade}}{b_{blade} D_{prop}} V_{maxial} - \frac{a_{blade} {\lambda_a}^2}{2 b_{blade} D_{prop}} V_{maxial} + A_P$$

Equation 4.44

where

$$A_P = A_{p1} + A_{p1}\lambda_a + A_{p2}p_a + A_{p3}{\lambda_a}^2 + A_{p4}\lambda_a p_a + A_{p5}{p_a}^2 + A_{p6}{\lambda_a}^3 + A_{p7}{\lambda_a}^2 p_a + A_{p8}\lambda_a {p_a}^2 + A_{p9}{p_a}^3 + A_{p10}{\lambda_a}^4 + A_{p11}{\lambda_a}^3 p_a + A_{p12}{\lambda_a}^2 {p_a}^2 + A_{p13}\lambda_a {p_a}^3 + A_{p14}{p_a}^4$$

Equation 4.45

Transverse Flow

The study into the effect of mean transverse flow on the registration of the meters leveraged the effort by Fulford et al. While this was discussed in the literature review, it is felt by the author that it is important to reiterate the key findings of this effort. This study researched the effect of transverse and axial flow on the current meters investigated over the course of this thesis and found that while there was an appreciable effect resulting from the ratio of axial to transverse flow there was a nominal impact of flow rate on accuracy of the meter registration. Given this, the author elected to digitize the results of the investigation and utilize the results to determine an appropriate function for the propeller transverse drag coefficient. The use of field determined data enables the derived equation to represent the interaction of the flow field with the traverse area of the propeller blades as a function of incoming flow angle. The accuracy values provided by Fulford at increasingly oblique angles of incident on the propeller, where then back converted to rotation rate induced by the oblique flow. This rotation rate was then used in combination with the axial and transverse velocities found at each angle of incident to assess the appropriate propeller transverse drag coefficient. This was enabled by the fact that only mean axial and transverse flow were studied and therefore Equation 4.40 above is reduced to Equation 4.46. A continuous equation for the drag coefficient across all incident angles was determined using a least squares regression technique for each of the current meters investigated. As a result the transverse drag is equivalent to Equation 4.47, which revises the other equations above. The results of the individual drag coefficient calculation and the least squares regression coefficient are found in Tables 4.15 and 4.16 respectively (the last term in the table represents the R^2

value of the least squares fit). It should be noted that the order of the regression was selected to balance the goodness-of-fit while minimizing the presence of Runge's Phenomenon.

$$\overline{V_{meter}} = \frac{C_{friction}}{\rho b_{blade} {D_{prop}}^4} - \frac{a_{blade}}{b_{blade} D_{prop}} V_{maxial} - \frac{N_{Blade} C_{mdrag} A_{Blade} R_{Mblade}}{2 b_{blade} {D_{prop}}^4} \frac{{V_{mTrans}}^2}{V_{maxial}}$$

Equation 4.46

$$C_{mdrag} = C_{d1} {\theta_{Offset}}^6 + C_{d2} {\theta_{Offset}}^5 + C_{d3} {\theta_{Offset}}^4 + C_{d4} {\theta_{Offset}}^3 + C_{d5} {\theta_{Offset}}^2 + C_{d6} \theta_{Offset} + C_{d7}$$

Equation 4.47

Transverse Turbulent Pulsations

The study into the effect of transverse turbulence on current meters used the investigation results from Jepson because it demonstrated the effect of this over a wide range of turbulence intensities for several different current meter types. This study was performed by exposing the current meters to steady axial flow and transverse turbulent pulsations, thereby reducing Equation 4.40 above to a more simplified version as found in Equation 4.48 below. While Jepson did not perform the study on the current meters used for this study (he investigated the Ott 2-13194/2, Ott 2-13194/3, and Ott 2-13194/4), he observed a dependence on current meter blade pitch which enabled the author to develop a generalized formula for the transverse-turbulent drag coefficient as a function of turbulent intensity and blade pitch.

The first step in this process involved calculating the traverse-turbulent drag coefficients for the current meters investigated by Jepson. In this process the author was able to leverage the results of calibration studies that were performed on the current meters by the manufacturer.[61] This provided the values for the first two termed of Equation 4.48 however because detailed engineering drawings were unavailable, the author to calculated the required blade characteristics (a_{blade} and b_{blade}) using these values. The known relationship between the first two terms of Equation 4.48 and the velocity-rotation slop and

velocity-rotation offset (documented in the current meter calibration process in the background section) allowed the author to develop an equation for the requisite current meter characteristics as found in Equations 4.49 and 4.50. The determination of these values required the author to make the underlying assumption that the friction between the propeller and the central hub was equivalent to 3.8E-6 N m sec^{-1}. This value was determined valid because it was experimentally established on a similar instrument and because the current meters are required to be industry to be appropriately lubricated to minimize friction between the propeller and the hub.[39][62][64] Using the value, along with known dimensions of the current meter the author to assed the transverse-turbulent drag coefficient at each point were testing data was available. This data then allowed the author to develop a polynomial function (Equation 4.52) which represented the response of the system to both turbulent intensity and propeller blade pitch with a high degree of accuracy. The coefficient equation is demonstrated below with the corresponding coefficients found in Table 4.17. It should be noted by the reader that a 3rd order regression was employed because higher order models demonstrated Runge's Phenomenon and therefore despite their ability better to reproduce the point values used to inform the regression they were not used. In addition to this the author limited the data used in the analysis to turbulent intensities under 0.825. This was done because the resulting coefficient equation could reproduce the dataset within this range to a much higher degree of accuracy. Furthermore, because of the accelerating nature of the draft tube, it is unlikely that turbulent intensities would be this high locally due to the accelerating nature of the flow.[110]

$$\overline{V_{meter}} = \frac{C_{friction}}{\rho b_{blade} {D_{prop}}^4} - \frac{a_{blade}}{b_{blade} D_{prop}} V_{maxial} - \frac{N_{Blade} C_{mdrag} A_{Blade} R_{Mblade} {\lambda_t}^2}{4 b_{blade} {D_{prop}}^4} \frac{{V_{mTrans}}^2}{V_{maxial}}$$

Equation 4.48

$$a_{blade} = \frac{b_{cal} C_{friction}}{\rho {D_{prop}}^3}$$

Equation 4.49

$$b_{blade} = \frac{m_{cal} C_{friction}}{\rho {D_{prop}}^4}$$

Equation 4.50

$$\overline{V_{meter}} = \frac{C_{friction}}{\rho b_{blade} {D_{prop}}^4} - \frac{a_{blade}}{b_{blade} D_{prop}} V_{maxial} - \frac{N_{Blade} A_{Blade} R_{Mblade} {\lambda_t}^2}{4 b_{blade} {D_{prop}}^4} \frac{{V_{mTrans}}^2}{V_{maxial}} C_{mdrag-Turb}$$

Equation 4.51

$$C_{mdrag-Turb} = C_{dt_1} + C_{dt_2}\lambda_t + C_{dt_3}K + C_{dt_4}{\lambda_t}^2 + C_{dt_5}\lambda_t K + C_{dt_6}K^2 + C_{dt_7}{\lambda_t}^3 + C_{dt_8}{\lambda_t}^2 K + C_{dt_9}\lambda_t K^2 + C_{dt_10}K^3$$

Equation 4.52

Current Meter Response Equation

Using the information derived from physical experiments which investigate the individual attributes which affect current meter performance the author was then able to develop a holistic equation for the response of the meters assuming a superposition of these effects. Local hydraulic characteristics determined through the numerical methods discussed above will then be used to populate this equation to determine the rotational speed of the current meter propeller. This rotational speed was then inputted into the known calibration function for the current meter to determine what velocity the sensor would record.

$$\overline{V_{meter}} = \frac{C_{friction}}{\rho b_{blade} {D_{prop}}^4} - \frac{a_{blade}}{b_{blade} D_{prop}} V_{maxial} - \frac{a_{blade} {\lambda_a}^2}{2 b_{blade} D_{prop}} V_{maxial} + A_P - \frac{N_{Blade} C_{mdrag} A_{Blade} R_{Mblade}}{2 b_{blade} {D_{prop}}^4} \frac{{V_{mTrans}}^2}{V_{maxial}} - \frac{N_{Blade} A_{Blade} R_{Mblade} {\lambda_t}^2}{4 b_{blade} {D_{prop}}^4} \frac{{V_{mTrans}}^2}{V_{maxial}} C_{mdrag-Turb}$$

Equation 4.53

Flow Rate Estimation

The overall flow rate recorded by the array of current meters was assessed using the calculated individual velocities determined at each point where current meters were simulated within the flow field. The placement of the sensors follows the log-linear profile dictated by industry code as does the conversion from the individual sensor velocities to the flow rate. Both equations can be found in the background sections above. The study was performed using a generalized numerical code developed by the author to simulate both the individual recorded velocities of the four different types of current meters investigated and the resultant flow rate predicted by the simulated current meters. The code leverages the inverse distance weighting technique discussed above and allows the user to read in the required hydraulic characteristics (Cartesian spatial components, Cartesian velocity components, and turbulent kinetic energy values) directly from the CFD model along with the simulation location to simulate the desired resolution of current meters. The simulated current meter resolution ranges from 5 (the minimum amount) to 15 in increments of two for both the vertical and horizontal direction. The resulting total resolution, ranges from 5 to 225 sensor points within each bay. This range was selected because it not only encapsulates the range of current meters required by industry standards as a function of the flow path cross-sectional area (120 to 180) but it also gives a more comprehensive understanding of sensor accuracy outside of this window.[37] Furthermore, the range of current meters was selected to demonstrate the effect of the ratio of horizontal to vertical sensor resolution. The results of this investigation can be observed in the subsequent section however, given the volume of total results (four current meter types, three bays and six flow rates) and the relatively consistent nature of the accuracy evolution across flow rates only the mean sensor accuracy at each level of sensor resolution will be displayed in the results. The generalized inverse distance weighting based current meter simulation code will be displayed in Appendix 2 below.

Acoustic Time of Flight Simulation

Unlike the current meters the acoustic time of flight instrumentation is not comprised of a physical structure which is manipulated by the fluid in the conduit. Given this the author did not model the response of the acoustic time of flight transducers to see what would be recorded, rather the author constrained the investigation to determine what they would directly measure. The decision to do so is supported by the results contained in the literature review, which demonstrate that under nominal operating conditions factors such as turbulence and path elongation do not have a significant effect on the recorded result. As such the modeling of the acoustic pulse accuracy primarily investigates the effect of transverse flow on the recorded as well as the effect of the vertical angle of the acoustic pulse. Modeling of the acoustic pulse was performed by assessing the characteristics of flow at points along the acoustic pulse path (Figure 4.25). The acoustic time of flight paths were modeled in the same location that they were mounted within the bays during testing. This modeling location allowed the sensors to not only validate the computational fluid dynamic models, it also acts to demonstrate the accuracy of application of the most feasible location. This section will initially address how the response of an individual acoustic time of flight flow path was modeled. Once discussed the author will then demonstrate how this was leveraged to simulate the response of both single and double acoustic paths. Finally, this section will go into how a range of acoustic paths was modeled to demonstrate the evolution in flow measurement accuracy because of increased acoustic path application.

Individual Acoustic Time of Flight Simulation

The initial stage of modeling the acoustic pulse required the determination of the spatial locations of the points along the acoustic path are determined. The evaluation is represented by 50 points were distributed equally as specified in Equation 4.54 below. Once the locations were determined the Cartesian velocity components were evaluated using the nearest neighbor and inverse distance weighting technique discussed above. The points were then numerically

averaged the using trapezoidal technique (Equation 4.55) this method was leveraged because it enabled the computational assessment of the response of the acoustic time of flight more rapidly than other numerical methods. In addition, the high resolution of the evaluation points allowed the method to be implemented with a high degree of confidence.

$$\begin{aligned}(x_{api}, y_{api}, x_{api}) \\ &= (x_{apb}, y_{apb}, x_{apb}) \\ &+ \frac{(x_{ape}, y_{ape}, x_{ape}) - (x_{apb}, y_{apb}, x_{apb})}{\sqrt{(x_{ape} - x_{apb})^2 + (y_{ape} - y_{apb})^2 + (z_{ape} - z_{apb})^2}} i_{ap}\end{aligned}$$

Equation 4.54

$$(u_{apa}, v_{apa}, w_{apa}) = \frac{1}{P_{AP}} \sum_{i=1}^{N_{AP}+1} \frac{P_{AP}\left[(u_{apl_i+1}, v_{apl_i+1}, w_{apl_i+1}) - (u_{apl_i}, v_{apl_i}, w_{apl_i})\right]}{2N_{AP}}$$

Equation 4.55

The Cartesian velocity components were then leveraged to assess the velocity that the acoustic time of flight transducer would record subject to the hydraulic conditions in the intake. This was done by determining the mean velocity components that were in line with the acoustic pulse. The angles were assessed by the geometry of both the upstream and downstream mounting locations along with the distance between the two locations as well as the number of acoustic paths modeled. The total magnitude of the velocities in line with the pulse was then used to assess what velocity would be measured by the acoustic time of flight path under the assumption of strictly axial flow (Equation 4.56). The recorded velocity represents the velocity that would be measured by a single acoustic path from the left to right. The single acoustic path process is demonstrated for a two-dimensional case in Figure 4.24 below. While the

numerical process is performed in three dimensions, the geometrical constraints of the display medium constrain an effective diagram to two dimensions. A mirrored acoustic pulse was then modeled and the equivalent magnitude was calculated from right to left. These were then averaged to determine the velocity that would be recorded with a dual acoustic path as is recommended in the industry procedure.

$$V_{AM} = \frac{u_{apa}\cos(\theta_{apx}) + V_{apa}\cos(\theta_{apy}) + w_{apa}\cos(\theta_{apz})}{\cos(\theta_{apz})}$$

Equation 4.56

It should be noted by the reader that, unlike the modeling of current meter response, the simulation of the acoustic time of flight technique leverages the conceptual model of the response of the sensors rather than using a physical representation of the sensors itself. This simplification was implemented because enabled the author to focus the research on the effect of transverse flow on measurement accuracy, which has been demonstrated to be the primary concern of the hydropower industry a review of the literature. This simplification has reduces the ability of the simulation to fully represent the average transect velocity because it does not simulate features of the pulse-fluid interaction including: path elongation, pulse-particulate interaction and the impact of changing fluid parameters on the acoustic transmission. The last of these was not investigated because the CFD models assumed incompressible, with adiabatic flow conditions. Given this the author was unable to include a model that would take into account the varying speed of sound in water. Pulse-particulate interaction has the potential to affect the accuracy of the measured flow rate because suspended particulates have the ability to both backscatter the acoustic pulse and disrupt the pulse in such a way that it cannot be reliably measured by the receiving transducer. In addition to this the author precluded the investigation of this because there was no reliable information regarding the

extent of particulates suspended in the flow. The final attribute of pulse fluid interaction that was not included was acoustic path lengthening. This lengthening is caused because the turbulent nature of the fluid flow causes the volume of fluid containing the acoustic pulse to vacillate backwards and forwards. This effect then occurs over the entire pulse length, incurring path elongation which is a function of the ratio of local turbulence levels to the speed of sound in water. This elongation causes the acoustic pulse to have a longer transit time and therefore decreases the average path velocity. Mechanisms to model the effect of path elongation are included in the future work section of the dissertation, however it should be noted that previous research into the simulation of acoustic time of flight flow measurement demonstrated that straight line acoustic pulse propagation is appropriate when the Mach number is less than 0.1.[113] Local Mach numbers ranged from 0.0005 to 0.0013 in flows through the intake in the measurement volume and therefore this method was assessed to be acceptable for this research.

Flow Rate Estimation

The overall flow rate recorded by the array of acoustic time of flight paths was assessed using the measured mean velocities determined at each point where paths were simulated within the flow field. The placement of the paths followed the Gauss-Lagrange Method prescribed in the industry test codes as does the conversion from the recorded velocities to an overall flow rate.[6][37] The equations for both the appropriate height of the acoustic paths as well as the weighting of the path results can be found in the background section above. To perform this investigation the author developed a generalized numerical post-processing code designed to read in Cartesian velocity characteristics and simulate both the measured mean velocities along paths at the appropriate locations within the flow and the corresponding recorded flow rate resulting from the measured velocities. The numerical code evaluates both single and double acoustic paths in the specified volume, thereby demonstrating the effect that transverse flow has on

flow accuracy and allowing an investigation into the economic merits of the use of a double path. The code for the generalized inverse distance weighting simulation is displayed in Appendix 3 below. The simulated acoustic time of flight resolution ranges from 1 single path to 11 double acoustic paths within each bay. As a result, the total resolution within each bay ranges from 1 to 22 acoustic paths. This range was selected because it encapsulates the range of paths traditionally prescribed by industry test codes and demonstrates the performance of meters both above and below this range. As with the current meter investigation, the values from this study contained in the results section will be constrained to the total flow measurement accuracy resulting from single and dual acoustic paths averaged across all the six flow rates simulated. The entirety of the results will be displayed in the appendices below.

Indicated Unit Characteristic Curve

The final stage in the sensor simulation section of the research was the determination of the effect that the level of instrumentation used to record the flow rate affected the measured unit efficiency over the range of flow rates studied. This was done using the power and head measurements taken from Unit 4 during site testing. These values were then combined with the measured flow rate resulting from each level of instrumentation that was studied in the section above using Equation 4.57 presented flow. This process was done at each of six flow rates investigated as a part of this study thereby producing a series of discrete efficiency measurement over the production range of the units. These values there then leveraged to develop a continuous curve describing the measured unit performance using a least squares polynomial regression as per industry test codes. Rather than using the traditional 5th order polynomial fit, a 3rd order was leveraged as this was found to provide a smoother fit of the efficiency data that was assessed to be more representative of the performance of the unit than more undulating curve produced by the higher order curves. The 3rd order curve performed admirably, achieving a minimum R^2 value of 0.97.[37]

$$\eta_{mes} = \frac{P_{Gen}}{g\rho Q_{mes} H}$$

Equation 4.57

Value Establishment

The following section of the work will outline the process in which the actual value of the individual flow meters was established. This section leverages not only the information regarding the increasing levels of accuracy associated with the sensors, it also uses the historic power production of Lower Granite and value of electrical data from the Mid-Columbia clearing house. While discussed at length subsequently the process below is built on the fundamental assumption that the amount of power generated by the plant operator is based largely on the amount of available water for generation. Using the operational assumption along with the established discrepancy in indicated plant performance it is possible to assess the opportunity cost associated using an inaccurate unit curve to determine the appropriate loading of a unit. The process is demonstrated in Figure 4.26, where it can be observed that the under prediction of unit efficiency leads to a simultaneous conservation of water and under production of the hydropower plant. One final attribute of note is that the subsequent investigation will be constrained in the analysis of the results from the current meter flow measurement accuracy. The analysis will be done in two separate ways the first, which is designed to replicate the results associated with the static placement of current meters will study the effect of equivalent increases in sensor resolution both vertically and horizontally. The second method, designed to study the effect of the dynamic current meter application, will leverage the accuracy resulting from the application of the highest vertical resolution studied and then incrementally step through increasing levels of horizontal current meter resolution. The acoustic time of flight paths will be evaluated for their value using the results of acoustic paths from individual directions, (left to right and right to left) as well as from both directions (dual paths).

Optimal Plant Dispatch Curve

Prior to the implementation of such an analysis, it is critical to understand how the hydropower plant itself will be loaded based on the indicated unit performance as this demonstrates the efficiency of the of the plant overall. In the process of determining the optimal plant loading, the author used the family of units assumption, which states that the performance of one unit will be similar to that of others of the same manufacture. While this has been shown to not always be accurate it is felt appropriate for this work given both that it is a common assumption within industry and there was no other information regarding the performance of the other units. Under this assumption, the author developed a post-processing code which established the power level at which it was optimal from an efficiency standpoint to bring additional units online, until the point at which the plant was at full capacity. It is important to note that the optimization process evaluated the performance of the system at a series of discrete points at (0.5 MW increments) rather than over a continuous curve. The reason that this method was employed rather than a least squares style fitting is that the optimal plant performance at the transition between bringing another unit online is comprised of a shape which would not be captured with such a method. The performance of the different combinations of units is demonstrated in Figure 4.27 below and the performance of the plant under optimal dispatch after this process can be seen in Figure 4.28 below. This optimal dispatch process was performed for both the known operational characteristics of Unit 4 as well as the system efficiencies recorded by all the sensor types and at all sensor resolutions investigated. The types of sensors studied were: the acoustic time of flight single path (left to right), the acoustic time of flight (right to left), the acoustic time of flight dual path, the general current meter, the Ott C31-1 (Plastic) current meter, the Ott C31-1 (Metal) current meter, the Ott C31-A current meter, and the C31-R current meter.

Determination of Operational Opportunity Cost

Once the optimal unit dispatch was established using the performance metrics established by the different quantities of applied sensors, the opportunity cost established associated with such operation was investigated. This process used the historic operation of the plant along with the price of electricity established in the mid-Columbia interconnect discussed above. To do this the author developed a post-processing code (Appendix 4) to calculate the differential between the amount of power that was produced based on the measured system performance and the operational system performance. This differential as seen in Figure 4.25 was calculated on an hourly basis and then summed to determine the cumulative daily power generation opportunity cost. This value was then multiplied by both the high and low price of power from the interconnect on that day to demonstrate the range of revenue that could have been acquired with the power. The value of the flow was then calculated as the differential between revenue acquired at the high and low price of electricity. The evaluation process assumes therefore that with increasingly accurate flow plant operators will be able to generate power at the maximum daily electrical price instead of the minimum daily price. The method ensures that all the water which should pass through the powerhouse does, instead it focuses on when the power is produced throughout the day and how shifts in this can be leveraged for additional plant revenue.

There are four additional assumptions that also accompany this process, the first of which being that the hydroplant accepts the price of power available to it rather than competitively bid into the market. The second attribute assumption intrinsic to this process is that the additional power generated does not affect the price of power within the region. While this would drive down the price of power to an extent, this was judged to be an appropriate simplification given the relatively small amount of additional power that would be generated through optimal measurement. The third assumption was that the head in the hydroplant was

held constant and was not affected by the modification of the plant generation. The final assumption that was embedded within the model was that the plant operated strictly as a run-of-river type plant and therefore did not store the additional water represented by the increasingly accurate flow measurement to generate power on subsequent days. This process was leveraged given both the temporal resolution of the value of power (daily as opposed to hourly) and the relatively small amount of storage that the plant possesses given its Mainstem characteristics. In addition, the author filled in the cost of electricity data on the days where information was unavailable using linear interpolation between points. This method was used because of the relatively short period of information gaps (a maximum of 2 days). The opportunity cost evaluation process then resulted in a daily opportunity cost for the sub-optimal use of water associated with each type and extent of flow measurement and was performed for the entire 2016 year to provide information as to the annual effect of this.

Value of Flow Measurement Accuracy

The final stage of research then leveraged the opportunity costs along with the cost of flow measurement instrumentation to establish the actual value of the instrumentation. This was done through an investigation of the incremental cost of flow sensors and the incremental reduction in opportunity cost associated with the application of said sensors. Given the method used, the process resulted in the value associated in stepping from the lowest level of instrumentation to the flow measurement accuracy associated with the next resolution step, and so forth, up the highest level of sensor resolution studied (though the notes at the bottom should be evaluated in the case of the acoustic time of flight application). Unfortunately, this method does not provide information regarding the value of the lowest level of flow measurement accuracy because there was no information for the assumed characteristics of the unit that would be used in the absence of any form of flow measurement. The incremental value of flow measurement was determined by the reduction in opportunity cost that the increase in flow

measurement sensors provided and the incremental cost of the sensors was determined as the cost of additional instrumentation. The latter leveraged information provided by several manufacturers of both the acoustic time of flight and current meters, however the specifics of instrumentation cost are not specifically addressed due to concerns regarding information sensitivity. There are several attributes that should be considered with the establishment of the cost of index testing. The first is that it is assumed that the application of the flow measurement instrumentation is applied during a scheduled shutdown of the plant, and therefore the opportunity cost of plant production is not addressed. In addition to this, the cost of labor, mounting materials and control instrumentation were not included in the cost evaluation. The reason for the omission of these values was because they are highly variable, and not publicly available. In addition to this, the mounting requirements for both the static current meter and acoustic time of flight application is highly site specific as access to the measurement site as well as the condition of the site significantly impacts the cost of the measurement. The decision omits the values is also supported by the fact that the author is strictly constraining the analysis to the incremental cost of sensor application and does not take into account the cost for the application of the lowest level of instrumentation. It is assumed that achieving this nominal level of instrumentation will carry a significant percentage of the omitted costs. Furthermore, it is assumed that the instrumentation will be purchased for the site testing rather than rented. In addition, the cost of the incremental cost of the instrumentation was assumed to represent an increase in each of the bays within the Unit 4 however, given that it was assumed that the unit characteristics were assumed to be identical, this was only done for one of the six units at Lower Granite. Finally, the incremental value approach required a mild modification in the case of the acoustic time of flight application given its non-monotonic nature. If such an analysis was not modified the incremental value would drive the ideal number of acoustic paths towards a local minimum rather than global ones. To this end, the author omitted the points which drew the value to the local minimum

specifically 3,4, 7 and 8 acoustic paths. The removal of these specific points allowed for the data from the most paths to be retained. Furthermore, it should be noted that the incremental costs and benefits between paths with data points artificially remove reflect both the cost between the points themselves. As stated above in the background section discussing the roles and impact of flow measurement quantifying the value of flow measurement is an extremely difficult process. Given this the method outlined above represents an initial process to evaluate the specific value of flow measurement. Naturally subsequent research should be performed explicitly investigating the value of water within mainstem type hydroplants. Such research could then readily leverage the tools and techniques created in this research. To this end the author also included the incremental reduction in the opportunity water cost in relation to the cost of sensors required to achieve said reduction within the results of this dissertation.

CHAPTER FIVE
RESULTS

The following chapter is designed to provide the reader with a comprehensive understanding of the results of the research process outlined above. Relevant aspects of the CFD model, sensors post-processor, and value of flow measurement will be presented and then discussed in turn.

Computational Fluid Dynamics Modeling

The results of the computational fluid dynamic modeling of this research are largely focused on determining the ability of the developed model to represent the hydraulic characteristics present within the short converging intake. Given this, the CFD results will contain the four primary sections: the preliminary boundary condition study, the mesh resolution study, the residual analysis, the study to attempt to reproduce recirculation at the acoustic time of flight sensor section, and the validation of the model using the acoustic time of flight data extracted during turbine operation as well as the distribution of the flow rate through the intake bays.

Boundary Condition and Turbulence Model Preliminary Investigation

As established in the methods section, because the upstream flow conditions at the site were unknown a boundary condition investigation was performed to determine the flow direction which best represented the distribution of fluid velocity within the intake. In addition to this, the preliminary study investigated the effect of different turbulent closure models on the accuracy of the CFD model. The accuracy resulting from both attributes was studied using information resulting from the model and site testing. The most holistic indicator of system accuracy was the distribution of flow between the intake bays and the results of the eight different permutations can be seen in Table 5.1 and when examined in relation to the distribution of flow observed during testing the percent accuracies present in Table 5.2 were developed. The results of this test show that while all

of the investigated models perform relatively well, the shear stress transport closure model in combination with the flow from all of the forebay boundaries provided the most realistic aggregated bay distribution.

When the results of the computational models are then compared to the data extracted from the physical model several things can be observed. The variation is best displayed in the Figures 5.1 and 5.2 which graphically represent the variation that exists between the velocities extracted at the centerline of Bay A. The figures show that the upstream velocities from both the physical and computational model demonstrate a reasonable level of agreement below the centerline of the conduit, however after this they begin to diverge with the physical model providing significantly higher values than the computational models. The values downstream velocities calculated in the CFD model show much better agreement with the physical model, however the flow near the top of the conduit still demonstrates a higher fluid velocity than the computational model. This suggests to the author that fluid flow is concentrated in the center of the conduit near the top of the bay for reasons that are not captured in the computational model. It is important to note however that no evidence of the recirculation found in the field testing was observed in the physical model, as the downstream velocity measurement was in position to capture this hydraulic phenomenon. This suggesting that this was caused by a geometrical or hydraulic attribute of the flow path not included in the physical model. When the results of the point discrepancies are compared using the Analysis of Variance test (Table 5.3) the discrepancies between the upstream section and the CFD results are significant, whereas the downstream section are much less so. It should be noted that the difference between the hydraulic structure was particularly pronounced in the k-ε closure model with flow in the axial and left direction in the downstream model. In addition to this the upstream model demonstrated significant variance with axial flow for both the shear stress transport and k-ε closure modes.

The final component of the preliminary investigation was a comparison of the velocities recorded by the acoustic time of flight paths during the field testing those that would have been recorded given the velocity distribution of the calculated CFD models. This comparison was achieved using the acoustic time of flight post-processing code described above to calculate the velocity for nine dual acoustic paths because this was the level of resolution provided by the field tests. As stated above the field test demonstrated a negative velocity at the top of each of the intake bays, whereas none of the computational models were able to replicate this in any meaningful way. The discrepancy can be observed in Figure 5.3 which was taken from the comparison performed in Bay C. This result typifies those found in the other two intake bays, where it can be observed that in the middle of the intake the fluid velocity is higher in the field test than in the computational model. Conversely, at the edges of the intake, the CFD model produces higher velocities than the field model as this ensures establishes a common flow rate through the bay. As with the physical model testing the author performed an ANOVA test to quantify the differences, as found in Table 5.4 where it can be seen that the overall agreement between the CFD model and the validation test data was much better despite the presence of the recirculation zone. When the results of this preliminary investigation are compared to each other to determine the appropriate boundary condition and closure model it was established by the author that the shear stress model with flow from all directions provided the flow field which most reliably represented the velocity distribution within Unit 4.

Mesh Resolution Study

The next stage of the investigation was performed to determine the viability of the mesh employed in the CFD model. As described above this process involved the use of a mesh resolution study where the results of the mesh intended for use in the remainder of the research was compared to the results of a slightly more dense (and therefor more computationally intensive) mesh. As the research was

dependent on the distribution of hydraulic characteristics within the flow field the author developed a post-processing code to compare 8,000 points within each of the bays to the results of each of the two models investigated. The R^2 comparisons of the Cartesian velocity components aggregated in Table 5.5 below. In addition to this it was felt important to the author for the comprehension of the reader to visualize the comparison and therefore the characteristics at each point are displayed in Figures 5.4 through 5.6. The result of this study demonstrates that there is an acceptably small variation that exists between the results of the two models. The further analysis of the two models demonstrates that the largest overall variation occurs within the velocity transverse to the main flow (the u velocity), and the primary variation between the two models between all the hydraulic characteristics is at the lower end of the spectrum investigated. In addition, the author took the opportunity to demonstrate the spectrum of distances between the point of hydraulic interest and the nearest point calculated by the CFD model. The histogram for all 8,000 points are demonstrated in Figures 5.7 to 5.9 below for both the mesh used in the research as well as the mesh used for the resolution study. This serves to both provide insight into the validity of the mesh study by establishing the distinction between the meshes, as well as displaying the minimum anticipated distances between the point of interest and its nearest CFD neighbor.

Residual Analysis

The following section is will address the analysis of the residuals present within the computational fluid dynamic model. The residuals are discussed because they represent important indicators of the stability and stability of the CFD model. Each of the computational models developed in this research was set to run for 3,500 iterations to ensure that the model had converged to an overall solution. Figure 5.10 below is the residual plot resulting from the 290 m^3sec^{-1} model, where it can be observed that the average residuals are higher than those typically desired in CFD models. As these residuals are similar to those observed

in the other flow rates modeled for this research the author investigated further in two primary ways. The first was the development of a series of threshold figures to demonstrate where in the computational domain the residuals were higher than the average residual found in Figure 5.10 (Figure A5.1 to A5.6 in Appendix 5). In this examination, it became apparent that a clear majority of the cells with high residuals existed in the downstream sub-domain of the model. Given the location of the residuals, it is felt by the author that the size of the residuals is a result of the inherently transient nature of flow in this region being ill-suited to the steady state model used to simulate it. The second method used to investigate the effect of the residuals on the appropriateness of the CFD models for the simulation of the sensors involved the development of a histogram of residuals specifically in the sensor simulation region of the domain. These are specifically discretized into the different hydraulic characteristics (Figure 5.11) and demonstrate that local residuals are largely beneath 0.01 thereby providing sufficient confidence for the use of the CFD data in the modeling of sensors within the intake.

As-Built Recirculation Investigation

The following section will discuss the results on behalf of the author to replicate the recirculation zone that was documented in the measurement volume of the acoustic time flow meter. As stated above three different permutations were performed in an attempt to replicate the recirculation: alteration of forebay turbulent intensity, altering surface roughness, and altering the physical domain of the intake itself. While a small recirculation zone was formed in all of the simulations developed it was insufficient to reach even the beginning of the volume where the acoustic paths were located (3.81 meters downstream of the gate slot) much less to the center of the acoustic path (5.7 meters downstream) which would be the minimum required for the acoustic paths to register a variation that significant. The characteristics of the recirculation zone the recirculation zones associated with each permutation investigated are displayed

in Table 5.6 below with dimensions corresponding to those outlined in Figure 5.12. In addition to this Figure 5.13 is a local pressure diagram with isobars representing the low pressure zone which drives the recirculation in Bay C at a flow rate of 290 m^3sec^{-1}. From this result several things can be observed outside of the fact that none of the variations produced an acceptable recirculation zone. The first is that changing the slip condition from a strict no-slip condition to riveted steel caused the recirculation zone to shrink appreciably. Secondly it was demonstrated that both the inlet intensity and the presence of the gate slot had a nominal impact on the formation of a significant recirculation zone in the intake.

As-Build Modification Recirculation Investigation

As stated in the methods above the author also performed a series of modifications on the as-built structure in an attempt to reproduce the recirculation zone that was observed during the field testing. Computational models were produced at 290 m^3sec^{-1} for each of the geometries, and these were then compared to the field velocity distribution in an effort to select the as-built modification which was most appropriate. Given the number of permutations within the results (nine different domain types, each with three different bays, each with three different types of acoustic sensor applications) the results presented within this section will be constrained to Bay A. As with other validations that occurred in this research the author compared the dual acoustic path velocities recorded during the unit testing to those that would be recorded in the CFD models of Unit 4 using the acoustic time of flight simulation tool. The simulated velocity profiles are demonstrated in Figure 5.14 and the specific values associated values are located in Table 5.7. The computed values were then compared to the field data to identify which combination of as-built modifications and surface roughness which best reproduced the velocity distribution measured in Unit 4. The percent difference between the individual field measurements and computed measurements were assessed and then averaged as seen in Table 5.8. It should be noted that the uppermost field

measurement was not taken into account during this process as it was found to induce extremely high percent differences which overwhelmed the effect percent difference observed between the other acoustic transects. Based on this analysis the author elected to utilize the combination of the straight obstruction and the bottom surface roughness equivalent to that of 20 times riveted steel (0.18 meters) (White, 2006) to develop the secondary range of CFD models of the unit. In addition to establishing the As-Built permutations which best represent the velocity distribution in the intake the investigation has reviled an extremely interesting interplay between the interplay between the height of the obstruction and the surface roughness's impact on the velocity distribution.

Model Validation

While it was demonstrated in the section above that the recirculation zone was not able to be fully replicated the author still performed the validation methods described in the methods section above. The first of these used, the percent bay flow distribution, was found to be replicated to a high degree of accuracy by the CFD models (Table 5.9). The second validation procedure investigated the ability of the CFD models to reproduce the transect velocities recorded by the acoustic time of flight sensors in the dam. The procedure to do so was done in three distinct methods as discussed in the methods section above, with the first being the development of an ANOVA test for all the sets developed (Table 5.10). The second method investigated is in the determination of the percent accuracy of the individual velocities recorded by the sensors in both the field test and the CFD. The average value of this for each of the dual paths developed along with the standard deviation of the values can be found in Tables 5.11 and 5.12. The final method used was a visual comparison of the flow profiles used in this research. Given that the total number of graphs (18 total) the author has elected to constrain the comparison figures to Bays A, B and C for at the flow rate of 634 m^3sec^{-1} for brevity (Figures 5.15, 5.16, and 5.17 respectively). The analysis of the flow profile demonstrates to the author that there is an unknown hydraulic

process occurring within the bays responsible for the recirculation, and therefore the inaccuracy associated with the flow profile. While mechanisms to address this will be enumerated in the subsequent chapter it is felt by the author that the recirculation is a result of the components of the fish bypass system not being appropriately included within the computational model due to their unknown specifications. Outside of this, it is possible to observe that the acoustic paths lower within the bay have much higher levels of accuracy and furthermore the low levels of standard deviation demonstrate the relative consistency of these values.

Flow Meter Simulation

The following section will demonstrate the results of the investigation into the evolution of flow measurement accuracy that occurs because of the number of applied sensors. As stated in the methods section above this, initially entailed a study into the appropriate technique to interpolate the hydraulic conditions at CFD determined points within the flow field to specific points for the simulation of flow measurement sensors. The results (found in Table 5.13) demonstrate that that most appropriate numerical technique is the inverse distance weighting method with a power of 3 and a radius of influence of 0.2 meters. In addition to this the author took the opportunity to assess the number of points that were leveraged in the use of different radii of influence. To this end the author developed a histogram outlining the number of point within a 0.2-meter and 0.3-meter radius (Figure 5.18). This investigation then outlined that a smaller radius of influence with a weighting factor which heavily favored the nearby points was optimal for use in the research. The results demonstrate that the radius of influence played the primary role in the development of the appropriate result, with the power being largely secondary. It should be noted by the reader that the results of the 0.3 radius of vary; they are displayed as similar values however due to rounding (the latter value is actually 0.009% more accurate). In addition to this it is important to note that the subsequent discussion will initially address the

results of the As-Built investigation and then the As-Built modification investigation.

Current Meter Simulation

The next section of this chapter will address the results of the investigation into the increasing levels of accuracy associated with the application of additional levels of current meters. This was done for the five different types of current meters studied in this thesis (Generalized Meter, Ott C31-1(Plastic), Ott C31-1(Metal), Ott C31-A, and Ott C31-R). The evolution of this accuracy was found to be extremely consistent across flow rates enabling the author to reliably demonstrate the results of each current meter type with average percent accuracy tables (Table 5.14 to 5.18) and the standard deviation between all the bays for all of the flow rates investigated over the course of the research (Table 5.17 to 5.21). In these results, several important aspects can be observed. The first is that the increase in accuracy associated with the further application of current meters begins to saturate at the end of the simulation envelope. In addition, the errors in accuracy resulting from the physical nature of the current meters can be distinguished from those simply from the numerical method used employed by the industry standards. When this is addressed further it becomes evident that as increasing numbers of current meters are applied the differential between the accuracy of the general and the physical meters experiences a significant reduction. For the C31-1(Plastic), C31-1(Metal), C31-A and C31-R this represents a value of 0.96, 0.98, 0.49 and 0.95 percent respectively. In this research, the C31-A model provided the best flow measurement accuracy in all the bays and flow rates investigated.

As prefaced in the introduction to this section the author also analyzed the ability of the current meters to accurately record flow rates given the velocity distribution calculated using the modified as-built drawings of Unit 4. Unlike the above only

three different types of current meters were studied in this section of the research: the Generalized Meter, the Ott C31-1(Plastic), and the Ott C31-Type A. The reason for the limitation is because the obstruction imposed in the CFD modeling caused significant levels of transverse flow near the uppermost rows of simulated current meters. While the author simulated all five types of meters as a part of the investigation the resulting velocities from the Ott C31-1 (Metal) and Ott C31-Type R applications were highly erratic, particularly at low numbers of simulated application and therefore the author made the decision to constrain the subsequent analysis. As with before the average flow measurement accuracy associated with each type of current meter is displayed below along with its corresponding standard deviation (Tables 5.24 to 5.29). This investigation reveals several interesting attributes both in regards to the individual results to themselves but also when compared to the results of the as-built study. In regards to the former it can be observed that the current meters consistently over record the flow rate, however this decreases as the number of current meters applied increases. The difference between the flow rate recorded by the minimum and maximum number of current meters is 5.1, 5.6, and 5.7 percent of the operational flow rate for the General, Ott C31-1(Plastic) and Ott C31-Type A respectively. The difference between the idealized performance of the General Current Meter and the two physical current meters also produced interesting results with the Type A underperforming the General Meter consistently at an average of 0.44 percent. The Ott C31-1(Plastic) also was less effective at measuring the flow rates than the General meter by an average of 0.84 percent. It should be noted that in both cases the differential between the generalized result and the physical current meters reduced as increasing numbers of current meters were applied. When the differential between the generalized and physical meters are compared at the highest and lowest levels of sensor resolution the ratio between the former and the latter was found to be 1:2.29 and 1:3.71 for the Ott C31-1(Plastic) and Ott C31-Type A respectively. In addition to this it is important to discuss the variation in current meter performance between the

different flow rates as demonstrated in the standard deviation of the results. The average standard deviation for the three simulated current meters was found to be consistent with average values of 1.07, 1.19 and 1.18 for the General, Plastic and Type A current meters. As with the difference between the physical and generalized sensors the standard deviation was found to decrease as additional sensors were applied. Overall the Ott C31-Type A was the most effective of the physical meters investigated with an average increased performance over the Ott C31-1(Plastic) by 0.4 percent.

When the results of the As-Built current meters investigation were compared to the modified As-Built current meter study there were two primary differences that occurred. The first of these is that the modified As-Built investigation consistently outperformed the As-Built current meter simulations. As the lowest level of all the current meters simulated this was by an average of 8.29 percent, however as the sensor resolution increased to its maximum this decreased to a difference of 0.89 percent. This evolution was observed to be largely dependent on the vertical resolution of the number of sensors applied, with the largest reduction being observed in the step from a vertical resolution of 5 to 7 current meters. The difference between the modified As-Built and As-Built reduces by an average of 43.8 in this step and beyond this, only fractions of the improvement were observed. This improvement occurred in the instance between the lowest two levels of vertical resolution. Given the arrangement it is suspected by the author that the lower than typical recorded flow rate recorded in the modified As-Built model is a result of the relatively large numbers of current meters located near the top of the bays where transverse flow was high. The transverse flow was found to cause the current meters to under predicted the local velocities in the testing performed by Jepson and therefore this is thought to be the cause of slightly higher levels of accuracy. As vertical resolution increased, the relative impact of the physically highest current meters decreased, thereby increasing the recorded flow rate to nearly that observed in the As-Built Geometry. The second

observation resulting from the comparison of the As-Built to the Modified As-Built results is associated with the variation in the Standard Deviation in current meter performance across the range of flow rates investigated. The General simulated current meters resulting from the As-Built CFD simulations were observed to have lower slightly lower levels of standard deviation (an average of 0.57) than its Modified As-Built counterpart whereas the Ott C31-1(Plastic) and the Ott C31-Type A have slightly higher levels. In the case of each respectively the modified geometry produces an average improvement of 0.59 and 0.64.

When the results of current meter accuracy are constrained to the static and dynamic representations it is possible to determine the evolution of the recorded characteristic curve as the number of meters increases. In the interest of brevity, the figures associated with this work will be placed in Appendix 6 below however the differential between the mean measured and operational unit performance is displayed below to facilitate the discussion of the results. In the two figures (Figure 5.19 and 5.20), which depict the As-Built static and dynamic method respectively, it is possible to observe several things. Naturally the static method demonstrates a higher differential at lower levels of resolution before achieving the same level of accuracy at the end. Beyond this however it is possible to observe that in both cases there are two distinct slopes which describe the increase in accuracy that occurs. In the case of the static application, the break between the two slopes occurs at the application of the 9th current meter in both the vertical and horizontal direction. The initial slope represents an increase in accuracy of 2.11 percent for each sensor placed in the vertical and horizontal direction whereas the slope after this, the increase in accuracy is limited to 0.11 percent. The dynamic current meter application has a similar change in slope, however this occurs between the application of the 7th and 9th meter. The initial slope demonstrates an increase in accuracy of 0.93 percent per meter applied whereas the latter is reduced to an increase of 0.003 percent. At the highest level of current meter resolution investigated there was a systematic error which

resulted in an over prediction of the flow rate between 3.0 and 2.6 percent. An analysis of the current meter characteristic curve in the Modified As-Built geometry can be found in Figures 5.21 and 5.22 for the static and transiting current meter respectively. As with the As-Built application the static application was found to have a significantly higher initial level of inaccuracy than the transiting current meters. In the static application, a significant increase in accuracy was observed in the first step, however after this initial step only incremental increases in accuracy were found to occur in the subsequent applications of current meters (0.2 percent average accuracy increase per step in resolution). An inspection of the transient current meter simulation reviled that the initial increase in sensor accuracy also provided the largest increase in flow measurement accuracy. However interestingly, the step from 7 to 9 current meters incurred a slight loss in accuracy, likely due to a fortuitous alignment of the velocity within the bay and the placement of the sensors. When the As-Built results are compared to the Modified As-Built results, it can be observed that higher levels result from the modified CFD from the lowest levels of sensor application to the highest.

Acoustic Time of Flight Simulation

The investigation of the increasing into the change in flow measurement accuracy associated with increasing levels of flow measurement accuracy has yielded several interesting results as well. Most pressing of these, naturally, is the accuracy evolution based on the number of sensors applied to the bays. This can be found in Figure 5.23 which demonstrates the percent recorded flow rate as a function of both the number of flow paths and the flow rate itself. This figure demonstrates that the acoustic time of flight method varies significantly from the performance of the current meter in that the flow rate itself actually plays a significant role in the accuracy of the measurement method, demonstrating the variability of the flow field in the downstream section where the acoustic time of

flight sensors was simulated. The effects of the unstable flow profile can be further observed in the operation of lower levels of acoustic path density. This is highlighted by the performance of two dual acoustic paths over the range of flow rates investigated. At the flow of 290, 368, 509, and 565 m^3sec^{-1} it can be observed that the paths demonstrate uncharacteristically high-performance levels, suggesting the presence of a fortuitous flow structure in the region. The other two flow rates however, act much more in accordance with the general trend of increasing accuracy. Despite the presence of the variation that exists in the performance of the acoustic time of flight method at two applied dual paths, the variation in the recorded flow rate generally decreases as the number applied dual paths increases (Figure 5.24). When considering the effect of the single acoustic paths which comprise both the dual and their own measurement function it can be observed that the acoustic path traveling from right to left records consistently higher velocities. This is likely a result of the proximity of the sensor location to the scroll case itself as this would lead to transverse flow in this direction. Further analysis demonstrates that these values are consistently between 1.5 and 2.5% of the flow traveling axially through this region (Figure 5.25). Unfortunately given the inconsistent nature of acoustic time of flight derived characteristic curves it was not possible to perform an analysis on the increasing levels of accuracy strictly due to the number of applied sensors as seen above in the current meter section. As such, the reader is directed to Figure 5.26 below which demonstrates the measured characteristic curve as a function of the number of dual acoustic paths applied to it (the single acoustic path results are Figures A6.11 and A6.12 of Appendix 6). The recorded curve demonstrates a higher initial accuracy than provided by the current meters and observed to rapidly (overall) approach the operational efficiency of the unit. Similarly, to the current meter results, there is a systematic over prediction at the highest levels of instrumentation ranging between 1.8 and 1.3 percent.

The following will discuss the results of the acoustic time of flight investigation using the CFD produced using the As-Built geometry modifications. The presence of the pronounced recirculation zone had a significant impact on the accuracy to which flow was measured in the intake as can be observed in Figure 5.27 below which demonstrates measurement accuracy resulting from varying quantities of dual paths over the range of flow rates. In this figure, it can be seen that both the number of sensors and the overall flow rate have an impact on the accuracy to which the flow rate can be calculated. In regards to the former there are three primary phases in the accuracy resulting from the acoustic time of flight sensors, with the first occurring in the application of 1 and 2 dual acoustic paths. It can be observed that at this level of instrumentation over prediction levels are high, and a slight loss in flow measurement accuracy is incurred as a result of the increase from one to two acoustic paths. The slightly higher initial accuracy is likely a result of fortuitous velocity distribution in the bays. The next phase of acoustic time of flight application is specific to the application of 3 dual acoustic paths, and this number of sensors appears to be a transitionary phase between the lower level of accuracy in the first phase and the higher level of accuracy occurring at the third phase. This final phase in acoustic path application ranges between 4 and 11 acoustic paths and while a slight overall increase in flow measurement accuracy is observed, the increase is limited to an average of 0.07 percent per additional acoustic path. In regards to the effect of the flow rate on measurement accuracy, different flow rates imposed slight variations on accuracy, however over all the same general trend in accuracy evolution was observed. The impact was found to be the highest at the lowest levels of simulated instrumentation (a maximum differential in accuracy of 4.53 percent) however as increasing numbers of acoustic paths were added this was reduced to 1.2 percent. The maximum differential in flow measurement accuracy resulting from different flow rates as a function of the number of applied dual paths can is demonstrated in Figure 5.28 where it can be observed that the evolution is roughly exponential. The asymptotic nature of the growth, unfortunately indicates

that the difference in flow measurement accuracy resulting from different flow rates will not be resolved through the application of additional sensors.

While like before the acoustic time of flight sensors consistently over predict the flow rate, the evolution in accuracy as well as the highest level of accuracy achievable is different. At lower numbers of sensors (1 and 2 dual paths) the extent of the over prediction is nearly double that found in the As-Built CFD results however it rapidly becomes more accurate overall than the As-Built results. As interesting dynamic can be observed in the single and double path results in Figure 5.27 which displays the evolution of the measured characteristic curve as a function of the number of applied dual acoustic time of flight paths. It can be determined that the single acoustic path performs better than the double dual acoustic paths in four of the six flow rates. This is likely a result off a surreptitious alignment of the velocity profile and the placement of the acoustic paths. However because this only occurs in four of the six flow rates it can be observed that the hydraulic structures are dependent on the flow rate, with the largest difference occurring at a flow rate of 509 m^3sec^{-1}.

Value Analysis

The final stage of the research involved the determination of the specific value associated with increasing levels of flow measurement instrumentation and followed the methodology outlined above. This section will be discretized into a discussion of the optimized unit dispatch, the opportunity cost associated with each level of instrumentation, and the incremental cost to benefit ratio associated with applying further levels of instrumentation.

Optimized Hydroplant Dispatch

Understanding the value of flow sensors initially required that the optimized unit dispatch of the plant can be determined using the performance of increasing numbers of units to meet load (Figure 5.30). This process resulted in the development of the measured performance of the optimized dispatch of the plant

as recorded by the different types and quantities of sensors investigated by the research. Figures 5.31, 5.32, and 5.33 demonstrate the results of this process for the general current meter in both its static and dynamic application as well as the dual acoustic time of flight application. In these images the differential between the measured and operational performance of the unit experiences a measurable reduction as the application transitions from the static to the dynamic and the time of flight methods in turn. To explore this further the author then developed Figures 5.28 and 5.29 which compare the measured optimized plant dispatch of the three different methods explored with the former representing the lowest level of sensor application and the latter the highest level. In this, it can be observed that the acoustic time of flight method provides slightly (0.79%) more accurate results at 11 applied dual paths. It should be noted that for the purpose of brevity this section only addresses the results of the As-Built section, and while the Modified As-Built results were produced over the course of the research they are not discussed.

Opportunity Cost Analysis

The next phase of calculating the value of flow measurement accuracy resulted in developing an understanding of the opportunity cost associated with misallocating water resources within the reservoir system itself. As discussed in the methods section above this involved the use of historic price and site specific generation data. Using this information the author produced the annual opportunity costs that would result from each level of flow measurement application in both the As-Built and Modified As-Built geometries. The results of the As-Built study are presented in Figures (- to-) as a function of the percent total revenue generated by the plant over the analyzed year. This analysis reveals several interesting attributes of the results. In regards to the current meters, the opportunity cost follows the general trend demonstrated in the accuracy of current meter performance displayed above. The Ott C31-A meter provided the best performance overall, with a small differential observed between

this and the general (idealized) current meter. The acoustic time of flight application, as was demonstrated in the evolution of the meter accuracy, has a more convoluted path towards increasing accuracy as increasing numbers of sensors are applied given that the application of the second acoustic path produces an uncharacteristically high level of accuracy. The opportunity cost can then be further analyzed through an investigation of the incremental reduction in opportunity cost associated with a corresponding incremental increase in sensor quantity. This is displayed in Figures 5.30 and 5.31 where the former demonstrates the average incremental reduction in opportunity cost for both the static and dynamic current meter application and the latter demonstrates the incremental improvement associated with the different acoustic applications. The current meter values are displayed as average values across the different types of sensors because a there is a nominal variance between these values (a maximum standard deviation of 0.03) It should be noted by the reader that the value on the x-axis represents the upper value used in the incremental analysis. The incremental analysis shows that the current meter accuracy increases monotonically whereas the acoustic time of flight meters do not. The results of a similar investigation on the Modified As-Built sensors can be seen in Figures 5.41 to 5.45 below. Figure 5.41 shows the evolution in opportunity cost as a function of total plant revenue for static current meter application. In this it can be observed that the opportunity cost reduction is constantly lower than that produced by the As-Built geometry. This is largely a result of the increased initial accuracy of the current meters. A similar evolution in opportunity cost as a function of the number of transiting current meters can be observed in Figure 5.42. As with the evolution of flow measurement accuracy a small inflection point is present at the application of 7 current meters. The following figure demonstrates the opportunity cost ratio as a function of the number of dual and single acoustic paths. There are two interesting factors that should be observed in this figure. The first of these is the slight increase in opportunity cost between a single and double acoustic path, as stated earlier this is assumed to be a

fortuitous alignment of the hydraulic structure. The second interesting factor is that the dual acoustic path is not bracketed by the single acoustic path opportunity cost ratios beyond 8 acoustic paths. This is a result of the slight loss in flow measurement accuracy that is observed in the single acoustic paths with 9 or more total paths, however because dual paths are a result of the averaged single paths, a reduction in opportunity cost is still observed. Figure 5.44 demonstrates the average incremental reduction in opportunity cost as result of the number of applied static and transiting current meters. While the static current meter application has a higher initial level of opportunity cost reduction by the third increase in current meter resolution the subsequent increases in applied sensors yield a similar effect on reduced opportunity cost. Figure 5.45 demonstrates the same inspection, albeit on the acoustic time of flight paths. The figures demonstrates that, after the slight loss of improvement resulting from the initial step significant benefits can be gained with that application of additional meters until roughly five paths were applied for flow measurement. After this point incremental reductions in opportunity cost are limited.

Value Analysis

The incremental analysis was then leveraged in the determining overall value of increases in the number of applied current meters and acoustic time of flight paths as enumerated in the appropriate methodology outlined above. The results of the As-Built current meter study can be found in Tables 5.30 and 5.31 for the static application and the dynamic method respectively. In this it should be observed that the economically appropriate number of current meters to achieve a positive cost to benefit ratio over the course of a year is 11 of the Ott C31-1 (Plastic) and 9 of the Ott C31-1(Metal), Ott C31-A and Ott C31-R current meters when applied in the static method outlined above. When the dynamic method is investigated the appropriate number of current meters for application is 11 meters, regardless of the number of current meter to achieve an appropriate benefit ratio over the course of a year. When these values are then analyzed to

determine the total period required to achieve a cost-benefit ratio of one the results are demonstrated in Tables 5. and 5.25. It should be noted that the dynamic current meter application is constrained to less than 11 meters because the incremental improvement is negative, suggesting that no further improvements in accuracy can be achieved. From this analysis it can be seen that the maximum payback period of the current meters is 30.69 years. The analysis of the acoustic time of flight application is made somewhat more complicated by the multimodal nature of the incremental increase in system accuracy. As such, in the development of these results the author followed the procedure outlined in the value section above and have omitted the values assessed by 3,4,7, and 8 acoustic paths to ensure an usable representation of the value associated with the application of acoustic time of flight paths. The results of the investigation can be found in Table 5.26 where it can be seen that the appropriate number of acoustic paths is 10, given that after this the achievable accuracy levels saturate.

The results of the Modified As-Built investigation are studied in Tables 5.35 to 5.39. It should be noted that in the C31-1(Plastic) current meter provides the highest cost benefit ratio and therefore the shortest payback period. While the current meters do not saturate in a similar way found in the As-Built analysis, a negative value can be observed in the transition from 7 to 9 dynamic current meters. Given an overall comparison between the As-Built and Modified As-Built the payback periods are consistently shorter. The only improvement with a payback period under a year was the increase from 5 to 7 current meters. This was found to be constant for all three of the current meter types studied in both of their applications. The longest payback period was found to be for the Ott31-Type A current meter (18 years). In considering the application of the acoustic time of flight simulation to the Modified As-Built it should be first observed that due to the non-monotonic nature of increases in flow measurement accuracy the author elected to not include 2, 4, 5,8, and 9 acoustic paths in the incremental

analysis. While the total cost of the step is included in the analysis the losses in improvement in these steps were omitted to ensure the applicability of the results. In Table 5.39 which documents the incremental value of the Modified Ab-Built acoustic time of flight application it can be observed that the cost benefit ratio remains above 1 for all of the investigated steps and therefore the research recommends that the application of 11 dual acoustic paths.

As stated in the methods it was felt important by the author to include the results of the investigation as a function of the reduction in suboptimally assigned water per dollar invested in flow measurement sensors. These results can be observed below in Tables 5.40 to 5.45 below for each of the six cases of flow measurement accuracy investigated. The primary rationale for the inclusion of these values within the results is that the author fully acknowledges that the quantified value of water focuses on its effective application for electricity generation and therefore does not reflect the full value of the water. These results will hopefully readily enable further expanded research in this field.

CHAPTER SIX
SUMMARY, CONCLUSIONS AND RECOMMENDATIONS

A numerical investigation was performed to study the value of flow measurement accuracy in hydropower plants with short converging intakes. This effort was specifically focused on Lower Granite Lock and Dam because the site not only had the requisite intake geometry, it also was able to provide information critical for the realization of the research. While this work is focused on Lower Granite, the results have the capability to provide guidance for not only the accuracy of various quantities of flow measurement instrumentation but also the economic implications of an investment in said instrumentation. Furthermore, the tools developed over the course of this investigation were specifically designed to be applicable to a wide range dams, as well as other hydraulic structures, requiring only a slight modification in system variables. Development of the code in such a soft manner will enable the sensitivities of short converging intake flow measurement accuracy to be rapidly investigated using CFD model of other short converging intake geometries. The computational tools developed are comprised of a sensor simulation module which allows the user to simulate the flow rate recorded by any quantity of current meters or acoustic time of flight paths. The value analysis module then reads in the measured optimized plant dispatch patterns associated the results in the first module and combines them with daily electrical market data and plant power production to provide an understanding of the opportunity cost resulting from each level of instrumentation.

Summary and Conclusions

In Chapter One the role of flow measurement accuracy in hydropower plant operation and the lack of guidance in flow measurement procedures in short converging intakes motivating this research is introduced. The chapter culminates with the research questions which were answered over the course of this dissertation.

Chapter Two outlines the different types of hydroplant intakes as well as the current state of understanding of the different disciplines which comprise the research. This study demonstrated that a majority of CFD models are constrained to steady state and are performed using Reynolds-averaged Navier-Stokes turbulent closure models. The chapter also demonstrated that the application of the acoustic time of flight flow measurement technique was primarily sensitive to transverse flow, with the effect of turbulent fluctuations being largely averaged out over time. Current meter research demonstrated the influence of both transverse and pulsating flow on the registration of the meters, however, the level of effect appeared to be largely sensor specific. This chapter culminated with a description of the important physical and operational details of Lower Granite. In regards to the former, Lower Granite employs a fish screen to reduce the number of fish entering the unit itself. This is important because it is suspected that the presence of an unknown component of the fish bypass system what not included in the CFD model thereby leading to an inability to reproduce the recirculation zone recorded within the intakes. The operational data used in the research included both historic generation of Lower Granite and historic electrical pricing from the Mid-Columbia Intercontinental Exchange.

The Third Chapter outlines computational fluid dynamic theory relevant to the research. The chapter was included to provide the reader with an understanding of the fundamentals of the method, as the research used a commercial solver (Star-CCM+) was used in the research. The two closure models and their associated implications were addressed. In particular, the role of the y+ value in the solution of the SST model was discussed and its implementation in Star-CCM+ was discussed. In addition to this discussion the author presented the results of two investigations demonstrating the ability of Star-CCM+ to produce physical results over a range of y+ values.

Chapter Four outlines the methods employed for this research and therefore represents a significant portion of this document. The first section of this chapter focuses on the development of the CFD models of Lower Granite and delves into the discrepancies that exist between the physical and computational domain. With the exception of the modeling of the trashrack, the computational domain upstream of the distributor closely matches that of the physical domain. Downstream of distributor simplifications were made to the distributor, turbine and outlet structure of the plant itself. The initial two were done due to a lack of information and to streamline the modeling process overall. The last simplification of the domain was performed to ensure the convergence of the computational model. In addition, the CFD section of Chapter Four addresses the appropriate modeling of the outlet boundary condition given the modification of the outlet. Furthermore the section addressed the tests that were performed during this research to: determine the appropriate upstream boundary condition, attempt to recreate the recirculation observed during the site testing, and validate the CFD models developed.

The second section of Chapter Four addressed the methods leveraged by the author to model both current meters and acoustic time of flight paths using the information available from the CFD models. The modeling of the current meters presented leverages a series of historical experiments on current meters to develop a holistic model for the response of the current meter based on a summation of the torques influencing the meter itself. This process demonstrates the influences of different hydraulic factors and expands significantly beyond the initial studies demonstrated in the literature review. As such this development of a generalized function for the response of different types of current meters represents a novel contribution developed over the course of this dissertation. The modeling of the acoustic time of flight paths was performed in a much more straightforward procedure as this was demonstrated to provide reliable results in the hydraulic conditions where the paths were simulated.

The final section of Chapter Four outlined the value determination process employed in the research. The end goal of this section was to quantify the benefit derived from the incremental application of additional flow meters and compare it to the cost associated with such an application. To this end the author developed a numerical code to determine the optimized plant dispatch recorded by each level of flow measurement instrumentation investigated. Using this information along with the operational efficiency of the plant, the historic generation of the plant, and the historic energy prices the author then outlined an analysis which enabled the assessment of the incremental opportunity cost. This was then compared with sensor costs provided by the relevant industries to determine the point where the application of additional sensors no longer provided a positive economic impact.

Chapter 5 then discusses the results associated with the methods outlined in the previous chapter. The CFD model testing found that upstream forebay flow from all directions used in concert provided the most representative flow field. Furthermore, despite significant efforts on behalf of the author it was not possible to reproduce the recirculation zone in the intake bays that was recorded during unit testing using the As-Built geometry provided. As outlined above, this is felt to be a result of an unknown aspect of the fish bypass system not being included in the computational model. As a result validation of the As-Built CFD provided mixed results. The initial phase, which investigated the distribution of flow within the bays, found excellent agreement between the CFD models and the field data. Given the lack of recirculation in the As-Built, the investigation at this site demonstrated poor alignment along the top two acoustic paths, however along the remaining acoustic paths a reasonable level of accuracy was attained. To replicate the effects of the recirculation zone on local flow measurement and the economic viability of sensor application the author performed another initial study on the effect of surface roughness and the characteristics of an obstruction placed within the flow path. A straight obstruction with a bay floor roughness of

20 times that of riveted steal was found to produce the velocity distribution most similar to that found in the feel. Using these characteristics the author produced a series of additional CFD models of Unit 4.

The chapter also contained the results of the sensor simulation section. In the simulation of the current meters demonstrated several interesting attributes. The first of these is that the current meters simulated in the As-Built models consistently over predict the flow rate through the unit, ranging from an average high value of 115.83 to a low of 102.88 of the operational flow rate traveling through the plant. The former of these occurred at the lowest level of sensor application (5 by 5 current meter array) and the latter occurred at the highest level of sensors investigated (15 by 15 current meter array). It was found that the performance of the sensors is relatively insensitive to the flow rate through the plant. The general, idealized, sensor was found to outperform the four different physical sensors that were modeled, however of these, the Ott C31-A type meter consistently provides the highest level of accuracy of the sensors investigated. The acoustic time of flight meters in the As-Built model were found to also consistently over-predict the flow rate through the plant, with the average highest over prediction equivalent to 107.37 and the average lowest equivalent to 101.8 percent of the flow rate through the unit. It should be noted however that the performance of the acoustic application was found to be dependent on flow rate, specifically at low levels of instrumentation. In the case of the Modified As-Built models several interesting attributes should be noted. The first is that the local hydraulic conditions preclude the application of two types of current meters: the C31-1(Metal) and the C31-Type R. This was due to the high levels of oblique flow that the obstruction induced on the uppermost current meters. At the lowest resolution the average recorded flow rate was 107.36 which evolved to 101.8 at the highest resolution. While the generalized current meter performed the best the physical meter which performed the best was the Type A Current Meter. When the acoustic time of flight method was applied to the Modified As-Built CFD

models it was found that the average accuracy at the lowest resolution was 109.06 percent the flow rate whereas at the highest level of accuracy it was found to be 100.48.

Chapter 5 also contained the value analysis section simulated the static and dynamic current meter applications as well as the three different acoustic time of flight methods. This section observed that the incremental reductions in opportunity cost associated with increases in the number of sensors had two distinct phases. The first phase took place at low levels of instrumentation and observed significant reductions in opportunity cost for each increase in sensor application. The second phase entailed a leveling of the opportunity cost where the application of additional sensors did not yield significant improvements. The transition between these proved to be important because this was the point where it became economically unfeasible to invest any further in sensors. This transition took place at 11 horizontal current meters for the dynamic application, an array of 15 by 15 current meters for the static application and 10 acoustic paths.

In summary, the research presented above represents the first significant investigation quantifying the value of flow measurement accuracy in short converging intakes. As a part of this the author developed a computational post processing tool suite capable of being used to readily simulate flow measurement accuracy, given the appropriate CFD results. The work developed demonstrated the sensitivities of not only the sensors to the hydraulic conditions but also of the flow rate and plant revenue to the sensors themselves. This effort will act as a guidance point for the hydropower industry for the appropriate number and type of sensors to be applied during unit testing. In addition to this the research demonstrated a systematic over prediction error in flow measurement accuracy that occurs even once the improvement in accuracy has been saturated in the case of the CFD models that were produced using the As-Built Unit 4 geometry.

The sensor simulations using the Modified As-Built geometry possessed a nominal level of over prediction. The difference between the two results suggests that there is potential for improvement in the numerical method employed in the conversion from the recorded velocity to the overall flow rate to broaden the applicability of the numerical method.

Recommendations

Flow measurement has long been understood to represent a critical attribute of the effective operation of hydropower plants. The work presented above represents the first of a series of studies that should be performed to fully explore and document this concept. Further investigations should be performed to fully understand the sensitivities of the flow profile at the measurement location to the different geometrical characteristics that exist across the spectrum of short converging intake types. Enhanced computational fluid dynamic capabilities should be brought online to enable transient modeling of the flow within the intakes such that the temporal characteristics of the flow, such as pulsation and turbulent intensity can be fully documented. In regards to the computational modeling of Lower Granite itself, further studies should be performed in concert with Lower Granite staff to determine the specific source of the recirculation within the inlet. This not only has implications for flow measurement, it also has the potential to affect the operational lifespan of the plant itself. When considering the modeling of the sensors themselves physical modeling should ideally take place for both the current meters and the acoustic time of flight sensors. This would allow the validity of the current representation to be fully explored and if necessary, modified to better demonstrate the response of the meters. In addition current meter modeling the accuracy of the acoustic time of flight methodology can be improved by modeling the effect of path elongation. This process should follow the ray trace method outlined by Weber in 2003. There are four primary aspects of the current value analysis process that can be improved upon. The first of these is the development of a more cohesive

understanding of the cost of implementation of the sensors themselves. Such knowledge will prove to be significantly beneficial to the hydropower industry as this will provide a measure of predictability of in the process. The second improvement that can be performed is to better reflect the true value of flow measurement within the system, the current research only focuses on the effect that flow measurement has on generation and while this is important there are several other attributes which should be included to provide a holistic understanding. These include the confirmation of contractual unit performance requirements as well as downstream water passage requirements. The third expansion of the value analysis research should be focused on enabling a holistic understanding of the value of optimal unit dispatch. As stated previously, optimal unit dispatch depends on an accurate understanding of the performance of each of the units within a plant. The tools and techniques developed in this research will enable the rapid modeling of flow measurement accuracy through multiple units in a plant, thereby documenting the indicated performance difference between them. This can then be used to quantify the value and document the sensitivities of optimal unit dispatch. It should be noted that this was not explored in this research because it not only would drive the focus of the work away from flow measurement accuracy specifically it would also require that the author artificially impose variations in unit performance rather than assess them directly from CFD models of the different units. The final aspect that should be included in the value assessment is a modification of the existing technique to reflect an optimization of reservoir operation. Such a model will represent the means by which the plant can store water that it does not need to pass, and then leverage this water for additional generation when electricity prices are highest. The implementation of these recommendations will build on the guidance and methodology put forth by this research to provide an industry-wide tool which will enable the maximization of energy production through the existing hydroelectric infrastructure.

WORKS CITED

[1] Aakti, B., & Staubli, T. A. (2015). Discharge Measurement in a Short Intake with a Converging Section - A Case Study. *HydroVision International 2015* (pp. 1-9). Portland: PennWell.

[2] Alming, K. (1965). Measurements on current meters in skew and rotating flow. *ICMG 1965* (pp. 1-26). International Group for Hydraulic Efficiency Measurement.

[3] Almquist, C. W., Taylor, J. W., & Walsh, J. T. (2011). Kootenay Canal Flow Rate Measurement Comparison Test Using Intake Methods. *HydroVision 2011* (pp. 1-17). Louisville: PenWell.

[4] Almquist, C., & Taylor, J. (2010). Hydro-Quebec Experience with Discharge Measurement in Short Converging Intatkes. *Hydro 2010.* Lisbon: International Journal on Hydropower and Dams.

[5] American Society of Civil Engineers. (1995). *Guidelines for Desing of Intakes for Hydroelectic Plans.* New York: American Society of Civil Engineers.

[6] American Society of Mechanical Engineers. (2011). *ASME PTC 18-2011 Hydraulic Turbines and Pump-Turbines.* New York: The American Society of Mechanical Engineers.

[7] Baglietto, E. (2015). Turubulence Modelin and the art of CFD. *Star Global Conference 2015.* San Diego: Massachusetts Institute of Technology.

[8] Bonneville Power Administration. (2013). *Fact Sheet: Marketing Hydropower.* Bonneville Power Administration.

[9] Bouhadji, D., Lemon, D., Topham, D., Billenness, D., & Fissel, D. (2003). CFD Analysis of Turbulent Flows in Hydroelectric Plant Intakes Application to ASFM Technology. *WaterPower 13.* ASL AQFlow Inc.

[10] Bureau of Indian Standards. (2012). *Indian Standard 11388: Recomendations for Design of Trashracks for Intakes.* New Delhi: Bureau of Indian Standards.

[11] Casartelli, E., & Ledergerber, N. (2010). Aspects of the Numberical Simulation for the Flow in Penstocks. *IGHEM-2010* (pp. 234-242). Roorkee: International Group for Hydropower Efficiency Measurement.

[12] Celik, I. (1999). *Introductory Turbulence Modeling .* Morgantown: West Virginia University.

[13] Cheesewright, L., & C., C. (2004). The dynamic response of small turbine flow meters in liquid flows. *Flow Measurement and Instrumentation*, 239-248.

[14] Christian, M. (2014). *Development and Operation of the Flow Measurement Accuracy Assessment Tool.* Evergreen: Hydro Research Foundation.

[15] Christian, M., & Smith, B. (2016). *Flow Measurement Value Analysis Research (Under Review).* Oak Ridge: Oak Ridge National Laboratory.

[16] Christian, M., Lee, K., Smith, B., & Hadjerioua, B. (2015). Imapct of the NUmber of Applied Current Meter Sensors on the Accuracy of Flow Rate Measurements across a Range of Hydroelectric Facilities Indicative of the Domestic Hydropower Fleet. *HydroVision International 2015* (pp. 1-16). Portland: PennWell

[17] Cook, J., & Walsh, J. (2008). Optimization of Hydro-Power Plants for Generation . *IGHEM 2008* (pp. 1-10). Milan: International Group for Hydrualic Efficiency Measurement.

[18] Cook, J., Walsh, J., & Veitch, J. (1993). Improving Performance with a Hydro Control System. *Waterpower '93.* Nashville: American Society of Civel Engineers.

[19] Cook, T., & Faulkner, H. (1997). *Development of a More Fish-Tolerant Turbine Runer Advanced Hydropower Turbine Project.* Idaho National Engineering Laboratory .

[20] Cushman-Roisin, B. (2014). *Environmental Fluid Mechanics.* John Wiley & Sons: New York.

[21] Darcy, H. (1856). *Fontanies Publiques de la Ville de Dijon.* Librairie des Corps Imperiaux des Ponts et Chaussees et des Mines.

[22] Eaton, K., & Johnson, J. (1981). A review of reserach on subsonic turbulent flow reattachment. *AIAA Journal*, 1093-1100.

[23] Electric Power Research Insitute. (2014). *Evaluating the Effects of Uncertanty in Unit Characteristics on the Operation and Optimization of Multiunit Hydroplants.* Palo Alto: Electric Power Research Insitute.

[24] Electric Power Research Institute. (2002). *Flow Measurement at Hydro Facilities, Achieving Efficiency, Compliance and Optimal Operation.* Palo Alto: Electric Power Reserach Institiute.

[25] Engineers, U. S. (n.d.). *Lower Granite Dam 2.*

[26] Federal Energy Regulatory Commission Division of Hydropower Administration & Compliance. (2015). *Compliance Handbook.* Federal Energy Regulatory Commission.

[27] Finardi, E. S., & Sagastizabal, C. (2005). Solving the Unit Commitment Proble of Hydropower Plants via Lagrangian Relation and Sequential Quadratic Programming. *Computational and Applied Mathmatics*, 317-341.

[28] Fischer, M. (1966). Versuche über den Einfluss der turbulenten Strömung auf hydrometrische Flügel der Nachahmung der Turbulenz im Schlepptank. *ICMG 1966* (pp. 1-19). International Group for Hydrualic Efficiency Measurement.

[29] Flury, K., & Frischknecht, R. (2012). *Life Cycle Inventories of Hydroelectric Power Generation.* Uster: ESU-Services.

[30] Forsund, F. (2007). *Hydropower Economics.* New York: Springer.

[31] Fulford, J. (1995). Effects of Pulsating Flow on Current Meter Performance. *Proceedings of 1st International Conference on Water Resources Engineering* (pp. 1-5). San Antonio: American Society of Civil Engineers.

[32] Fulford, J., Thibodeaux, K., & Kaehrle, W. (1994). Comparision of Current Meters used for Stream Gaging. *Fundamentals and Advancements in Hydraulic Measurements and Experimentation Proceedings of the Symposium on Fundamentals and Advancements in Hydraulic Measurements and Experimentation* (pp. 1-10). Buffalo: Journal of the American Water Resources Association .

[33] González Salgado, D. V. (2013). Turbine acceptance tests at Frieira HPP, Miño River, Spain with Acoustic Scintillation Flow Meter and Current Meters. *HydroVision International* (pp. 1-9). Denver: PennWell.

[34] Hammond, T., & Collins, M. (1972). Flume studies of the response of various current meter rotor/propellers to combinations of unidirectional and oscillary flow. *Deutsche Hydrografische Zeitschrift*, 39-58.

[35] Harding, S., Romero-Gomez, P., & Richmond, M. (2016). *Performance of Virtual Current Meters in Hydroelectric Turbine Intakes.* Richland : U.S. Department of Energy.

[36] Herschy, R. (1985). *Streamflow Measurement.* London: CRC Press.

[37] International Electrotechnical Commission. (1991). *IEC 60041:1991 Field Acceptance Tests to Determine the Hydraulci Performance of Hydrualic Turbines, Storage Pumps and Pump-Turbines.* Geneva: International Electrotechnical Commission.

[38] International Finance Corporation. (n.d.). *Hydroelectric Power: A Guide for Developers and Investors.* Stuttgart: Fichtner.

[39] International Organization for Standardization. (2007). *International Standard 3455: Hydrometry- Calibration of Current Meters in Straight Open Tanks.* Geneva: International Organization for Standardization.

[40] International Organization for Standardization. (2008). *International Standard ISO 3354: Measurement of Clean Water Flow in Closed Conduits - Velocity-Area Method using Current Meters in Full Conduits and under Regula Flow Conditions.* Geneva: International Organization for Standarization.

[41] Isomoto, K., & Honami, S. (1989). The effect of inlet turbulence intensity on the reattachment process over a backwards-facing step. *Journal of Fluid Engineering*, 87-92.

[42] Jager, H., & Smith, B. (2008). Sustainable reservoir operation: can we generate hydropower and preserve ecosystem values. *River Research and Applicatoins*, 340-352.

[43] Jepson, P. (1967). Current Meter Errors Under Pulsating Flow Conditions. *Jornal Mechanical Engineering Science*, 45-53.

[44] Jones, F., & Harris, G. (1992). ITS-90 Density of Water Fomulation for Volumetric Standards Calibration . *Journal of Reserach of the National Insitute of Standards and Technology*, 336-340.

[45] Jones, G., Laughton, M., & Say, M. (1993). *Electrical Engineer's Reference Book .* Oxford: Butterworth Heinemann.

[46] Khan, L., Wicklein, E., Rashid, M., Ebner, L., & Richards, N. (2004). Computational Fluid Dynamics Modeling of Turbine Intake Hydraulics at a Hydropower Plant. *Journal of Hydraulic Research*, 61-69.

[47] Kolupaila, S. (1957). Use of Current Meters in Turbulent and Diverging Channels. *AIGG 11th General Assembly* (pp. 437-444). Toronto: Internationl Union of Geodesy and Geophysics.

[48] Kondo, J., Naito, G.-i., & Fujinawa, Y. (1971). Response of Cup Anemometer in Turbulence. *Journal of the Meteorological Society of Japan*, 63-74.

[49] Lee, K., Christian, M., & Smith, B. ((Pending Review)). *Hydropower Flow Measurement In the United States.* Oak Ridge: Oak Ridge National Laboratory.

[50] Lemon, D., Bouhadji, L., Jiang, J., & Topham, D. (2004). Applying CFD Analysis to Predicting ASFM bias in Low Head Intakes with Difficult Hydraulic Conditions. *IGHEM-2004* (pp. 1-16). Lucerne: International Group for Hydraulic Efficiency Measurement.

[51] March, P. A. (2001). Knowledge Management System for Water Resources Promotes Benificial Paradigm Shifts fo Optimize Energy and Enviornment. *Ineramerican Dialogue on Water Management.* Parana.

[52] March, P., Wolff, P., Smith, B., Zhang, Q. F., & Dham, R. (2012). *Data-Based Performance Asessments for the DOE Hydropower Advancement Project. .* Doylestown: Hydro Performance Processes Inc.

[53] Mathews, J. H., & Fink, K. D. (2004). *Numerical Methods Using Matlab.* New Jersey: Prentice-Hall Inc.

[54] Matthews, G., Swan, G., & Smith, J. (1977). Improved Bypass and Collection System for Protection of Juvenile Salmon and Steelhead Trout at Lower Granite. *Marine Fisheries Review*, 1-5.

[55] Menter, F. (1994). Two-Equation Eddy-Viscosity Turbulence Models for Engineerign Applications. *AIAA Journal*, 1598-1605.

[56] Munson, B., Young, D., Okiishi, T., & Huebsch, W. (2009). *Fundimentals of Fluid Mechnaics.* Jefferson City: John Wiley & Sons Inc.

[57] NASA Langley Research Center Turbulence Modeling Resource. (2014, December 5). *SST/SST-V Expected Results - 2D Zero Pressure Gradient Flat Plate* . Retrieved from Turbulence Modeling Resource : https://turbmodels.larc.nasa.gov/flatplate_sst.html

[58] Nicolle, J., & Proulx, G. (2010). A new method for continous efficiency measurement for hydraulic turbines. *International Group for Hydraulic Efficiency Measurement* (pp. 198-205). Roorkee: IGHEM.

[59] Oak Ridge National Laboratory. (2012). *Flaming Gorge Hydropower Facility: Final Assessment Report.* Oak Ridge: United States Department of Energy.

[60] Oak Ridge National Laboratory. (2012). *Rhodhiss Hydropower Facility.* Oak Ridge: United States Department of Energy.

[61] Ott Hydromet. (1963). *Current Meter Calibration Records.* Ott Hydromet.

[62] Ott Hydromet GmbH. (n.d.). *Operating Instructions Universal Current Meter C31.* Kempten: Ott Hydromet GmbH.

[63] Ott, L. (1925). *Theorie un Konstanten bestimmung des hydrometrishen Flugels.* Berlin: Julius Springer.

[64] Ower, E. (1937). On the response of a vane anemometer to an air stream of pulsating speed. *The London, Edinburgh and Dublin Phiosophical Magazine and Jornal of Science*, 992-1004.

[65] Pacific Northwest Waterway Association. (2007). *Lower Monumental Lock Rehabilitation.* Walla Walla: U.S. Army Corps of Engineers.

[66] Prasad, V., Khare, R., & Chincholikar, A. (2010). Hydrualic Performance of Elbow Draft Tube For Different Geomentric Configurations using CFD. *IGHEM 2010* (pp. 252-256). Roorkee: International Group for Hydraulic Efficiency Measurement.

[67] Prosser, M. (1977). *The Hydraulic Desing of Pump Sumps and Intakes.* Bedford: British Hydromechanics Research Association .

[68] Proulx, G., & Cloutier, E. (2011). Hydro-Quebec Expereicne with Discharge Measurement in Short Converging Intakes. *HydroVision International 2011* (pp. 1-13). Sacrimento: PennWell.

[69] Proulx, G., Clouter, E., Bouhadji, L., & Lemon, D. (2004). Comparison of Discharge Measurement by Current Meter and Acoustic Scintillation Methods at La Grande-1. *IGHEM 2004* (pp. 1-13). Lucerne: International Group for Hydraulic Eficiency Measurement.

[70] Reeb, B., Candel, I., Proulx, G., & Lemon, D. (2012). Investigation of the Perfomrance of Acoustic Scintillation Flow Meter when Turbulence Levels are Low. *HydroVision International 2012* (pp. 1-12). Louisville: PennWell.

[71] Rittmeyer. (2014). *RISONIC Flow Sensors*. Retrieved from Instrumentation: http://www.rittmeyer.com/en/products-and-solutions/instrumentation/flow-sensors.html

[72] Rittmeyer. (2017). *Rinsonic Pipe Transducer Dimentions.* Baar: Rittmeyer.

[73] Saric, S., Jakirlic, S., & Tropea, C. (2005). A Periodically Perturbed Backward-Face Step Flow by Means of LES, DES and T-RANS: An Example of Flow Separation Control. *Journal of Fluids Engineering*, 879-887.

[74] Shepard, D. (1968). A two-dimensional interpolation function for irregularly-spaced data. *Proceedings of the 1968 ACM National Conerence* (pp. 517–524). Association for Computing Machinery.

[75] Siemens. (2016). *Star-CCM+ User Guide.* Siemens.

[76] Smith, B. (2001). *Hydropower Advancment Project CH 3.1.1.1.* Oak Ridge: U.S. Department of Energy.

[77] Staubli, T. (1988). Propeller-type Current Meters. *Dischage and Velocity Measurement*, 95-100.

[78] Staubli, T. (2011). *Numerical Flow Simulation of Hydraulic Machinery and their Components.*

[79] Staubli, T., Luscher, B., Senn, F., & Widmer, M. (2007). CFD Optimized Acoustic Flow Measurement and Laboratory Verification. *Hydro 2007* (pp. 1-7). Granada: The International Journal on Hydropower & Dams.

[80] Strunz, T., Wiest, A. F., & Frohlich, T. (2004). Influence of Turbulence on Ultrasonic Flow Measurements. *IGHEM 2004* (pp. 1-6). Lucerne: International Group for Hydraulic Efficiency Measurement.

[81] Taylor, J., Proulx, G., & Lampa, J. (2011). Turbine flow measurement in intakes: a cost-effective alternative to measurement in penstocks. *Hydro 2011* (pp. 1-10). International Journal on Hydropower and Dams.

[82] Tennekes, H., & Lumley, J. (1972). *A First Course in Turbulence.* Massachusets Insitute of Technology.

[83] Tennessee Valley Authority . (1959). *Mechnaical Design of Hydro Power Plants.* Washington D.C. : Government Printing Office.

[84] Tennessee Valley Authority. (1999). *Tennessee Valley Authority Blue Books.* Tennessee Valley Authority.

[85] The American Society of Mechanical Engineers. (2011). *ASME PTC 18-2011 Hydrualic Turbines and Pump Turbines Performance Test Codes.* New York: The American Society of Mechanical Engineers.

[86] The Committee on Hydropower Intakes of the Energy Division of the AmeriTcan Society of Civil Engineers. (1995). *Guidelines for Design of Intakes for Hydroelectric Plants.* New York : American Society of Civil Engineers.

[87] U.S. Army Corps of Engineeres. (2002). Turbine Passage Modification Plan. In U. A. Engineeres, *Lower Snake River Juvenile Salmon Migration Feasibility Report/Enviornmental Impact Statement* (pp. 1-22). U.S. Army Corps of Engineeres.

[88] U.S. Army Corps of Engineers. (1974). *Lower Granite Unit 4 Technical Drawings.* Portland: U.S. Army Corps of Engineers.

[89] U.S. Army Corps of Engineers. (1994). *Lower Snake River Biological Drawdown Test Draft Enviornmental Impact Statement.* Walla Walla: U.S. Army Corps of Engineers.

[90] U.S. Army Corps of Engineers. (2002). *Lower Snake River Juvenile Salmon Migration Feasibility Report/Environmental Impact Statement: Annex A.* Walla Walla: U.S. Army Coprs of Engineers.

[91] U.S. Army Corps of Engineers. (2002). *Lower Snake River Juvenile Salmon Migration Feasiblity Report/Environemntal Impact Statement: Appendix D- Natural River Drawdown Engineering.* Walla Walla: U.S. Army Corps of Engineer.

[92] U.S. Army Corps of Engineers. (2004). *Lower Granite Lock and Dam Unit 4 Index Test.* Walla Walla: U.S. Army Corps of Engineers.

[93] U.S. Army Corps of Engineers. (2014). *Lower Snake River Programmatic Sediment Managment Plan, Final Enviornmental Impact Statement.* Walla Walla: U.S. Army Corps of Engineers.

[94] U.S. Army Corps of Engineers. (n.d.). *Dataquery 2.0*. Retrieved from http://www.nwd-wc.usace.army.mil/dd/common/dataquery/www/?k=lower granite

[95] U.S. Army Corps of Engineers. (n.d.). *Lower Granite Lock and Dam Project Information*. Retrieved from Walla Walla District Locks and Dams: http://www.nww.usace.army.mil/Locations/District-Locks-and-Dams/Lower-Granite-Lock-and-Dam/

[96] U.S. Army Corps of Engineers. (n.d.). *Lower Monumental Lock and Dam Project Information*. Retrieved from District Locks and Dams: http://www.nww.usace.army.mil/Locations/District-Locks-and-Dams/Lower-Monumental-Lock-and-Dam/

[97] U.S. Army Corps of Engineers. (n.d.). *Water Management for the Pacific Northwest Reservior System.*

[98] U.S. Bureau of Reclamation. (1994). *Vallecito Dam Flow Measurement and Wier Calibration.* Denver: U.S. Department of the Interior.

[99] U.S. Bureau of Reclamation. (2001). Current Meters. In U. B. Reclamation, *Water Measurement Manual.* Washington D.C.: U.S. Government Printing Office.

[100] U.S. Energy Information Administration . (2011, June 16). *Age of Electric Power Generators Varies Widely*. Retrieved from Today in Energy: http://www.eia.gov/todayinenergy/detail.php?id=1830

[101] U.S. Energy Information Administration. (2015). *Electric Power Monthly.* Washington: U.S. Department of Energy.

[102] U.S. Energy Information Administration. (2017). *Electricity-Historical.* Retrieved from Wholesale Electricity and Natural Gas Market Data: https://www.eia.gov/electricity/wholesale/#history

[103] United States Army Corps of Engineers Portland District Hydroelectric Design Center. (2005). *Stay Vane and Wicket Gate Relationship Study.* United States Army Corps of Engineers.

[104] United States Bureau of Reclamation. (1987). *Design of Small Dams.* Washington D.C.: U.S. Government Printing Office.

[105] Valeport Limited. (1996). *"BRAYSTOKE" BFM001 & BF002 Current Flow Meters Operating Manual For Use with Model 0012B Control Display Unit.* Devon: Valeport Limited.

[106] Von Schon, H. (1911). *Hydro-electric Practice: A practical Manual of the Development of Water Power, its Conversion to Electrical Energy and its Distant Transmission.* Philadelphia: J.B. Lippincott Company.

[107] Walsh, J. (2017, Feburary 28). Acoustic Time of Flight Best Practices Discussion. (M. Christian, Interviewer)

[108] Walsh, J., & Miller, G. (n.d.). *Acoustic Flowmeter Analysis in Low-Head Applications.*

[109] Weber, F. (2003). *Ultrasonic Beam Propagation in Turbulent Flow: Dissertation.* Worcester: Worcester Polytechnic Institute.

[110] White, F. (2006). *Viscous Fluid Flow.* Boston: McGraw-Hill.

[111] Wilcox, D. C. (2010). *Turbulence Modeling for CFD.* La Canada: DCW Industries.

[112] Yarnell, D., & Nagleer, F. (1931). Effect of Turbulence on the Registration of Curent Meters. *Transactions of the American Society of Civil Engineers*, 766-795.

[113] Yeh, T., & Mattingly, G. (1997). Computer Simulations of Ultrasonic Flow Meter Performance in Ideal and Non-Ideal Pipe Flows. *ASME Fluid Engineer Division Sumer Meeting Proceedings.* American Society of Mechanical Engineers.

APPENDICES

Appendix 1: Mesh Independence Study Code

```
%Code to compare CFD simulations (Individual bay to individual bay)
%Note: This material was developed in support of Mark Christian's Ph.D.
%thesis and should be cited as such.
%
%Approved for Public Distribution

%House Keeping
clc
clear all
close all

%User Interface Section
x_point_resolution=20;
y_point_resolution=20;
z_point_resolution=20;
num_histogram_bins=10;
distance_histogram_bins=80;
outlier_percentage=10; %Cannot by 100%
total_point_count=x_point_resolution*y_point_resolution*z_point_resolut
ion;
Bay_Shift_Coefficient=0;
%Data Read in
CFDFile1_name='565CMS-SST-ALR-Bay-A-Low-Res.csv';
%'632.26_trashrack_bay_b.csv';'632.26_trashrack_bay_b.csv';
CFD_Data1= csvread(CFDFile1_name,1,0);
size_subset1=size(CFD_Data1);
sz_CFD1=size_subset1(1,1);
x_data=CFD_Data1(:,5);
y_data=CFD_Data1(:,6);
z_data=CFD_Data1(:,7);
u_data=CFD_Data1(:,1);
v_data=CFD_Data1(:,2);
w_data=CFD_Data1(:,3);
k_data=CFD_Data1(:,4);
CFD_Data1=[x_data, y_data, z_data, u_data, v_data, w_data, k_data];
%429.93_Highest_bay_b
%One that will be assumed as "proper"
CFDFile2_name= '565CMS-SST-ALR-Bay-A.csv';
%'632.26_trashrack_bay_b.csv'632.26CMS_High_bay_a
CFD_Data2= csvread(CFDFile2_name,1,0);
size_subset2=size(CFD_Data2);
sz_CFD2=size_subset2(1,1);
x_data=CFD_Data2(:,5);
y_data=CFD_Data2(:,6);
z_data=CFD_Data2(:,7);
u_data=CFD_Data2(:,1);
v_data=CFD_Data2(:,2);
w_data=CFD_Data2(:,3);
k_data=CFD_Data2(:,4);
CFD_Data2=[x_data, y_data, z_data, u_data, v_data, w_data, k_data];
bay_shift_factor=0;
%Cartisian Locations of ATF "Pole" Corners
```

```
Point_1=
[8.6614+bay_shift_factor*8.61095139077517,1.75588326,36.772162];
%[close_x, bottom_y, upstream_z][8.7465442,1.8368414,36.7653368]
Point_2=
[8.6614+bay_shift_factor*8.61095139077517,18.18044759,39.61777146914];
%[close_x, top_y, upstream_z][8.7465442,19.521086,36.7653368]
Point_3=
[15.19555+bay_shift_factor*8.61095139077517,1.75588326,36.772162];
%[far_x, bottom_y, upstream_z][15.078,1.8368414,36.7653368]
Point_4=
[15.19555+bay_shift_factor*8.61095139077517,18.18044759,39.61777146914]
; %[far_x, top_y, upstream_z][15.078,19.521086,36.7653368]

Point_5=
[8.6614+bay_shift_factor*8.61095139077517,1.280793,39.5143344771];
%[close_x, bottom_y, downstream_z]
Point_6=
[8.6614+bay_shift_factor*8.61095139077517,17.006951,42.1412855129];
%[close_x, top_y, downstream_z]
Point_7=
[15.19555+bay_shift_factor*8.61095139077517,1.280793,39.5143344771];
%[far_x, bottom_y, downstream_z]
Point_8=
[15.19555+bay_shift_factor*8.61095139077517,17.006951,42.1412855129];
%[far_x, top_y, downstream_z]
Point_Compilation=[Point_1;Point_2;Point_3;...
    Point_4;Point_5;Point_6;Point_7;Point_8];

%Determining Spacial Location of Comparison Points
xspacing=linspace(Point_Compilation(1,1),Point_Compilation(3,1),x_point
_resolution);

    %Calculating Z-Spacing Lenght 1b-4t and 2b-3t
    %Lenght 1 (Pt. 3-7)
    Lenght1=((Point_Compilation(3,2)-
Point_Compilation(7,2))^2+(Point_Compilation(3,3)-
Point_Compilation(7,3))^2)^(1/2);
    angle1=atan((Point_Compilation(3,2)-
Point_Compilation(7,2))/(Point_Compilation(7,3)-
Point_Compilation(3,3)));
        Path1_Spacing=linspace(0,Lenght1,z_point_resolution);
        Lenght_1_spacial=zeros(z_point_resolution,3);
        for i=1:z_point_resolution

Lenght_1_spacial(i,2)=Point_Compilation(7,2)+(Point_Compilation(7,2)-
(Point_Compilation(3,2)-Path1_Spacing(1,z_point_resolution+1-
i)*sin(angle1)))+(Point_Compilation(3,2)-Point_Compilation(7,2));

Lenght_1_spacial(i,3)=(Point_Compilation(3,3)+Path1_Spacing(1,i)*cos(an
gle1));
        end
```

```
    Lenght4=((Point_Compilation(4,2)-
Point_Compilation(8,2))^2+(Point_Compilation(4,3)-
Point_Compilation(8,3))^2)^(1/2);
    angle4=atan((Point_Compilation(4,2)-
Point_Compilation(8,2))/(Point_Compilation(8,3)-
Point_Compilation(4,3)));
    Path4_Spacing=linspace(0,Lenght4,z_point_resolution);
        Lenght_4_spacial=zeros(z_point_resolution,3);
        for i=1:z_point_resolution

Lenght_4_spacial(i,2)=Point_Compilation(8,2)+(Point_Compilation(8,2)-
(Point_Compilation(4,2)-Path4_Spacing(1,z_point_resolution+1-
i)*sin(angle4)))+(Point_Compilation(4,2)-Point_Compilation(8,2));

Lenght_4_spacial(i,3)=(Point_Compilation(4,3)+Path4_Spacing(1,i)*cos(an
gle4));
        end

    %Calculating the Y Spacing

Y_Z_comparision_points=zeros(y_point_resolution*z_point_resolution,3);
    %i=1;
    for i=1:z_point_resolution
        Subset_lenght=((Lenght_4_spacial(i,3)-
Lenght_1_spacial(i,3))^2+(Lenght_4_spacial(i,2)-
Lenght_1_spacial(i,2))^2)^(1/2);
        Subset_angle=atan((Lenght_4_spacial(i,3)-
Lenght_1_spacial(i,3))/(Lenght_4_spacial(i,2)-Lenght_1_spacial(i,2)));

subset_lenght_spacing=linspace(0,Subset_lenght,y_point_resolution);
        for j=1:y_point_resolution
            Y_Z_comparision_points((i-
1)*y_point_resolution+j,2)=Lenght_4_spacial(i,2)-
subset_lenght_spacing(1,j)*cos(Subset_angle);
            Y_Z_comparision_points((i-
1)*y_point_resolution+j,3)=Lenght_1_spacial(i,3)+subset_lenght_spacing(
1,j)*sin(Subset_angle);
        end

    end

 Comparison_points=repmat(Y_Z_comparision_points,x_point_resolution,1);
 for i=1:x_point_resolution
     Comparison_points(y_point_resolution*z_point_resolution*(i-
1)+1:y_point_resolution*z_point_resolution*i)=ones(y_point_resolution*z
_point_resolution,1).*xspacing(1,i);
 end

%Continuous plotting diagram
figure
scatter3(Point_Compilation(:,1),Point_Compilation(:,3),Point_Compilatio
n(:,2))
title('Assessment Points')
```

```
xlabel('Conduit Width')
ylabel('Stream Lenght')
zlabel('Conduit Height')
hold on
scatter3(Comparison_points(:,1),Comparison_points(:,3),Comparison_point
s(:,2))
hold off
%
%---------Section 2: Calculation of Nearest Neighbor Values at the
Points---------
Data_Set_1_Vals=[Comparison_points, zeros(total_point_count,5)];
for i=1:total_point_count
    assessment_point=Comparison_points(i,1:3);
    point_distance=9999999999;
    data_holder=zeros(1,8);
    i
    for j=1:sz_CFD1
        p2p_distance=((CFD_Data1(j,1)-
assessment_point(1,1))^2+(CFD_Data1(j,2)-
assessment_point(1,2))^2+(CFD_Data1(j,3)-
assessment_point(1,3))^2)^(1/2);
        if p2p_distance<=point_distance
            data_holder=[CFD_Data1(j,1:7),p2p_distance];
            point_distance=p2p_distance;
        end
    end
    data_holder(1,4:8);
    Data_Set_1_Vals(i,4:8)=data_holder(1,4:8);
end
%Data_Set_1_Vals
%}

Data_Set_2_Vals=[Comparison_points, zeros(total_point_count,5)];
for i=1:total_point_count
    assessment_point=Comparison_points(i,1:3);
    point_distance=9999999999;
    data_holder=zeros(1,8);
    i
    for j=1:sz_CFD2
        p2p_distance=((CFD_Data2(j,1)-
assessment_point(1,1))^2+(CFD_Data2(j,2)-
assessment_point(1,2))^2+(CFD_Data2(j,3)-
assessment_point(1,3))^2)^(1/2);
            %distance_holder(j,1)=p2p_distance; %Delete
            if p2p_distance<=point_distance
            %p2p_distance
            data_holder=[CFD_Data2(j,1:7),p2p_distance];
            point_distance=p2p_distance;
            end
    end
    %point_distance;
    Data_Set_2_Vals(i,4:8)=data_holder(1,4:8);
end
%Data_Set_2_Vals
```

```
%
figure
scatter3(Comparison_points(:,1),Comparison_points(:,3),Comparison_point
s(:,2))
title('Nearest Neighbor CFD Values')
xlabel('Conduit Width')
ylabel('Stream Lenght')
zlabel('Conduit Height')
hold on
quiver3(Comparison_points(:,1),Comparison_points(:,3),Comparison_points
(:,2),Data_Set_2_Vals(:,4),Data_Set_2_Vals(:,6),Data_Set_2_Vals(:,5))
quiver3(Comparison_points(:,1),Comparison_points(:,3),Comparison_points
(:,2),Data_Set_1_Vals(:,4),Data_Set_1_Vals(:,6),Data_Set_1_Vals(:,5))

%----------------Part 2 Data Processing----------------
Calculated_Val_Differential=[(Data_Set_1_Vals(:,4)-
Data_Set_2_Vals(:,4)),(Data_Set_1_Vals(:,5)-
Data_Set_2_Vals(:,5)),(Data_Set_1_Vals(:,6)-
Data_Set_2_Vals(:,6)),(Data_Set_1_Vals(:,7)-Data_Set_2_Vals(:,7))];
Percent_Val_Differential=[(1-abs((Data_Set_1_Vals(:,4)-
Data_Set_2_Vals(:,4))./Data_Set_2_Vals(:,4))).*100,...
    (1-abs((Data_Set_1_Vals(:,5)-
Data_Set_2_Vals(:,5))./Data_Set_2_Vals(:,5))).*100,...
    (1-abs((Data_Set_1_Vals(:,6)-
Data_Set_2_Vals(:,6))./Data_Set_2_Vals(:,6))).*100,...
    (1-abs((Data_Set_1_Vals(:,7)-
Data_Set_2_Vals(:,7))./Data_Set_2_Vals(:,7))).*100];

%----------------Differential Histograms--------------------------
%U Differential
u_histogram_binning=linspace(min(Calculated_Val_Differential(:,1)),max(
Calculated_Val_Differential(:,1)),num_histogram_bins);
u_differential_histogram=zeros(1,num_histogram_bins-1);
for i=1:total_point_count
    assessment_value=Calculated_Val_Differential(i,1);
    for j=1:num_histogram_bins-1
        if assessment_value>=u_histogram_binning(1,j) &&
assessment_value<=u_histogram_binning(1,j+1)
        u_differential_histogram(1,j)=u_differential_histogram(1,j)+1;
        end
    end

end
u_histogram_binning_chart=zeros(1,num_histogram_bins-1);
for r=1:num_histogram_bins-1
u_histogram_binning_chart(1,r)=(u_histogram_binning(1,r)+u_histogram_bi
nning(1,r+1))/2;
end
hold off
figure
bar(u_histogram_binning_chart,u_differential_histogram)
title('U Velocity Differentials')
xlabel('Point Velocity Differentials (m/s)')
ylabel('Counts')
```

```
%U Percent Differential
u_percent_histogram_binning=linspace(min(Percent_Val_Differential(:,1))
,max(Percent_Val_Differential(:,1)),num_histogram_bins);
u_percent_differential_histogram=zeros(1,num_histogram_bins-1);
for i=1:total_point_count
    assessment_value=Percent_Val_Differential(i,1);
    for j=1:num_histogram_bins-1
        if assessment_value>=u_percent_histogram_binning(1,j) &&
assessment_value<=u_percent_histogram_binning(1,j+1)

u_percent_differential_histogram(1,j)=u_percent_differential_histogram(
1,j)+1;
        end
    end

end
u_percent_histogram_binning_chart=zeros(1,num_histogram_bins-1);
for r=1:num_histogram_bins-1
u_percent_histogram_binning_chart(1,r)=(u_percent_histogram_binning(1,r
)+u_percent_histogram_binning(1,r+1))/2;
end
hold off
figure
bar(u_percent_histogram_binning_chart,u_percent_differential_histogram)
title('U Percent Similarity Histogram')
xlabel('Percent Similarity (%)')
ylabel('Counts')

%V Differential
v_histogram_binning=linspace(min(Calculated_Val_Differential(:,2)),max(
Calculated_Val_Differential(:,2)),num_histogram_bins);
v_differential_histogram=zeros(1,num_histogram_bins-1);
for i=1:total_point_count
    assessment_value=Calculated_Val_Differential(i,2);
    for j=1:num_histogram_bins-1
        if assessment_value>=v_histogram_binning(1,j) &&
assessment_value<=v_histogram_binning(1,j+1)
        v_differential_histogram(1,j)=v_differential_histogram(1,j)+1;
        end
    end

end
v_histogram_binning_chart=zeros(1,num_histogram_bins-1);
for r=1:num_histogram_bins-1
v_histogram_binning_chart(1,r)=(v_histogram_binning(1,r)+v_histogram_bi
nning(1,r+1))/2;
end
hold off
figure
bar(v_histogram_binning_chart,v_differential_histogram)
title('V Velocity Differentials')
xlabel('Point Velocity Differentials (m/s)')
```

```
ylabel('Counts')

%V Percent Differential
v_percent_histogram_binning=linspace(min(Percent_Val_Differential(:,2))
,max(Percent_Val_Differential(:,2)),num_histogram_bins);
v_percent_differential_histogram=zeros(1,num_histogram_bins-1);
for i=1:total_point_count
    assessment_value=Percent_Val_Differential(i,2);
    for j=1:num_histogram_bins-1
        if assessment_value>=v_percent_histogram_binning(1,j) &&
assessment_value<=v_percent_histogram_binning(1,j+1)

v_percent_differential_histogram(1,j)=v_percent_differential_histogram(
1,j)+1;
        end
    end
end
v_percent_histogram_binning_chart=zeros(1,num_histogram_bins-1);
for r=1:num_histogram_bins-1
v_percent_histogram_binning_chart(1,r)=(v_percent_histogram_binning(1,r
)+v_percent_histogram_binning(1,r+1))/2;
end
hold off
figure
bar(v_percent_histogram_binning_chart,v_percent_differential_histogram)
title('V Percent Similarity Histogram')
xlabel('Percent Similarity (%)')
ylabel('Counts')

%W Differential
w_histogram_binning=linspace(min(Calculated_Val_Differential(:,3)),max(
Calculated_Val_Differential(:,3)),num_histogram_bins);
w_differential_histogram=zeros(1,num_histogram_bins-1);
for i=1:total_point_count
    assessment_value=Calculated_Val_Differential(i,3);
    for j=1:num_histogram_bins-1
        if assessment_value>=w_histogram_binning(1,j) &&
assessment_value<=w_histogram_binning(1,j+1)
        w_differential_histogram(1,j)=w_differential_histogram(1,j)+1;
        end
    end

end
w_histogram_binning_chart=zeros(1,num_histogram_bins-1);
for r=1:num_histogram_bins-1
w_histogram_binning_chart(1,r)=(w_histogram_binning(1,r)+w_histogram_bi
nning(1,r+1))/2;
end
hold off
figure
bar(w_histogram_binning_chart,w_differential_histogram)
title('W Velocity Differentials')
xlabel('Point Velocity Differentials (m/s)')
ylabel('Counts')
```

```
%W Percent Differential
w_percent_histogram_binning=linspace(min(Percent_Val_Differential(:,3))
,max(Percent_Val_Differential(:,3)),num_histogram_bins);
w_percent_differential_histogram=zeros(1,num_histogram_bins-1);
for i=1:total_point_count
    assessment_value=Percent_Val_Differential(i,3);
    for j=1:num_histogram_bins-1
        if assessment_value>=w_percent_histogram_binning(1,j) &&
assessment_value<=w_percent_histogram_binning(1,j+1)
w_percent_differential_histogram(1,j)=w_percent_differential_histogram(
1,j)+1;
        end
    end
end
w_percent_histogram_binning_chart=zeros(1,num_histogram_bins-1);
for r=1:num_histogram_bins-1
w_percent_histogram_binning_chart(1,r)=(w_percent_histogram_binning(1,r
)+w_percent_histogram_binning(1,r+1))/2;
end
hold off
figure
bar(w_percent_histogram_binning_chart,w_percent_differential_histogram)
title('W Percent Similarity Histogram')
xlabel('Percent Similarity (%)')
ylabel('Counts')

%K Differential
k_histogram_binning=linspace(min(Calculated_Val_Differential(:,4)),max(
Calculated_Val_Differential(:,4)),num_histogram_bins);
k_differential_histogram=zeros(1,num_histogram_bins-1);
for i=1:total_point_count
    assessment_value=Calculated_Val_Differential(i,1);
    for j=1:num_histogram_bins-1
        if assessment_value>=k_histogram_binning(1,j) &&
assessment_value<=k_histogram_binning(1,j+1)
        k_differential_histogram(1,j)=k_differential_histogram(1,j)+1;
        end
    end
end
k_histogram_binning_chart=zeros(1,num_histogram_bins-1);
for r=1:num_histogram_bins-1
k_histogram_binning_chart(1,r)=(k_histogram_binning(1,r)+k_histogram_bi
nning(1,r+1))/2;
end
hold off
figure
bar(k_histogram_binning_chart,k_differential_histogram)
title('TKE Differentials')
xlabel('Point Velocity Differentials (K/kg)')
ylabel('Counts')

%K Percent Differential
```

```
k_percent_histogram_binning=linspace(min(Percent_Val_Differential(:,4))
,max(Percent_Val_Differential(:,4)),num_histogram_bins);
k_percent_differential_histogram=zeros(1,num_histogram_bins-1);
for i=1:total_point_count
    assessment_value=Percent_Val_Differential(i,4);
    for j=1:num_histogram_bins-1
        if assessment_value>=k_percent_histogram_binning(1,j) &&
assessment_value<=k_percent_histogram_binning(1,j+1)

k_percent_differential_histogram(1,j)=k_percent_differential_histogram(
1,j)+1;
        end
    end
end
k_percent_histogram_binning_chart=zeros(1,num_histogram_bins-1);
for r=1:num_histogram_bins-1
k_percent_histogram_binning_chart(1,r)=(k_percent_histogram_binning(1,r
)+k_percent_histogram_binning(1,r+1))/2;
end
hold off
figure
bar(k_percent_histogram_binning_chart,k_percent_differential_histogram)
title('TKE Percent Similarity Histogram')
xlabel('Percent Similarity (%)')
ylabel('Counts')

%-------------------------Charting Nearest Neighbor Distances---------
---
max_distance_options=[max(Data_Set_1_Vals(:,8)),
max(Data_Set_2_Vals(:,8))];
max_distance_spread=max(max_distance_options);
min_distance_options=[min(Data_Set_1_Vals(:,8)),
min(Data_Set_2_Vals(:,8))];
min_distance_spread=min(min_distance_options);

distance_to_point_binning=linspace(min_distance_spread,max_distance_spr
ead,distance_histogram_bins);

CFD1_distance_histogram=zeros(1,distance_histogram_bins-1);
for i=1:total_point_count
    assessment_value=Data_Set_1_Vals(i,8);
    for j=1:distance_histogram_bins-1
        if assessment_value>=distance_to_point_binning(1,j) &&
assessment_value<=distance_to_point_binning(1,j+1)
        CFD1_distance_histogram(1,j)=CFD1_distance_histogram(1,j)+1;
        end
    end
end

CFD2_distance_histogram=zeros(1,distance_histogram_bins-1);
for i=1:total_point_count
    assessment_value=Data_Set_2_Vals(i,8);
    for j=1:distance_histogram_bins-1
```

```
        if assessment_value>=distance_to_point_binning(1,j) &&
assessment_value<=distance_to_point_binning(1,j+1)
        CFD2_distance_histogram(1,j)=CFD2_distance_histogram(1,j)+1;
        end
    end
end

distance_histogram_binning_chart=zeros(1,distance_histogram_bins-1);
for r=1:distance_histogram_bins-1
distance_histogram_binning_chart(1,r)=(distance_to_point_binning(1,r)+d
istance_to_point_binning(1,r+1))/2;
end
hold off

figure
bar(distance_histogram_binning_chart,CFD1_distance_histogram)
title('Nearest Neighbor Distance')
hold on
bar(distance_histogram_binning_chart,CFD2_distance_histogram,'r')
alpha(.5)
hold off

figure
scatter3(Comparison_points(:,1),Comparison_points(:,3),Comparison_point
s(:,2))
title('CFD Resulting Differentials')
xlabel('Conduit Width')
ylabel('Stream Lenght')
zlabel('Conduit Height')
hold on
quiver3(Comparison_points(:,1),Comparison_points(:,3),Comparison_points
(:,2),Calculated_Val_Differential(:,1),Calculated_Val_Differential(:,3)
,Calculated_Val_Differential(:,2))

%Visually Graphs the top "N" Percent of Discrepancies
rms_vals_pt1=(Calculated_Val_Differential(:,1).^2+Calculated_Val_Differ
ential(:,2).^2+Calculated_Val_Differential(:,3).^2).^(1/2);
[sorted_rms,point_count]=sort(rms_vals_pt1);
point_count_pull=point_count(round(total_point_count*(1-
outlier_percentage/100)):total_point_count,1);
highest_outliers=zeros(round(outlier_percentage/100*total_point_count),
6);
for i=1:(outlier_percentage/100*total_point_count)

highest_outliers(i,1:6)=[Comparison_points(point_count_pull(i,1),1),...
        Comparison_points(point_count_pull(i,1),2),...
        Comparison_points(point_count_pull(i,1),3),...
        Calculated_Val_Differential(point_count_pull(i,1),1),...
        Calculated_Val_Differential(point_count_pull(i,1),2),...
        Calculated_Val_Differential(point_count_pull(i,1),3)];
end
figure
```

```
scatter3(Comparison_points(:,1),Comparison_points(:,3),Comparison_point
s(:,2),'.')
title('Highest Level Differences')
xlabel('Conduit Width')
ylabel('Stream Lenght')
zlabel('Conduit Height')
hold on
quiver3(highest_outliers(:,1),
highest_outliers(:,3),highest_outliers(:,2),...
    highest_outliers(:,4), highest_outliers(:,6),highest_outliers(:,5))
alpha(.7)
hold off

%Charts out the R- Squared
figure
u_r2=((total_point_count*sum(Data_Set_2_Vals(:,4).*Data_Set_1_Vals(:,4)
)-sum(Data_Set_2_Vals(:,4))*sum(Data_Set_1_Vals(:,4)))...
    /((total_point_count*sum(Data_Set_2_Vals(:,4).^2)-
sum(Data_Set_2_Vals(:,4))^2)^(1/2)*(total_point_count*sum(Data_Set_1_Va
ls(:,4).^2)-sum(Data_Set_1_Vals(:,4))^2)^(1/2)))^2
scatter(Data_Set_2_Vals(:,4),Data_Set_1_Vals(:,4))
title('U R2')
figure
v_r2=((total_point_count*sum(Data_Set_2_Vals(:,5).*Data_Set_1_Vals(:,5)
)-sum(Data_Set_2_Vals(:,5))*sum(Data_Set_1_Vals(:,5)))...
    /((total_point_count*sum(Data_Set_2_Vals(:,5).^2)-
sum(Data_Set_2_Vals(:,5))^2)^(1/2)*(total_point_count*sum(Data_Set_1_Va
ls(:,5).^2)-sum(Data_Set_1_Vals(:,5))^2)^(1/2)))^2
scatter(Data_Set_2_Vals(:,5),Data_Set_1_Vals(:,5))
title('V R2')
figure
w_r2=((total_point_count*sum(Data_Set_2_Vals(:,6).*Data_Set_1_Vals(:,6)
)-sum(Data_Set_2_Vals(:,6))*sum(Data_Set_1_Vals(:,6)))...
    /((total_point_count*sum(Data_Set_2_Vals(:,6).^2)-
sum(Data_Set_2_Vals(:,6))^2)^(1/2)*(total_point_count*sum(Data_Set_1_Va
ls(:,6).^2)-sum(Data_Set_1_Vals(:,6))^2)^(1/2)))^2
scatter(Data_Set_2_Vals(:,6),Data_Set_1_Vals(:,6))
title('W R2')
figure
k_r2=((total_point_count*sum(Data_Set_2_Vals(:,7).*Data_Set_1_Vals(:,7)
)-sum(Data_Set_2_Vals(:,7))*sum(Data_Set_1_Vals(:,7)))...
    /((total_point_count*sum(Data_Set_2_Vals(:,7).^2)-
sum(Data_Set_2_Vals(:,7))^2)^(1/2)*(total_point_count*sum(Data_Set_1_Va
ls(:,7).^2)-sum(Data_Set_1_Vals(:,7))^2)^(1/2)))^2

scatter(Data_Set_2_Vals(:,7),Data_Set_1_Vals(:,7))
title('TKE R2')
```

Appendix 2: Current Meter Simulation Code

```
%Mark Christian
%Note: This material was developed in support of Mark Christian's Ph.D
%thesis and should be cited as such.
%
%Approved for Public Distribution

%House Keeping
clc
clear all
close all
%_____________Data Read In_____________
%----------Declared Variables----------
%.xlxs files
%{
CFD_Info ='CFD_Sample_0.3m_tolerance.xlsx';
%'channel_with_support.xlsx';%File with CFD information
'CFD_Rech_Channel_test.xlsx';%
CFD_Values = xlsread(CFD_Info);
sz=size(CFD_Values);
length_CFD=sz(1,1);
%}
%.csv files
%
CFDfilename = '633CMS-SST-ALR-A.csv';
CFD_Values = csvread(CFDfilename,2,0);
sz=size(CFD_Values);
length_CFD=sz(1,1);
%}

x_data=CFD_Values(:,5);
y_data=CFD_Values(:,6);
z_data=CFD_Values(:,7);
u_data=CFD_Values(:,1);
v_data=CFD_Values(:,2);
w_data=CFD_Values(:,3);
k_data=CFD_Values(:,4);
CFD_Values=[x_data, y_data, z_data, u_data, v_data, w_data, k_data];

Horz_Density=5; %Horizontal CM Resolution (x direction)
Vert_Density=5; %Vertical CM Resolution (y direction)
Horz_Density_Cap=15;
Vert_Density_Cap=15;
Horz_Density_Step=2;
Vert_Density_Step=2;
hoz_counts=1;
verz_counts=1;
Horz_Density_Initial=Horz_Density;

Solution_Matrix_C31G=zeros((Horz_Density_Cap-
Horz_Density)/2+1,(Vert_Density_Cap-Vert_Density)/2+1);
Solution_Matrix_C31P=zeros((Horz_Density_Cap-
Horz_Density)/2+1,(Vert_Density_Cap-Vert_Density)/2+1);
```

```
Solution_Matrix_C31M=zeros((Horz_Density_Cap-
Horz_Density)/2+1,(Vert_Density_Cap-Vert_Density)/2+1);
Solution_Matrix_C31A=zeros((Horz_Density_Cap-
Horz_Density)/2+1,(Vert_Density_Cap-Vert_Density)/2+1);
Solution_Matrix_C31R=zeros((Horz_Density_Cap-
Horz_Density)/2+1,(Vert_Density_Cap-Vert_Density)/2+1);

bay_shift_factor=1;
conduit_min_height=1.963079667931308;%1.8368414;%0;0.00.0; %0.1722;%
conduit_max_height=19.5;%19.7027315;;%1;%0.81;%0.9932;%
%
conduit_max_width=15.19555;%+bay_shift_factor*8.61095139077517;%1;%1;%.
6096;%
conduit_min_width=8.6614;%+bay_shift_factor*8.61095139077517;%0;
%}
%{
conduit_max_width=23.59659958;%:%+bay_shift_factor*8.61095139077517;%1;
%1;%.6096;%
conduit_min_width=17.27235222;%+bay_shift_factor*8.61095139077517;%0;
%}
%{
conduit_max_width=32.13100051879883;+bay_shift_factor*8.61095139077517;
%1;%1;%.6096;%conduit_min_width=8.6614+bay_shift_factor*8.6109513907751
7;%0;
conduit_min_width=25.730199813842773;%+bay_shift_factor*8.6109513907751
7;%0;
%}
downstream_location=35.5762461;%36.7653368;%0.39624; 4.7;%%z location
of the cross section 2.1;.25;%
propeller_diameter=0.0499872;%0.164; %feet standard-ish
m=8; %conduit friction factor (typically 8 but between 4-14)
CFD_Specificed_Flow_Rate=3;



%-----------Data Processing

x_column=1;
y_column=2;
z_column=3;
u_column=4;
v_column=5;
w_column=6;
k_column=7;
point_1=1;
point_2=2;
point_3=3;
point_4=4;
radius_of_influence=0.2;
IWD_power=3;

while Vert_Density<=Vert_Density_Cap
```

```
while Horz_Density<=Horz_Density_Cap

%-------SOLUTION POINT CALCULATION-----------
%Horz_Density=5; %Horizontal CM Resolution (x direction)
%Vert_Density=5; %Vertical CM Resolution (y direction)
turb_period=3; %cycles/sec
%Current Meter Characteristics
%ott_p=[K, b_cal, m_cal, N_b, A_b, R_m, a_p,b_p, cdtheta_1 to
cdtheta_7]
ott_p=[0.25, 0.00213, 0.2545, 2, 0.003328987, 0.037,
0.189045780020484,-0.378091560040967,0,0,-4.9871174374257E-
07,0.0000717854569419595,-
0.00276229459292349,0.0122545061152683,0.0184295940176016,0.956969,0.12
5];
ott_m=[0.25, 0.02652, 0.2603, 2, 0.003328987, 0.037,
0.189045780020484,-0.378091560040967,0,-3.4165246038E-10,-
1.7654668507487E-07,0.000022979171337173,-0.00003820979001945,-
0.0396891935744748,-0.00693705159424107,0.9775,0.125];
ott_a=[0.125, 0.03871, 0.12834, 2, 0.002262709, 0.0305,
0.335640753479021,-0.419550941848776,-4.27705440088E-
09,1.00474652437127E-06,-0.0000920763072517899,0.00412286841530141,-
0.0908716074611249,0.806585525482404,0.00135535891388017,0.9984,0.1];
ott_r=[0.25 0.02316, 0.25085, 2, 0.002588754,0.0305,
0.159510219297216,-0.398775548243039,2.49361505878E-09,-
6.4245835473906E-07,0.0000647527970138312,-
0.00318547058862095,0.0765847217706312,-
0.726240299213572,0.00159518140114834,0.997957,0.1];

ax_co=[0,0.378493808692751,0.0173599138636449,-0.575086186886789,-
0.0819862650023583,0.000754745051349909,1.1056449969671,0.0415993297963
425,0.0133404073702818,-0.000759445263605786,-0.486793749676385,-
0.0124422149814773,-0.0018868813610166,-
0.000718852541353602,0.0000545300249586028];
trav_p_co=[0.0732126930101304,-
0.47279662762535,0.0245046198894603,0.972832510436222,0.057265430476086
2,-0.213750607506066,-0.667483631153662,0.0637423622074004,-
0.195069170544584,0.375630382388398];
obqfctr1=[3E-10, 2E-08, -1E-07, -8E-05, -0.0039, 0.1173, 2.134];
%Valeport 002
obqfctr2=[8E-10, -2E-08, -5E-08, 9E-05, -0.0142, -0.1575, 1.2799];
%Valeport 001
obqfctr3=[5E-10, -2E-08, 3E-07, 9E-05, -0.0114, -0.1247, 0.6779]; %Ott
C31 Metal
obqfctr4=[9E-10, 2E-08, -3E-06, -5E-05, -0.0074, 0.0328, 1.668]; %Ott
C31 Plastic

Sensor_Recorded_Values=zeros(Horz_Density*Vert_Density,7);

%Front End Stuff
Solution_Point=zeros(Horz_Density*Vert_Density,3);
Solution_Point(1:Horz_Density*Vert_Density,3)=downstream_location;
conduit_width=conduit_max_width-conduit_min_width;
conduit_height=conduit_max_height-conduit_min_height;
horizontal_r_p=conduit_width/2-0.75*propeller_diameter;
```

```
vertical_r_p=conduit_height/2-0.75*propeller_diameter;

%Horizontal Array
horizont=zeros(Horz_Density,1);
horizont((Horz_Density-1)/2+1,1)=conduit_width/2+conduit_min_width;
i=1;
while i <= (Horz_Density-1)/2
    horizont((Horz_Density-
1)/2+1+i,1)=conduit_width/2+conduit_min_width+...
        horizontal_r_p*(i/((Horz_Density-1)/2))^(1/2);
    horizont((Horz_Density-1)/2+1-
i,1)=conduit_width/2+conduit_min_width-...
        horizontal_r_p*(i/((Horz_Density-1)/2))^(1/2);
    i=i+1;
end

%vertical array
verts=zeros(Vert_Density,1);
verts((Vert_Density-1)/2+1,1)=conduit_height/2+conduit_min_height;
i=1;
while i <= (Vert_Density-1)/2
    verts((Vert_Density-
1)/2+1+i,1)=conduit_height/2+conduit_min_height+...
        vertical_r_p*(i/((Vert_Density-1)/2))^(1/2);
    verts((Vert_Density-1)/2+1-
i,1)=conduit_height/2+conduit_min_height-...
        vertical_r_p*(i/((Vert_Density-1)/2))^(1/2);
    i=i+1;
end

%populating the solution point matrix
Solution_Point(1:Horz_Density*Vert_Density,1)=repmat(horizont,Vert_Dens
ity,1);
for i=1:Vert_Density
Solution_Point((i-1)*Horz_Density+1:i*Horz_Density,2)=verts(i,1);
end

%{
figure
scatter3(Solution_Point(:,1),Solution_Point(:,3),Solution_Point(:,2),'f
illed')
hold on
scatter3(CFD_Values(:,x_column),CFD_Values(:,z_column),CFD_Values(:,y_c
olumn),'.')
xlabel('Conduit Width-x')
ylabel('Stream Lenght-z')
zlabel('Conduit Height-y')
title('CFD Dataset')
%}
%Determine influence!

j=1;
points_of_influence=zeros(Horz_Density*Vert_Density,2);
```

```
while j<= Horz_Density*Vert_Density
    i=1;
num_points_included=1;
close_points=zeros(2,9);
while i<=length_CFD
distance=((Solution_Point(j,1)-CFD_Values(i,1))^2+(Solution_Point(j,2)-
CFD_Values(i,2))^2+...
    (Solution_Point(j,3)-CFD_Values(i,3))^2)^(1/2);
if distance<= radius_of_influence
    close_points(num_points_included,2:9)=[distance, CFD_Values(i,:)];
    num_points_included=num_points_included+1;
end
points_of_influence(j,1:2)=[j,num_points_included];
i=i+1;
end
k=1;
for k=1:(num_points_included-1)
close_points(k,1)=1/(close_points(k,2)).^IWD_power;
end
solution_fill=zeros((num_points_included-1),4);
k=1;
for k=1:(num_points_included-1)
solution_fill(k,1)=close_points(k,1)*close_points(k,6);
solution_fill(k,2)=close_points(k,1)*close_points(k,7);
solution_fill(k,3)=close_points(k,1)*close_points(k,8);
solution_fill(k,4)=close_points(k,1)*close_points(k,9);
end
Solution_Point(j,4)=sum(solution_fill(:,1))/sum(close_points(:,1));
Solution_Point(j,5)=sum(solution_fill(:,2))/sum(close_points(:,1));
Solution_Point(j,6)=sum(solution_fill(:,3))/sum(close_points(:,1));
Solution_Point(j,7)=sum(solution_fill(:,4))/sum(close_points(:,1));
j=j+1;
end

%THIS SECTION ASSUMES PERFECT RECORDING OF AXIAL VELOCITY
CM_Sensed_Velocities=Solution_Point(:,6);

%This is where the values are converted into a predicted flow rate
vertical_averages=zeros(Vert_Density,1); %where the hoz averages will
be placed
vert_count=1;
while vert_count<=Vert_Density
hoz_values=zeros(Horz_Density,1);
%Exterior Points Corrected!!!!!!!!
hoz_values(1,1)=CM_Sensed_Velocities((vert_count-
1)*Horz_Density+1,1)*...
(m/(m+1)*(Solution_Point((vert_count-1)*Horz_Density+1,1)-
conduit_min_width)/conduit_width+...
1/(12*m)*((Solution_Point((vert_count-1)*Horz_Density+2,1)-...
Solution_Point((vert_count-1)*Horz_Density+1,1))/conduit_width)^2*...
(conduit_width/(Solution_Point((vert_count-1)*Horz_Density+1,1)-
conduit_min_width))+...
7/12*(Solution_Point((vert_count-1)*Horz_Density+2,1)-...
Solution_Point((vert_count-1)*Horz_Density+1,1))/conduit_width-...
```

```
1/12*(Solution_Point((vert_count-1)*Horz_Density+3,1)-...
Solution_Point((vert_count-1)*Horz_Density+2,1))/conduit_width);

hoz_values(Horz_Density,1)=CM_Sensed_Velocities((vert_count)*Horz_Densi
ty,1)*...
(m/(m+1)*(conduit_max_width-
Solution_Point((vert_count)*Horz_Density,1))/conduit_width+...
1/(12*m)*((Solution_Point((vert_count)*Horz_Density,1)-...
Solution_Point((vert_count)*Horz_Density-1,1))/conduit_width)^2*...
conduit_width/(conduit_max_width-
Solution_Point((vert_count)*Horz_Density,1))+...
7/12*(Solution_Point((vert_count)*Horz_Density,1)-...
Solution_Point((vert_count)*Horz_Density-1,1))/conduit_width-...
1/12*(Solution_Point((vert_count)*Horz_Density-1,1)-...
Solution_Point((vert_count)*Horz_Density-2,1))/conduit_width);

%Exterior Adjacent
hoz_values(2,1)=CM_Sensed_Velocities((vert_count-
1)*Horz_Density+2,1)*...
(1/2*(Solution_Point((vert_count-1)*Horz_Density+2,1)-...
Solution_Point((vert_count-1)*Horz_Density+1,1))/conduit_width+...
7/12*(Solution_Point((vert_count-1)*Horz_Density+3,1)-...
Solution_Point((vert_count-1)*Horz_Density+2,1))/conduit_width-...
1/12*(Solution_Point((vert_count-1)*Horz_Density+4,1)-...
Solution_Point((vert_count-1)*Horz_Density+3,1))/conduit_width);

hoz_values(Horz_Density-
1,1)=CM_Sensed_Velocities((vert_count)*Horz_Density-1,1)*...
(1/2*(Solution_Point((vert_count)*Horz_Density,1)-...
Solution_Point((vert_count)*Horz_Density-1,1))/conduit_width+...
7/12*(Solution_Point((vert_count)*Horz_Density-1,1)-...
Solution_Point((vert_count)*Horz_Density-2,1))/conduit_width-...
1/12*(Solution_Point((vert_count)*Horz_Density-2,1)-...
Solution_Point((vert_count)*Horz_Density-3,1))/conduit_width);

%Interior Points
Inside_Count=3;
while Inside_Count<=(Horz_Density-2)
hoz_values(Inside_Count,1)=CM_Sensed_Velocities((vert_count-1)*...
    Horz_Density+Inside_Count,1)*(7/12*(Solution_Point((vert_count-
1)*...
    Horz_Density+Inside_Count+1,1)-Solution_Point((vert_count-1)*...
    Horz_Density+Inside_Count,1))/conduit_width+...
    7/12*(Solution_Point((vert_count-1)*Horz_Density+Inside_Count,1)-
...
    Solution_Point((vert_count-1)*Horz_Density+Inside_Count-
1,1))/conduit_width-...
    1/12*(Solution_Point((vert_count-1)*Horz_Density+Inside_Count+2,1)-
...
    Solution_Point((vert_count-
1)*Horz_Density+Inside_Count+1,1))/conduit_width-...
    1/12*(Solution_Point((vert_count-1)*Horz_Density+Inside_Count-1,1)-
...
```

```
    Solution_Point((vert_count-1)*Horz_Density+Inside_Count-
2,1))/conduit_width);
Inside_Count=Inside_Count+1;
end
vertical_averages(vert_count,1)=sum(hoz_values);
vert_count=vert_count+1;
end

verts_values=zeros(Vert_Density,1);
%Exterior_Points
verts_values(1,1)=vertical_averages(1,1)*(m/(m+1)*(verts(1,1)-
conduit_min_height)/conduit_height+...
    1/(12*m)*((verts(2,1)-verts(1,1))/conduit_height)^2*...
    conduit_height/(verts(1,1)-conduit_min_height)+7/12*((verts(2,1)-
verts(1,1))/...
    conduit_height)-1/12*(verts(3,1)-verts(2,1))/conduit_height);

verts_values(Vert_Density,1)=vertical_averages(Vert_Density,1)*(m/(m+1)
*...
    (conduit_max_height-verts(Vert_Density,1))/conduit_height+...
    1/(12*m)*((verts(2,1)-verts(1,1))/conduit_height)^2*...
    conduit_height/(conduit_max_height-
verts(Vert_Density,1))+7/12*((verts(2,1)-verts(1,1))/...
    conduit_height)-1/12*(verts(3,1)-verts(2,1))/conduit_height);

%Exterior Adjacent
verts_values(2,1)=vertical_averages(2,1)*(1/2*(verts(2,1)-
verts(1,1))/...
    conduit_height+7/12*(verts(3,1)-verts(2,1))/conduit_height-...
    1/12*(verts(4,1)-verts(3,1))/conduit_height);

verts_values(Vert_Density-1,1)=vertical_averages(Vert_Density-1,1)*...
    (1/2*(verts(Vert_Density,1)-verts(Vert_Density-1,1))/...
    conduit_height+7/12*(verts(Vert_Density-1,1)-...
    verts(Vert_Density-2,1))/conduit_height-...
    1/12*(verts(Vert_Density-2,1)-verts(Vert_Density-
3,1))/conduit_height);

%Interior Points
Interior_Count=3;
while Interior_Count<=(Vert_Density-2)

verts_values(Interior_Count,1)=vertical_averages(Interior_Count,1)*...
    (7/12*(verts(Interior_Count+1,1)-verts(Interior_Count,1))/...
        conduit_height+7/12*(verts(Interior_Count,1)-
verts(Interior_Count-1,1))/...
        conduit_height-1/12*(verts(Interior_Count+2,1)-
verts(Interior_Count+1,1))/...
        conduit_height-1/12*(verts(Interior_Count-1,1)-
verts(Interior_Count-2,1))/...
        conduit_height);
    Interior_Count=Interior_Count+1;
end
```

```
Average_Velocity=sum(verts_values);
Recorded_Flow_Rate=abs((conduit_max_height-
conduit_min_height)*(conduit_max_width-
conduit_min_width)*Average_Velocity);
Solution_Point_a=Solution_Point;
CFD_Values_a=CFD_Values;
Solution_Matrix_C31G(verz_counts,hoz_counts)=Recorded_Flow_Rate;

%-------------------------Section for Ott C31-1 Plastic----------------
----------
CM_Sensed_Velocities=zeros(Horz_Density*Vert_Density,1); %Horizontal CM
Resolution (x direction)
oblique_angle=zeros(Horz_Density*Vert_Density,1);
for gr=1:Horz_Density*Vert_Density
    oblique_mag=(Solution_Point(gr,4)^2+Solution_Point(gr,5)^2)^(1/2);

total_mag=(Solution_Point(gr,4)^2+Solution_Point(gr,5)^2+Solution_Point
(gr,6)^2)^(1/2);
    inagle=atan(oblique_mag/Solution_Point(gr,6))*180/pi();%<- theta in
degrees
    oblique_angle(gr,1)=inagle;
    turb_vel=((2*Solution_Point(gr,7))^2/3)^(1/2);%<-isotropic
turbulence assumed
    axial_intensity=turb_vel/Solution_Point(gr,6);
    trans_intensity=turb_vel/oblique_mag;
    ap=ax_co(1,1)+ax_co(1,2)*axial_intensity+...
        ax_co(1,3)*turb_period+ax_co(1,4)*axial_intensity^2+...

ax_co(1,5)*axial_intensity*turb_period+ax_co(1,6)*turb_period^2+...
ax_co(1,7)*axial_intensity^3+ax_co(1,8)*axial_intensity^2*turb_period+.
..
ax_co(1,9)*axial_intensity*turb_period^2+ax_co(1,10)*turb_period^3+...
ax_co(1,11)*axial_intensity^4+ax_co(1,12)*axial_intensity^3*turb_period
+...
ax_co(1,13)*axial_intensity^2*turb_period^2+ax_co(1,14)*axial_intensity
*turb_period^3+...
        ax_co(1,15)*turb_period^4;%<-General!!
cmd=ott_p(1,9)*inagle^6+ott_p(1,10)*inagle^5+ott_p(1,11)*inagle^4+...

ott_p(1,12)*inagle^3+ott_p(1,13)*inagle^2+ott_p(1,14)*inagle^1+ott_p(1,
15);%<-Specific to Current meter
cmdt=trav_p_co(1,1)+trav_p_co(1,2)*trans_intensity+trav_p_co(1,3)*ott_p
(1,1)+...
trav_p_co(1,4)*trans_intensity^2+trav_p_co(1,5)*trans_intensity*ott_p(1
,1)+...
trav_p_co(1,6)*ott_p(1,1)^2+trav_p_co(1,7)*trans_intensity^3+...
trav_p_co(1,8)*trans_intensity^2*ott_p(1,1)+trav_p_co(1,9)*trans_intens
ity*ott_p(1,1)^2+...
        trav_p_co(1,10)*ott_p(1,1)^3;%<-Specific to Current meter
    v_rev=-ott_p(1,2)/ott_p(1,3)+...
        1/ott_p(1,3)*Solution_Point(gr,6)+...
        1/ott_p(1,3)*axial_intensity^2/2*Solution_Point(gr,6)+...
        ap-...
```

```
(ott_p(1,4)*ott_p(1,5)*ott_p(1,6))/(2*ott_p(1,8)*ott_p(1,16))*cmd*obliq
ue_mag^2/Solution_Point(gr,6)-...

(ott_p(1,4)*ott_p(1,5)*ott_p(1,6))/(4*ott_p(1,8)*ott_p(1,16))*trans_int
ensity^2*oblique_mag^2/Solution_Point(gr,6)*cmdt;
    v_v=ott_p(1,3)*v_rev+ott_p(1,2);
    Solution_Point(gr,6);

CM_Sensed_Velocities(gr,1)=v_v;%total_mag+total_mag*oblique_impact/100;
end

%CM_Sensed_Velocities=Solution_Point(:,6);
%oblique_impact_factors
%This is where the values are converted into a predicted flow rate
vertical_averages=zeros(Vert_Density,1); %where the hoz averages will
be placed
vert_count=1;
while vert_count<=Vert_Density
hoz_values=zeros(Horz_Density,1);
%Exterior Points Corrected!!!!!!!!
hoz_values(1,1)=CM_Sensed_Velocities((vert_count-
1)*Horz_Density+1,1)*...
(m/(m+1)*(Solution_Point((vert_count-1)*Horz_Density+1,1)-
conduit_min_width)/conduit_width+...
1/(12*m)*((Solution_Point((vert_count-1)*Horz_Density+2,1)-...
Solution_Point((vert_count-1)*Horz_Density+1,1))/conduit_width)^2*...
(conduit_width/(Solution_Point((vert_count-1)*Horz_Density+1,1)-
conduit_min_width))+...
7/12*(Solution_Point((vert_count-1)*Horz_Density+2,1)-...
Solution_Point((vert_count-1)*Horz_Density+1,1))/conduit_width-...
1/12*(Solution_Point((vert_count-1)*Horz_Density+3,1)-...
Solution_Point((vert_count-1)*Horz_Density+2,1))/conduit_width);

hoz_values(Horz_Density,1)=CM_Sensed_Velocities((vert_count)*Horz_Densi
ty,1)*...
(m/(m+1)*(conduit_max_width-
Solution_Point((vert_count)*Horz_Density,1))/conduit_width+...
1/(12*m)*((Solution_Point((vert_count)*Horz_Density,1)-...
Solution_Point((vert_count)*Horz_Density-1,1))/conduit_width)^2*...
conduit_width/(conduit_max_width-
Solution_Point((vert_count)*Horz_Density,1))+...
7/12*(Solution_Point((vert_count)*Horz_Density,1)-...
Solution_Point((vert_count)*Horz_Density-1,1))/conduit_width-...
1/12*(Solution_Point((vert_count)*Horz_Density-1,1)-...
Solution_Point((vert_count)*Horz_Density-2,1))/conduit_width);

%Exterior Adjacent
hoz_values(2,1)=CM_Sensed_Velocities((vert_count-
1)*Horz_Density+2,1)*...
(1/2*(Solution_Point((vert_count-1)*Horz_Density+2,1)-...
Solution_Point((vert_count-1)*Horz_Density+1,1))/conduit_width+...
7/12*(Solution_Point((vert_count-1)*Horz_Density+3,1)-...
Solution_Point((vert_count-1)*Horz_Density+2,1))/conduit_width-...
```

```
1/12*(Solution_Point((vert_count-1)*Horz_Density+4,1)-...
Solution_Point((vert_count-1)*Horz_Density+3,1))/conduit_width);

hoz_values(Horz_Density-
1,1)=CM_Sensed_Velocities((vert_count)*Horz_Density-1,1)*...
(1/2*(Solution_Point((vert_count)*Horz_Density,1)-...
Solution_Point((vert_count)*Horz_Density-1,1))/conduit_width+...
7/12*(Solution_Point((vert_count)*Horz_Density-1,1)-...
Solution_Point((vert_count)*Horz_Density-2,1))/conduit_width-...
1/12*(Solution_Point((vert_count)*Horz_Density-2,1)-...
Solution_Point((vert_count)*Horz_Density-3,1))/conduit_width);

%Interior Points
Inside_Count=3;
while Inside_Count<=(Horz_Density-2)
hoz_values(Inside_Count,1)=CM_Sensed_Velocities((vert_count-1)*...
    Horz_Density+Inside_Count,1)*(7/12*(Solution_Point((vert_count-
1)*...
    Horz_Density+Inside_Count+1,1)-Solution_Point((vert_count-1)*...
    Horz_Density+Inside_Count,1))/conduit_width+...
    7/12*(Solution_Point((vert_count-1)*Horz_Density+Inside_Count,1)-
...
    Solution_Point((vert_count-1)*Horz_Density+Inside_Count-
1,1))/conduit_width-...
    1/12*(Solution_Point((vert_count-1)*Horz_Density+Inside_Count+2,1)-
...
    Solution_Point((vert_count-
1)*Horz_Density+Inside_Count+1,1))/conduit_width-...
    1/12*(Solution_Point((vert_count-1)*Horz_Density+Inside_Count-1,1)-
...
    Solution_Point((vert_count-1)*Horz_Density+Inside_Count-
2,1))/conduit_width);
Inside_Count=Inside_Count+1;
end
vertical_averages(vert_count,1)=sum(hoz_values);
vert_count=vert_count+1;
end

verts_values=zeros(Vert_Density,1);
%Exterior_Points
verts_values(1,1)=vertical_averages(1,1)*(m/(m+1)*(verts(1,1)-
conduit_min_height)/conduit_height+...
    1/(12*m)*((verts(2,1)-verts(1,1))/conduit_height)^2*...
    conduit_height/(verts(1,1)-conduit_min_height)+7/12*((verts(2,1)-
verts(1,1))/...
    conduit_height)-1/12*(verts(3,1)-verts(2,1))/conduit_height);
verts_values(Vert_Density,1)=vertical_averages(Vert_Density,1)*(m/(m+1)
*...
    (conduit_max_height-verts(Vert_Density,1))/conduit_height+...
    1/(12*m)*((verts(2,1)-verts(1,1))/conduit_height)^2*...
    conduit_height/(conduit_max_height-
verts(Vert_Density,1))+7/12*((verts(2,1)-verts(1,1))/...
    conduit_height)-1/12*(verts(3,1)-verts(2,1))/conduit_height);
%Exterior Adjacent
```

```
verts_values(2,1)=vertical_averages(2,1)*(1/2*(verts(2,1)-
verts(1,1))/...
    conduit_height+7/12*(verts(3,1)-verts(2,1))/conduit_height-...
    1/12*(verts(4,1)-verts(3,1))/conduit_height);

verts_values(Vert_Density-1,1)=vertical_averages(Vert_Density-1,1)*...
    (1/2*(verts(Vert_Density,1)-verts(Vert_Density-1,1))/...
    conduit_height+7/12*(verts(Vert_Density-1,1)-...
    verts(Vert_Density-2,1))/conduit_height-...
    1/12*(verts(Vert_Density-2,1)-verts(Vert_Density-
3,1))/conduit_height);

%Interior Points
Interior_Count=3;
while Interior_Count<=(Vert_Density-2)

verts_values(Interior_Count,1)=vertical_averages(Interior_Count,1)*...
    (7/12*(verts(Interior_Count+1,1)-verts(Interior_Count,1))/...
        conduit_height+7/12*(verts(Interior_Count,1)-
verts(Interior_Count-1,1))/...
        conduit_height-1/12*(verts(Interior_Count+2,1)-
verts(Interior_Count+1,1))/...
        conduit_height-1/12*(verts(Interior_Count-1,1)-
verts(Interior_Count-2,1))/...
        conduit_height);
    Interior_Count=Interior_Count+1;
end

Average_Velocity_C31P=sum(verts_values);
Recorded_Flow_Rate_C31P=abs((conduit_max_height-
conduit_min_height)*(conduit_max_width-
conduit_min_width)*Average_Velocity_C31P);
Solution_Point_a=Solution_Point;
CFD_Values_a=CFD_Values;
Solution_Matrix_C31P(verz_counts,hoz_counts)=Recorded_Flow_Rate_C31P;
%
%-------------------------Section for OTT C31-1 Metal------------------
--------
CM_Sensed_Velocities=zeros(Horz_Density*Vert_Density,1); %Horizontal CM
Resolution (x direction)
oblique_angle=zeros(Horz_Density*Vert_Density,1);
for gr=1:Horz_Density*Vert_Density
    oblique_mag=(Solution_Point(gr,4)^2+Solution_Point(gr,5)^2)^(1/2);

total_mag=(Solution_Point(gr,4)^2+Solution_Point(gr,5)^2+Solution_Point
(gr,6)^2)^(1/2);
    inagle=atan(oblique_mag/Solution_Point(gr,6))*180/pi();
    oblique_angle(gr,1)=inagle;

    turb_vel=((2*Solution_Point(gr,7))^2/3)^(1/2);%<-isotropic
turbulence assumed
    axial_intensity=turb_vel/Solution_Point(gr,6);
    trans_intensity=turb_vel/oblique_mag;
```

```
    ap=ax_co(1,1)+ax_co(1,2)*axial_intensity+...
        ax_co(1,3)*turb_period+ax_co(1,4)*axial_intensity^2+...

ax_co(1,5)*axial_intensity*turb_period+ax_co(1,6)*turb_period^2+...
ax_co(1,7)*axial_intensity^3+ax_co(1,8)*axial_intensity^2*turb_period+.
..
ax_co(1,9)*axial_intensity*turb_period^2+ax_co(1,10)*turb_period^3+...
ax_co(1,11)*axial_intensity^4+ax_co(1,12)*axial_intensity^3*turb_period
+...
ax_co(1,13)*axial_intensity^2*turb_period^2+ax_co(1,14)*axial_intensity
*turb_period^3+...
        ax_co(1,15)*turb_period^4;%<-General!!
cmd=ott_m(1,9)*inagle^6+ott_m(1,10)*inagle^5+ott_m(1,11)*inagle^4+...
ott_m(1,12)*inagle^3+ott_m(1,13)*inagle^2+ott_m(1,14)*inagle^1+ott_m(1,
15);%<-Specific to Current meter
cmdt=trav_p_co(1,1)+trav_p_co(1,2)*trans_intensity+trav_p_co(1,3)*ott_m
(1,1)+...
trav_p_co(1,4)*trans_intensity^2+trav_p_co(1,5)*trans_intensity*ott_m(1
,1)+...
trav_p_co(1,6)*ott_m(1,1)^2+trav_p_co(1,7)*trans_intensity^3+...

trav_p_co(1,8)*trans_intensity^2*ott_m(1,1)+trav_p_co(1,9)*trans_intens
ity*ott_m(1,1)^2+...
        trav_p_co(1,10)*ott_m(1,1)^3;%<-Specific to Current meter
    v_rev=-ott_m(1,2)/ott_m(1,3)+...
        1/ott_m(1,3)*Solution_Point(gr,6)+...
        1/ott_m(1,3)*axial_intensity^2/2*Solution_Point(gr,6)+...
        ap-...
(ott_m(1,4)*ott_m(1,5)*ott_m(1,6))/(2*ott_m(1,8)*ott_m(1,16))*cmd*obliq
ue_mag^2/Solution_Point(gr,6)-...
(ott_m(1,4)*ott_m(1,5)*ott_m(1,6))/(4*ott_m(1,8)*ott_m(1,16))*trans_int
ensity^2*oblique_mag^2/Solution_Point(gr,6)*cmdt;
    v_v=ott_m(1,3)*v_rev+ott_m(1,2);
    Solution_Point(gr,6);
CM_Sensed_Velocities(gr,1)=v_v;%total_mag+total_mag*oblique_impact/100;
end

%CM_Sensed_Velocities=Solution_Point(:,6);
%oblique_impact_factors
%This is where the values are converted into a predicted flow rate
vertical_averages=zeros(Vert_Density,1); %where the hoz averages will
be placed
vert_count=1;
while vert_count<=Vert_Density
hoz_values=zeros(Horz_Density,1);
%Exterior Points Corrected!!!!!!!!
hoz_values(1,1)=CM_Sensed_Velocities((vert_count-
1)*Horz_Density+1,1)*...
(m/(m+1)*(Solution_Point((vert_count-1)*Horz_Density+1,1)-
conduit_min_width)/conduit_width+...
1/(12*m)*((Solution_Point((vert_count-1)*Horz_Density+2,1)-...
Solution_Point((vert_count-1)*Horz_Density+1,1))/conduit_width)^2*...
(conduit_width/(Solution_Point((vert_count-1)*Horz_Density+1,1)-
conduit_min_width))+...
```

```
7/12*(Solution_Point((vert_count-1)*Horz_Density+2,1)-...
Solution_Point((vert_count-1)*Horz_Density+1,1))/conduit_width-...
1/12*(Solution_Point((vert_count-1)*Horz_Density+3,1)-...
Solution_Point((vert_count-1)*Horz_Density+2,1))/conduit_width);

hoz_values(Horz_Density,1)=CM_Sensed_Velocities((vert_count)*Horz_Densi
ty,1)*...
(m/(m+1)*(conduit_max_width-
Solution_Point((vert_count)*Horz_Density,1))/conduit_width+...
1/(12*m)*((Solution_Point((vert_count)*Horz_Density,1)-...
Solution_Point((vert_count)*Horz_Density-1,1))/conduit_width)^2*...
conduit_width/(conduit_max_width-
Solution_Point((vert_count)*Horz_Density,1))+...
7/12*(Solution_Point((vert_count)*Horz_Density,1)-...
Solution_Point((vert_count)*Horz_Density-1,1))/conduit_width-...
1/12*(Solution_Point((vert_count)*Horz_Density-1,1)-...
Solution_Point((vert_count)*Horz_Density-2,1))/conduit_width);

%Exterior Adjacent
hoz_values(2,1)=CM_Sensed_Velocities((vert_count-
1)*Horz_Density+2,1)*...
(1/2*(Solution_Point((vert_count-1)*Horz_Density+2,1)-...
Solution_Point((vert_count-1)*Horz_Density+1,1))/conduit_width+...
7/12*(Solution_Point((vert_count-1)*Horz_Density+3,1)-...
Solution_Point((vert_count-1)*Horz_Density+2,1))/conduit_width-...
1/12*(Solution_Point((vert_count-1)*Horz_Density+4,1)-...
Solution_Point((vert_count-1)*Horz_Density+3,1))/conduit_width);

hoz_values(Horz_Density-
1,1)=CM_Sensed_Velocities((vert_count)*Horz_Density-1,1)*...
(1/2*(Solution_Point((vert_count)*Horz_Density,1)-...
Solution_Point((vert_count)*Horz_Density-1,1))/conduit_width+...
7/12*(Solution_Point((vert_count)*Horz_Density-1,1)-...
Solution_Point((vert_count)*Horz_Density-2,1))/conduit_width-...
1/12*(Solution_Point((vert_count)*Horz_Density-2,1)-...
Solution_Point((vert_count)*Horz_Density-3,1))/conduit_width);

%Interior Points
Inside_Count=3;
while Inside_Count<=(Horz_Density-2)
hoz_values(Inside_Count,1)=CM_Sensed_Velocities((vert_count-1)*...
    Horz_Density+Inside_Count,1)*(7/12*(Solution_Point((vert_count-
1)*...
    Horz_Density+Inside_Count+1,1)-Solution_Point((vert_count-1)*...
    Horz_Density+Inside_Count,1))/conduit_width+...
    7/12*(Solution_Point((vert_count-1)*Horz_Density+Inside_Count,1)-
...
    Solution_Point((vert_count-1)*Horz_Density+Inside_Count-
1,1))/conduit_width-...
    1/12*(Solution_Point((vert_count-1)*Horz_Density+Inside_Count+2,1)-
...
    Solution_Point((vert_count-
1)*Horz_Density+Inside_Count+1,1))/conduit_width-...
```

```
    1/12*(Solution_Point((vert_count-1)*Horz_Density+Inside_Count-1,1)-
...
    Solution_Point((vert_count-1)*Horz_Density+Inside_Count-
2,1))/conduit_width);
Inside_Count=Inside_Count+1;
end
vertical_averages(vert_count,1)=sum(hoz_values);
vert_count=vert_count+1;
end

verts_values=zeros(Vert_Density,1);
%Exterior_Points
verts_values(1,1)=vertical_averages(1,1)*(m/(m+1)*(verts(1,1)-
conduit_min_height)/conduit_height+...
    1/(12*m)*((verts(2,1)-verts(1,1))/conduit_height)^2*...
    conduit_height/(verts(1,1)-conduit_min_height)+7/12*((verts(2,1)-
verts(1,1))/...
    conduit_height)-1/12*(verts(3,1)-verts(2,1))/conduit_height);
verts_values(Vert_Density,1)=vertical_averages(Vert_Density,1)*(m/(m+1)
*...
    (conduit_max_height-verts(Vert_Density,1))/conduit_height+...
    1/(12*m)*((verts(2,1)-verts(1,1))/conduit_height)^2*...
    conduit_height/(conduit_max_height-
verts(Vert_Density,1))+7/12*((verts(2,1)-verts(1,1))/...
    conduit_height)-1/12*(verts(3,1)-verts(2,1))/conduit_height);

%Exterior Adjacent
verts_values(2,1)=vertical_averages(2,1)*(1/2*(verts(2,1)-
verts(1,1))/...
    conduit_height+7/12*(verts(3,1)-verts(2,1))/conduit_height-...
    1/12*(verts(4,1)-verts(3,1))/conduit_height);
verts_values(Vert_Density-1,1)=vertical_averages(Vert_Density-1,1)*...
    (1/2*(verts(Vert_Density,1)-verts(Vert_Density-1,1))/...
    conduit_height+7/12*(verts(Vert_Density-1,1)-...
    verts(Vert_Density-2,1))/conduit_height-...
    1/12*(verts(Vert_Density-2,1)-verts(Vert_Density-
3,1))/conduit_height);

%Interior Points
Interior_Count=3;
while Interior_Count<=(Vert_Density-2)

verts_values(Interior_Count,1)=vertical_averages(Interior_Count,1)*...
    (7/12*(verts(Interior_Count+1,1)-verts(Interior_Count,1))/...
        conduit_height+7/12*(verts(Interior_Count,1)-
verts(Interior_Count-1,1))/...
        conduit_height-1/12*(verts(Interior_Count+2,1)-
verts(Interior_Count+1,1))/...
        conduit_height-1/12*(verts(Interior_Count-1,1)-
verts(Interior_Count-2,1))/...
        conduit_height);
    Interior_Count=Interior_Count+1;
end
Average_Velocity_C31M=sum(verts_values);
```

```
Recorded_Flow_Rate_C31M=abs((conduit_max_height-
conduit_min_height)*(conduit_max_width-
conduit_min_width)*Average_Velocity_C31M);
Solution_Point_a=Solution_Point;
CFD_Values_a=CFD_Values;

Solution_Matrix_C31M(verz_counts,hoz_counts)=Recorded_Flow_Rate_C31M;
%-------------------------Section for OTT C31-A-------------------------
--
CM_Sensed_Velocities=zeros(Horz_Density*Vert_Density,1); %Horizontal CM
Resolution (x direction)
oblique_angle=zeros(Horz_Density*Vert_Density,1);
for gr=1:Horz_Density*Vert_Density
    oblique_mag=(Solution_Point(gr,4)^2+Solution_Point(gr,5)^2)^(1/2);

total_mag=(Solution_Point(gr,4)^2+Solution_Point(gr,5)^2+Solution_Point
(gr,6)^2)^(1/2);
    inagle=atan(oblique_mag/Solution_Point(gr,6))*180/pi();
    oblique_angle(gr,1)=inagle;



    turb_vel=((2*Solution_Point(gr,7))^2/3)^(1/2);%<-isotropic
turbulence assumed
    axial_intensity=turb_vel/Solution_Point(gr,6);
    trans_intensity=turb_vel/oblique_mag;
    ap=ax_co(1,1)+ax_co(1,2)*axial_intensity+...
        ax_co(1,3)*turb_period+ax_co(1,4)*axial_intensity^2+...

ax_co(1,5)*axial_intensity*turb_period+ax_co(1,6)*turb_period^2+...
ax_co(1,7)*axial_intensity^3+ax_co(1,8)*axial_intensity^2*turb_period+.
..
ax_co(1,9)*axial_intensity*turb_period^2+ax_co(1,10)*turb_period^3+...
ax_co(1,11)*axial_intensity^4+ax_co(1,12)*axial_intensity^3*turb_period
+...
ax_co(1,13)*axial_intensity^2*turb_period^2+ax_co(1,14)*axial_intensity
*turb_period^3+...
        ax_co(1,15)*turb_period^4;%<-General!!
cmd=ott_a(1,9)*inagle^6+ott_a(1,10)*inagle^5+ott_a(1,11)*inagle^4+...
ott_a(1,12)*inagle^3+ott_a(1,13)*inagle^2+ott_a(1,14)*inagle^1+ott_a(1,
15);%<-Specific to Current meter
cmdt=trav_p_co(1,1)+trav_p_co(1,2)*trans_intensity+trav_p_co(1,3)*ott_a
(1,1)+...
trav_p_co(1,4)*trans_intensity^2+trav_p_co(1,5)*trans_intensity*ott_a(1
,1)+...
trav_p_co(1,6)*ott_a(1,1)^2+trav_p_co(1,7)*trans_intensity^3+...
trav_p_co(1,8)*trans_intensity^2*ott_a(1,1)+trav_p_co(1,9)*trans_intens
ity*ott_a(1,1)^2+...
        trav_p_co(1,10)*ott_a(1,1)^3;%<-Specific to Current meter
    v_rev=-ott_a(1,2)/ott_a(1,3)+...
        1/ott_a(1,3)*Solution_Point(gr,6)+...
        1/ott_a(1,3)*axial_intensity^2/2*Solution_Point(gr,6)+...
        ap-...

(ott_a(1,4)*ott_a(1,5)*ott_a(1,6))/(2*ott_a(1,8)*ott_a(1,16))*cmd*obliq
```

```
ue_mag^2/Solution_Point(gr,6)-...
(ott_a(1,4)*ott_a(1,5)*ott_a(1,6))/(4*ott_a(1,8)*ott_a(1,16))*trans_int
ensity^2*oblique_mag^2/Solution_Point(gr,6)*cmdt;
    v_v=ott_a(1,3)*v_rev+ott_a(1,2);
    Solution_Point(gr,6);
CM_Sensed_Velocities(gr,1)=v_v;%total_mag+total_mag*oblique_impact/100;
end
%CM_Sensed_Velocities=Solution_Point(:,6);
%oblique_impact_factors
%This is where the values are converted into a predicted flow rate
vertical_averages=zeros(Vert_Density,1); %where the hoz averages will
be placed
vert_count=1;
while vert_count<=Vert_Density
hoz_values=zeros(Horz_Density,1);
%Exterior Points Corrected!!!!!!!!
hoz_values(1,1)=CM_Sensed_Velocities((vert_count-
1)*Horz_Density+1,1)*...
(m/(m+1)*(Solution_Point((vert_count-1)*Horz_Density+1,1)-
conduit_min_width)/conduit_width+...
1/(12*m)*((Solution_Point((vert_count-1)*Horz_Density+2,1)-...
Solution_Point((vert_count-1)*Horz_Density+1,1))/conduit_width)^2*...
(conduit_width/(Solution_Point((vert_count-1)*Horz_Density+1,1)-
conduit_min_width))+...
7/12*(Solution_Point((vert_count-1)*Horz_Density+2,1)-...
Solution_Point((vert_count-1)*Horz_Density+1,1))/conduit_width-...
1/12*(Solution_Point((vert_count-1)*Horz_Density+3,1)-...
Solution_Point((vert_count-1)*Horz_Density+2,1))/conduit_width);

hoz_values(Horz_Density,1)=CM_Sensed_Velocities((vert_count)*Horz_Densi
ty,1)*...
(m/(m+1)*(conduit_max_width-
Solution_Point((vert_count)*Horz_Density,1))/conduit_width+...
1/(12*m)*((Solution_Point((vert_count)*Horz_Density,1)-...
Solution_Point((vert_count)*Horz_Density-1,1))/conduit_width)^2*...
conduit_width/(conduit_max_width-
Solution_Point((vert_count)*Horz_Density,1))+...
7/12*(Solution_Point((vert_count)*Horz_Density,1)-...
Solution_Point((vert_count)*Horz_Density-1,1))/conduit_width-...
1/12*(Solution_Point((vert_count)*Horz_Density-1,1)-...
Solution_Point((vert_count)*Horz_Density-2,1))/conduit_width);

%Exterior Adjacent
hoz_values(2,1)=CM_Sensed_Velocities((vert_count-
1)*Horz_Density+2,1)*...
(1/2*(Solution_Point((vert_count-1)*Horz_Density+2,1)-...
Solution_Point((vert_count-1)*Horz_Density+1,1))/conduit_width+...
7/12*(Solution_Point((vert_count-1)*Horz_Density+3,1)-...
Solution_Point((vert_count-1)*Horz_Density+2,1))/conduit_width-...
1/12*(Solution_Point((vert_count-1)*Horz_Density+4,1)-...
Solution_Point((vert_count-1)*Horz_Density+3,1))/conduit_width);

hoz_values(Horz_Density-
1,1)=CM_Sensed_Velocities((vert_count)*Horz_Density-1,1)*...
```

```
(1/2*(Solution_Point((vert_count)*Horz_Density,1)-...
Solution_Point((vert_count)*Horz_Density-1,1))/conduit_width+...
7/12*(Solution_Point((vert_count)*Horz_Density-1,1)-...
Solution_Point((vert_count)*Horz_Density-2,1))/conduit_width-...
1/12*(Solution_Point((vert_count)*Horz_Density-2,1)-...
Solution_Point((vert_count)*Horz_Density-3,1))/conduit_width);

%Interior Points
Inside_Count=3;
while Inside_Count<=(Horz_Density-2)
hoz_values(Inside_Count,1)=CM_Sensed_Velocities((vert_count-1)*...
    Horz_Density+Inside_Count,1)*(7/12*(Solution_Point((vert_count-
1)*...
    Horz_Density+Inside_Count+1,1)-Solution_Point((vert_count-1)*...
    Horz_Density+Inside_Count,1))/conduit_width+...
    7/12*(Solution_Point((vert_count-1)*Horz_Density+Inside_Count,1)-
...
    Solution_Point((vert_count-1)*Horz_Density+Inside_Count-
1,1))/conduit_width-...
    1/12*(Solution_Point((vert_count-1)*Horz_Density+Inside_Count+2,1)-
...
    Solution_Point((vert_count-
1)*Horz_Density+Inside_Count+1,1))/conduit_width-...
    1/12*(Solution_Point((vert_count-1)*Horz_Density+Inside_Count-1,1)-
...
    Solution_Point((vert_count-1)*Horz_Density+Inside_Count-
2,1))/conduit_width);
Inside_Count=Inside_Count+1;
end
vertical_averages(vert_count,1)=sum(hoz_values);
vert_count=vert_count+1;
end

verts_values=zeros(Vert_Density,1);
%Exterior_Points
verts_values(1,1)=vertical_averages(1,1)*(m/(m+1)*(verts(1,1)-
conduit_min_height)/conduit_height+...
    1/(12*m)*((verts(2,1)-verts(1,1))/conduit_height)^2*...
    conduit_height/(verts(1,1)-conduit_min_height)+7/12*((verts(2,1)-
verts(1,1))/...
    conduit_height)-1/12*(verts(3,1)-verts(2,1))/conduit_height);

verts_values(Vert_Density,1)=vertical_averages(Vert_Density,1)*(m/(m+1)
*...
    (conduit_max_height-verts(Vert_Density,1))/conduit_height+...
    1/(12*m)*((verts(2,1)-verts(1,1))/conduit_height)^2*...
    conduit_height/(conduit_max_height-
verts(Vert_Density,1))+7/12*((verts(2,1)-verts(1,1))/...
    conduit_height)-1/12*(verts(3,1)-verts(2,1))/conduit_height);

%Exterior Adjacent
verts_values(2,1)=vertical_averages(2,1)*(1/2*(verts(2,1)-
verts(1,1))/...
```

```
    conduit_height+7/12*(verts(3,1)-verts(2,1))/conduit_height-...
    1/12*(verts(4,1)-verts(3,1))/conduit_height);

verts_values(Vert_Density-1,1)=vertical_averages(Vert_Density-1,1)*...
    (1/2*(verts(Vert_Density,1)-verts(Vert_Density-1,1))/...
    conduit_height+7/12*(verts(Vert_Density-1,1)-...
    verts(Vert_Density-2,1))/conduit_height-...
    1/12*(verts(Vert_Density-2,1)-verts(Vert_Density-
3,1))/conduit_height);

%Interior Points
Interior_Count=3;
while Interior_Count<=(Vert_Density-2)

verts_values(Interior_Count,1)=vertical_averages(Interior_Count,1)*...
    (7/12*(verts(Interior_Count+1,1)-verts(Interior_Count,1))/...
        conduit_height+7/12*(verts(Interior_Count,1)-
verts(Interior_Count-1,1))/...
        conduit_height-1/12*(verts(Interior_Count+2,1)-
verts(Interior_Count+1,1))/...
        conduit_height-1/12*(verts(Interior_Count-1,1)-
verts(Interior_Count-2,1))/...
        conduit_height);
    Interior_Count=Interior_Count+1;
end

Average_Velocity_C31A=sum(verts_values);
Recorded_Flow_Rate_C31A=abs((conduit_max_height-
conduit_min_height)*(conduit_max_width-
conduit_min_width)*Average_Velocity_C31A);
Solution_Point_a=Solution_Point;
CFD_Values_a=CFD_Values;
Solution_Matrix_C31A(verz_counts,hoz_counts)=Recorded_Flow_Rate_C31A;

%-------------------------Section for Ott C31-R-----------------------
--
CM_Sensed_Velocities=zeros(Horz_Density*Vert_Density,1); %Horizontal CM
Resolution (x direction)
oblique_angle=zeros(Horz_Density*Vert_Density,1);
for gr=1:Horz_Density*Vert_Density
    oblique_mag=(Solution_Point(gr,4)^2+Solution_Point(gr,5)^2)^(1/2);
total_mag=(Solution_Point(gr,4)^2+Solution_Point(gr,5)^2+Solution_Point
(gr,6)^2)^(1/2);
    inagle=atan(oblique_mag/Solution_Point(gr,6))*180/pi();
    oblique_angle(gr,1)=inagle;
    turb_vel=((2*Solution_Point(gr,7))^2/3)^(1/2);%<-isotropic
turbulence assumed
    axial_intensity=turb_vel/Solution_Point(gr,6);
    trans_intensity=turb_vel/oblique_mag;
    ap=ax_co(1,1)+ax_co(1,2)*axial_intensity+...
        ax_co(1,3)*turb_period+ax_co(1,4)*axial_intensity^2+...
ax_co(1,5)*axial_intensity*turb_period+ax_co(1,6)*turb_period^2+...
ax_co(1,7)*axial_intensity^3+ax_co(1,8)*axial_intensity^2*turb_period+.
```

```
..
ax_co(1,9)*axial_intensity*turb_period^2+ax_co(1,10)*turb_period^3+...
ax_co(1,11)*axial_intensity^4+ax_co(1,12)*axial_intensity^3*turb_period
+...
ax_co(1,13)*axial_intensity^2*turb_period^2+ax_co(1,14)*axial_intensity
*turb_period^3+...
        ax_co(1,15)*turb_period^4;%<-General!!
cmd=ott_r(1,9)*inagle^6+ott_r(1,10)*inagle^5+ott_r(1,11)*inagle^4+...
ott_r(1,12)*inagle^3+ott_r(1,13)*inagle^2+ott_r(1,14)*inagle^1+ott_r(1,
15);%<-Specific to Current meter
cmdt=trav_p_co(1,1)+trav_p_co(1,2)*trans_intensity+trav_p_co(1,3)*ott_r
(1,1)+...
trav_p_co(1,4)*trans_intensity^2+trav_p_co(1,5)*trans_intensity*ott_r(1
,1)+...
 Re
trav_p_co(1,6)*ott_r(1,1)^2+trav_p_co(1,7)*trans_intensity^3+...

trav_p_co(1,8)*trans_intensity^2*ott_r(1,1)+trav_p_co(1,9)*trans_intens
ity*ott_r(1,1)^2+...
        trav_p_co(1,10)*ott_r(1,1)^3;%<-Specific to Current meter
    v_rev=-ott_r(1,2)/ott_r(1,3)+...
        1/ott_r(1,3)*Solution_Point(gr,6)+...
        1/ott_r(1,3)*axial_intensity^2/2*Solution_Point(gr,6)+...
        ap-...

(ott_r(1,4)*ott_r(1,5)*ott_r(1,6))/(2*ott_r(1,8)*ott_r(1,16))*cmd*obliq
ue_mag^2/Solution_Point(gr,6)-...

(ott_r(1,4)*ott_r(1,5)*ott_r(1,6))/(4*ott_r(1,8)*ott_r(1,16))*trans_int
ensity^2*oblique_mag^2/Solution_Point(gr,6)*cmdt;
    v_v=ott_r(1,3)*v_rev+ott_r(1,2);
    Solution_Point(gr,6);

CM_Sensed_Velocities(gr,1)=v_v;%total_mag+total_mag*oblique_impact/100;
end

%CM_Sensed_Velocities=Solution_Point(:,6);
%oblique_impact_factors
%This is where the values are converted into a predicted flow rate
vertical_averages=zeros(Vert_Density,1); %where the hoz averages will
be placed
vert_count=1;
while vert_count<=Vert_Density
hoz_values=zeros(Horz_Density,1);
%Exterior Points Corrected!!!!!!!!
hoz_values(1,1)=CM_Sensed_Velocities((vert_count-
1)*Horz_Density+1,1)*...
(m/(m+1)*(Solution_Point((vert_count-1)*Horz_Density+1,1)-
conduit_min_width)/conduit_width+...
1/(12*m)*((Solution_Point((vert_count-1)*Horz_Density+2,1)-...
Solution_Point((vert_count-1)*Horz_Density+1,1))/conduit_width)^2*...
(conduit_width/(Solution_Point((vert_count-1)*Horz_Density+1,1)-
conduit_min_width))+...
7/12*(Solution_Point((vert_count-1)*Horz_Density+2,1)-...
```

```
Solution_Point((vert_count-1)*Horz_Density+1,1))/conduit_width-...
1/12*(Solution_Point((vert_count-1)*Horz_Density+3,1)-...
Solution_Point((vert_count-1)*Horz_Density+2,1))/conduit_width);

hoz_values(Horz_Density,1)=CM_Sensed_Velocities((vert_count)*Horz_Densi
ty,1)*...
(m/(m+1)*(conduit_max_width-
Solution_Point((vert_count)*Horz_Density,1))/conduit_width+...
1/(12*m)*((Solution_Point((vert_count)*Horz_Density,1)-...
Solution_Point((vert_count)*Horz_Density-1,1))/conduit_width)^2*...
conduit_width/(conduit_max_width-
Solution_Point((vert_count)*Horz_Density,1))+...
7/12*(Solution_Point((vert_count)*Horz_Density,1)-...
Solution_Point((vert_count)*Horz_Density-1,1))/conduit_width-...
1/12*(Solution_Point((vert_count)*Horz_Density-1,1)-...
Solution_Point((vert_count)*Horz_Density-2,1))/conduit_width);

%Exterior Adjacent
hoz_values(2,1)=CM_Sensed_Velocities((vert_count-
1)*Horz_Density+2,1)*...
(1/2*(Solution_Point((vert_count-1)*Horz_Density+2,1)-...
Solution_Point((vert_count-1)*Horz_Density+1,1))/conduit_width+...
7/12*(Solution_Point((vert_count-1)*Horz_Density+3,1)-...
Solution_Point((vert_count-1)*Horz_Density+2,1))/conduit_width-...
1/12*(Solution_Point((vert_count-1)*Horz_Density+4,1)-...
Solution_Point((vert_count-1)*Horz_Density+3,1))/conduit_width);

hoz_values(Horz_Density-
1,1)=CM_Sensed_Velocities((vert_count)*Horz_Density-1,1)*...
(1/2*(Solution_Point((vert_count)*Horz_Density,1)-...
Solution_Point((vert_count)*Horz_Density-1,1))/conduit_width+...
7/12*(Solution_Point((vert_count)*Horz_Density-1,1)-...
Solution_Point((vert_count)*Horz_Density-2,1))/conduit_width-...
1/12*(Solution_Point((vert_count)*Horz_Density-2,1)-...
Solution_Point((vert_count)*Horz_Density-3,1))/conduit_width);

%Interior Points
Inside_Count=3;
while Inside_Count<=(Horz_Density-2)
hoz_values(Inside_Count,1)=CM_Sensed_Velocities((vert_count-1)*...
    Horz_Density+Inside_Count,1)*(7/12*(Solution_Point((vert_count-
1)*...
    Horz_Density+Inside_Count+1,1)-Solution_Point((vert_count-1)*...
    Horz_Density+Inside_Count,1))/conduit_width+...
    7/12*(Solution_Point((vert_count-1)*Horz_Density+Inside_Count,1)-
...
    Solution_Point((vert_count-1)*Horz_Density+Inside_Count-
1,1))/conduit_width-...
    1/12*(Solution_Point((vert_count-1)*Horz_Density+Inside_Count+2,1)-
...
    Solution_Point((vert_count-
1)*Horz_Density+Inside_Count+1,1))/conduit_width-...
```

```
    1/12*(Solution_Point((vert_count-1)*Horz_Density+Inside_Count-1,1)-
...
    Solution_Point((vert_count-1)*Horz_Density+Inside_Count-
2,1))/conduit_width);
Inside_Count=Inside_Count+1;
end
vertical_averages(vert_count,1)=sum(hoz_values);
vert_count=vert_count+1;
end

verts_values=zeros(Vert_Density,1);
%Exterior_Points
verts_values(1,1)=vertical_averages(1,1)*(m/(m+1)*(verts(1,1)-
conduit_min_height)/conduit_height+...
    1/(12*m)*((verts(2,1)-verts(1,1))/conduit_height)^2*...
    conduit_height/(verts(1,1)-conduit_min_height)+7/12*((verts(2,1)-
verts(1,1))/...
    conduit_height)-1/12*(verts(3,1)-verts(2,1))/conduit_height);

verts_values(Vert_Density,1)=vertical_averages(Vert_Density,1)*(m/(m+1)
*...
    (conduit_max_height-verts(Vert_Density,1))/conduit_height+...
    1/(12*m)*((verts(2,1)-verts(1,1))/conduit_height)^2*...
    conduit_height/(conduit_max_height-
verts(Vert_Density,1))+7/12*((verts(2,1)-verts(1,1))/...
    conduit_height)-1/12*(verts(3,1)-verts(2,1))/conduit_height);

%Exterior Adjacent
verts_values(2,1)=vertical_averages(2,1)*(1/2*(verts(2,1)-
verts(1,1))/...
    conduit_height+7/12*(verts(3,1)-verts(2,1))/conduit_height-...
    1/12*(verts(4,1)-verts(3,1))/conduit_height);

verts_values(Vert_Density-1,1)=vertical_averages(Vert_Density-1,1)*...
    (1/2*(verts(Vert_Density,1)-verts(Vert_Density-1,1))/...
    conduit_height+7/12*(verts(Vert_Density-1,1)-...
    verts(Vert_Density-2,1))/conduit_height-...
    1/12*(verts(Vert_Density-2,1)-verts(Vert_Density-
3,1))/conduit_height);

%Interior Points
Interior_Count=3;
while Interior_Count<=(Vert_Density-2)

verts_values(Interior_Count,1)=vertical_averages(Interior_Count,1)*...
    (7/12*(verts(Interior_Count+1,1)-verts(Interior_Count,1))/...
        conduit_height+7/12*(verts(Interior_Count,1)-
verts(Interior_Count-1,1))/...
        conduit_height-1/12*(verts(Interior_Count+2,1)-
verts(Interior_Count+1,1))/...
        conduit_height-1/12*(verts(Interior_Count-1,1)-
verts(Interior_Count-2,1))/...
        conduit_height);
```

```
    Interior_Count=Interior_Count+1;
end
Average_Velocity_C31R=sum(verts_values);
Recorded_Flow_Rate_C31R=abs((conduit_max_height-
conduit_min_height)*(conduit_max_width-
conduit_min_width)*Average_Velocity_C31R);
Solution_Point_a=Solution_Point;
CFD_Values_a=CFD_Values;
Solution_Matrix_C31R(verz_counts,hoz_counts)=Recorded_Flow_Rate_C31R;
hoz_counts=hoz_counts+1
Horz_Density=Horz_Density+Horz_Density_Step
end
Horz_Density=Horz_Density_Initial
Vert_Density=Vert_Density+Vert_Density_Step
hoz_counts=1
verz_counts=verz_counts+1
end
Solution_Matrix_C31G
Solution_Matrix_C31P
Solution_Matrix_C31M
Solution_Matrix_C31A
Solution_Matrix_C31R
```

Appendix 3: Acoustic Time of Flight Simulation Code

```
%Mark Christian
%Note: This material was developed in support of Mark Christian's Ph.D
%thesis and should be cited as such.
%
%Approved for Public Distribution

%House Keeping
clc
clear all
close all

%---Data Import and User Definitions---
%User Definitions
p_count=20;
number_of_sensors=1;

min_number_of_sensors=1;
max_number_of_sensors=11;
recorded_velocity=zeros(max_number_of_sensors,4);
recorded_flow_rate=zeros(max_number_of_sensors,4);

rad_influ1=.3;
%rad_influ2=.5;
idw_power=2;

%CFD Data
%.csv files
%
CFDfilename = '368CMS-SST-ALR-B.csv';
CFD_Data= csvread(CFDfilename,2,0);
size_subset=size(CFD_Data);
sz_CFD=size_subset(1,1);
%CFD Data Rearangement from u v w k x y z to x y z u v w k
ucfddata=CFD_Data(:,1);
vcfddata=CFD_Data(:,2);
wcfddata=CFD_Data(:,3);
kcfddata=CFD_Data(:,4);
xcfddata=CFD_Data(:,5);
ycfddata=CFD_Data(:,6);
zcfddata=CFD_Data(:,7);
CFD_Data=[xcfddata,ycfddata,zcfddata,ucfddata,vcfddata,wcfddata,kcfddat
a];
%
%.xlsx files
%{
CFDfilename =  'CFD_Sample_0.3m_tolerance.xlsx';
CFD_Data= xlsread(CFDfilename);
size_subset=size(CFD_Data);
sz_CFD=size_subset(1,1);
%}

%bay_shift=0;
```

```
%Cartisian Locations of ATF "Pole" Corners

%Bay A
%{
bay_shift_factor=0;
Point_1=
[8.6614+bay_shift_factor*8.61095139077517,1.197629647,40.1388707614736]
; %[close_x, bottom_y, upstream_z][8.7465442,1.8368414,36.7653368]
Point_2=
[8.6614+bay_shift_factor*8.61095139077517,17.93812355,40.1388707614736]
; %[close_x, top_y, upstream_z][8.7465442,19.521086,36.7653368]
Point_3=
[15.19555+bay_shift_factor*8.61095139077517,1.197629647,40.138870761473
6]; %[far_x, bottom_y, upstream_z][15.078,1.8368414,36.7653368]
Point_4=
[15.19555+bay_shift_factor*8.61095139077517,17.93812355,40.138870761473
6]; %[far_x, top_y, upstream_z][15.078,19.521086,36.7653368]

Point_5=
[8.6614+bay_shift_factor*8.61095139077517,0.544618,43.9309814761033];
%[close_x, bottom_y, downstream_z]
Point_6=
[8.6614+bay_shift_factor*8.61095139077517,16.1747,43.9309814761033];
%[close_x, top_y, downstream_z]
Point_7=
[15.19555+bay_shift_factor*8.61095139077517,0.544618,43.9309814761033];
%[far_x, bottom_y, downstream_z]
Point_8=
[15.19555+bay_shift_factor*8.61095139077517,16.1747,43.9309814761033];
%[far_x, top_y, downstream_z]
%}

%Bay B
%
bay_shift_factor=0;
Point_1= [17.27235222,1.197629647,40.1388707614736]; %[close_x,
bottom_y, upstream_z][8.7465442,1.8368414,36.7653368]
Point_2= [17.27235222,17.93812355,40.1388707614736]; %[close_x, top_y,
upstream_z][8.7465442,19.521086,36.7653368]
Point_3= [23.59659958,1.197629647,40.1388707614736]; %[far_x, bottom_y,
upstream_z][15.078,1.8368414,36.7653368]
Point_4= [23.59659958,17.93812355,40.1388707614736]; %[far_x, top_y,
upstream_z][15.078,19.521086,36.7653368]

Point_5= [17.27235222,0.544618,43.9309814761033]; %[close_x, bottom_y,
downstream_z]
Point_6= [17.27235222,16.1747,43.9309814761033]; %[close_x, top_y,
downstream_z]
Point_7= [23.59659958,0.544618,43.9309814761033]; %[far_x, bottom_y,
downstream_z]
Point_8= [23.59659958,16.1747,43.9309814761033]; %[far_x, top_y,
downstream_z]
%}
```

```
%Bay C
%{
bay_shift_factor=0;
Point_1= [25.730199813842773,1.197629647,40.1388707614736]; %[close_x,
bottom_y, upstream_z][8.7465442,1.8368414,36.7653368]
Point_2= [25.730199813842773,17.93812355,40.1388707614736]; %[close_x,
top_y, upstream_z][8.7465442,19.521086,36.7653368]
Point_3= [32.13100051879883,1.197629647,40.1388707614736]; %[far_x,
bottom_y, upstream_z][15.078,1.8368414,36.7653368]
Point_4= [32.13100051879883,17.93812355,40.1388707614736]; %[far_x,
top_y, upstream_z][15.078,19.521086,36.7653368]

Point_5= [25.730199813842773,0.544618,43.9309814761033]; %[close_x,
bottom_y, downstream_z]
Point_6= [25.730199813842773,16.1747,43.9309814761033]; %[close_x,
top_y, downstream_z]
Point_7= [32.13100051879883,0.544618,43.9309814761033]; %[far_x,
bottom_y, downstream_z]
Point_8= [32.13100051879883,16.1747,43.9309814761033]; %[far_x, top_y,
downstream_z]
%}

number_of_sensors=min_number_of_sensors;

while number_of_sensors<=max_number_of_sensors;

%}
Point_Compilation=[Point_1;Point_2;Point_3;...
    Point_4;Point_5;Point_6;Point_7;Point_8];

%---Determining the location of the sensors---
%Abisccia and Weights of the Gauss Quaterature
filename =  'Gaussian_Quadrature';
wghts_absica = xlsread(filename);
wght_absica_start=sum(2:number_of_sensors-1)+1;
wght_absica_end=sum(2:number_of_sensors);
gauss_wghts=wghts_absica(wght_absica_start:wght_absica_end,2);
gauss_abissica=wghts_absica(wght_absica_start:wght_absica_end,3);
gauss_abissica=sort(gauss_abissica,'descend');
odd_even_test=mod(number_of_sensors,2);
weight_holder=zeros(number_of_sensors,1);
if odd_even_test == 0 %then even
    i=1;
    placeholder=sort(gauss_wghts,'descend');
    while i<=(number_of_sensors)/2
        value_extract=placeholder(i*2);
        weight_holder((number_of_sensors)/2+1-i,1)=value_extract;
        weight_holder((number_of_sensors)/2+i,1)=value_extract;

    i=i+1;
    end

elseif number_of_sensors==1;
```

```
    gauss_abissica=0;
    weight_holder=2;
else %then odd
    placeholder=sort(gauss_wghts,'descend');
    weight_holder((number_of_sensors-1)/2+1,1)=placeholder(1,1);
    i=1;
    while i<=(number_of_sensors-1)/2
        value_extract=placeholder(1+i*2);
        weight_holder((number_of_sensors-1)/2+1-i,1)=value_extract;
        weight_holder((number_of_sensors-1)/2+1+i,1)=value_extract;
    i=i+1;
    end
end

%Graphing of Pole Vertexes
%
scatter3(Point_Compilation(:,1),Point_Compilation(:,3),Point_Compilatio
n(:,2),'*')
xlabel('Conduit Width (x value)')
ylabel('Conduit Lenght (z value)')
zlabel('Conduit Height (y value)')
title('Acoustic Sensor Model')
hold on
%}
%Determine Pole Distance
i=1;
j=1;
pole_sensor_locations=zeros(number_of_sensors*4,3);
while i<=8
    pole_distance_x=(Point_Compilation(i+1,1)-Point_Compilation(i,1));
    pole_distance_y=(Point_Compilation(i+1,2)-Point_Compilation(i,2));
    pole_distance_z=(Point_Compilation(i+1,3)-Point_Compilation(i,3));
pole_sensor_x_locations=gauss_abissica*pole_distance_x/2+pole_distance_
x/2+Point_Compilation(i,1);
pole_sensor_y_locations=gauss_abissica*pole_distance_y/2+pole_distance_
y/2+Point_Compilation(i,2);
pole_sensor_z_locations=gauss_abissica*pole_distance_z/2+pole_distance_
z/2+Point_Compilation(i,3);
    pole_sensor_locations((j-
1)*number_of_sensors+1:j*number_of_sensors,:)=[pole_sensor_x_locations,
pole_sensor_y_locations, pole_sensor_z_locations];
    i=i+2;
    j=j+1;
end
%scatter3(pole_sensor_locations(:,1),pole_sensor_locations(:,3),pole_se
nsor_locations(:,2),'.','y')

%Determine the calculation points along the acoustic paths
i=1;
acoustic_path_locations=zeros(p_count*number_of_sensors*2,3);
while i<=number_of_sensors
x_a_path_spacing=linspace(pole_sensor_locations(i+3*number_of_sensors,1
),pole_sensor_locations(i,1),p_count);
```

```
y_a_path_spacing=linspace(pole_sensor_locations(i+3*number_of_sensors,2
),pole_sensor_locations(i,2),p_count);
z_a_path_spacing=linspace(pole_sensor_locations(i+3*number_of_sensors,3
),pole_sensor_locations(i,3),p_count);
acoustic_path_locations((i-
1)*p_count+1:i*p_count,:)=[x_a_path_spacing.', y_a_path_spacing.',
z_a_path_spacing.'];
x_a_path_spacing=linspace(pole_sensor_locations(i+2*number_of_sensors,1
),pole_sensor_locations(i+number_of_sensors,1),p_count);
y_a_path_spacing=linspace(pole_sensor_locations(i+2*number_of_sensors,2
),pole_sensor_locations(i+number_of_sensors,2),p_count);
z_a_path_spacing=linspace(pole_sensor_locations(i+2*number_of_sensors,3
),pole_sensor_locations(i+number_of_sensors,3),p_count);
acoustic_path_locations((i-
1)*p_count+number_of_sensors*p_count+1:i*p_count+number_of_sensors*p_co
unt,:)=[x_a_path_spacing.', y_a_path_spacing.', z_a_path_spacing.'];
i=i+1;
end
%scatter3(acoustic_path_locations(:,1),acoustic_path_locations(:,3),aco
ustic_path_locations(:,2),'.')
%scatter3(CFD_Data(:,1),CFD_Data(:,3),CFD_Data(:,2),'.')

%Calculate Velocities at Acoustic Path Subsections
%for other models simply pull delete everything under here
calculated_values=zeros(p_count*number_of_sensors,7);
i=1; %steps through the acoustic path locations
number_of_influnece_points=zeros(p_count*number_of_sensors,1);
while i<=p_count*number_of_sensors*2
j=1; %steps through the points in the CFD_Data
fillpoints=zeros(1,9);
    fillcount=1;
    no_distance_test=0;
    while j<= sz_CFD
        distance_to_point=((acoustic_path_locations(i,1)-
CFD_Data(j,1))^2+...
        (acoustic_path_locations(i,2)-CFD_Data(j,2))^2+...
        (acoustic_path_locations(i,3)-CFD_Data(j,3))^2)^(1/2);
            if distance_to_point<=rad_influ1
                if distance_to_point == 0
                   hold_point=j;
                   no_distance_test=1;
                end
                fillpoints(fillcount,2:9)=[distance_to_point,
CFD_Data(j,:)];
                fillcount=fillcount+1;
            end
        j=j+1;
    end
    if fillcount==1
        fprintf('ERROR ERROR ERROR----NO POINT IN ROI\n')
        break
    end
    if no_distance_test == 1
        calculated_values(i,:)=CFD_Data(hold_point,:);
```

```
    else
    fillpoints(:,1)=1./(fillpoints(:,2).^idw_power);
    Point_u=sum(fillpoints(:,1).*fillpoints(:,6))/sum(fillpoints(:,1));
    Point_v=sum(fillpoints(:,1).*fillpoints(:,7))/sum(fillpoints(:,1));
    Point_w=sum(fillpoints(:,1).*fillpoints(:,8))/sum(fillpoints(:,1));
    Point_k=sum(fillpoints(:,1).*fillpoints(:,9))/sum(fillpoints(:,1));
    calculated_values(i,:)=[acoustic_path_locations(i,:), Point_u,...
        Point_v, Point_w, Point_k];
    end
    number_of_influnece_points(i,1)=fillcount-1;
    i=i+1;
end
%Modify Caculated for Zeros at Walls
i=1;
acoustic_distance=zeros(number_of_sensors*2,1);
cartizian_shift_angle=zeros(number_of_sensors*2,5);
while i<= number_of_sensors*2
    calculated_values((i-1)*p_count+1,4:7)=[0,0,0,0];
    calculated_values(i*p_count,4:7)=[0,0,0,0];
    acoustic_distance(i,1)=((calculated_values(i*p_count,1)-
calculated_values((i-1)*p_count+1,1))^2+...
        (calculated_values(i*p_count,2)-calculated_values((i-
1)*p_count+1,2))^2+...
        (calculated_values(i*p_count,3)-calculated_values((i-
1)*p_count+1,3))^2)^(1/2);
    cartizian_shift_angle(i,1:4)=[calculated_values(i*p_count,2),...
        calculated_values(i*p_count,3), calculated_values((i-
1)*p_count+1,2),...
        calculated_values((i-1)*p_count+1,3)];
    i=i+1;
end
cartizian_shift_angle(:,5)=tan((cartizian_shift_angle(:,3)-
cartizian_shift_angle(:,1))./...
    (cartizian_shift_angle(:,4)-cartizian_shift_angle(:,2)));
%quiver3(calculated_values(:,1),calculated_values(:,3),...
%    calculated_values(:,2),calculated_values(:,5),...
%    calculated_values(:,6),calculated_values(:,4))
%hold off
%Simulate the measured transect velocities
i=1; %Counts through the acoustic sensors
mean_transect_characteristics=zeros(number_of_sensors*2,4);
while i <= number_of_sensors*2
    j=1;
    holding_values=zeros(1,4);
    while j<=p_count-1
        distance=((calculated_values((i-1)*p_count+j+1,1)-
calculated_values((i-1)*p_count+j,1))^2+...
        (calculated_values((i-1)*p_count+j+1,2)-calculated_values((i-
1)*p_count+j,2))^2+...
        (calculated_values((i-1)*p_count+j+1,3)-calculated_values((i-
1)*p_count+j,3))^2)^(1/2);
        u_intermidate=(calculated_values((i-
1)*p_count+j,4)+(calculated_values((i-1)*p_count+j+1,4)-
calculated_values((i-1)*p_count+j,4)))*distance;
```

```
        v_intermidate=(calculated_values((i-
1)*p_count+j,5)+(calculated_values((i-1)*p_count+j+1,5)-
calculated_values((i-1)*p_count+j,5)))*distance;
        w_intermidate=(calculated_values((i-
1)*p_count+j,6)+(calculated_values((i-1)*p_count+j+1,6)-
calculated_values((i-1)*p_count+j,6)))*distance;
        k_intermidate=(calculated_values((i-
1)*p_count+j,7)+(calculated_values((i-1)*p_count+j+1,7)-
calculated_values((i-1)*p_count+j,7)))*distance;
        holding_values(1,1)=holding_values(1,1)+u_intermidate;
        holding_values(1,2)=holding_values(1,2)+v_intermidate;
        holding_values(1,3)=holding_values(1,3)+w_intermidate;
        holding_values(1,4)=holding_values(1,4)+k_intermidate;
        j=j+1;
    end

mean_transect_characteristics(i,1:4)=[holding_values(1,1)/acoustic_dist
ance(i,1),...

holding_values(1,2)/acoustic_distance(i,1),holding_values(1,3)/acoustic
_distance(i,1),...
        holding_values(1,4)/acoustic_distance(i,1)];
    i=i+1;
end
mean_transect_characteristics
assumed_u=1;
assumed_v=2;
assumed_w=3;
existing_angle_fluid=tan(mean_transect_characteristics(:,assumed_v)./me
an_transect_characteristics(:,assumed_w));
cartizian_shift_angle(:,5);
existing_magnitude_fluid=(mean_transect_characteristics(:,assumed_v).^2
+mean_transect_characteristics(:,assumed_w).^2).^(1/2);
modified_angle_fluid=existing_angle_fluid-cartizian_shift_angle(:,5);
new_v=sin(modified_angle_fluid(:,1)).*existing_magnitude_fluid;
new_w=cos(modified_angle_fluid(:,1)).*existing_magnitude_fluid;
modified_mean_transect_characteristics=[mean_transect_characteristics(:
,assumed_u),...
    new_v,new_w,mean_transect_characteristics(:,4)];

%Note:modified _mean_transect_characteristic(x and w)

%Path Lenght
i=1;
path_lenght_left_right=zeros(number_of_sensors,1);
path_lenght_right_left=zeros(number_of_sensors,1);
while i<= number_of_sensors
path_lenght_left_right(i,1)=((pole_sensor_locations(3*number_of_sensors
+i,1)-pole_sensor_locations(i,1))^2+...

(pole_sensor_locations(3*number_of_sensors+i,2)-
pole_sensor_locations(i,2))^2+...
```

```
(pole_sensor_locations(3*number_of_sensors+i,3)-
pole_sensor_locations(i,3))^2)^(1/2);
path_lenght_right_left(i,1)=((pole_sensor_locations(2*number_of_sensors
+i,1)-pole_sensor_locations(number_of_sensors+i,1))^2+...

(pole_sensor_locations(2*number_of_sensors+i,2)-
pole_sensor_locations(number_of_sensors+i,2))^2+...

(pole_sensor_locations(2*number_of_sensors+i,3)-
pole_sensor_locations(number_of_sensors+i,3))^2)^(1/2);
i=i+1;
end

%Path_Width and angles
path_width=zeros(number_of_sensors,1);
path_theta_left_right=zeros(number_of_sensors,1);
path_theta_right_left=zeros(number_of_sensors,1);
path_phi_left_right=zeros(number_of_sensors,1);
path_phi_right_left=zeros(number_of_sensors,1);
i=1;
while i<= number_of_sensors
    path_width(i,1)=abs(pole_sensor_locations(number_of_sensors+i,1)-
pole_sensor_locations(i,1));

path_theta_left_right(i,1)=acos(path_width(i,1)/path_lenght_left_right(
i,1));

path_theta_right_left(i,1)=acos(path_width(i,1)/path_lenght_right_left(
i,1));
    path_phi_left_right(i,1)=pi()/2-path_theta_left_right(i,1);
    path_phi_right_left(i,1)=pi()/2-path_theta_right_left(i,1);
    i=i+1;
end

%Axial Impacts
timing_left_right=zeros(number_of_sensors,1);
timing_right_left=zeros(number_of_sensors,1);
axial_impact_measured_left_right=zeros(number_of_sensors,1);
axial_impact_measured_right_left=zeros(number_of_sensors,1);
technically_removed_axial_impact=zeros(number_of_sensors,1);
i=1;
while i<= number_of_sensors
axial_impact_measured_left_right(i,1)=(modified_mean_transect_character
istics(i,1)*...
cos(path_theta_left_right(i,1))+modified_mean_transect_characteristics(
i,3)*...
        cos(path_phi_left_right(i,1)))/cos(path_phi_left_right(i,1));
axial_impact_measured_right_left(i,1)=(modified_mean_transect_character
istics(number_of_sensors+i,1)*...
cos(path_theta_right_left(i,1))+modified_mean_transect_characteristics(
number_of_sensors+i,3)*...
        cos(path_phi_right_left(i,1)))/cos(path_phi_right_left(i,1));
```

```
technically_removed_axial_impact(i,1)=(axial_impact_measured_left_right
(i,1)+axial_impact_measured_right_left(i,1))/2;
i=i+1;
end
%Measured Velocities
technically_removed_axial_impact;
axial_impact_measured_left_right;
axial_impact_measured_right_left;

%Flow Rate Measured Section
Average_Height=((((Point_Compilation(2,2)-Point_Compilation(1,2))+...
    (Point_Compilation(6,2)-Point_Compilation(5,2)))/2)+...
    (((Point_Compilation(4,2)-Point_Compilation(3,2))+...
    (Point_Compilation(8,2)-Point_Compilation(7,2)))/2))/2;
technically_removed_axial_impact_flow_rate=Average_Height/2*...
    sum(technically_removed_axial_impact.*weight_holder.*...
    ((path_lenght_left_right+path_lenght_right_left)./2).*...
    sin((path_phi_right_left+path_phi_left_right)./2));
axial_impact_measured_left_right=Average_Height/2*...
    sum(axial_impact_measured_left_right.*weight_holder.*...
    path_lenght_left_right.*sin((path_phi_right_left)));
axial_impact_measured_right_left=Average_Height/2*...
    sum(axial_impact_measured_right_left.*weight_holder.*...
    path_lenght_right_left.*sin((path_phi_left_right)));

%Demonstrate the number of influence points
%
figure
histogram(number_of_influnece_points)
xlabel('Number of Influence Points')
ylabel('Number of Points Influenced')
title('Influence Point Histogram')
%}
%recorded_velocity(number_of_sensors,:)=[number_of_sensors,technically_
removed_axial_impact,axial_impact_measured_left_right,axial_impact_meas
ured_right_left];
recorded_flow_rate(number_of_sensors,:)=[number_of_sensors,technically_
removed_axial_impact_flow_rate,axial_impact_measured_left_right,axial_i
mpact_measured_right_left];
number_of_sensors=number_of_sensors+1
end
recorded_flow_rate
```

Appendix 4: Opportunity Cost Code

```
%Mark Christian
%Note: This material was developed in support of Mark Christian's Ph.D
%thesis and should be cited as such.
%
%Approved for Public Distribution
%This is the code designed to determine the value of current meters

%House Keeping
clc
clear all
close all


%data readin
pricefilename = 'Power_Price.csv';
price_data= csvread(pricefilename,2,0);
size_subset=size(price_data);
sz_price=size_subset(1,1);

production_filename = 'Power_produced.csv';
production_data= csvread(production_filename,2,0);
size_subset=size(production_data);
sz_production=size_subset(1,1);

cm_static_eff_filename = 'trans_cm_eff.csv';
cm_static_eff_data= csvread(cm_static_eff_filename,2,0);
size_subset=size(cm_static_eff_data);
sz_cm_static_eff=size_subset(1,1);

%Constants
density=999;
grav=9.81;
head=30.4;
min_power=62;
num_sensor_alt=31;
%Water Consumed by the optimal unit dispach
Ideal_Assign_Cars=zeros(sz_cm_static_eff,3);
Ideal_Assign_Cars(:,1:2)=cm_static_eff_data(:,1:2);
for i=1:sz_cm_static_eff
Ideal_Assign_Cars(i,3)=(Ideal_Assign_Cars(i,1)*1000000)/(head*Ideal_Ass
ign_Cars(i,2)*density*grav);
end
Ideal_Assign_Cars;

%Analyzing the amount of power that could be produced each day
%column 1 volume of water column two
day_count=0;

sum_daily_flow=zeros(366,num_sensor_alt);
sum_daily_power=zeros(366,num_sensor_alt);
sum_daily_revenue_high=zeros(366,num_sensor_alt);
```

```
sum_daily_revenue_mid=zeros(366,num_sensor_alt);
sum_daily_revenue_low=zeros(366,num_sensor_alt);
%day_count=83
for day_count=0:363
power_value=price_data(day_count+1,:)
i=1; %This is one hour
daily_eff=zeros(24,num_sensor_alt);
daily_flow_sensed=zeros(24,num_sensor_alt);
daily_power_opertunity=zeros(24,num_sensor_alt);
%i=1;
for i=1:24
hourly_eff=zeros(1,num_sensor_alt);
hourly_flow_sensed=zeros(1,num_sensor_alt);
hourly_power_opertunity=zeros(1,num_sensor_alt);

 power_hour=production_data(i+day_count,1);
 if power_hour<=min_power
hourly_eff=zeros(1,num_sensor_alt);
hourly_flow_sensed=zeros(1,num_sensor_alt);
hourly_power_opertunity=zeros(1,num_sensor_alt);
 else
 %cycle to determine optimal efficiency
    %lower_braket
    starter_lower=0;
    j=1;
    while j<sz_cm_static_eff
    %while starter_lower <=power_hour
        %cm_static_eff_data(j,1)
       if cm_static_eff_data(j,1)<=power_hour
           starter_lower=cm_static_eff_data(j,1);
       end
    %end
    j=j+1;
    end
    %upper_braket
    starter_upper=99999999;
    k=1;
    while k<sz_cm_static_eff
    %while starter_lower <=power_hour
        %cm_static_eff_data(j,1)
       if power_hour <=cm_static_eff_data(sz_cm_static_eff-k+1,1)
           starter_upper=cm_static_eff_data(sz_cm_static_eff-k+1,1);
       end
    %end
    k=k+1;
    end


 f=1; %this value steps through the range of current meters
 for f=2:num_sensor_alt+1
     if starter_upper==starter_lower
     hourly_eff(1,f-1)=cm_static_eff_data(starter_lower-min_power+1,f);
     else
    hourly_eff(1,f-1)=cm_static_eff_data(starter_upper-min_power,f)-...
```

```
        (cm_static_eff_data(starter_upper-min_power,f)-
cm_static_eff_data(starter_lower-min_power,f))/...
        (cm_static_eff_data(starter_upper-min_power,1)-
cm_static_eff_data(starter_lower-min_power,1))*...
        (cm_static_eff_data(starter_upper-min_power,1)-power_hour);
     end

    hourly_flow_sensed(1,f-
1)=(power_hour*1000000)/(head*grav*density*hourly_eff(1,f-1));

    flow_starter_lower=0;
    flow_j=1;
    established_lower=1;
    while flow_j<sz_cm_static_eff
    %while starter_lower <=power_hour
        %cm_static_eff_data(j,1)
       if Ideal_Assign_Cars(flow_j,3)<=hourly_flow_sensed(1,f-1)
           flow_starter_lower=Ideal_Assign_Cars(flow_j,3);
           established_lower=established_lower+1;
       end
    %end
    flow_j=flow_j+i;
    end
    %upper_braket
    flow_starter_upper=99999999;
    flow_k=1;
    established_upper=1;
    while flow_k<sz_cm_static_eff
    %while starter_lower <=power_hour
        %cm_static_eff_data(j,1)
       if hourly_flow_sensed(1,f-1)
<=Ideal_Assign_Cars(sz_cm_static_eff-flow_k+1,3)
           flow_starter_upper=Ideal_Assign_Cars(sz_cm_static_eff-
flow_k+1,3);
           established_upper=established_upper+1;
       end
    %end
    flow_k=flow_k+1;
    end
    real_flow_lower=established_lower-1;
    real_flow_upper=sz_cm_static_eff-established_upper+2;

    if real_flow_upper==real_flow_lower
       hourly_power_opertunity(1,f-
1)=Ideal_Assign_Cars(real_flow_upper,1);
    else
        hourly_power_opertunity(1,f-
1)=Ideal_Assign_Cars(real_flow_upper,1)-...
        (Ideal_Assign_Cars(real_flow_upper,1)-
Ideal_Assign_Cars(real_flow_lower,1))/...
        (Ideal_Assign_Cars(real_flow_upper,3)-
Ideal_Assign_Cars(real_flow_lower,3))*...
        (Ideal_Assign_Cars(real_flow_upper,3)-hourly_flow_sensed(1,f-
1));
```

```
    end
 end
 end
daily_eff(i,:)=hourly_eff;
daily_flow_sensed(i,:)=hourly_flow_sensed;
hourlywatervolume=(60*60*24).*daily_flow_sensed;
daily_power_opertunity(i,:)=hourly_power_opertunity;
i=i+1;
end
sum_daily_flow(day_count+1,:)=sum(hourlywatervolume,1); %daily measured
volume of water passing through the powerhouse
sum_daily_power(day_count+1,:)=sum(daily_power_opertunity,1); %if the
recorded amount of water was used to produce power
sum_daily_revenue_high(day_count+1,:)=power_value(1,1).*sum(daily_power
_opertunity,1); %$ value of recorded
sum_daily_revenue_mid(day_count+1,:)=power_value(1,2).*sum(daily_power_
opertunity,1);
sum_daily_revenue_low(day_count+1,:)=power_value(1,3).*sum(daily_power_
opertunity,1);
end


high_op_cost=zeros(364,num_sensor_alt-1);
for height=1:364
for width=1:num_sensor_alt-1
high_op_cost(height,width)=sum_daily_revenue_high(height,width+1)-
sum_daily_revenue_high(height,1);
end
end

mid_op_cost=zeros(364,num_sensor_alt-1);
for height=1:364
for width=1:num_sensor_alt-1
mid_op_cost(height,width)=sum_daily_revenue_mid(height,width+1)-
sum_daily_revenue_mid(height,1);
end
end

low_op_cost=zeros(364,num_sensor_alt-1);
for height=1:364
for width=1:num_sensor_alt-1
low_op_cost(height,width)=sum_daily_revenue_low(height,width+1)-
sum_daily_revenue_low(height,1);
end
end
```

Appendix 5: Chapter 1 Figures and Tables

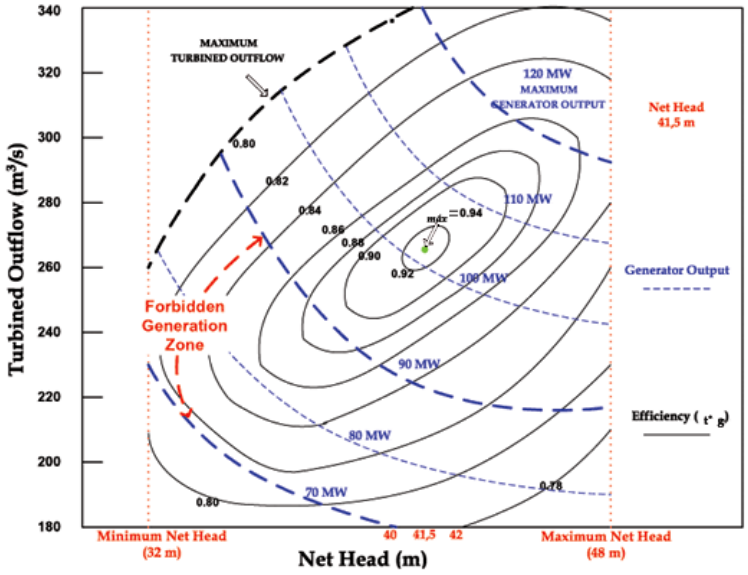

Figure 1.1: Hill Diagram

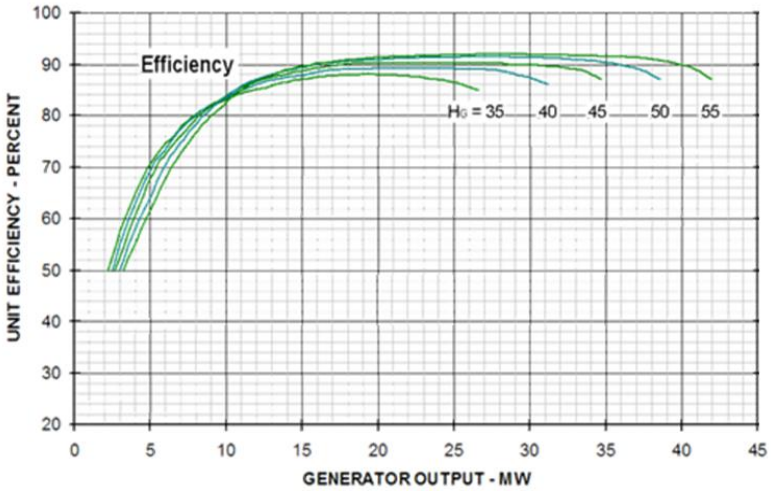

Figure 1.2: Unit Characteristic Curve

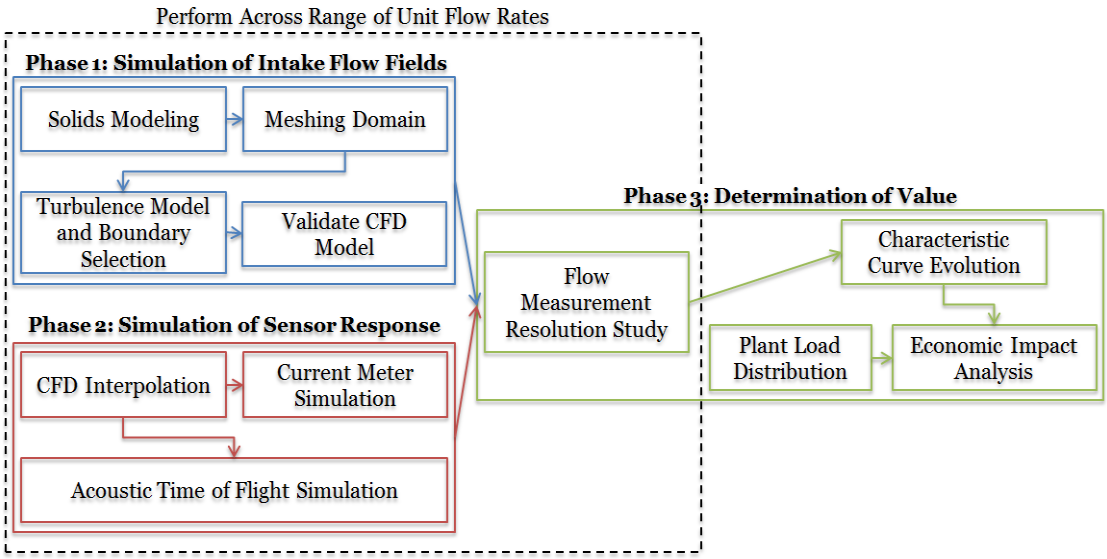

Figure 1.3: Research Work Structure

Appendix 6: Chapter 2 Figures and Tables

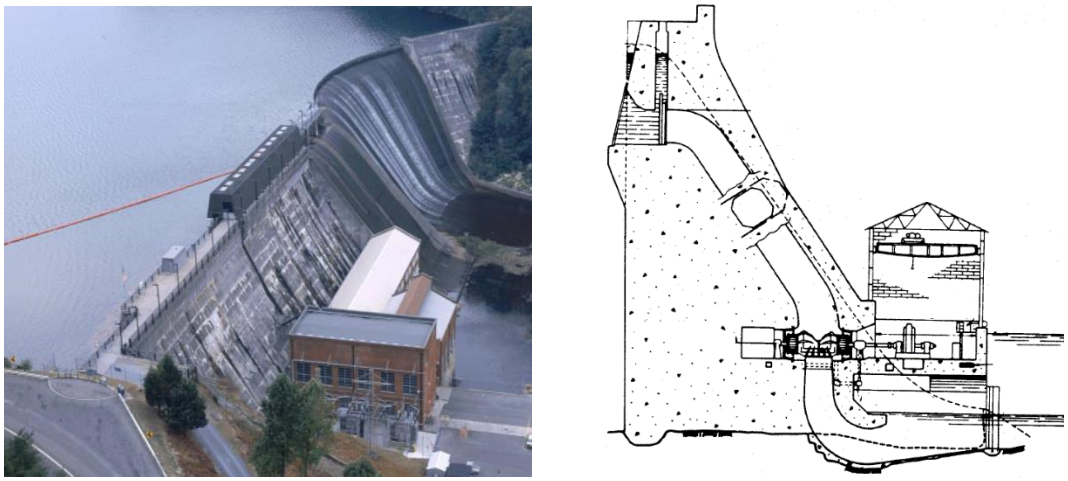

Figure 2.1: Storage Hydroplant

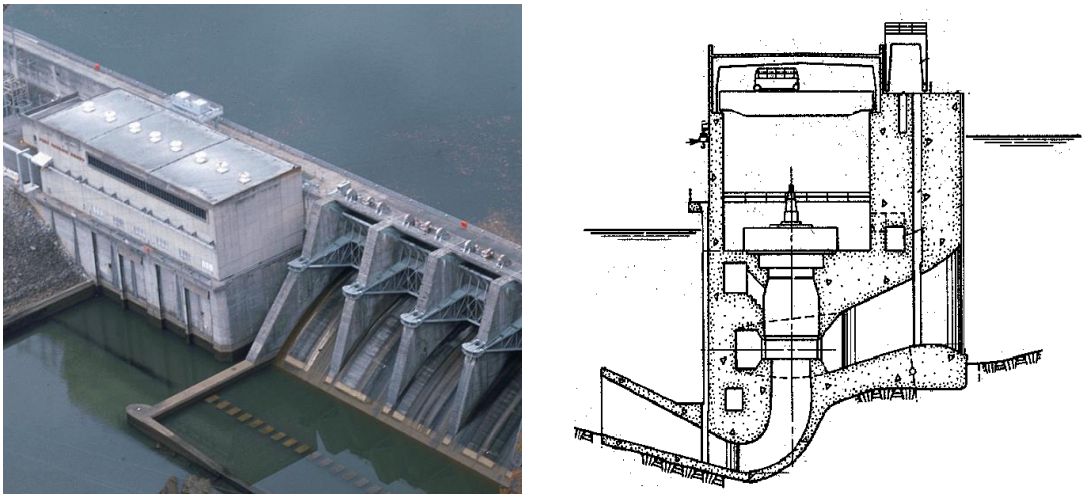

Figure 2.2: Mainstem Hydroplant

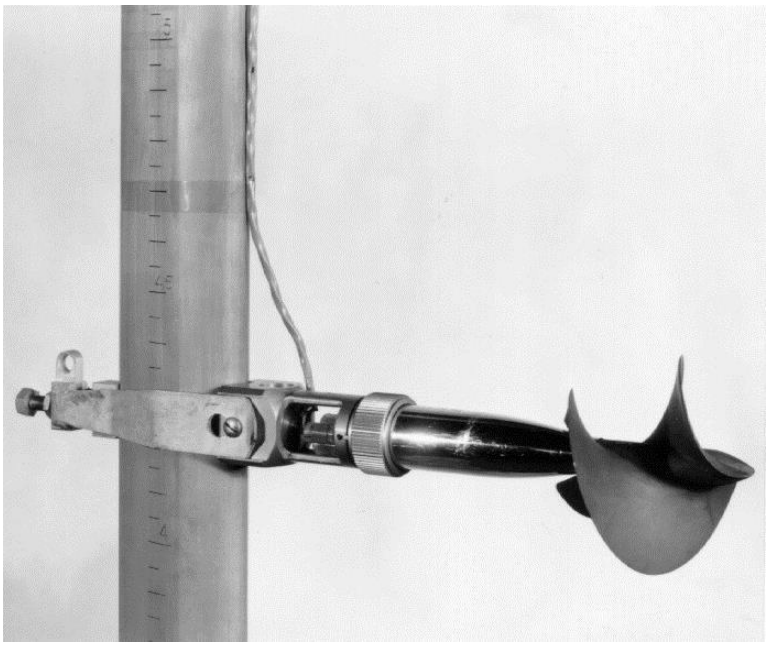

Figure 2.3: Current Meter

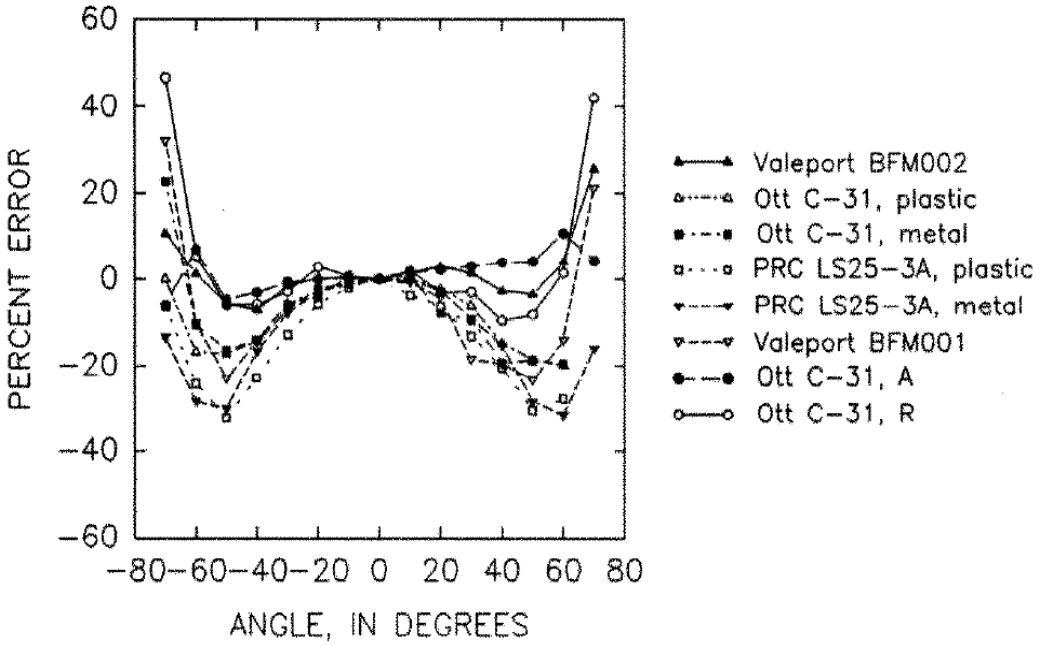

Figure 2.4: Current Meter Transverse Flow Response

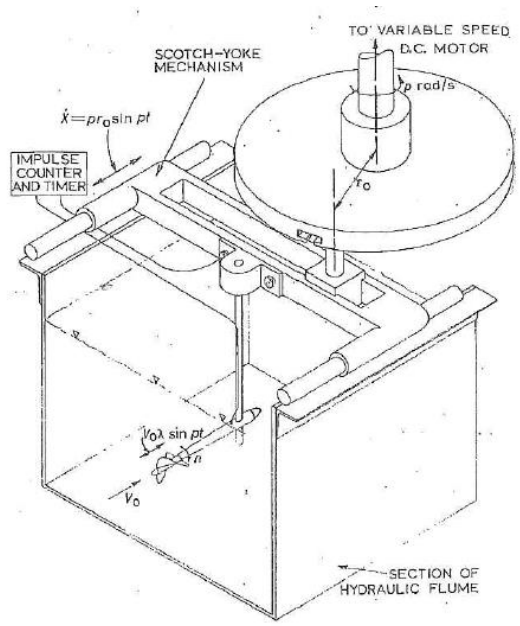

Figure 2.5: Turbulent Flow Scotch Yoke

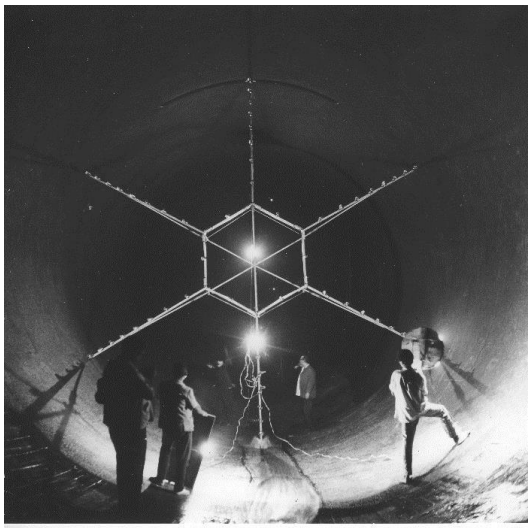

Figure 2.6: Current Meter Static Mounting

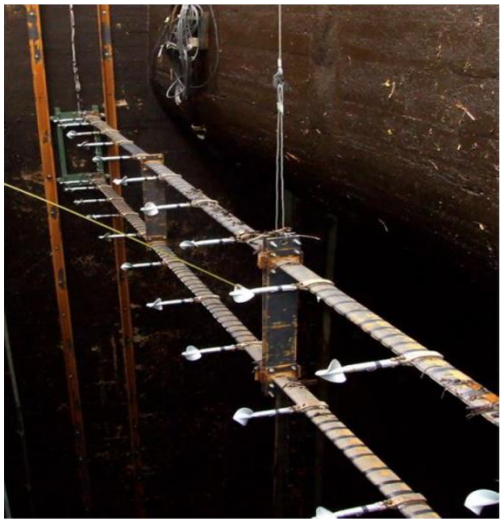

Figure 2.7: Dynamic Current Meter Mounting

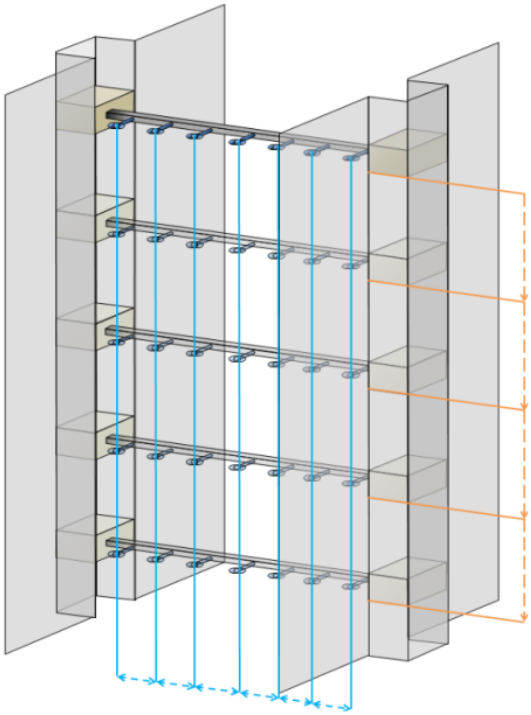

Figure 2.8: Dynamic Current Meter Operation

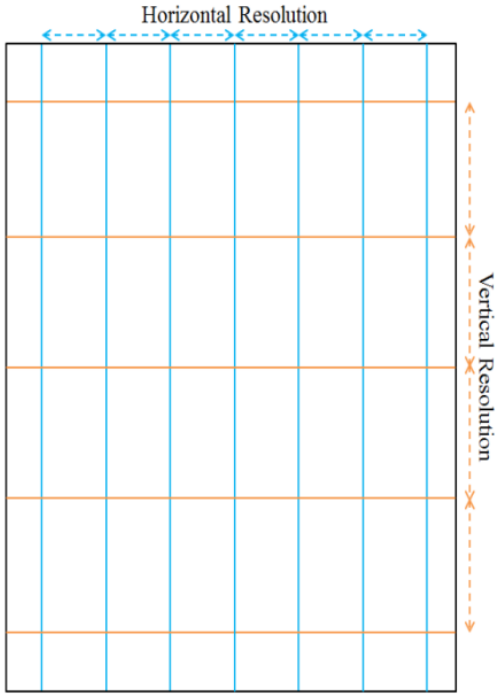

Figure 2.9: Dynamic Current Meter Resulting Vertical and Horizontal Resolution

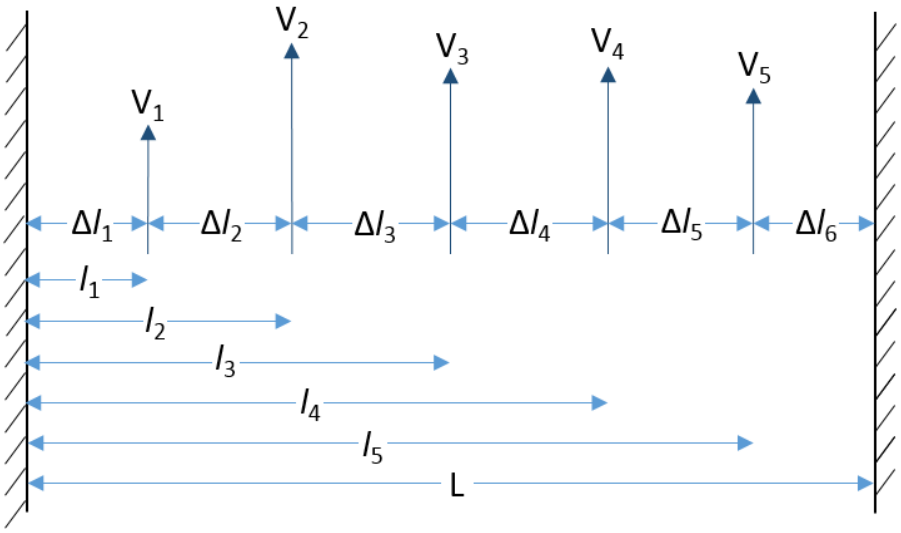

Figure 2.10: Current Meter Layout and Dimensions



Figure 2.11: Acoustic Time of Flight Transducer

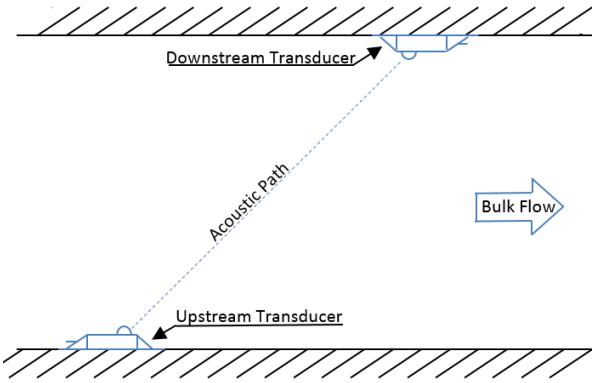

Figure 2.12: Single Path Acoustic Time of Flight Layout

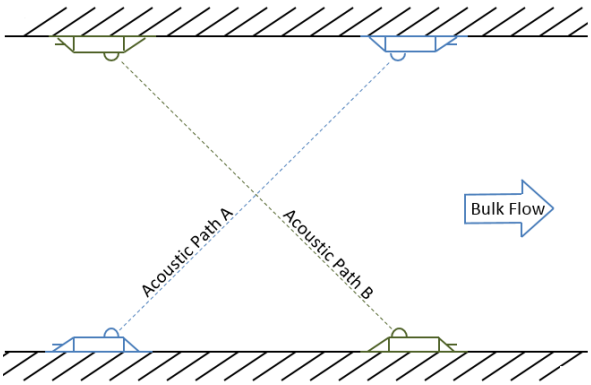

Figure 2.12: Dual Path Acoustic Time of Flight Layout

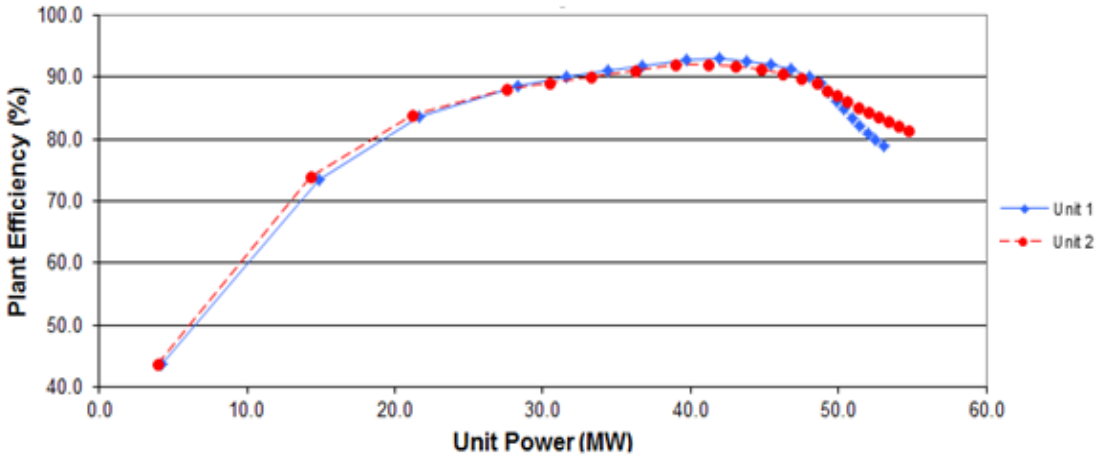

Figure 2.13: Unit Efficiency Curves

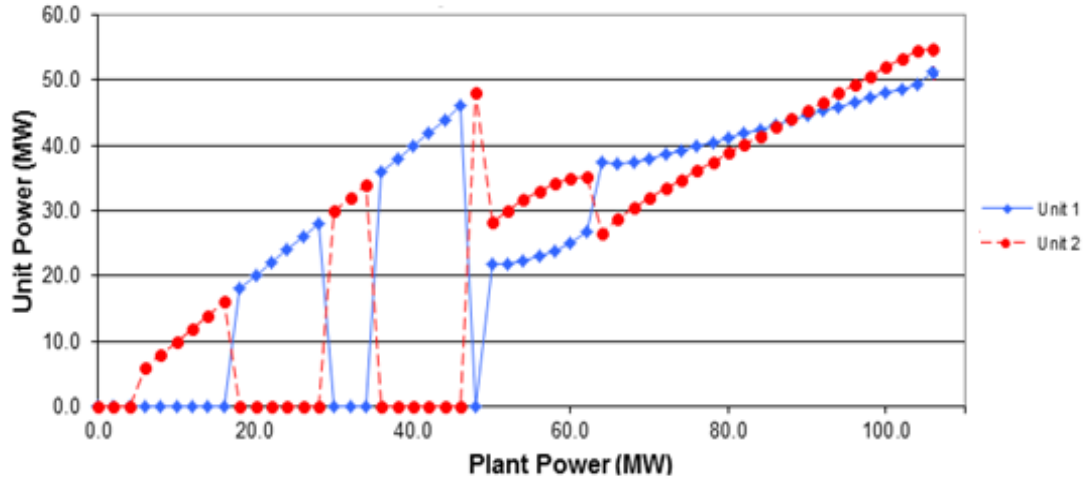

Figure 2.14: Optimized Unit Dispatch

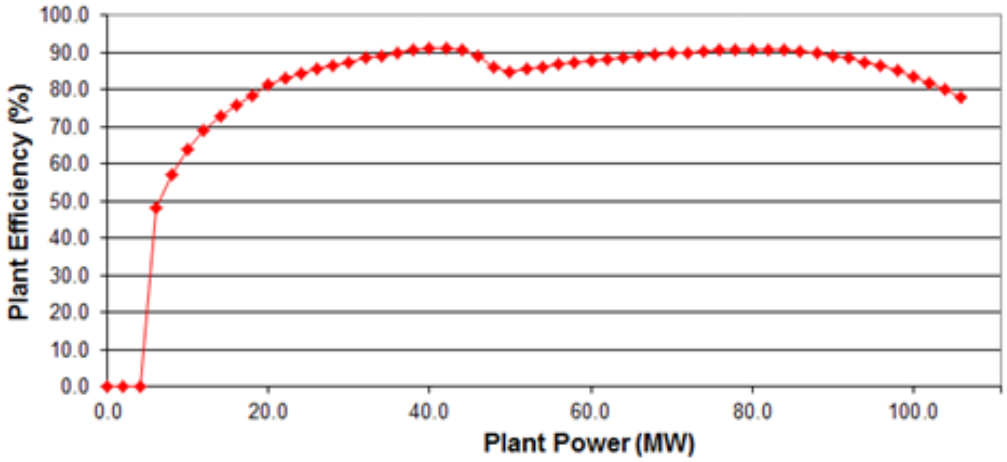

Figure 2.15: Optimum Plant Efficiency

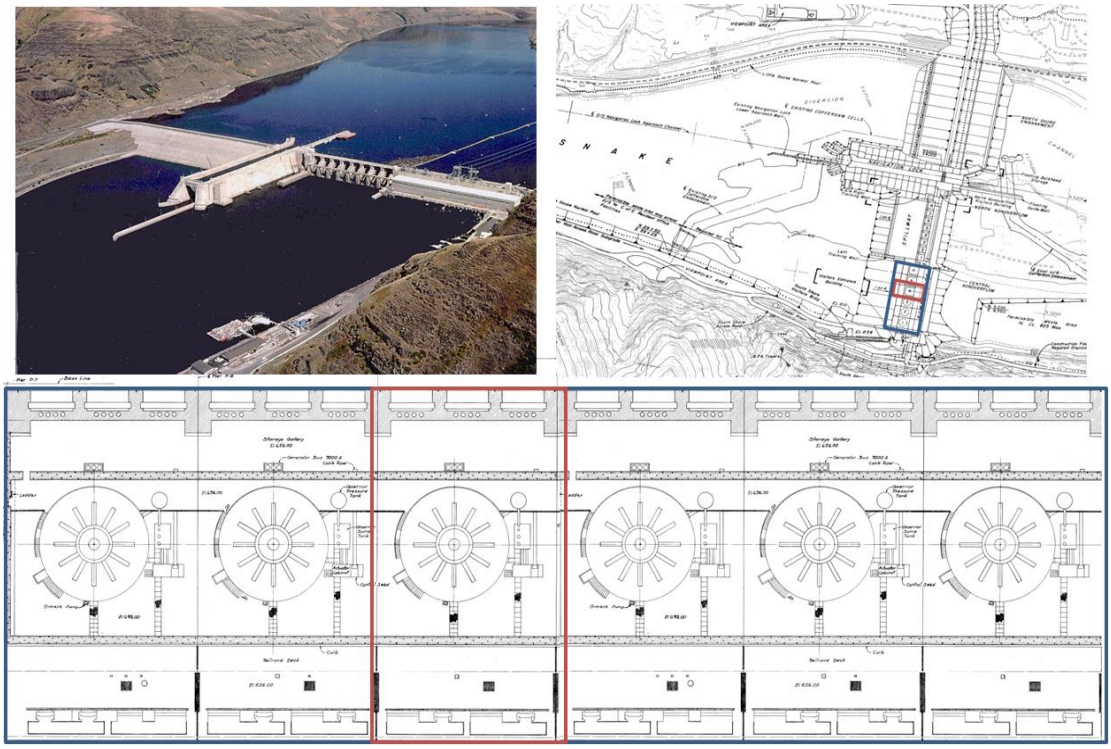

Figure 2.16: Lower Granite Lock and Dam

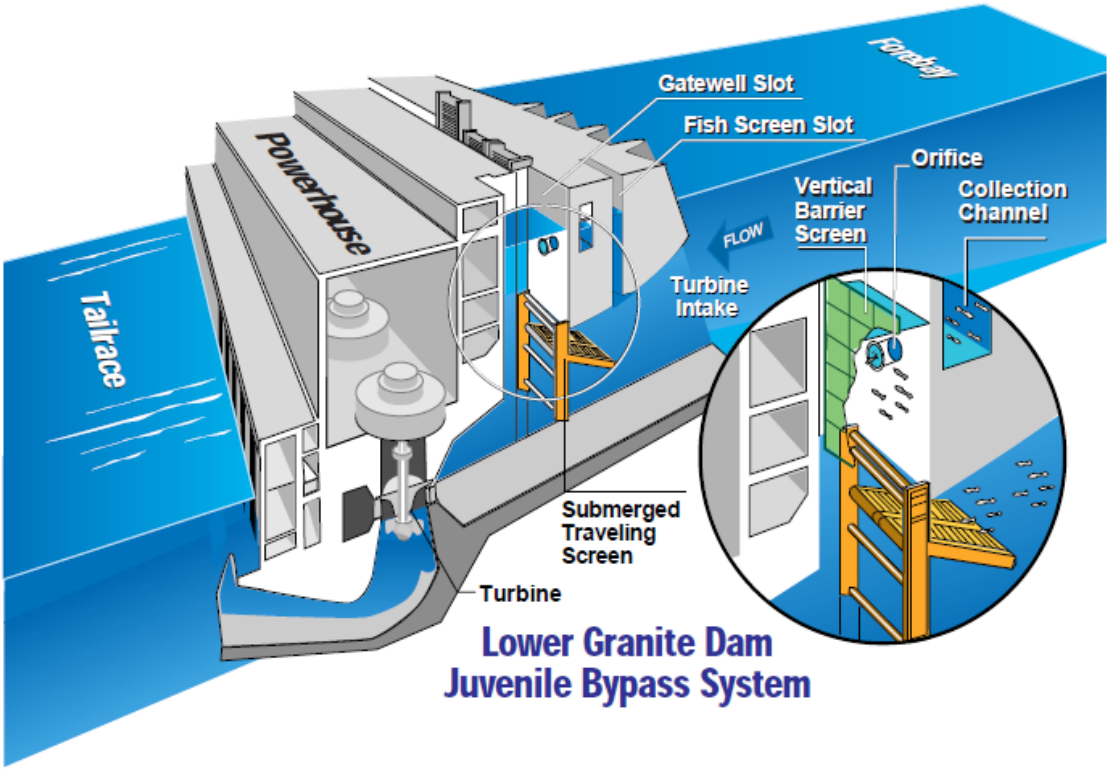

Figure 2.17: Lower Granite Fish Bypass System Overview

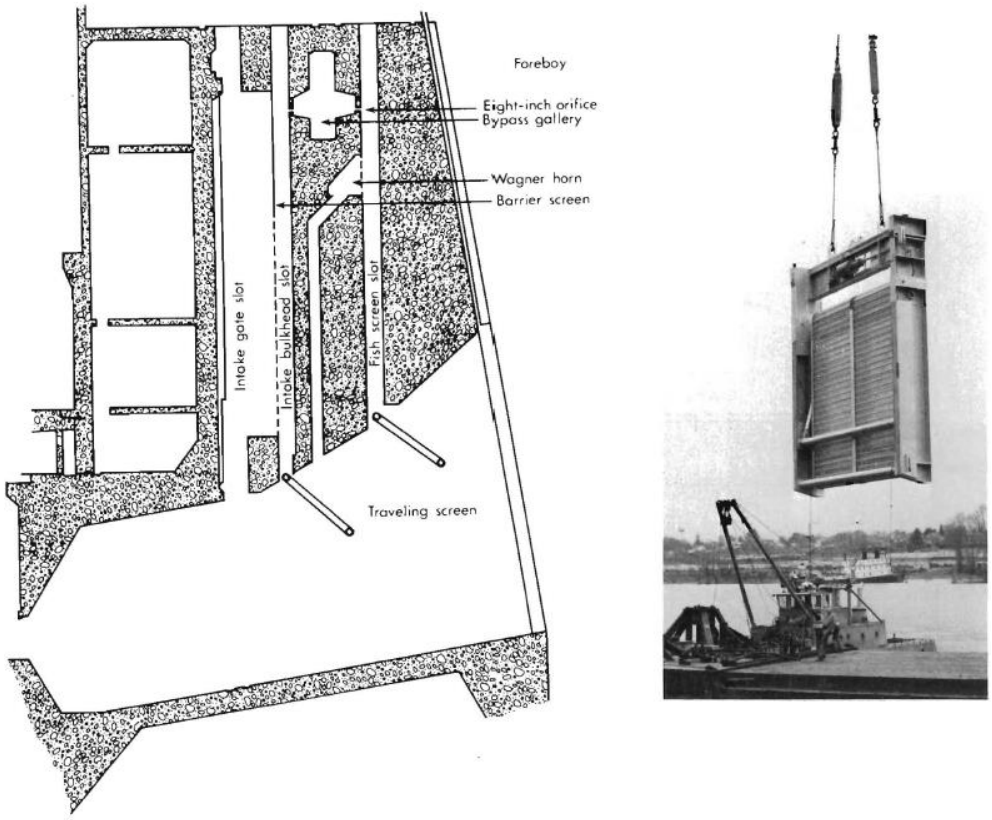

Figure 2.18: Lower Granite Fish Bypass Screen and Application Points

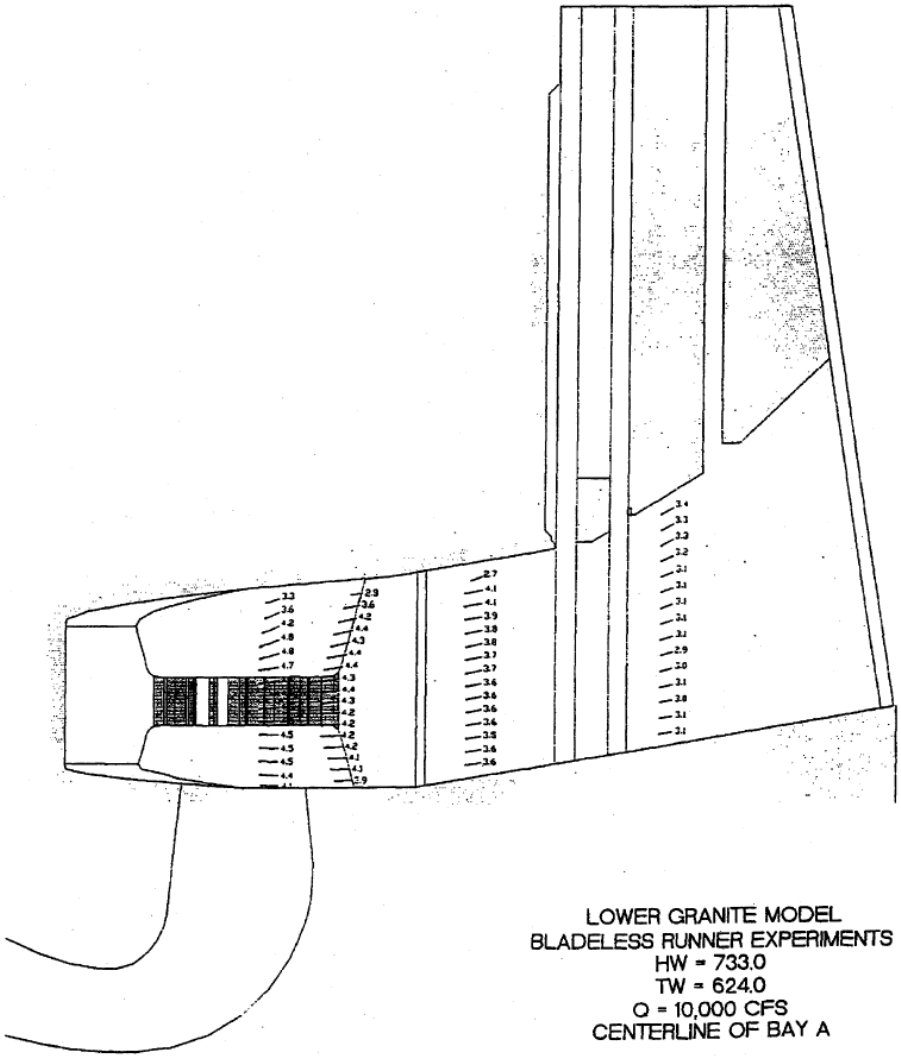

Figure 2.19: Lower Granite Bladeless Turbine Model Test Data

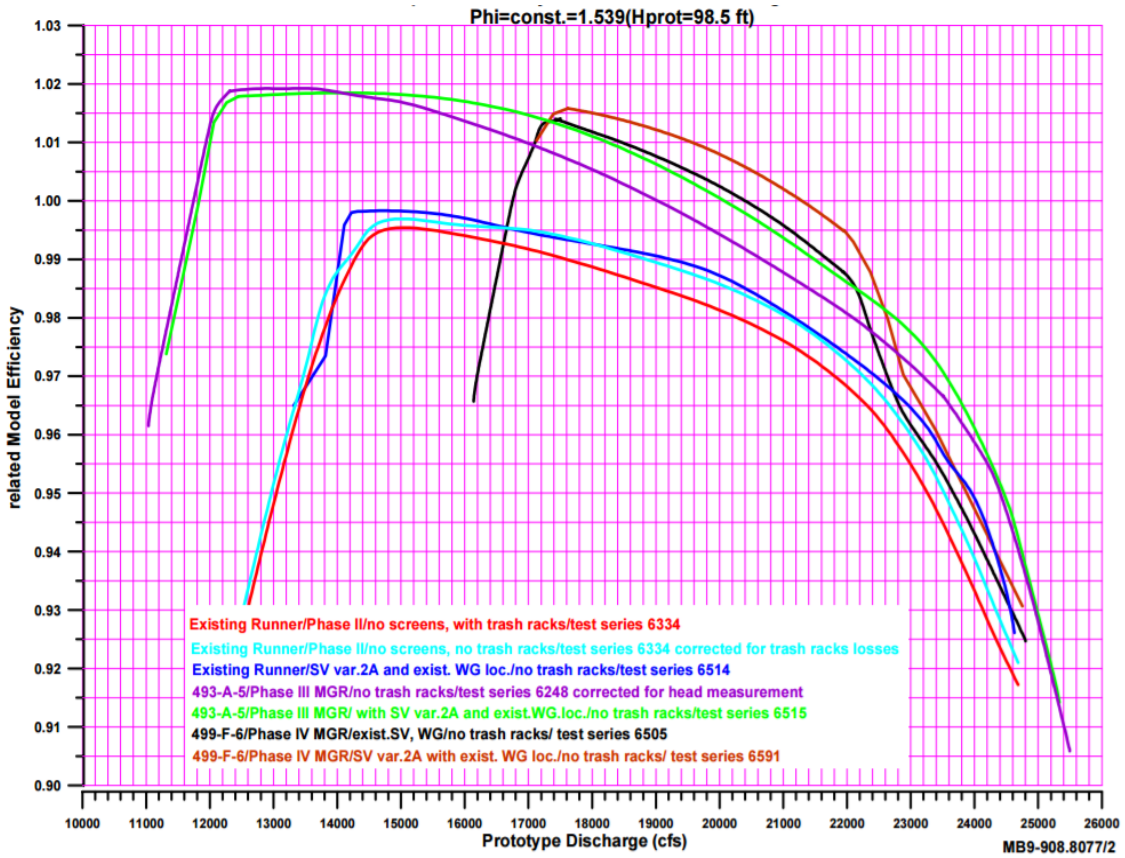

Figure 2.20 Lower Granite Modified Geometry Performance Test Data

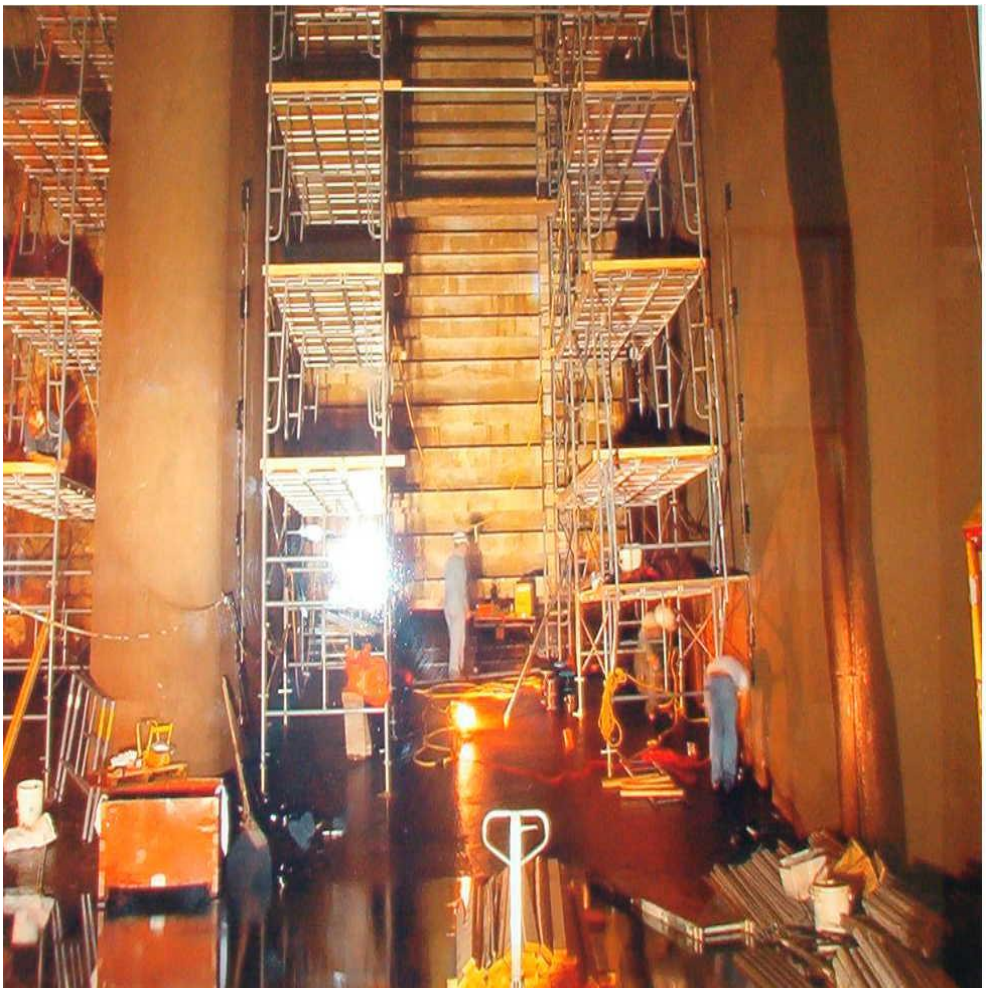

Figure 2.21: Installation of Acoustic Time of Flight Transducers

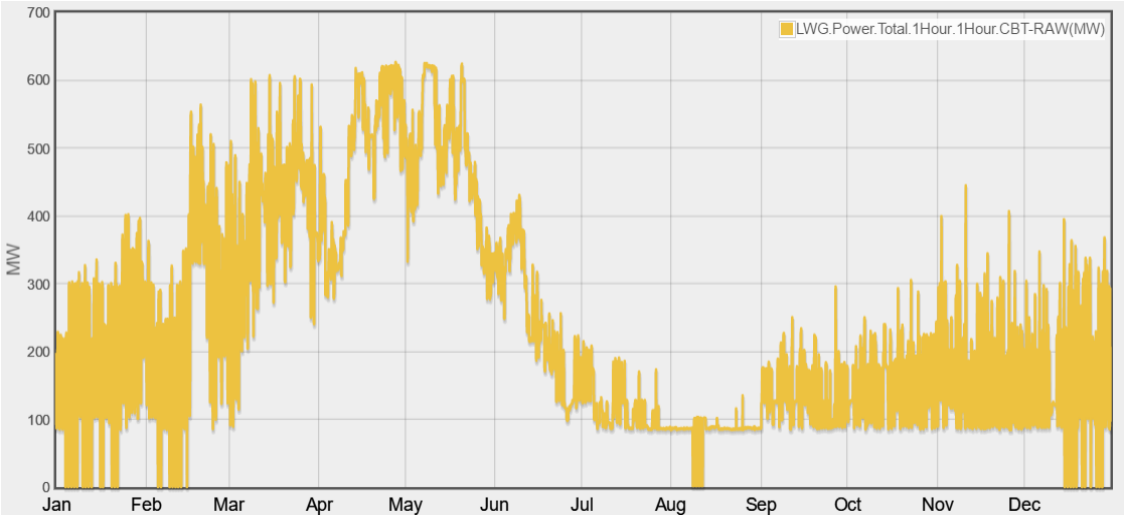

Figure 2.22a: Lower Granite 2016 Hourly Generation Chart

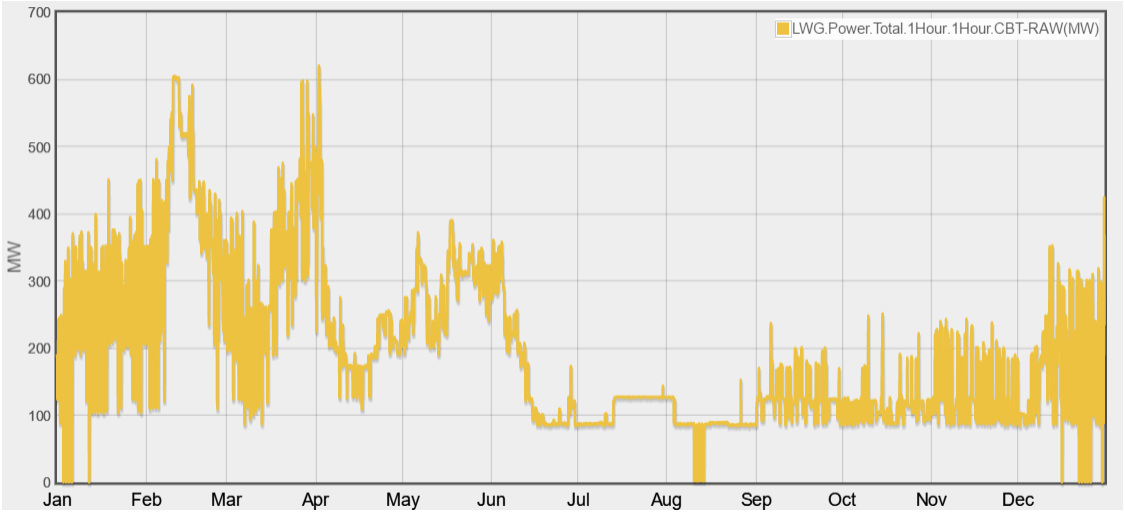

Figure 2.22b: Lower Granite 2015 Hourly Generation Chart

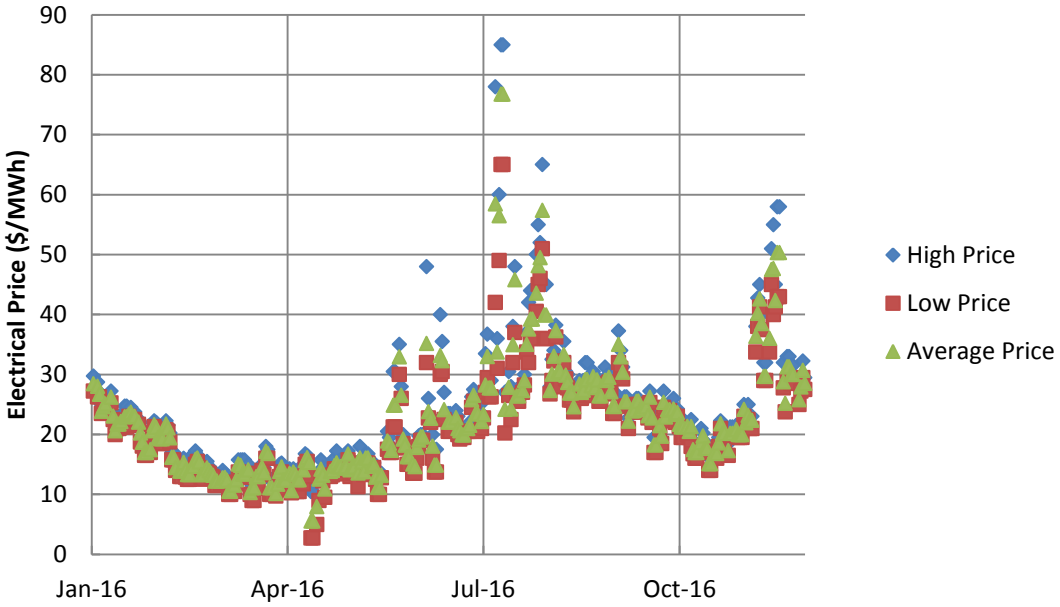

Figure 2.23: Mid-Columbia Electric Clearing Price in 2016

Appendix 7: Chapter 3 Figures and Tables

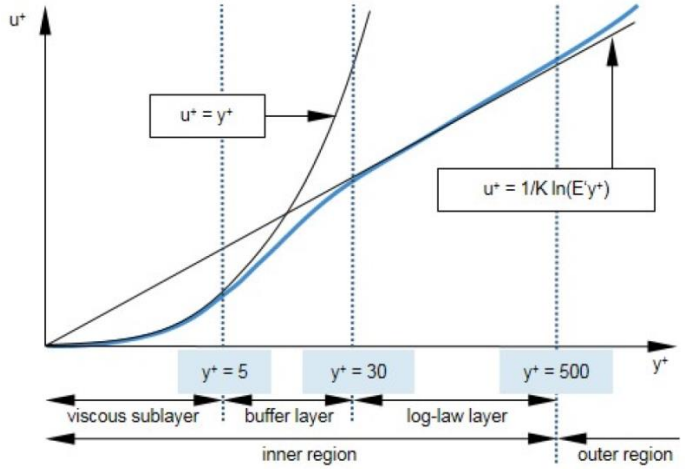

Figure 3.1: Wall Region Discretization and Treatment

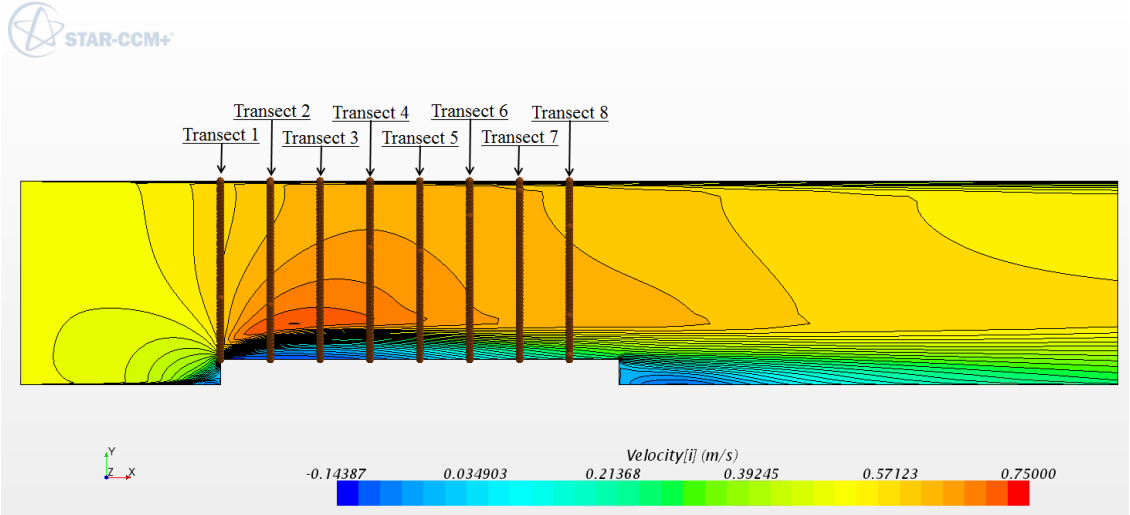

Figure 3.2: Forward Facing Step Velocity Contours and Comparison Transect Locations

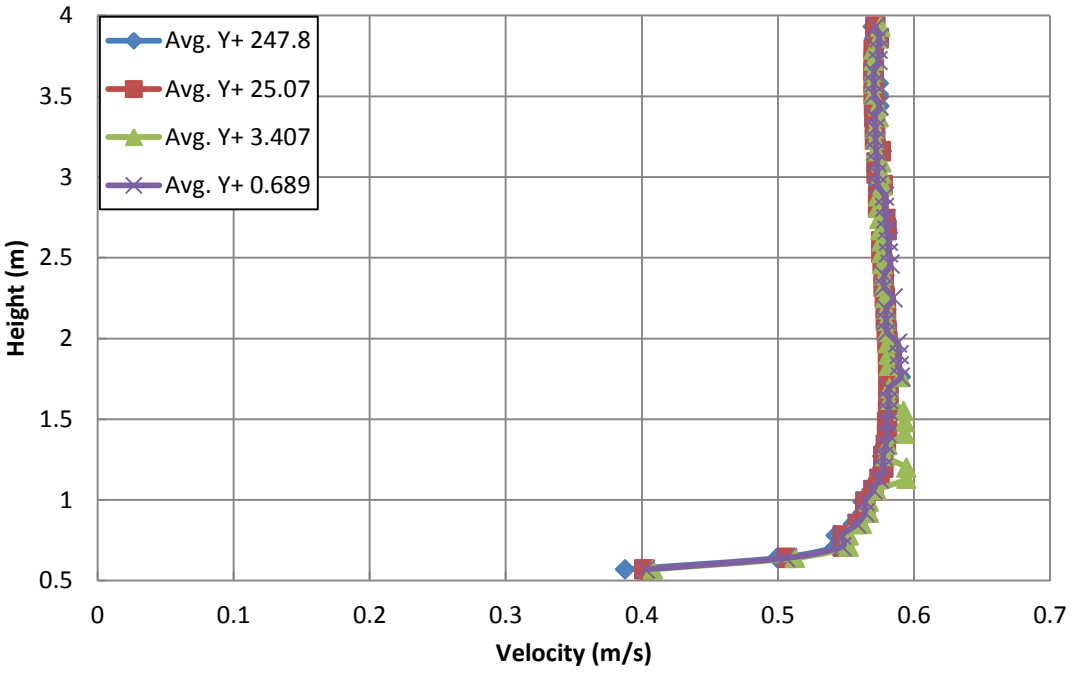

Figure 3.3: Transect 1 Freestream Velocity Profile

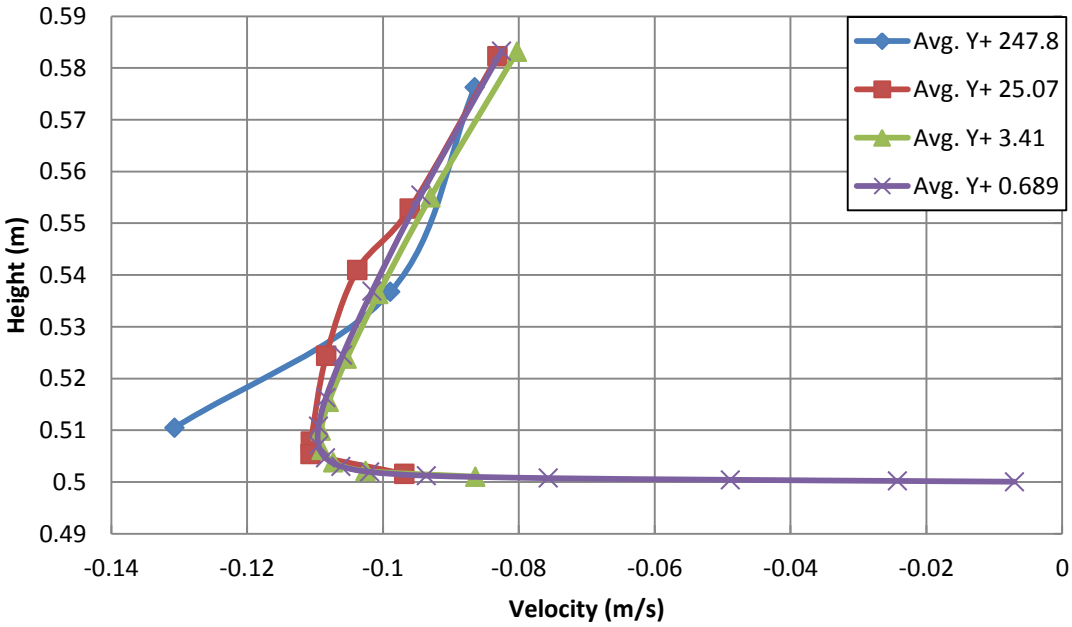

Figure 3.4: Transect 2 Near Wall Velocity Profile

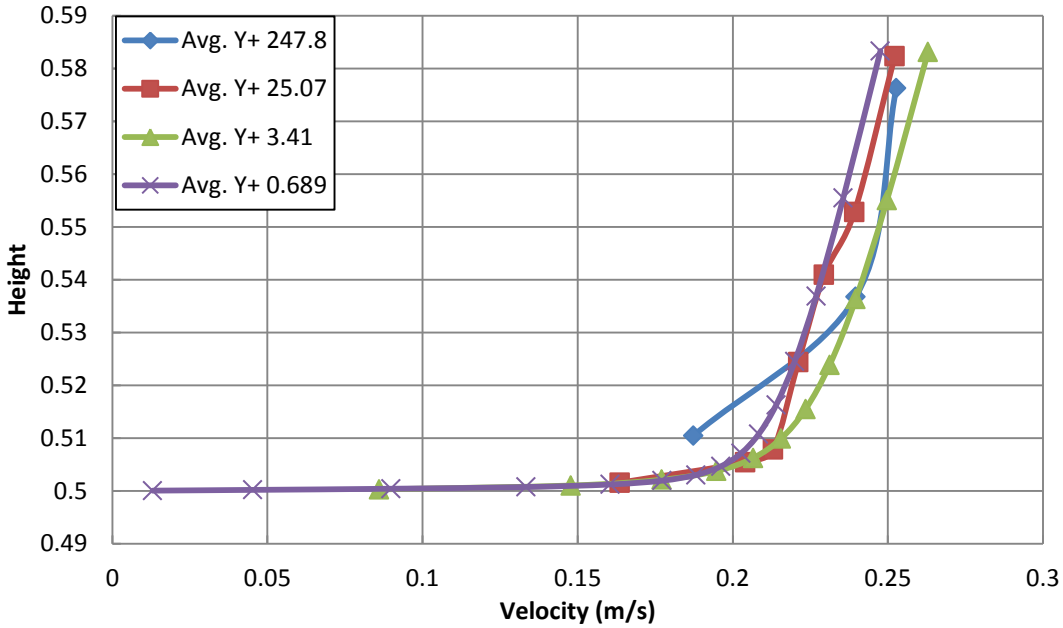

Figure 3.5: Transect 8 Near Wall Velocity Profile

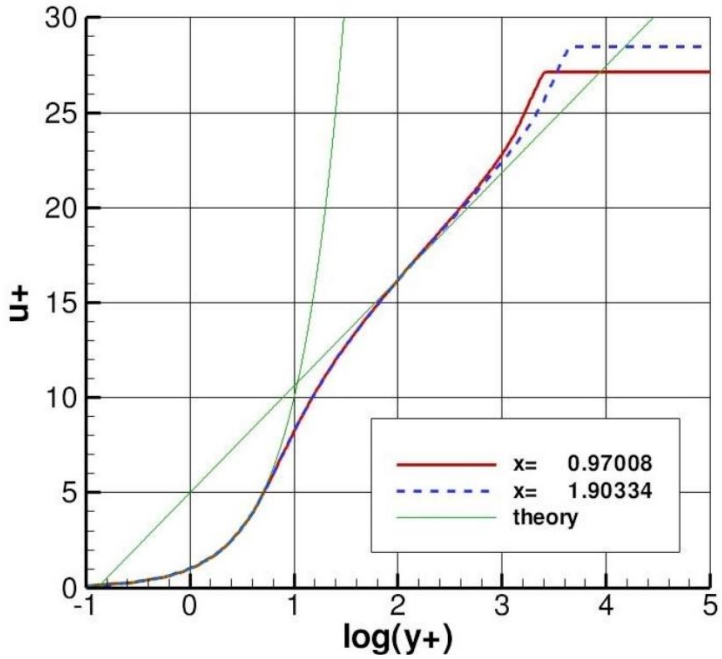

Figure 3.6: NASA Langley Near Wall Velocity Distribution

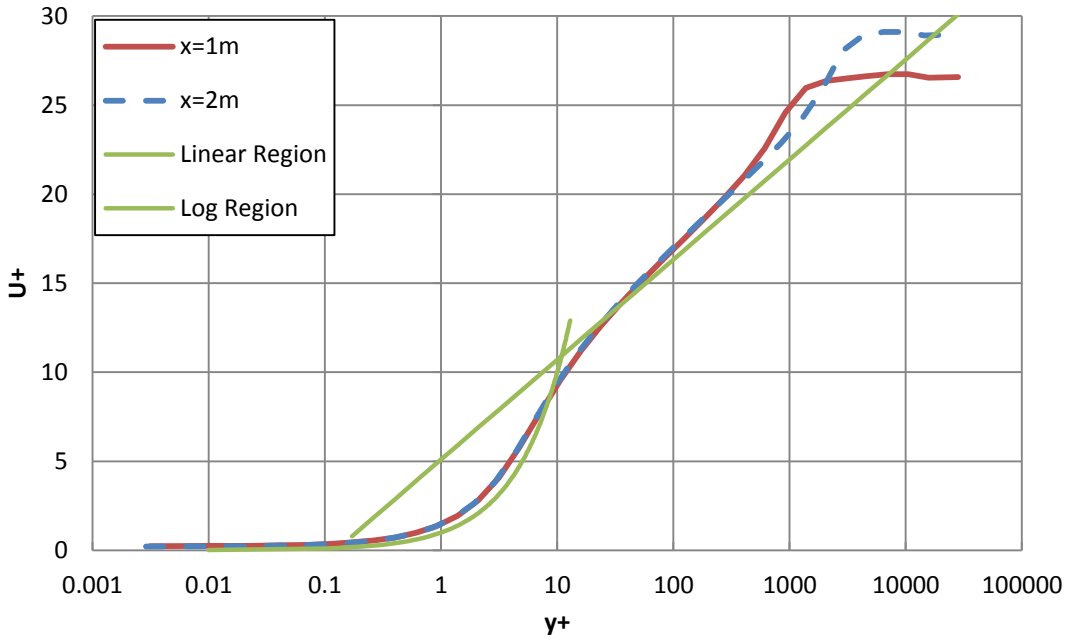

Figure 3.7: Star-CCM+ Near Wall Velocity Distribution at an Average Y+ of 0.2

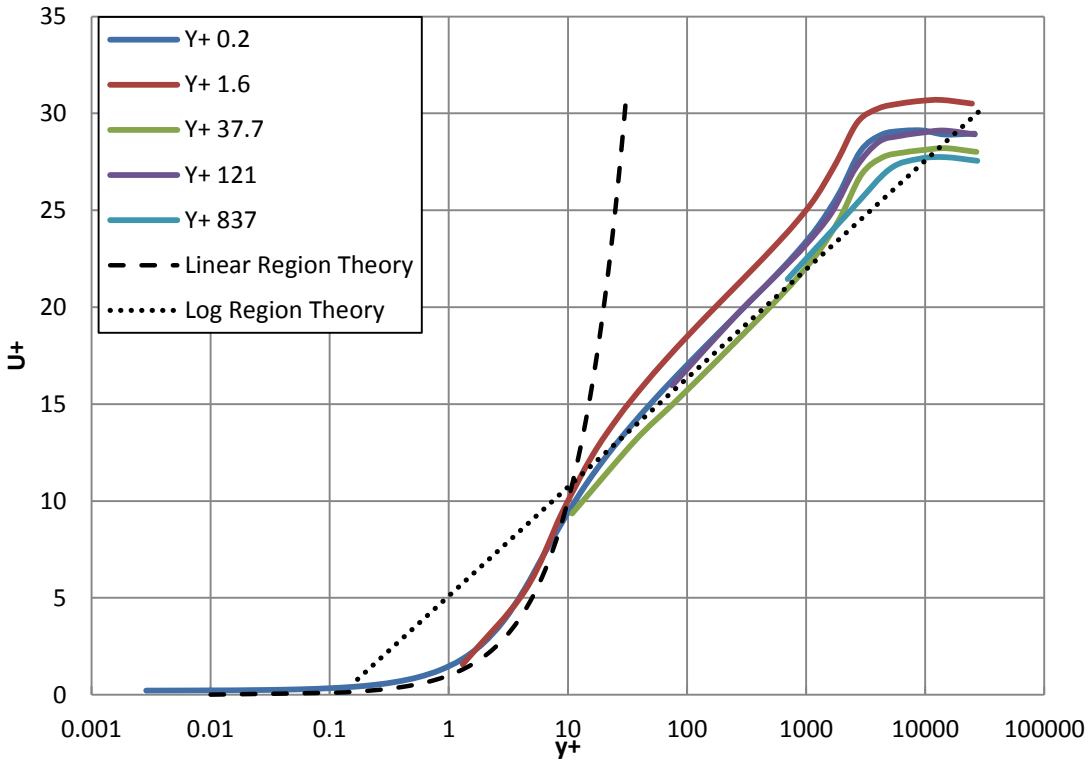

Figure 3.8: Near Wall Velocity Distribution Associated with Different Near Wall Mesh Resolutions at a Downstream Distance of 1 meter

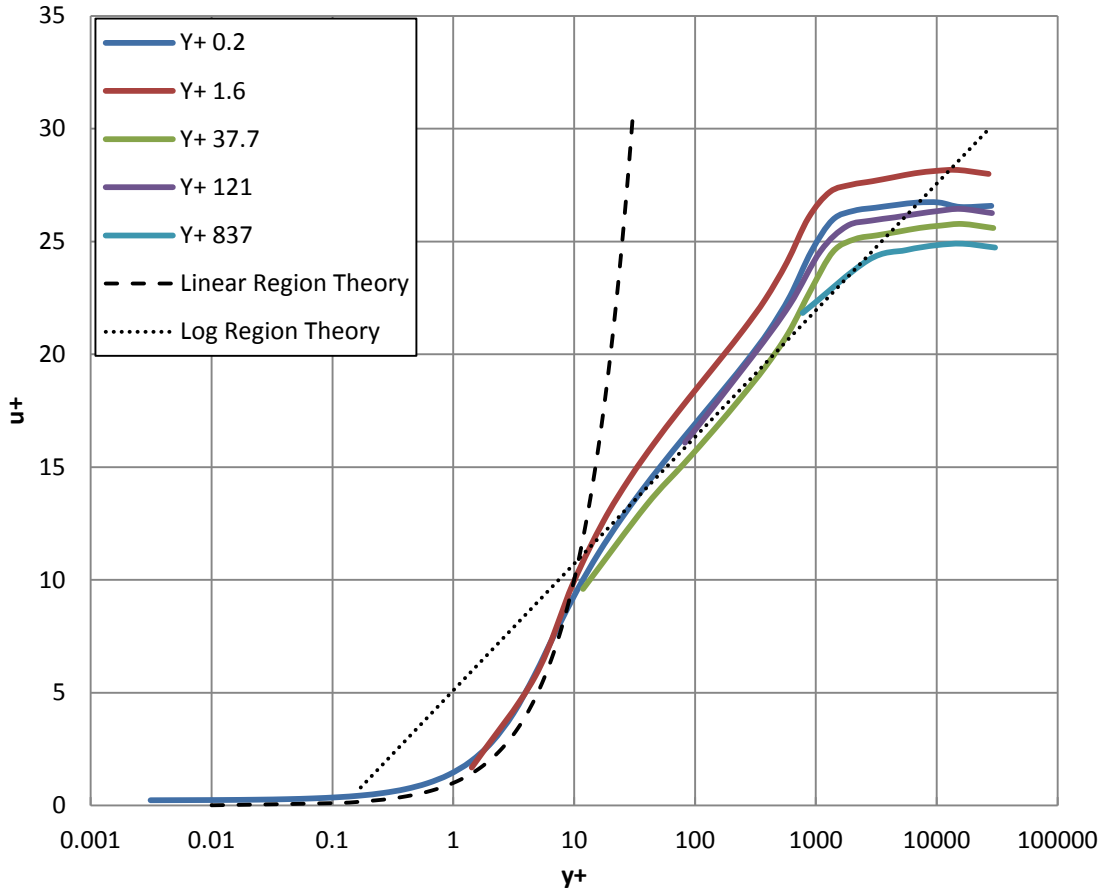

Figure 3.9: Near Wall Velocity Distribution Associated with Different Near Wall Mesh Resolutions at a Downstream Distance of 2 meter

Table 6.1. Front Facing Step Preliminary Investigation Specifications

Y+	0.689	3.407	25.07	247.8
Reattachment Length (m)	4.28	4.15	4.14	4.25

Appendix 8: Chapter 4 Figures and Tables

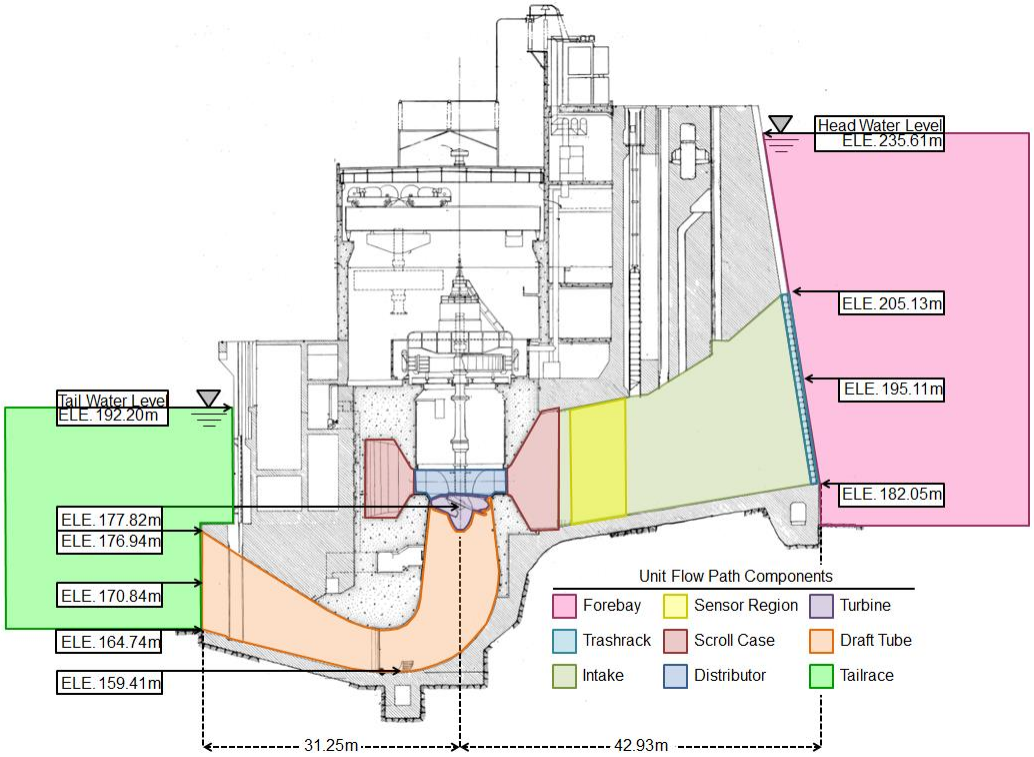

Figure 4.1: Subdomains of the Unit 4 Flow Path

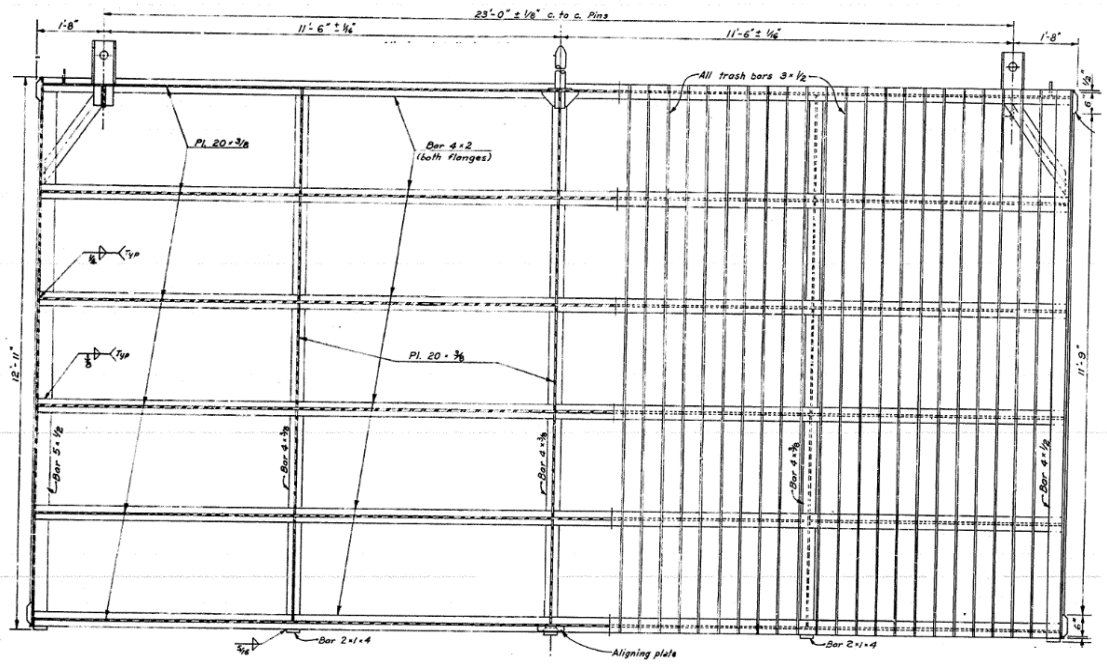

Figure 4.2a: Trashrack Engineering Drawing (Front View)

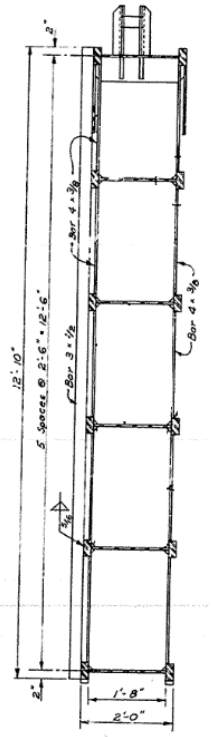

Figure 4.2b: Trashrack Engineering Drawing (Side View)

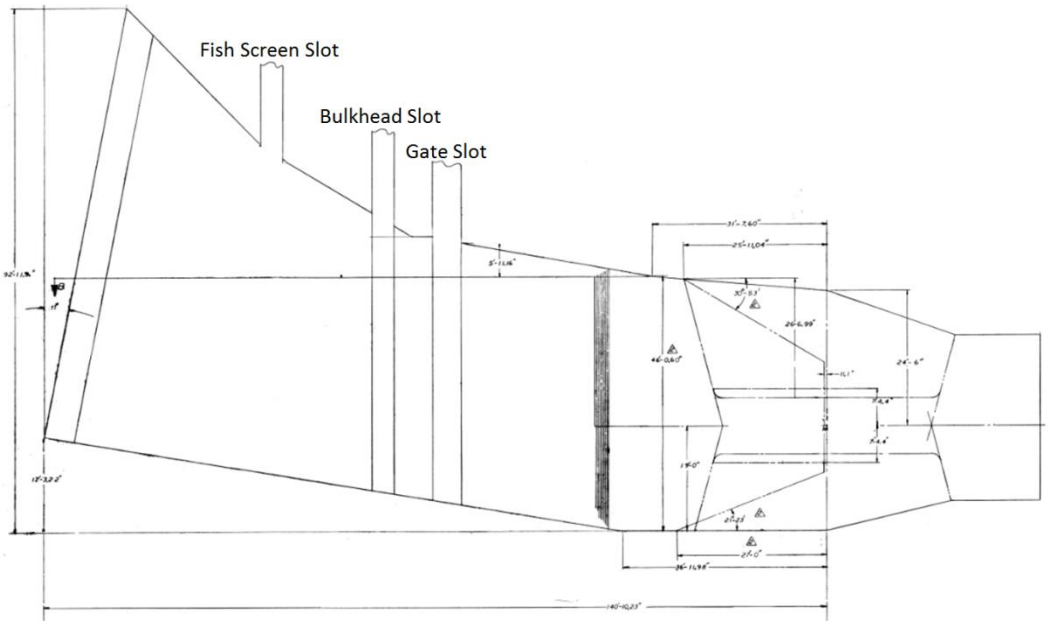

Figure 4.3: Intake Engineering Drawing (Plan View)

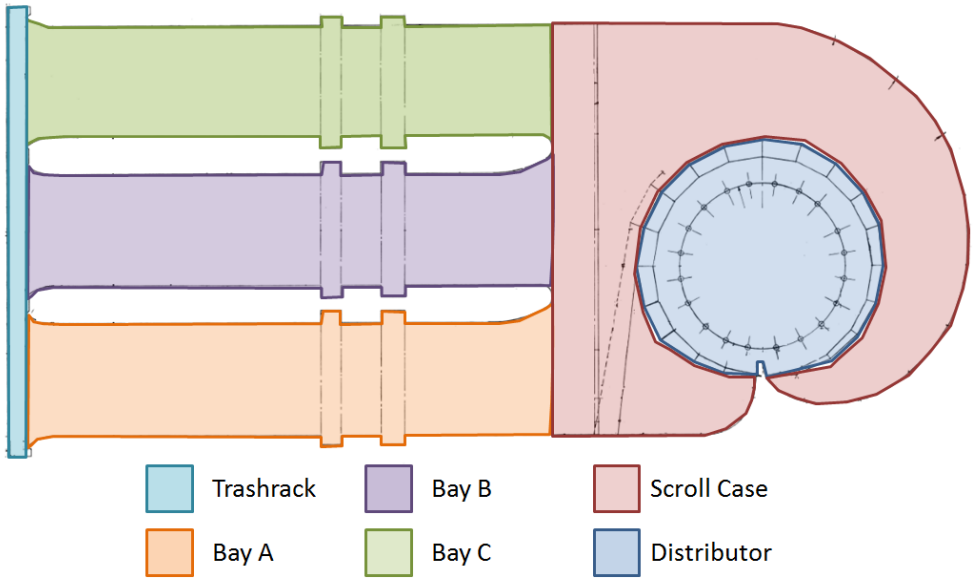

Figure 4.4: Intake Engineering Drawing (Top View)

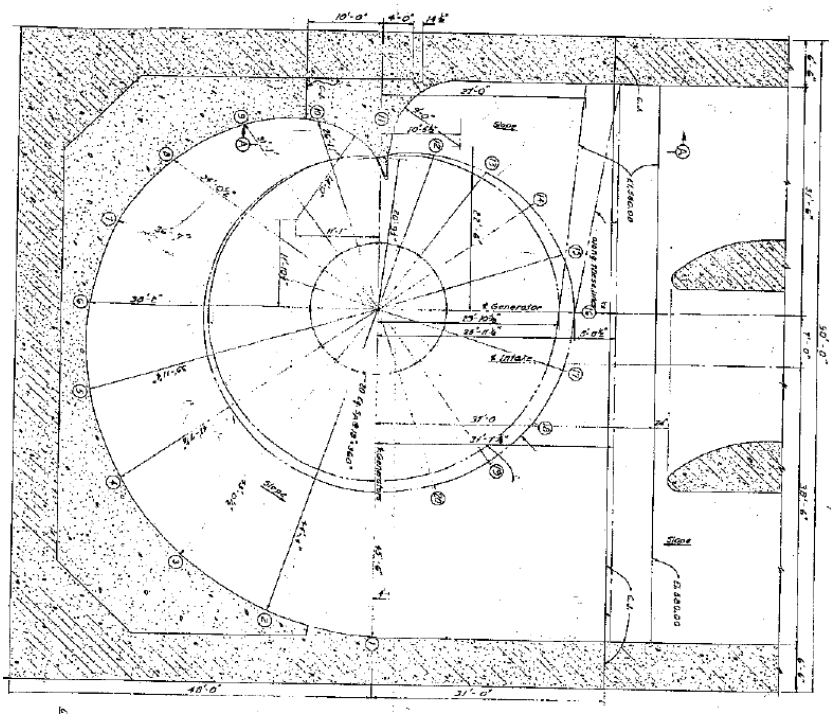

Figure 4.5a: Scroll Case Engineering Drawing (Top View)

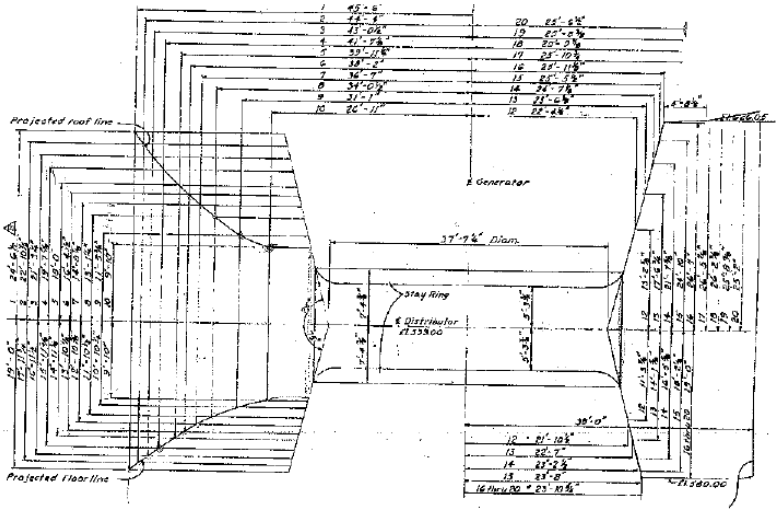

Figure 4.5b: Scroll Case Engineering Drawing (Transect Dimensions)

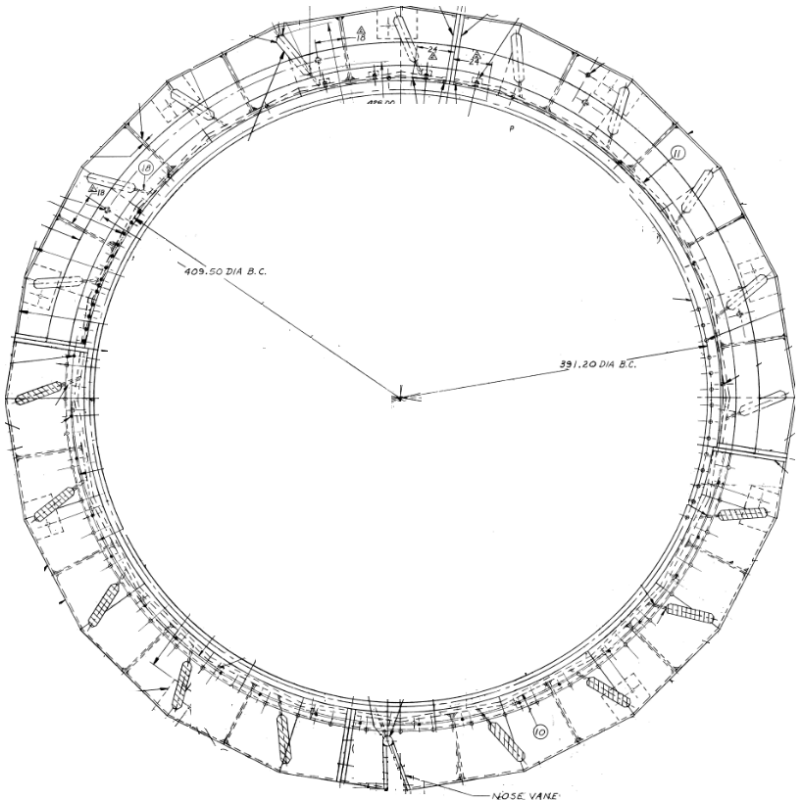

Figure 4.6a: Stay Ring Engineering Drawing (Top View)

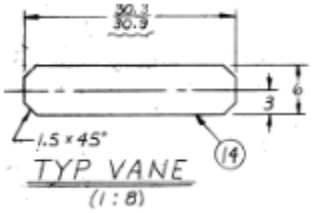

Figure 4.6b: Stay Vane Engineering Drawing (Transect Dimensions)

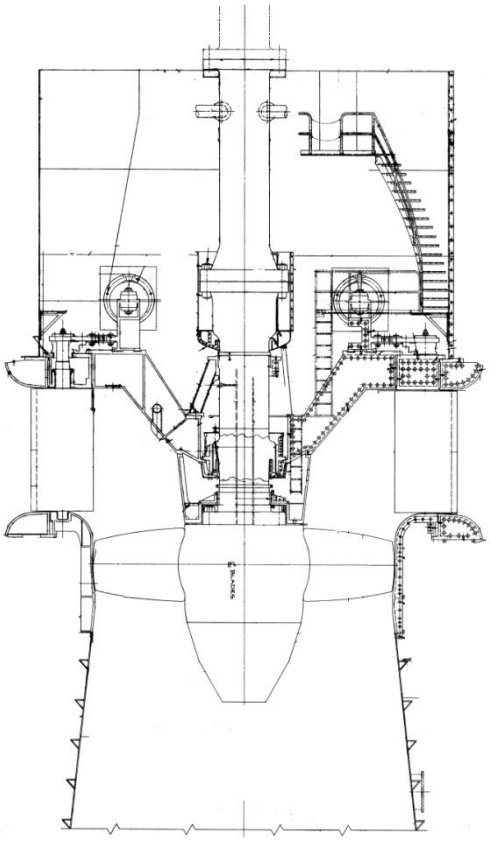

Figure 4.7: Turbine Engineering Drawing (Transect Dimensions)

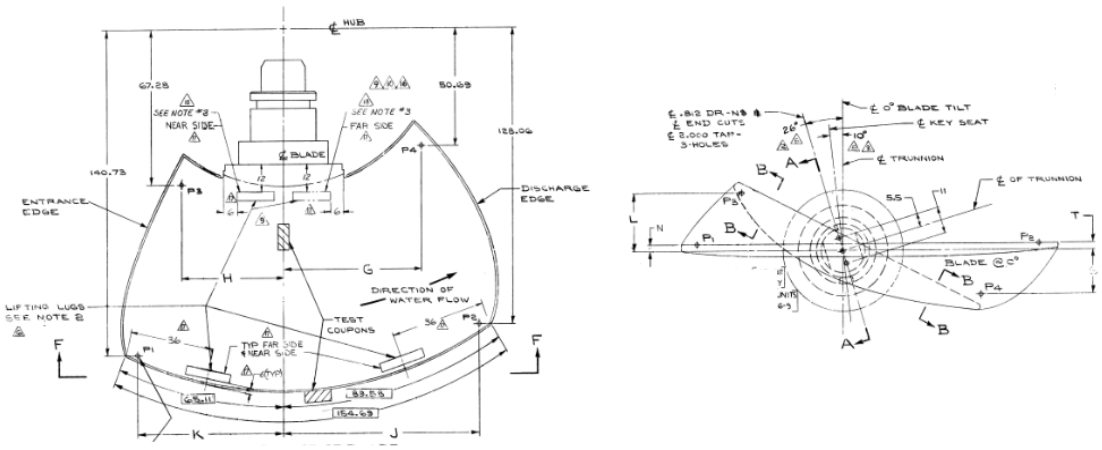

Figure 4.8: Turbine Blade Drawing (Transect Dimensions)

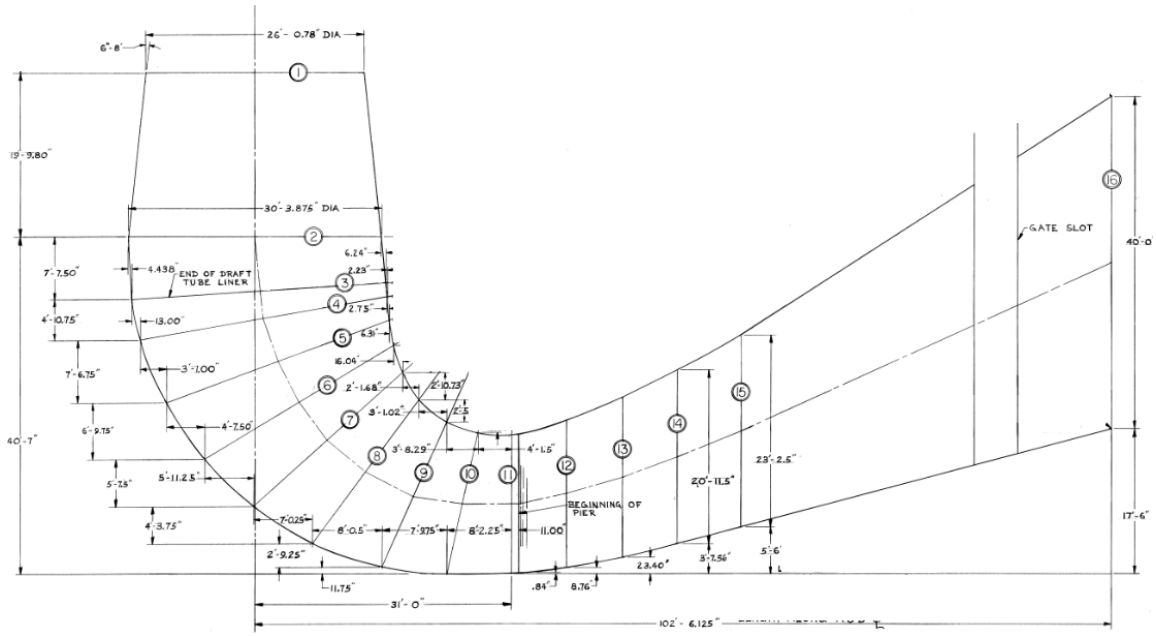

Figure 4.9: Draft Tube Engineering Drawing (Transect Dimensions)

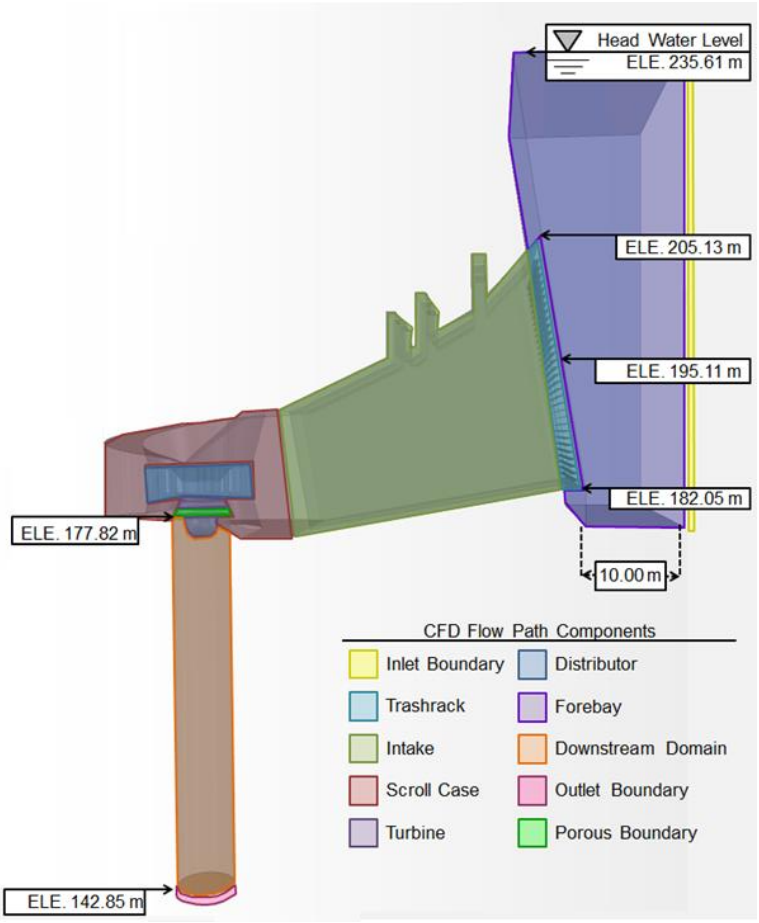

Figure 4.10: Subdomains of the Computational Domain

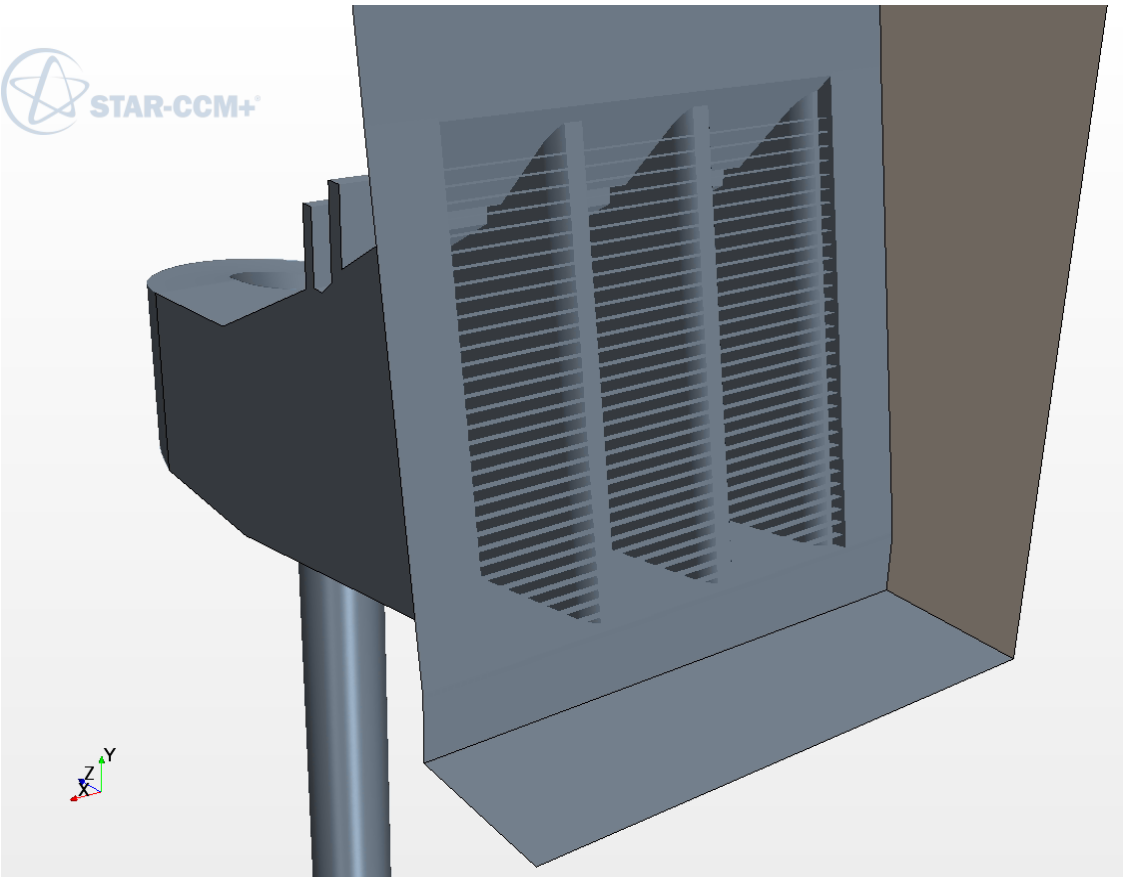

Figure 4.11: Computational Domain Trashracks

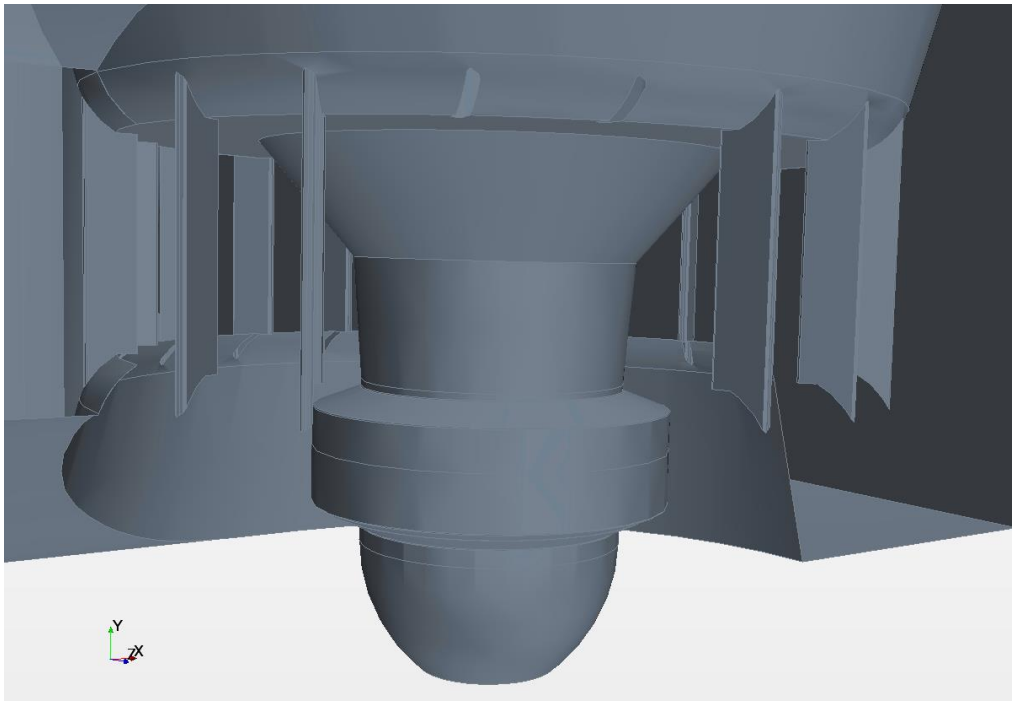

Figure 4.12a: Computational Turbine Model

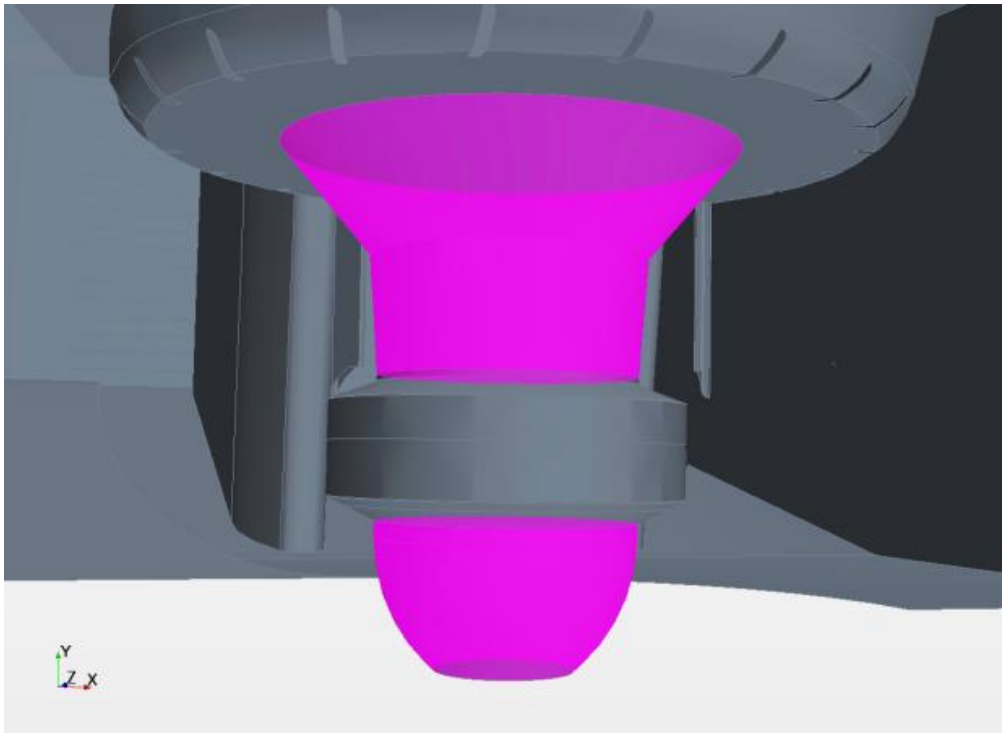

Figure 4.12b: Turbine Hub Subdomain of the Computational Domain

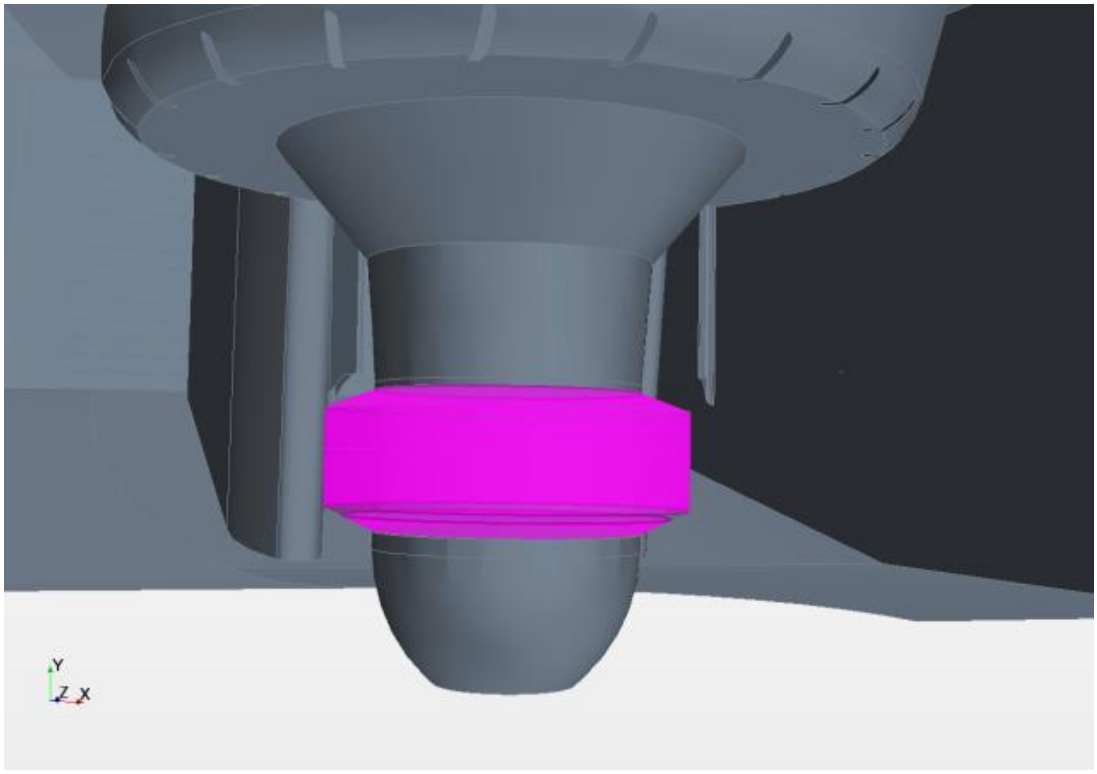

Figure 4.12c: Aggregated Blade Subdomain of the Computational Domain

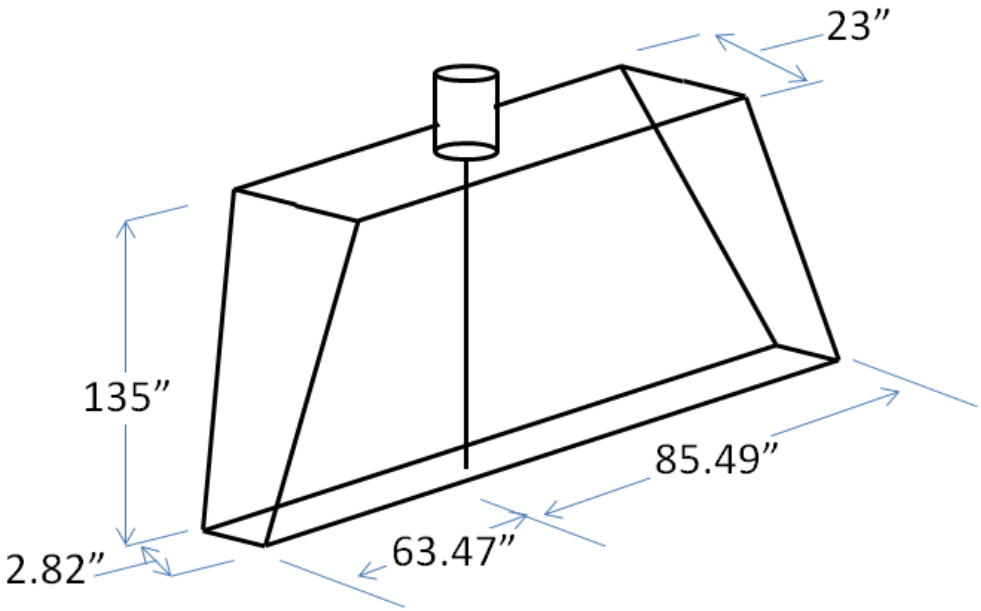

Figure 4.13: Simplified Turbine Blade Geometry

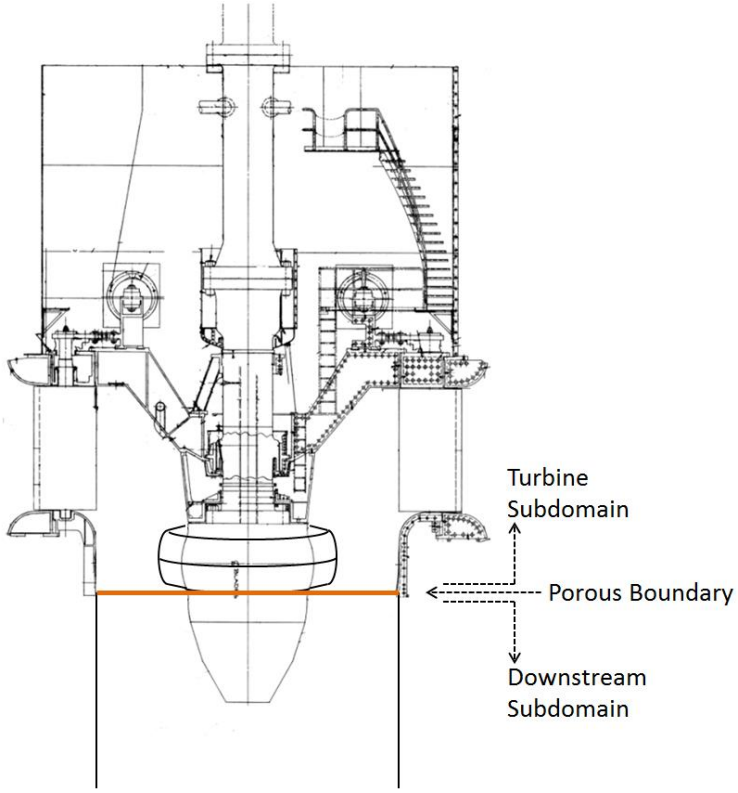

Figure 4.14: Simplified Turbine Blade Geometry

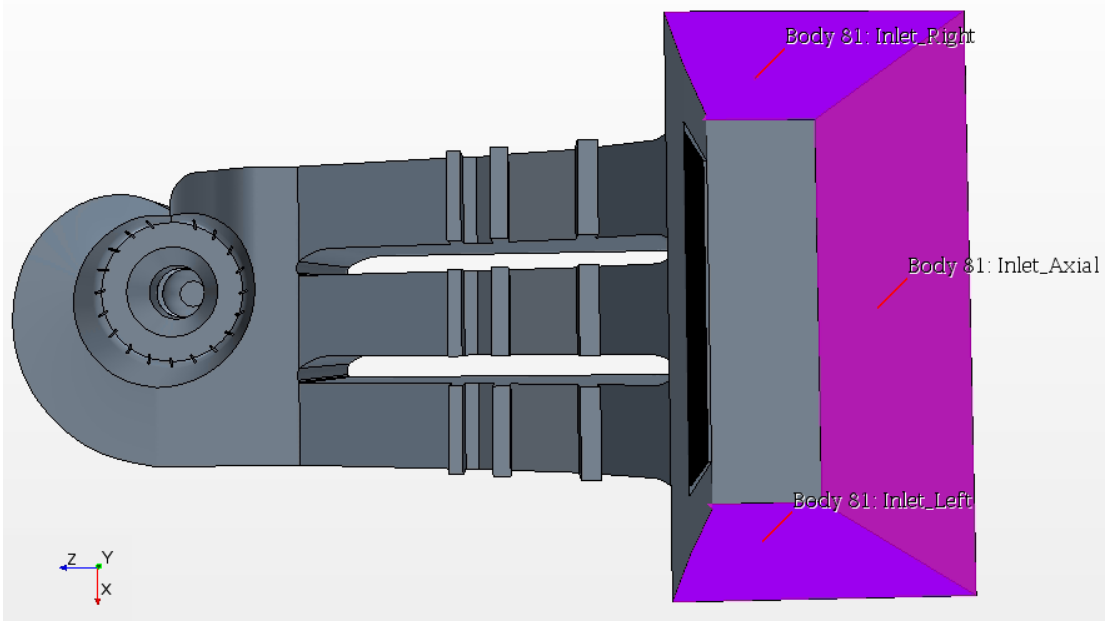

Figure 4.15: Forebay Boundary Labels

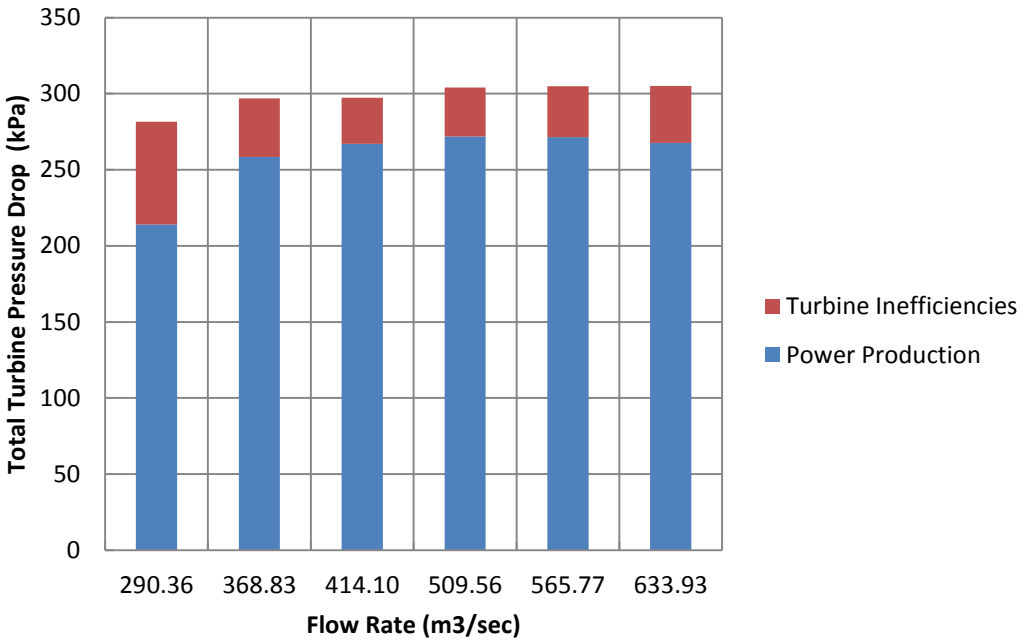

Figure 4.16: Turbine Pressure Drop over Flow Range of Unit 4

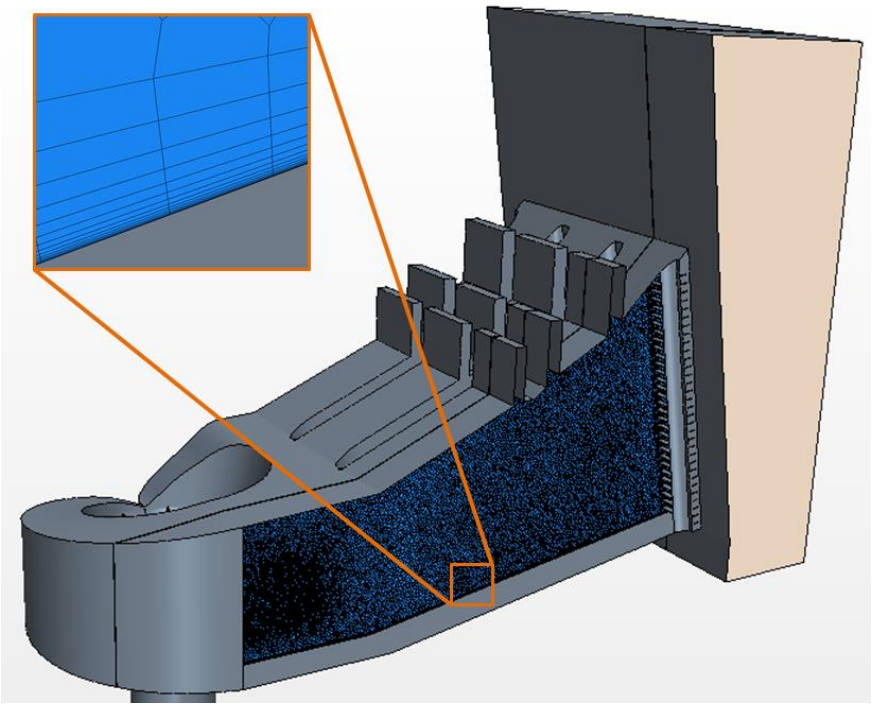

Figure 4.17: Prism Layer Resolution

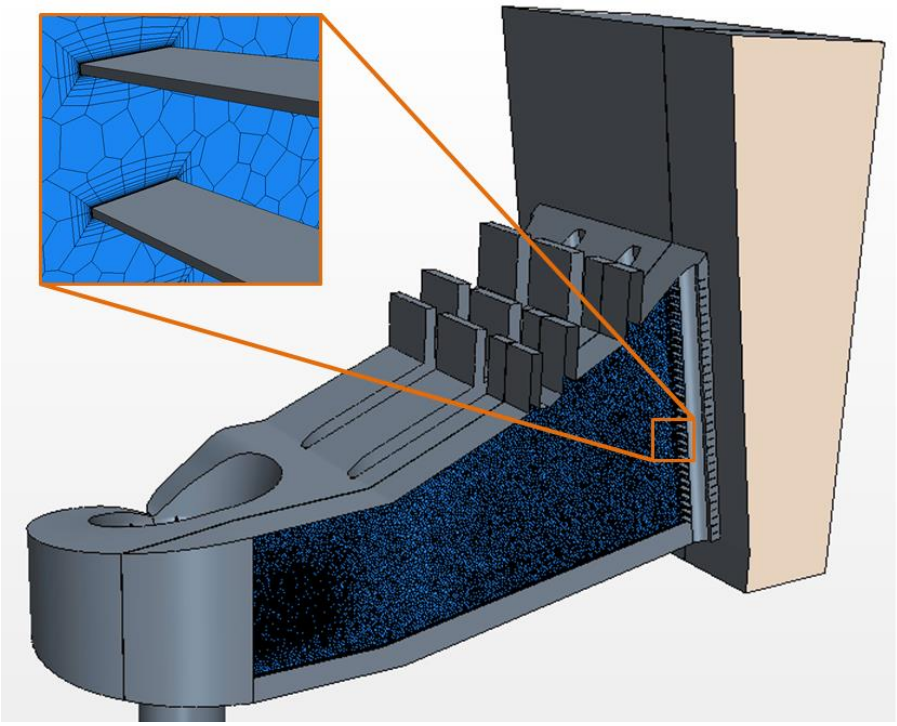

Figure 4.18: Thin Layer Resolution

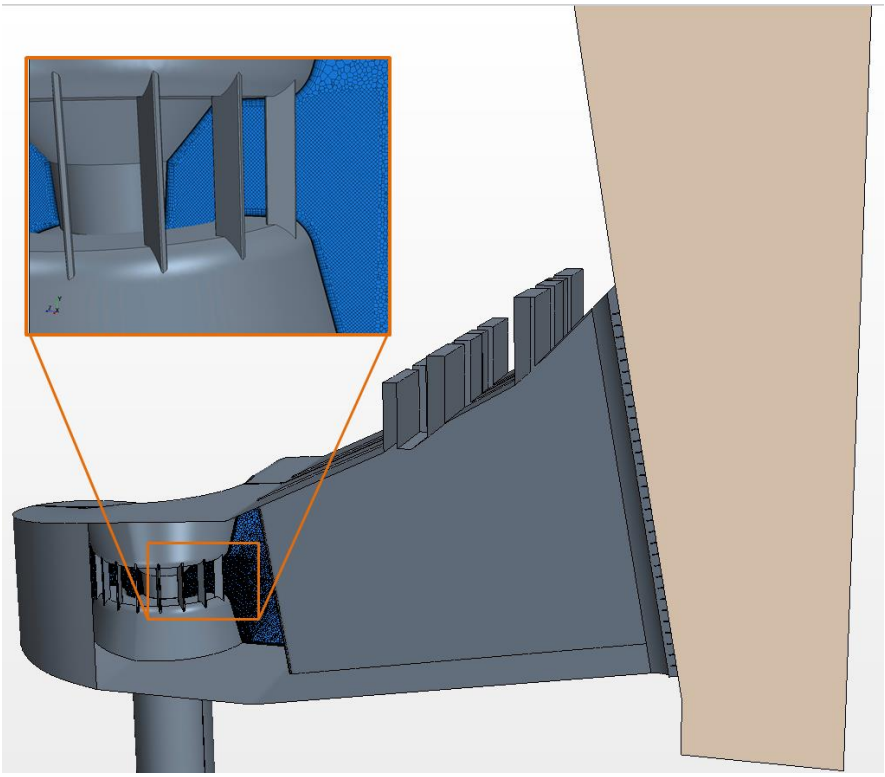

Figure 4.19: Enhanced Mesh Resolution

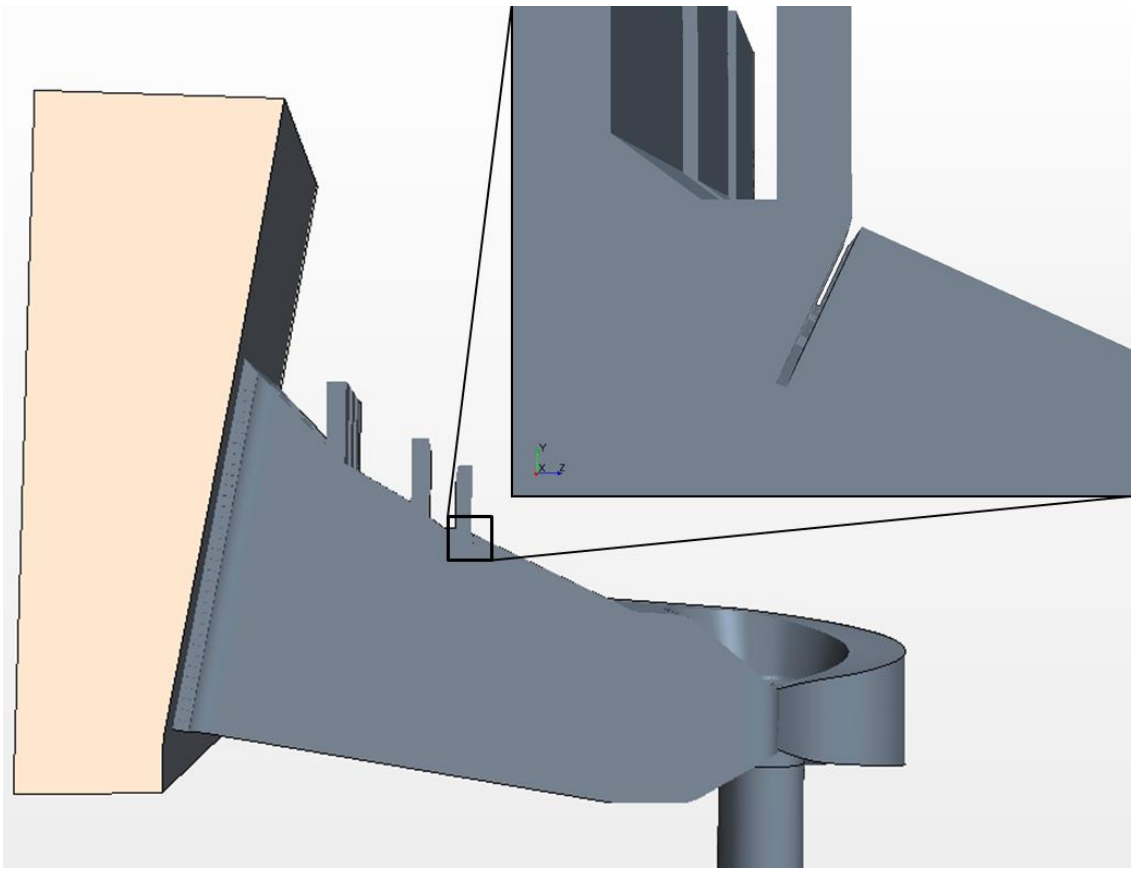

Figure 4:20: As-Build Angled Obstruction Modification

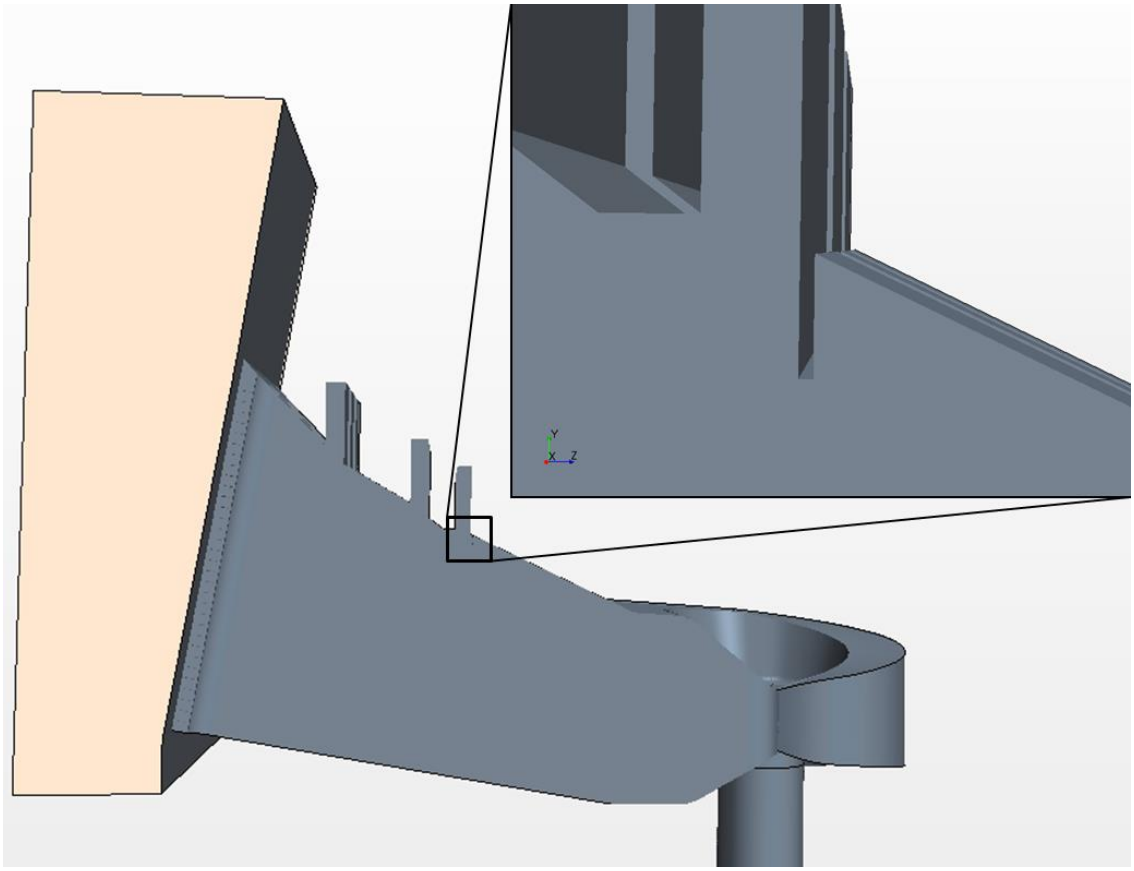

Figure 4.21: As-Build Straight Obstruction Modification

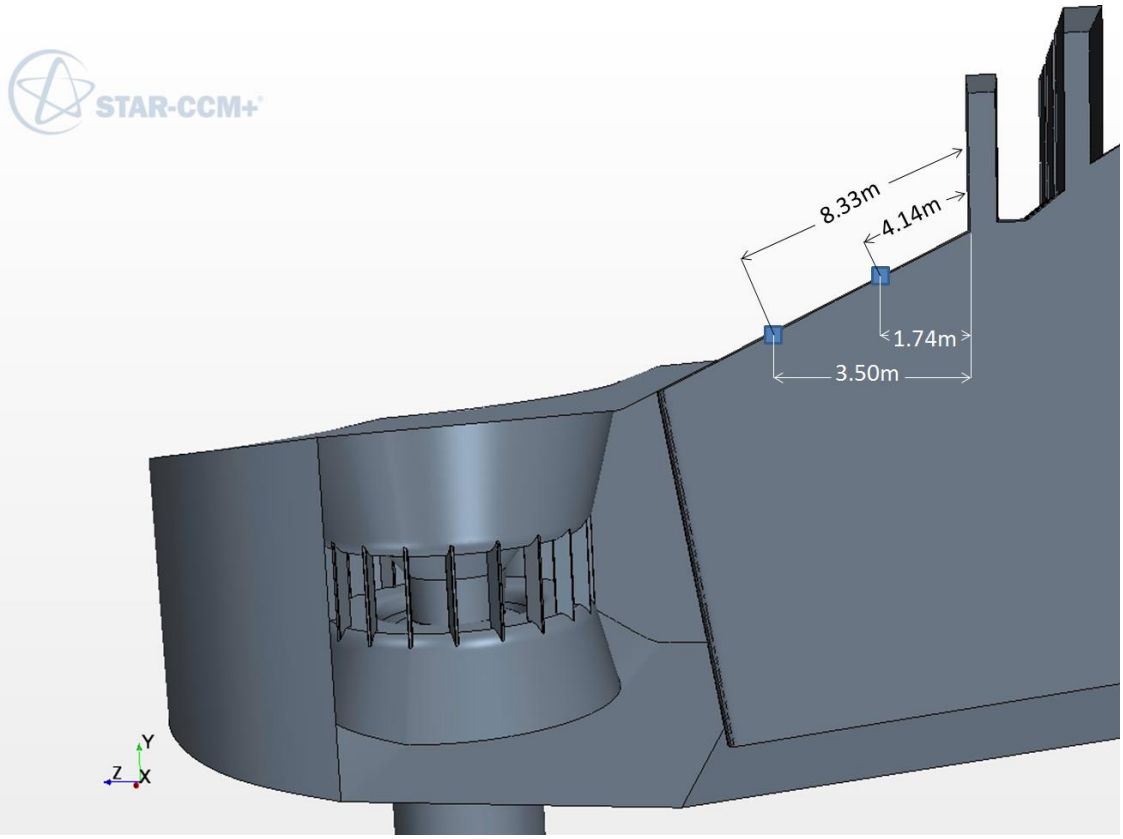

Figure 4.22: Acoustic Transducer Distances

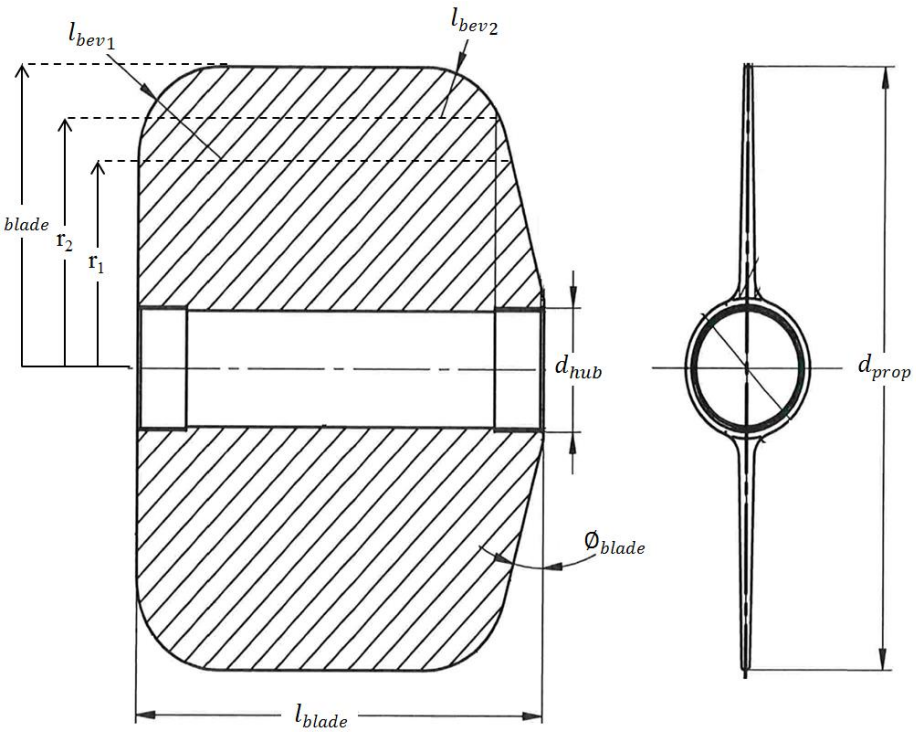

Figure 4.23: Current Meter Geometry

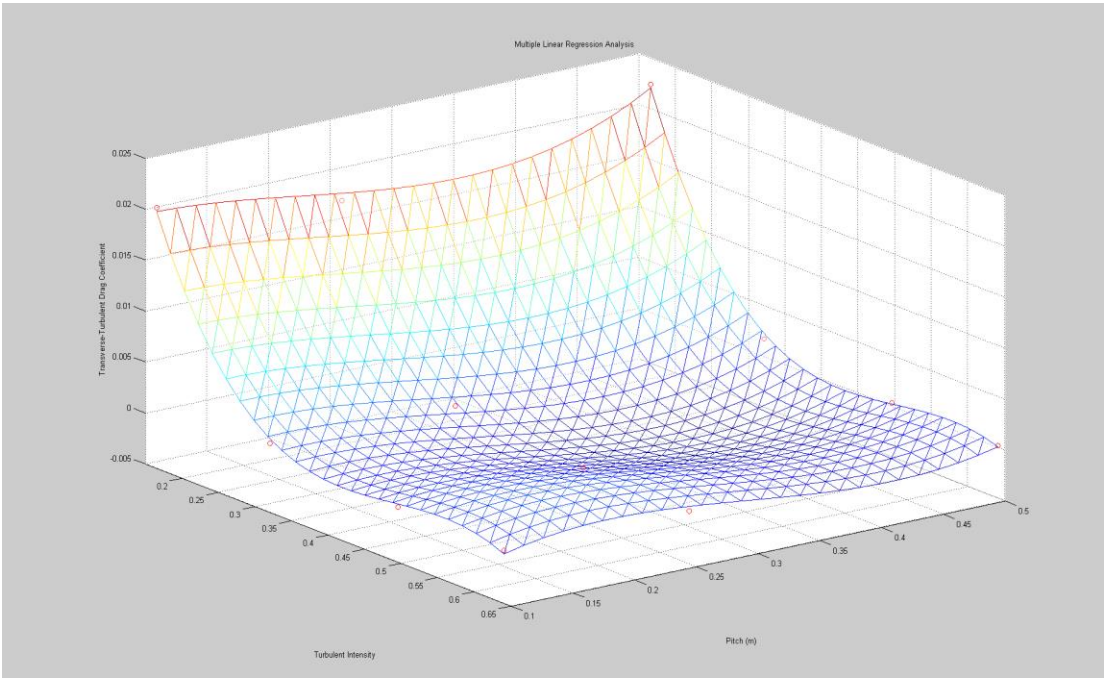

Figure 4.24: Least Squares Fit of Turbulent Transverse Drag Coefficient

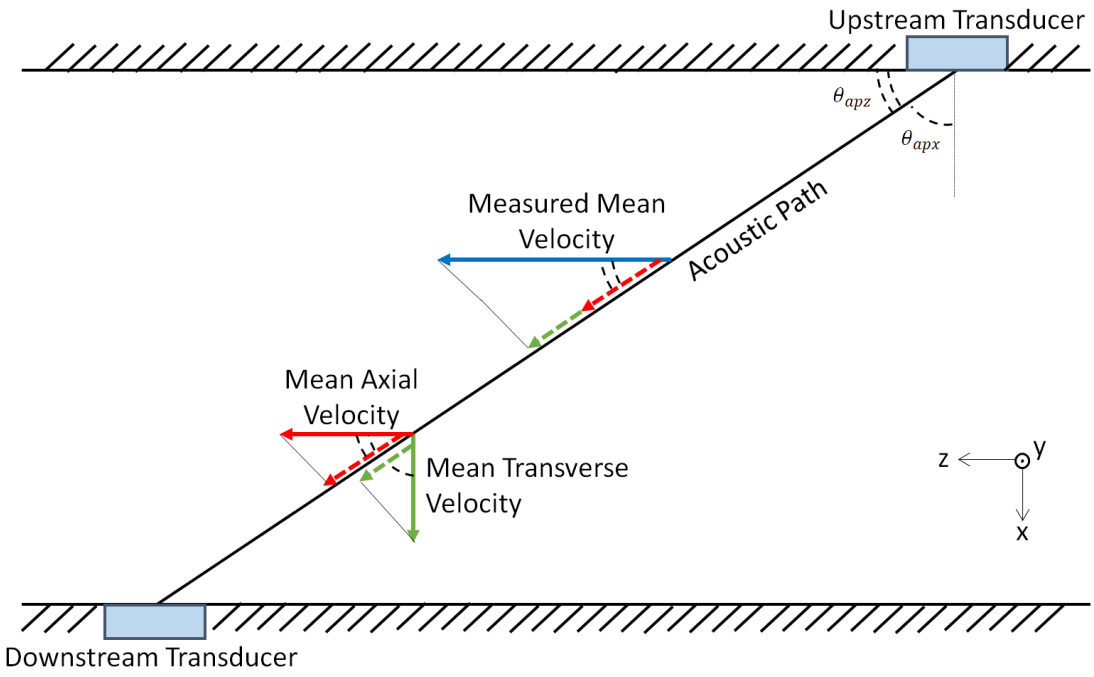

Figure 4.25: Acoustic Time of Flight Diagram

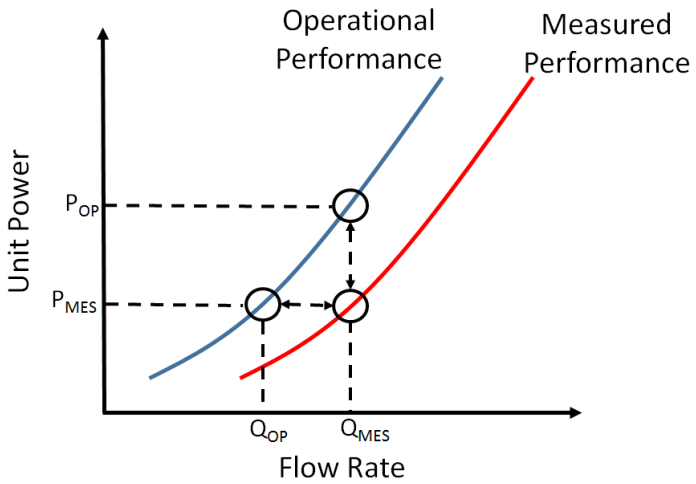

Figure 4.26: Flow Measurement Accuracy Opportunity Cost

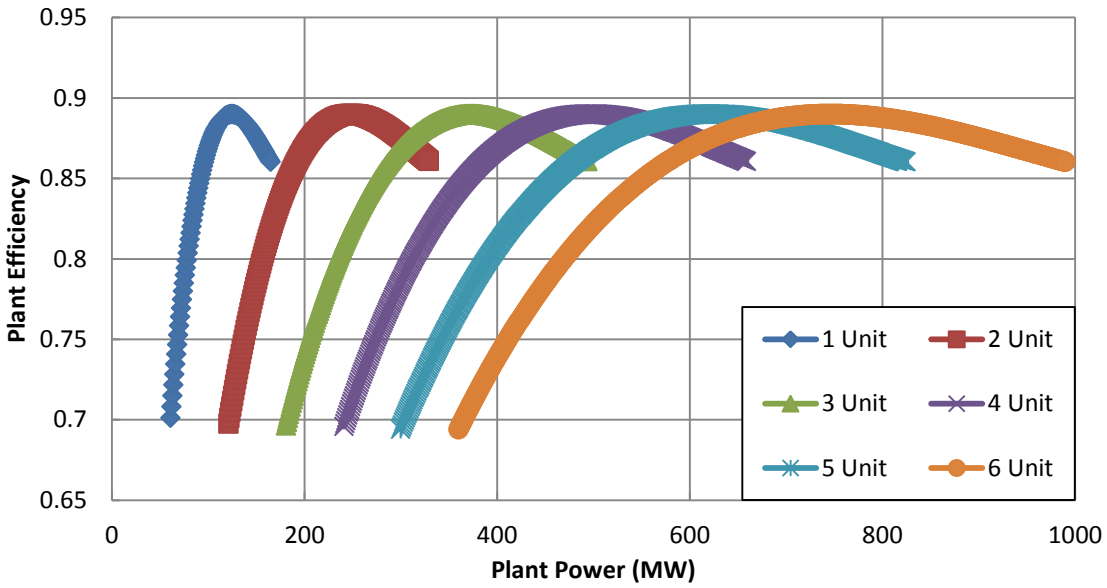

Figure 4.27: Performance of Unit Combinations

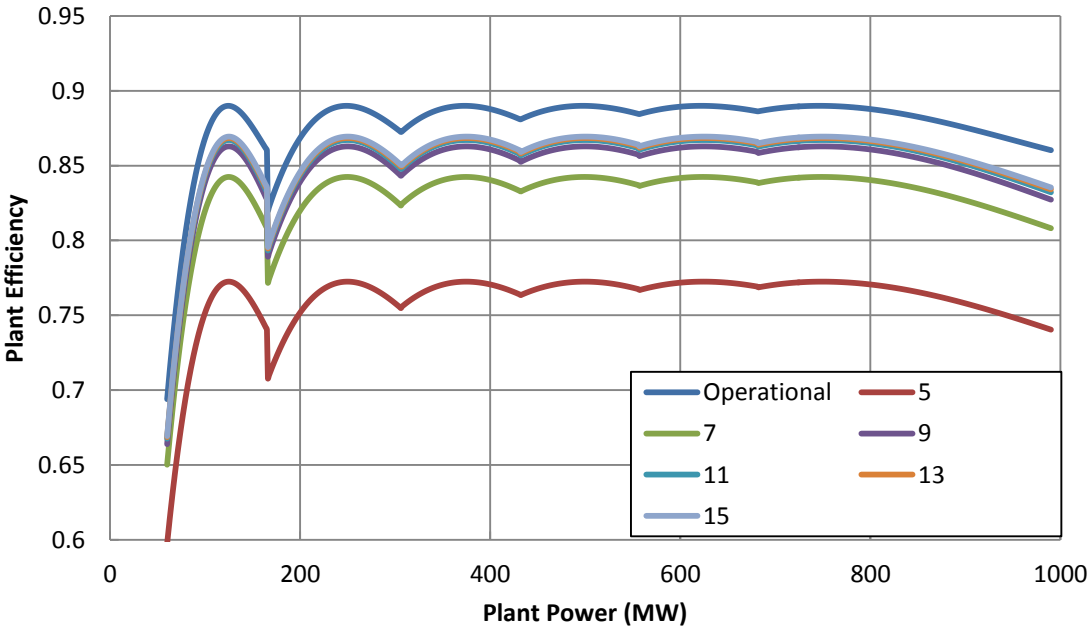

Figure 4.28: Optimal Dispatch of Units from General Static Current Meter Application

Table 6.1. Preliminary Investigation Specifications

Simulation Number	Closure Model	Right Inlet	Axial Inlet	Left Inlet
1	K-Eps	Symmetry	Mass Flow	Symmetry
2		Symmetry	Mass Flow	Mass Flow
3		Mass Flow	Mass Flow	Symmetry
4		Mass Flow	Mass Flow	Mass Flow
5	SST	Symmetry	Mass Flow	Symmetry
6		Symmetry	Mass Flow	Mass Flow
7		Mass Flow	Mass Flow	Symmetry
8		Mass Flow	Mass Flow	Mass Flow

Table 6.2. Preliminary Investigation Details

Total Flow Rate (kg sec^{-1})	Right Inlet (kg sec^{-1})	Axial Inlet (kg sec^{-1})	Left Inlet (kg sec^{-1})
290,360.47	64,428.80	64,428.80	161,502.87
368,826.32	81,839.78	81,839.78	205,146.76
414,104.88	91,886.75	91,886.75	230,331.39
509,560.82	113,067.70	113,067.70	283,425.41
565,769.66	125,540.02	125,540.02	314,689.62
633,928.20	140,663.88	140,663.88	352,600.43

Table 6.3. Turbine Head Loss Details

Flow Rate (m3/sec)	Turbine Head Loss (Pa)	Normal Velocity (m/sec)	Viscous Resistance Correction
290.36	281,474.84	18.26	0.67
368.83	296,978.94	23.19	-0.20
414.10	297,390.97	26.04	-0.58
509.56	304,023.18	32.04	-0.39
565.77	304,924.88	35.58	-0.06
633.93	305,043.34	39.86	0.54

Table 6.4. Turbine Efficiency Coefficients

Coefficient	Value
TC_1	1.67E-15
TC_2	-5.06E-12
TC_3	6.23E-09
TC_4	-3.98E-06
TC_5	1.38E-03
TC_6	-2.42E-01
TC_7	1.75E+01

Table 6.5. Generator Efficiency Coefficients.

Coefficient	Value
GC_1	-1.28E-20
GC_2	6.44E-15
GC_3	-1.28E-09
GC_4	1.17E-04
GC_5	9.47E+01

Table 6.6. Intake Headloss Coefficients

Coefficient	Value
GC_1	1.80E-20
GC_2	-1.42E-15
GC_3	4.40E-11
GC_4	-6.70E-07
GC_5	5.02E-03
GC_5	-1.45E+01

Table 6.7. Unit 4 Cumulative Head Loss Calculations

Flow Rate (m^3sec^{-1})	Turbine System Pressure Drop (m)	Trashrack and Intake Losses (m)	Draft Tube Headloss (m)	Total Headloss (m)	Outlet Pressure (Pa)
290.36	28.66	0.12	1.33	30.11	339,983.70
368.83	30.26	0.15	2.14	32.55	315,738.31
414.10	30.31	0.17	2.70	33.17	309,493.06
509.56	30.98	0.22	4.08	35.28	288,292.18
565.77	31.07	0.25	5.03	36.35	277,473.42
633.93	31.09	0.31	6.32	37.71	263,732.79

Table 6.8.Computational Domain Outlet Pressure Characteristics

Flow Rate (m^3sec^{-1})	Physical Domain Characteristics			Computation Domain Characteristics		
	Outlet Velocity (m sec^{-1})	Distance from Porous Boundary (m)	Outlet Pressure (Pa)	Outlet Velocity (m sec^{-1})	Distance from Porous Boundary (m)	Outlet Pressure (Pa)
290.36	1.10	6.98	339,984	7.91	45.00	-63774
368.83	1.40	6.98	315,738	10.05	45.00	-106841
414.10	1.57	6.98	309,493	11.28	45.00	-125986
509.56	1.93	6.98	288,292	13.88	45.00	-179270
565.77	2.14	6.98	277,473	15.41	45.00	-212083
633.93	2.40	6.98	263,733	17.27	45.00	-255579

Table 6.9.Mesh Quality Results

Face Validity			Volume Change		
Bottom of Range	Top of Range	Number of Cells	Bottom of Range	Top of Range	Number of Cells
0	0.5	0	Below 0		0
0.5	0.6	0	0.0	1.0E-6	0
0.6	0.7	0	1.0E-6	1.0E-5	0
0.7	0.8	0	1.0E-5	1.0E-4	0
0.8	0.9	1	1.0E-4	1.0E-3	4
0.9	0.95	3	1.0E-3	1.0E-2	654
0.95	1.0	50	1.0E-2	1.0E-1	47864
Equivalent to 1.0		14753130	1.0E-1	1.0	14704662

Table 6.10. Recirculation Zone Study As-Built and Surface Roughness Modifications

		Vault Celling Structure Permutations		
		As-Built	Straight Obstruction	Angled Obstruction
Bay Floor Roughness Permutations (m)	Smooth			
	0.09			
	0.18			

Table 6.11. Backwards Facing Step Velocity Polynomial Coefficients

Coefficient	Value
A_{BFS1}	0.4453
A_{BFS2}	0.0532
A_{BFS3}	1.2531
A_{BFS4}	-0.0011
A_{BFS5}	0.0584
A_{BFS6}	-0.8068
A_{BFS7}	-0.0010
A_{BFS8}	-0.0336
A_{BFS9}	0.1095
A_{BFS10}	-2.2053
A_{BFS11}	0.0001
A_{BFS12}	0.0023
A_{BFS13}	0.0106
A_{BFS14}	0.3000
A_{BFS15}	-0.3438

Table 6.12.Computational Domain Outlet Pressure Characteristics

Current Meter	Ott C31-1 Aluminum	Ott C31-1 Plastic	Ott C31-A Aluminum	Ott C31-R Aluminum
$\int_{R_h}^{R_t} l dr_{blade}$ (m^2)	3.33E-03	3.33E-03	2.26E-03	2.59E-03
$\int_{R_h}^{R_t} l {r_{blade}}^2 dr_{blade}$	2.64E-06	2.64E-06	1.19E-06	1.15E-06
I_{Prop} (kg m^2)	4.18E-05	2.58E-05	2.73E-05	1.56E-05

Table 6.13.Computational Domain Outlet Pressure Characteristics

Current Meter	Ott C31-1 Aluminum	Ott C31-1 Plastic	Ott C31-A Aluminum	Ott C31-R Aluminum
a_{blade}	1.89E-01	1.89E-01	3.36E-01	1.60E-01
b_{blade}	-3.78E-01	-3.78E-01	-4.20E-01	-3.99E-01

Table 6.14. Axial Pulsation Correction Factor Coefficients

Coefficient	Value
A_{p_1}	3.785E-01
A_{p_2}	1.736E-02
A_{p_3}	-5.751E-01
A_{p_4}	-8.199E-02
A_{p_5}	7.547E-04
A_{p_6}	1.106E+00
A_{p_7}	4.160E-02
A_{p_8}	1.334E-02
A_{p_9}	-7.594E-04
A_{p_10}	-4.868E-01
A_{p_11}	-1.244E-02
A_{p_12}	-1.887E-03
A_{p_13}	-7.189E-04
A_{p_14}	5.453E-05

Table 6.15. Individual Drag Coefficient Calculation Results

Angle (degrees)	Ott Plastic	Ott Metal	Ott A	Ott R
70	0.001598	0.104716	0.070861	0.121312
60	-0.188897	-0.159338	0.220495	0.022099
50	-0.380275	-0.340784	0.216021	-0.099459
40	-0.602388	-0.735257	0.338228	-0.245139
30	-0.525979	-0.776064	0.494918	-0.155366
20	-0.440561	-0.607675	0.948156	-0.942413
10	0.003112	-0.419723	2.287840	-2.190864
0	0.000000	0.000000	0.000000	0.000000

Table 6.16. Transverse Drag Coefficient Factor Coefficients

Value	Ott Plastic	Ott Metal	Ott A	Ott R
C_{d1}	0	0	-4.28E-09	2.49E-09
C_{d2}	0	-3.42E-10	1.00E-06	-6.42E-07
C_{d3}	-4.99E-07	-1.77E-07	-9.21E-05	6.48E-05
C_{d4}	7.18E-05	2.30E-05	4.12E-03	-3.19E-03
C_{d5}	-2.76E-03	-3.82E-05	-9.09E-02	7.66E-02
C_{d6}	1.23E-02	-3.97E-02	8.07E-01	-7.26E-01
C_{d7}	1.84E-02	-6.94E-03	1.36E-03	1.60E-03
R^2	0.957	0.978	0.998	0.998

Table 6.17. Transverse Turbulent Response Correction Factor Coefficients

Coefficient	Value
C_{dt_1}	0.073212693
C_{dt_2}	-0.472796628
C_{dt_3}	0.02450462
C_{dt_4}	0.97283251
C_{dt_5}	0.05726543
C_{dt_6}	-0.213750608
C_{dt_7}	-0.667483631
C_{dt_8}	0.063742362
C_{dt_9}	-0.195069171
C_{dt_10}	0.375630382

Appendix 9: Chapter 5 Figures and Tables

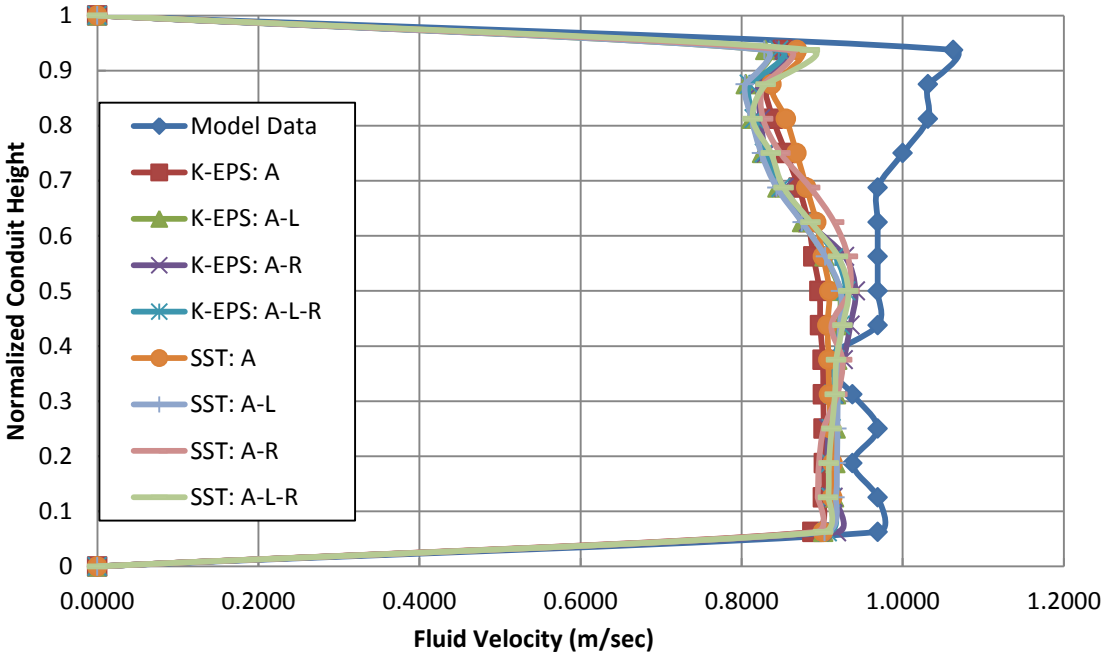

Figure 5.1: Upstream Model Preliminary Investigation Velocity Distribution

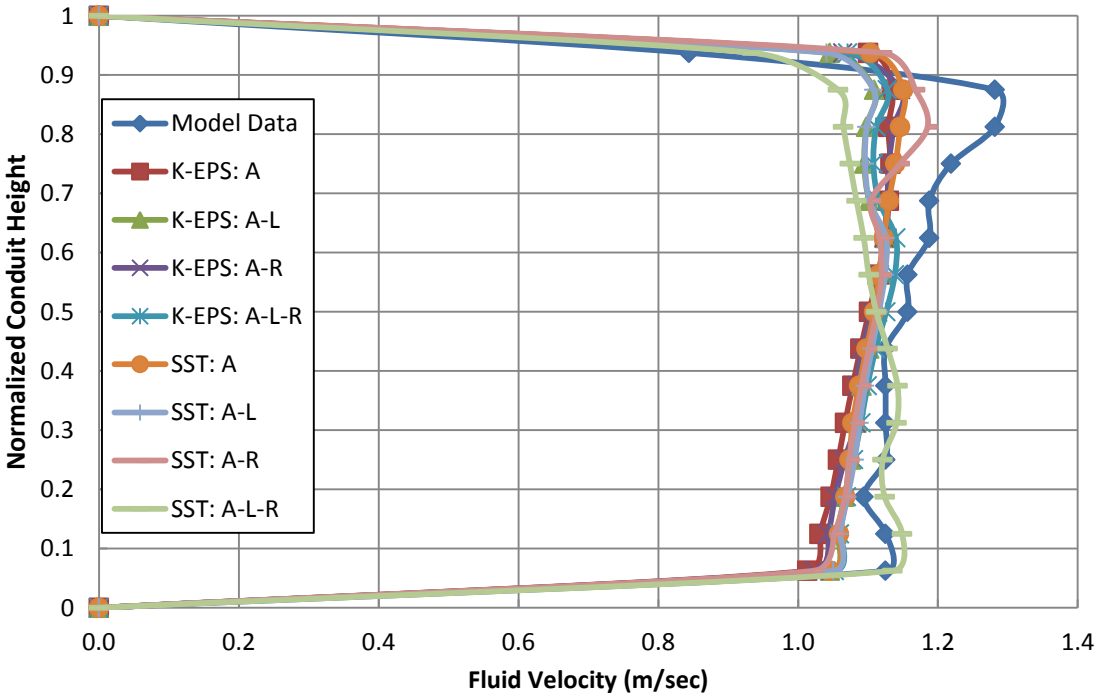

Figure 5.2: Downstream Model Preliminary Investigation Velocity Distribution

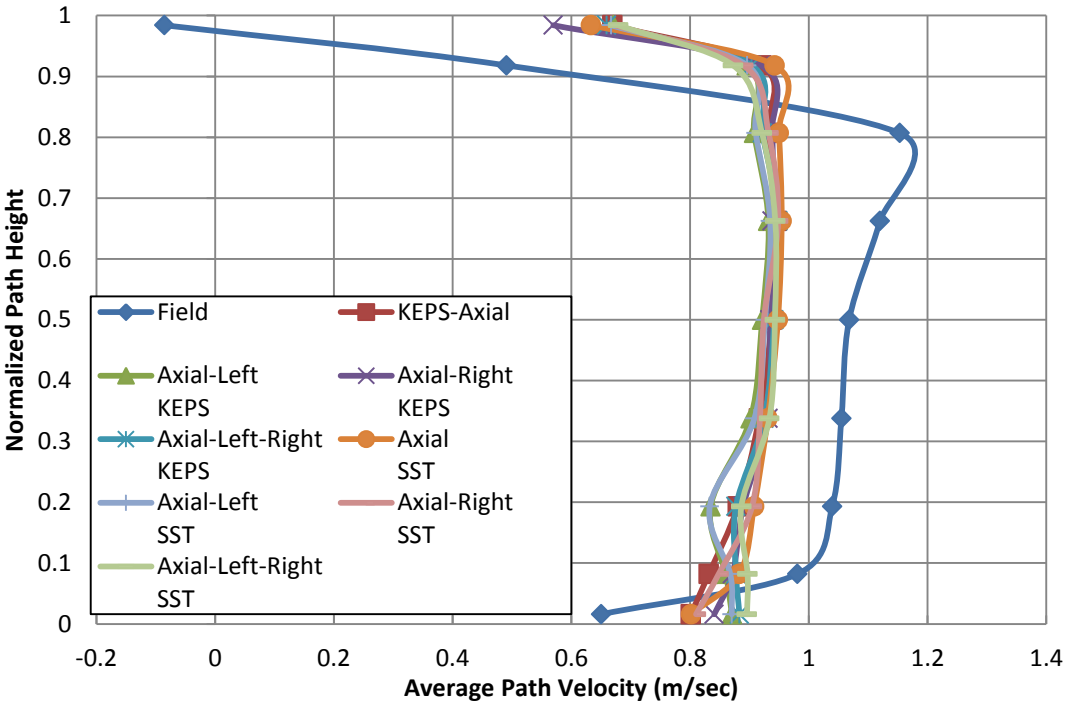

Figure 5.3: Bay C Acoustic Time of Flight Recorded Velocity Distribution

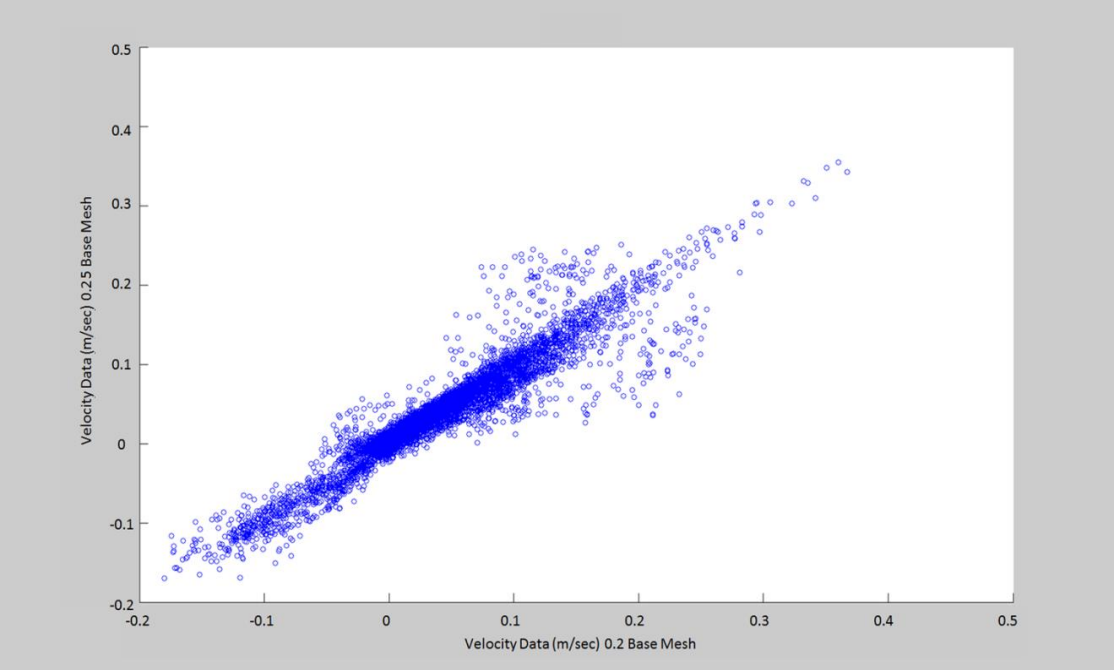

Figure 5.4a: Bay A-U Velocity Comparison

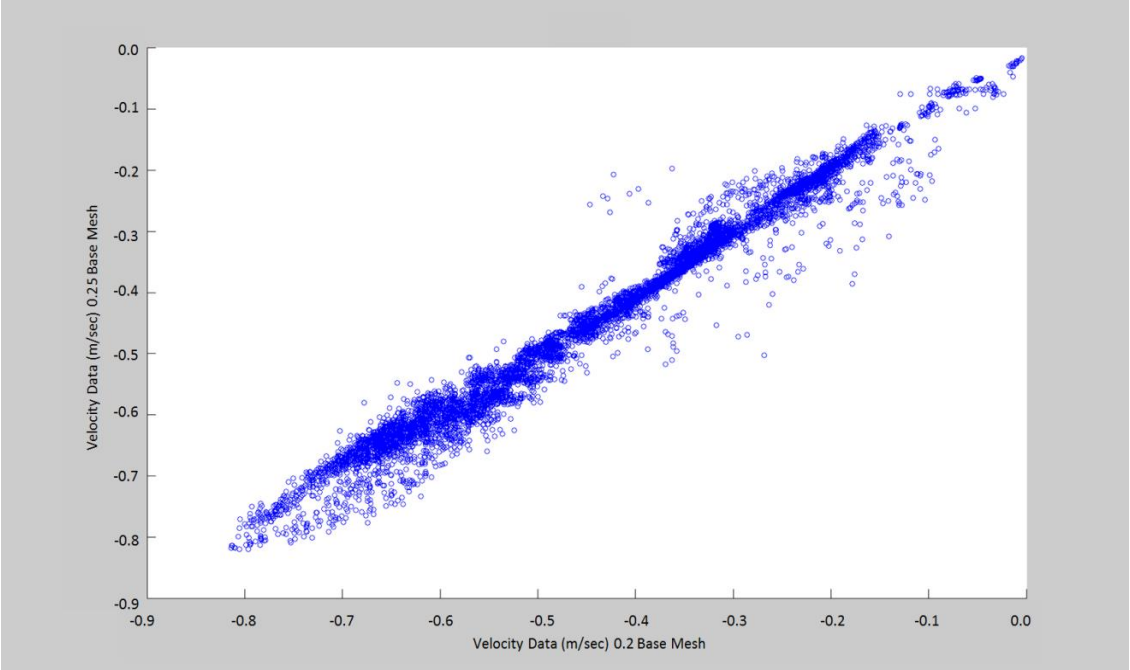

Figure 5.4b: Bay A-V Velocity Comparison

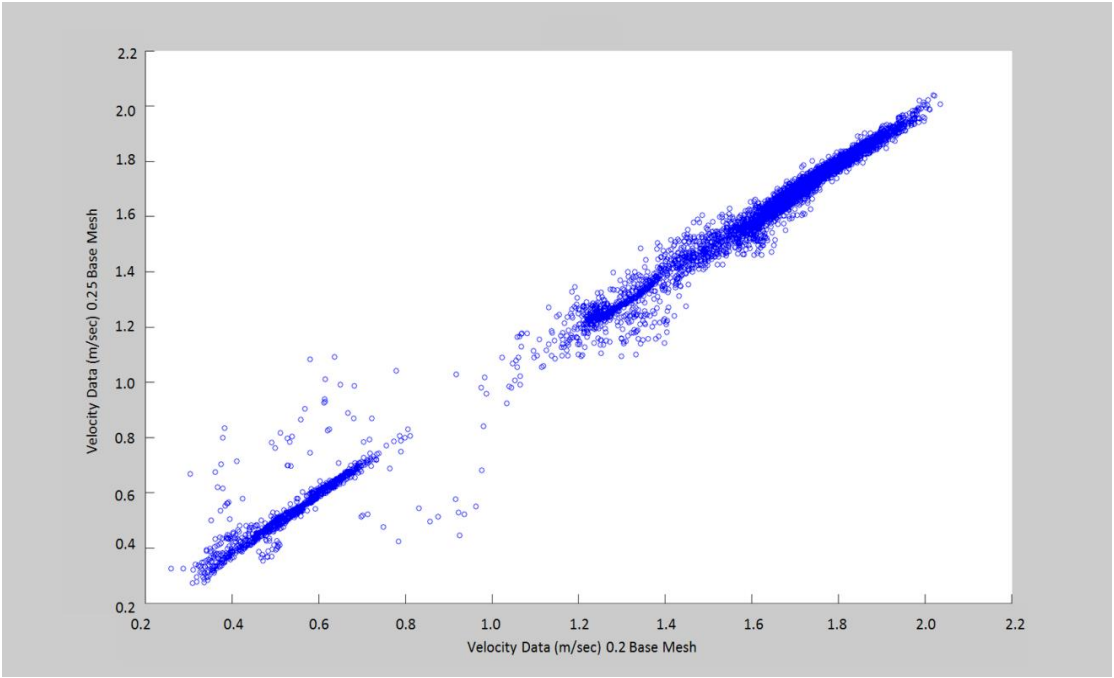

Figure 5.4c: Bay A-W Velocity Comparison

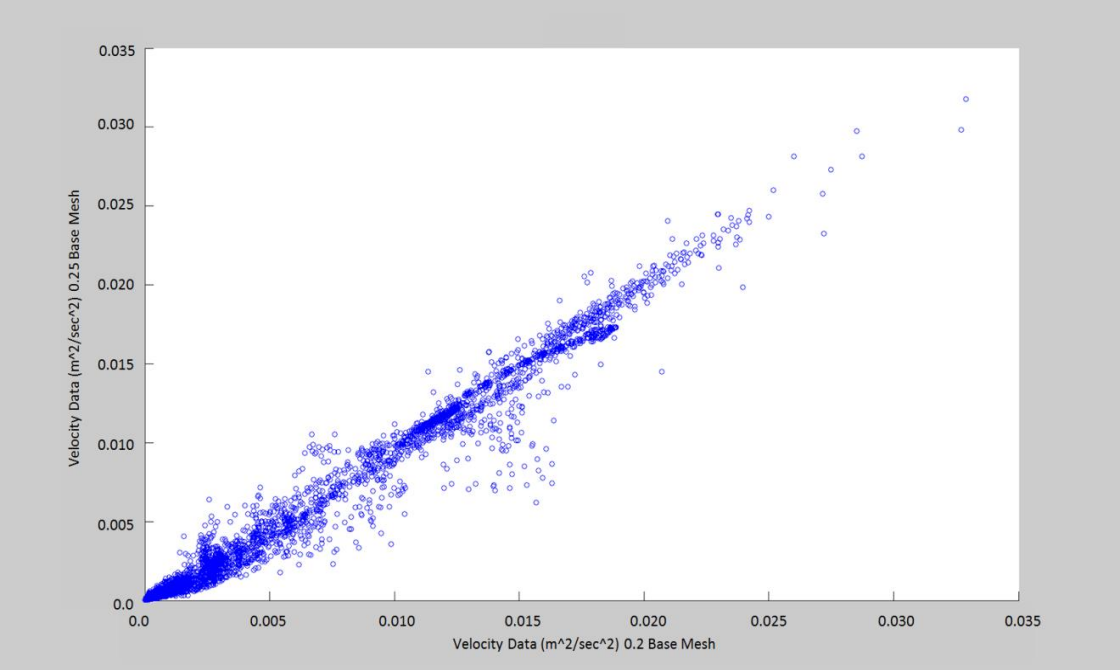

Figure 5.4d: Bay A-TKE Comparison

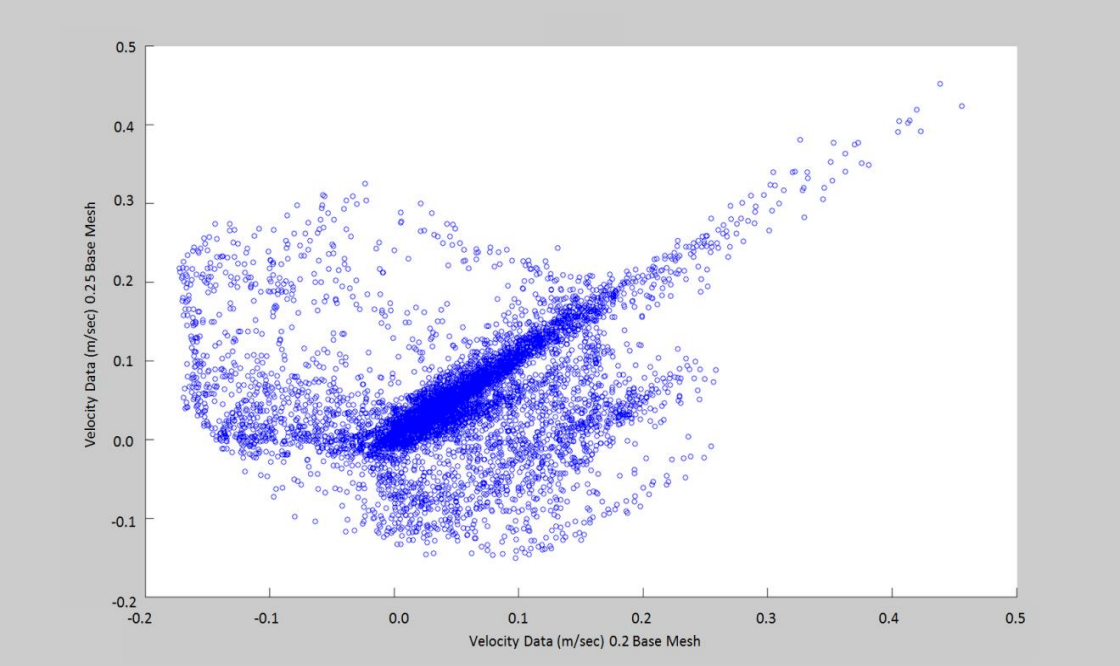

Figure 5.5a: Bay B-U Velocity Comparison

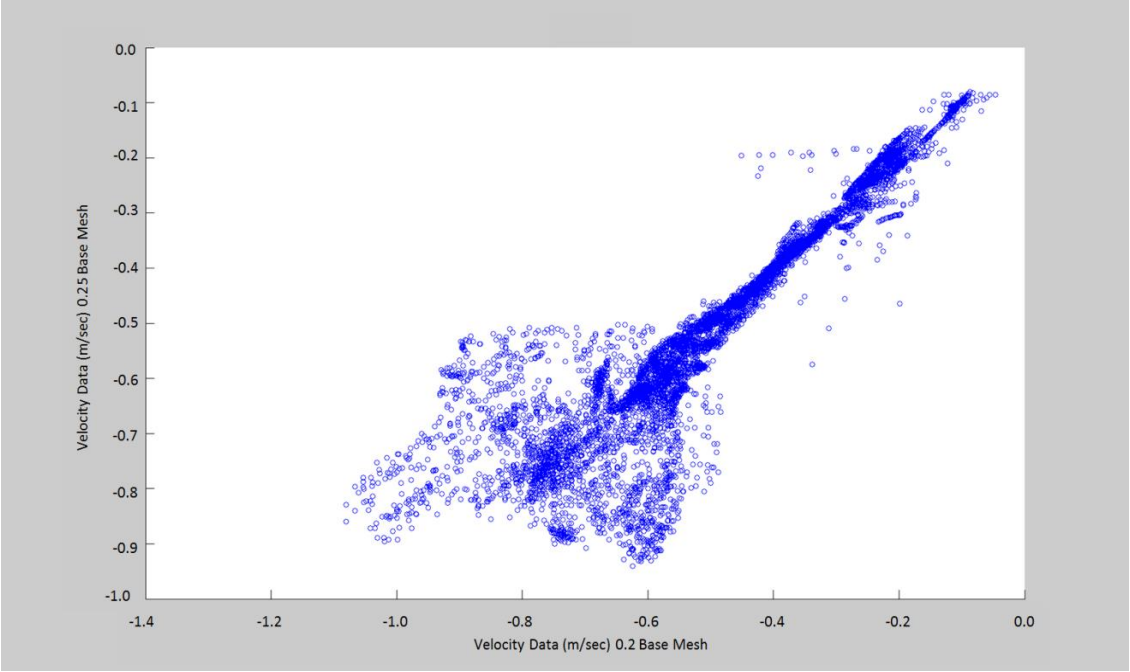

Figure 5.5b: Bay B-V Velocity Comparison

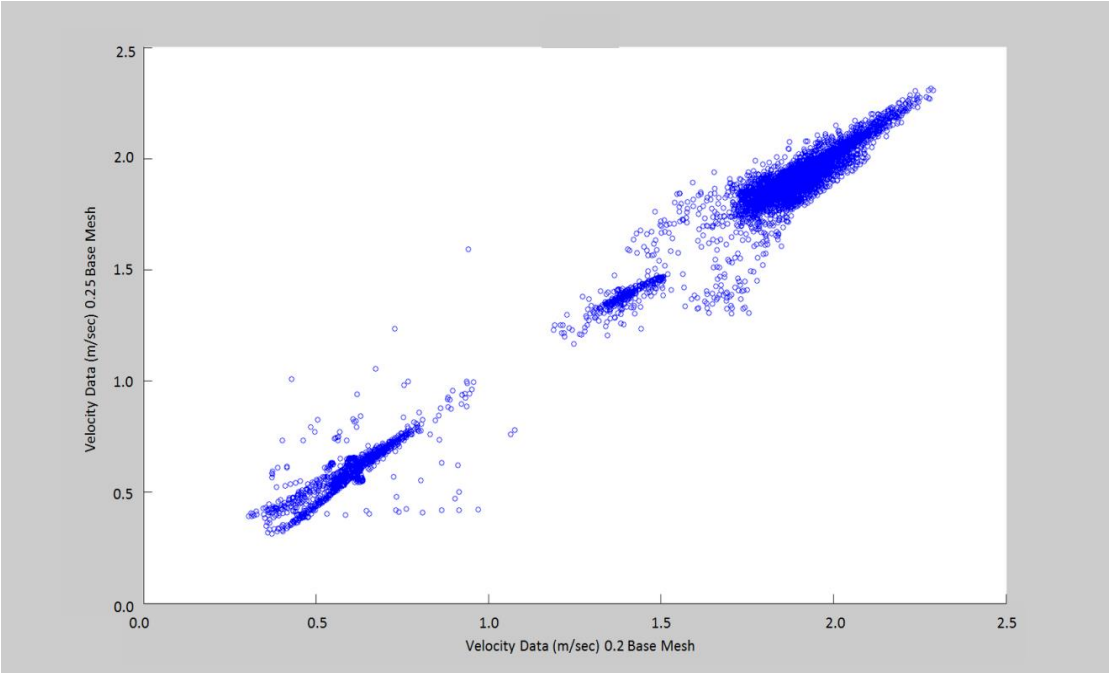

Figure 5.5c: Bay B-W Velocity Comparison

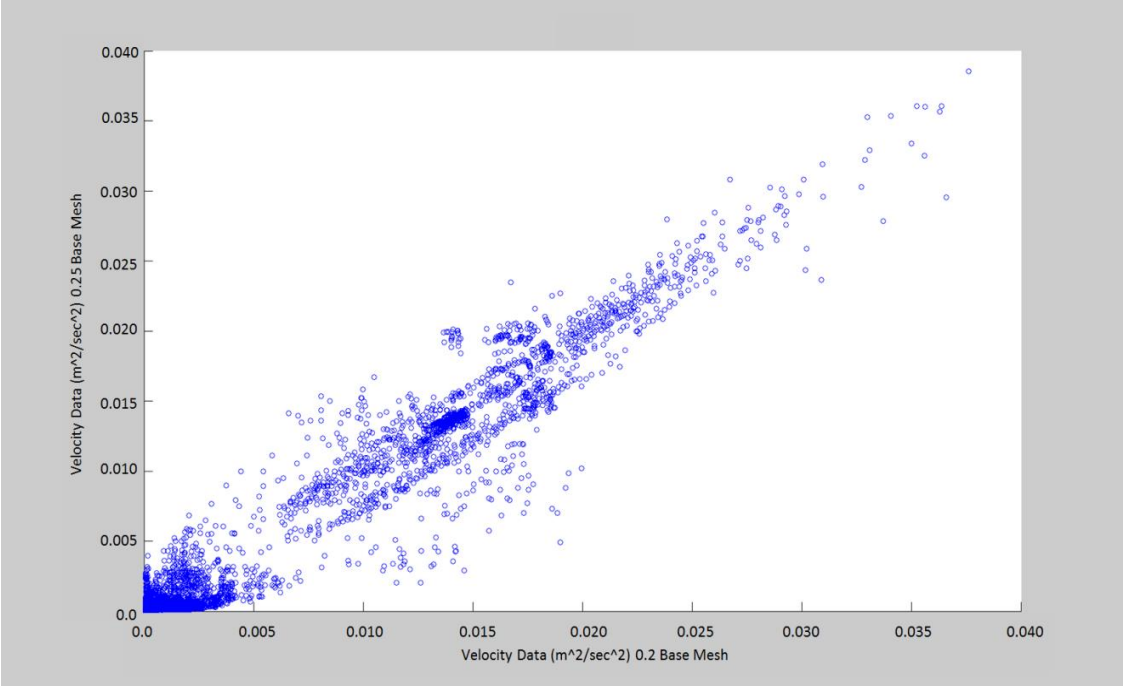

Figure 5.5d: Bay B-TKE Comparison

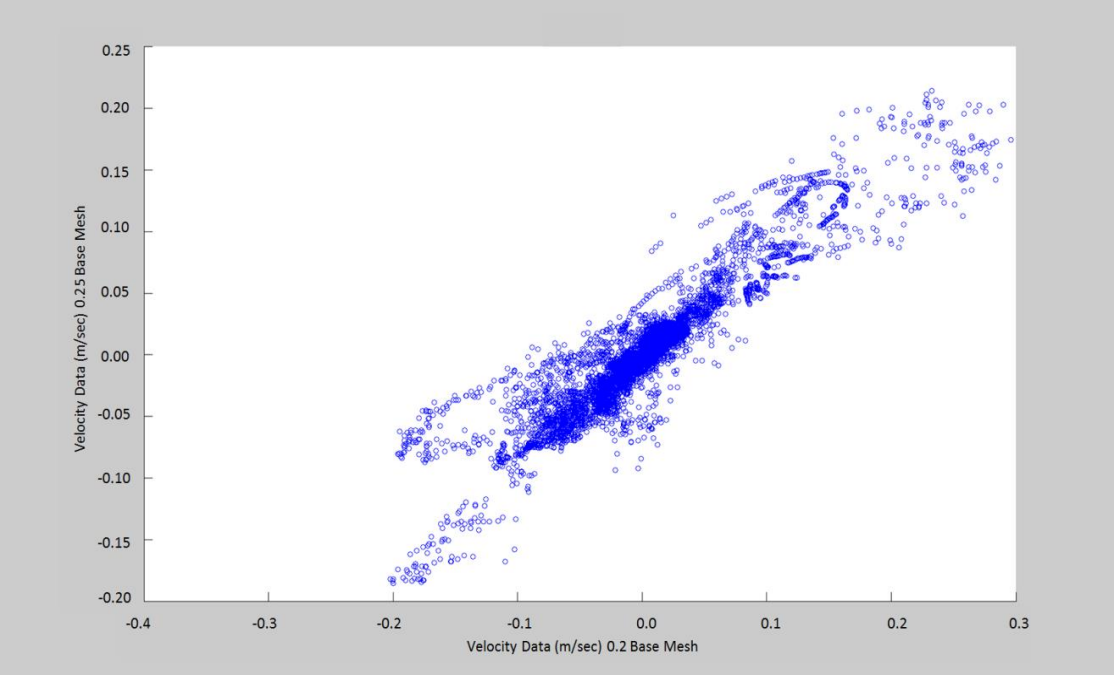

Figure 5.6a: Bay C-U Velocity Comparison

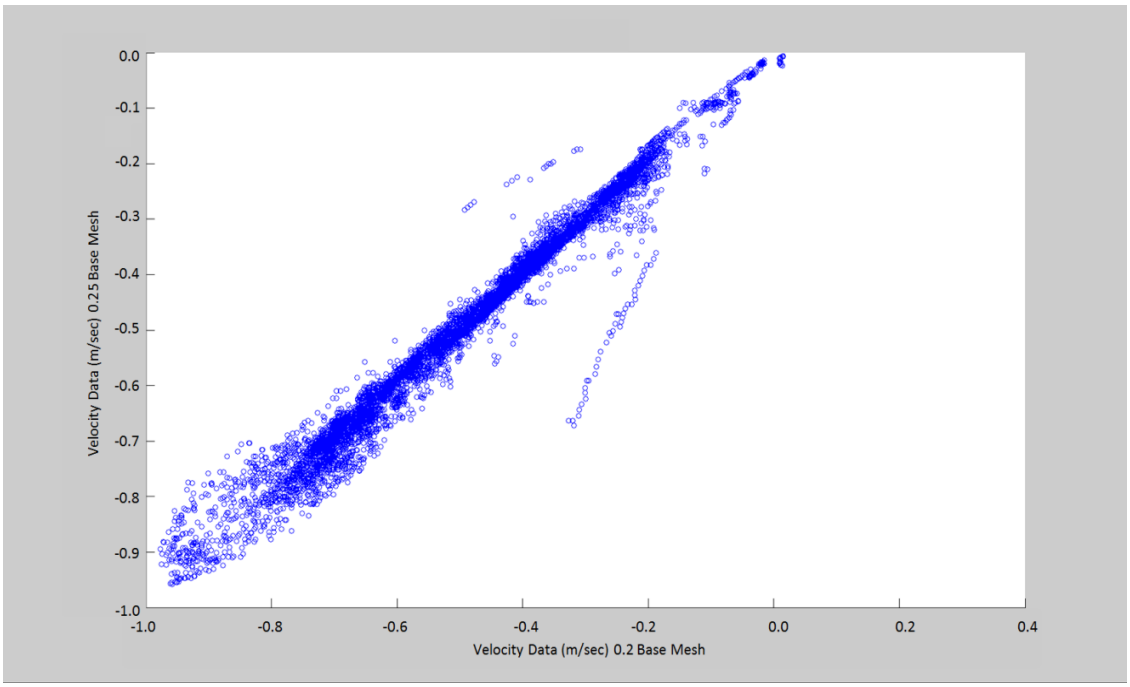

Figure 5.6b: Bay B-V Velocity Comparison

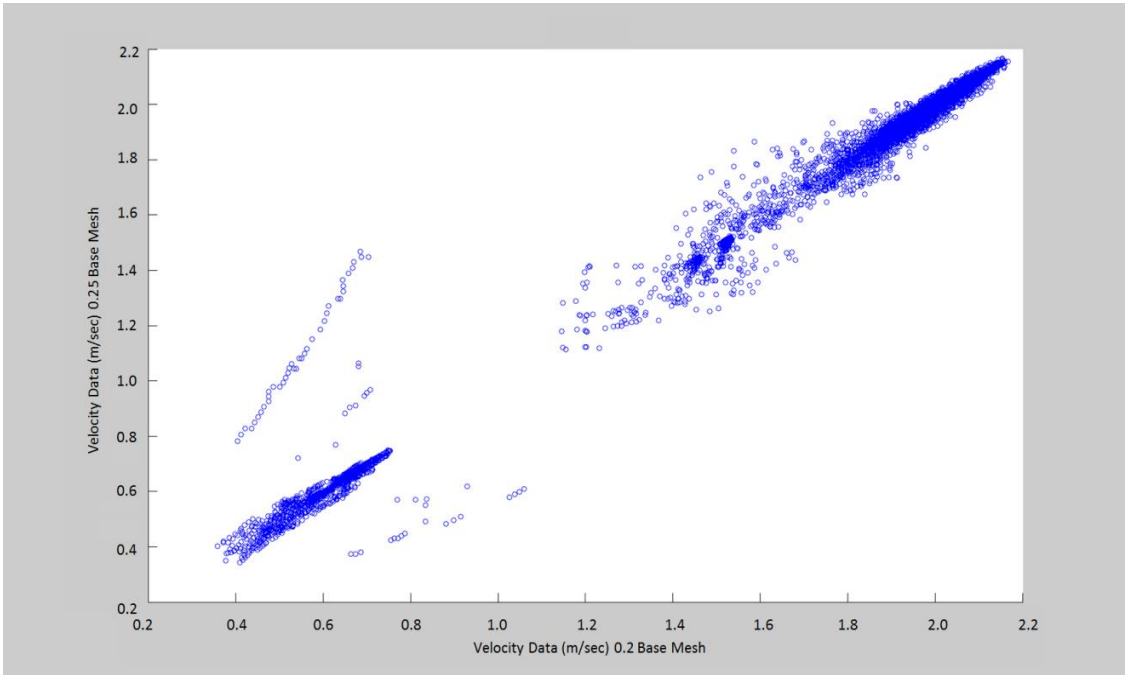

Figure 5.6c: Bay C-W Velocity Comparison

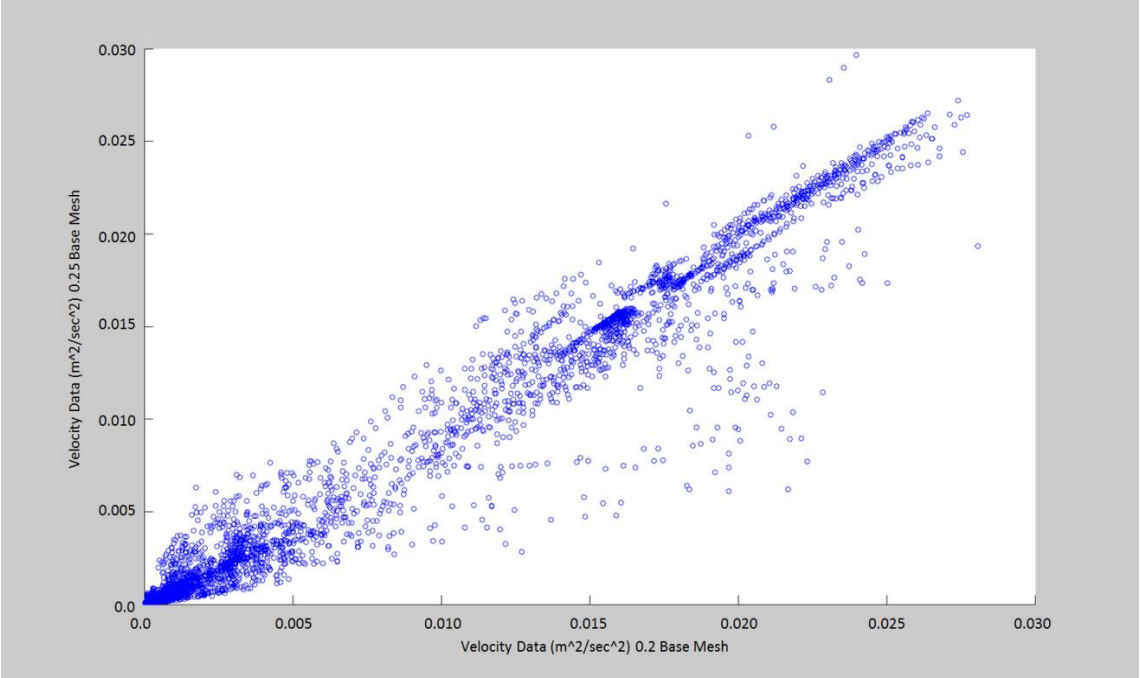

Figure 5.6d: Bay C-TKE Comparison

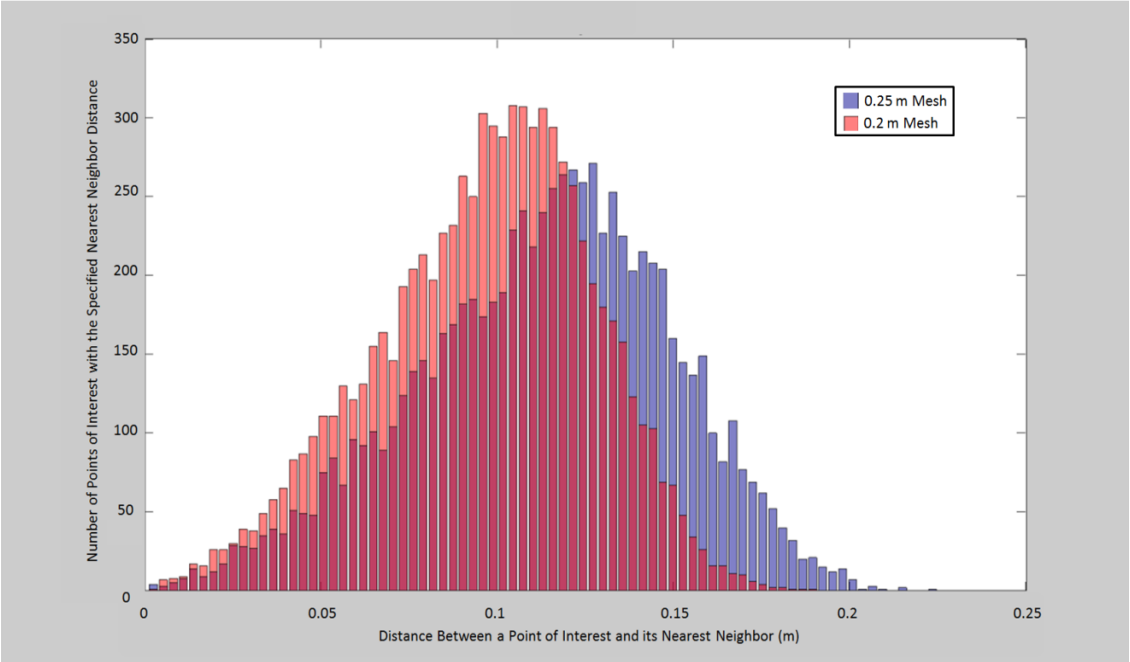

Figure 5.7: Bay A-Nearest Neighbor Histogram

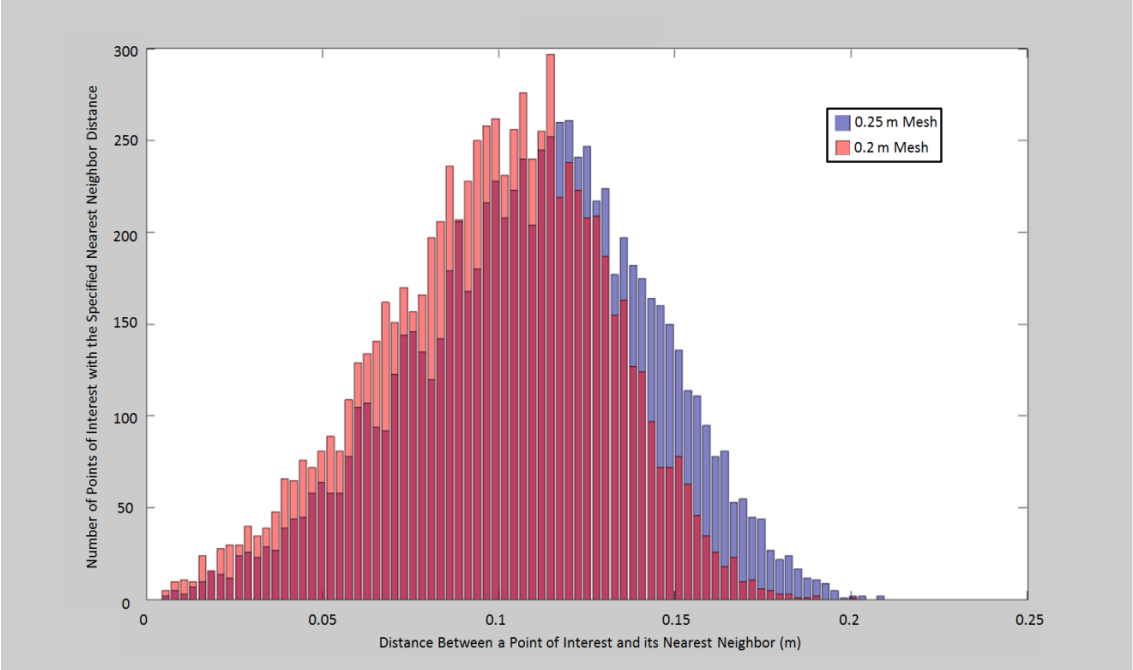

Figure 5.8: Bay B-Nearest Neighbor Histogram

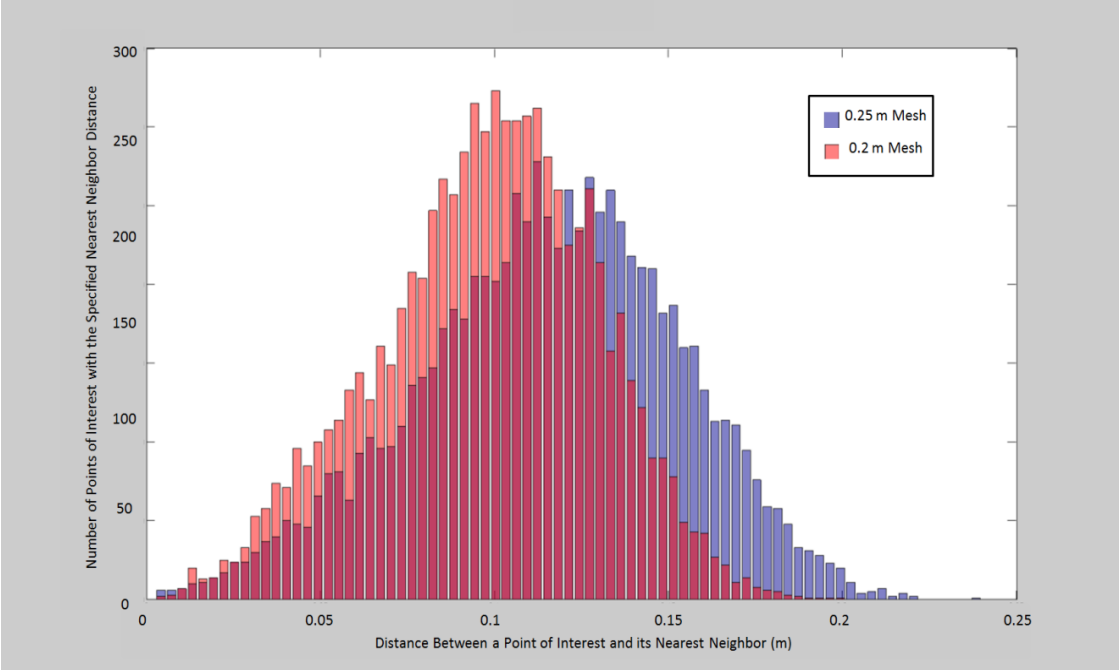

Figure 5.9: Bay C-Nearest Neighbor Histogram



Figure 5.10: CFD Residual Plot

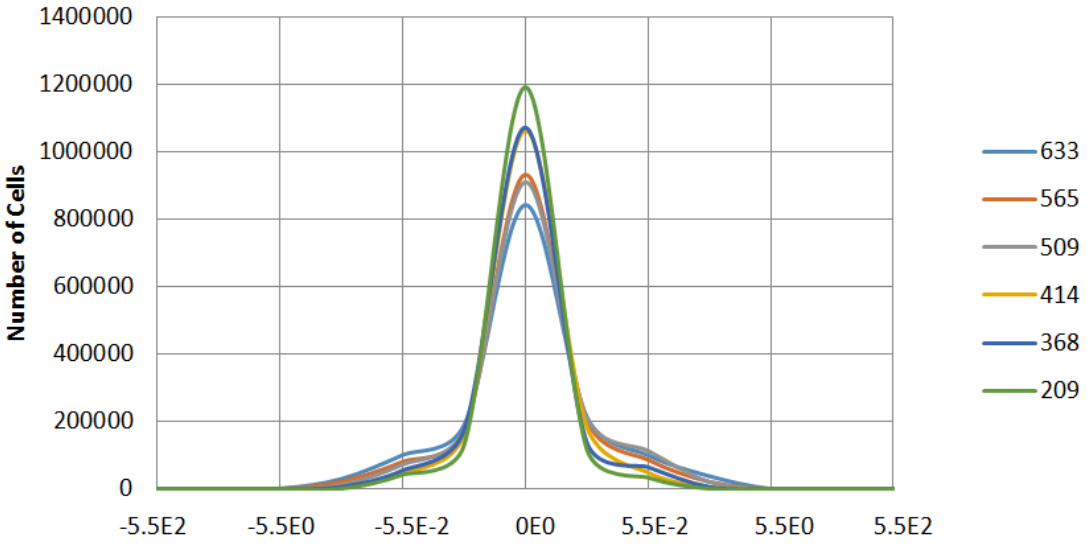

Figure 5.11a: Local U-Velocity Residual Histogram

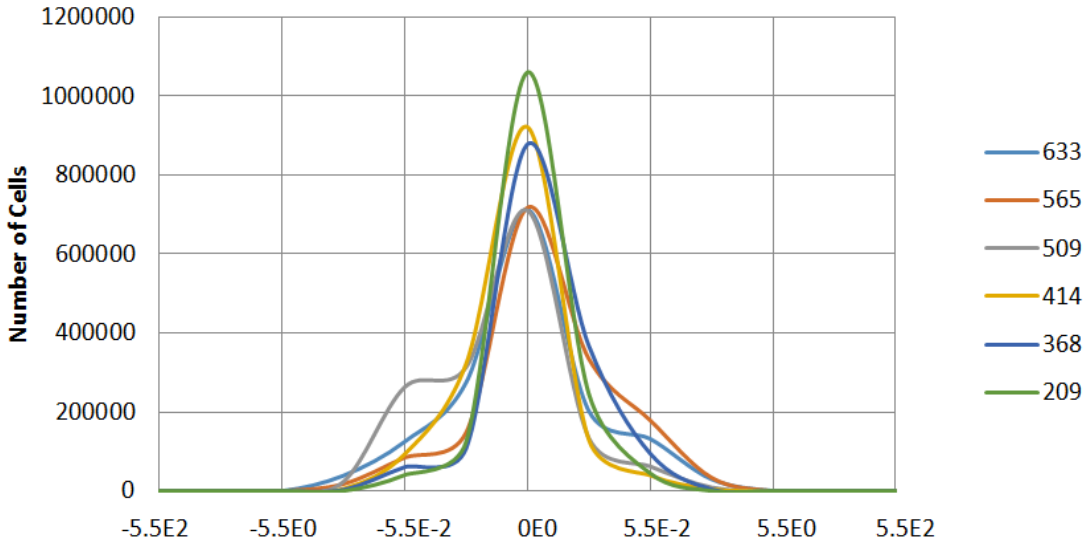

Figure 5.11b: Local V-Velocity Residual Histogram

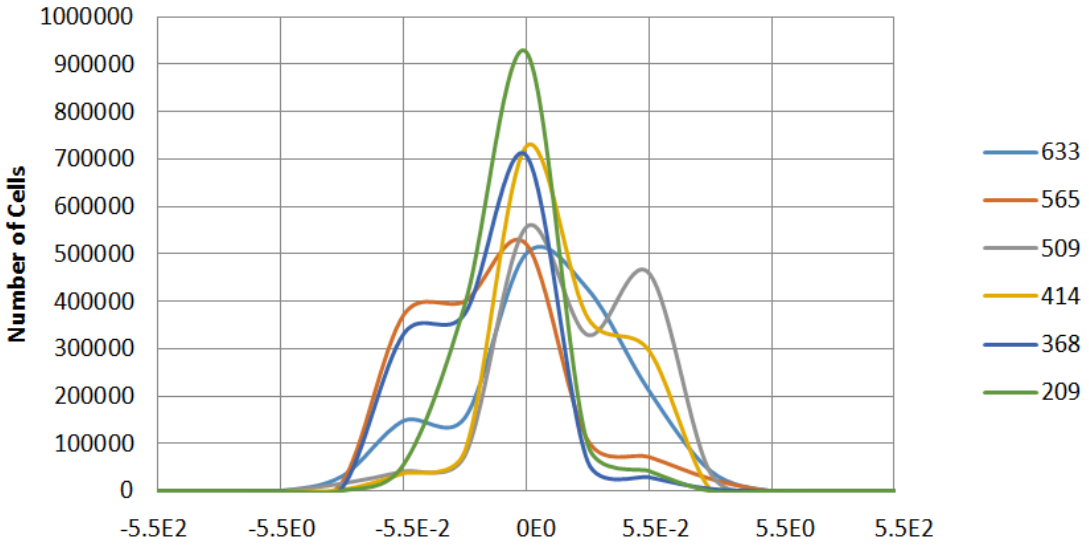

Figure 5.11c: Local W-Velocity Residual Histogram

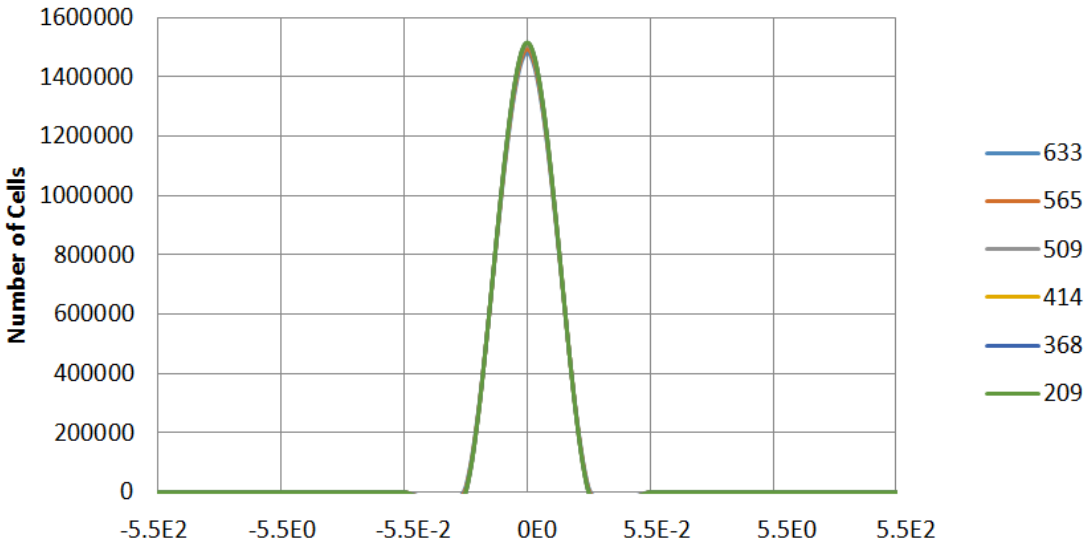

Figure 5.11d: Local TKE Residual Histogram

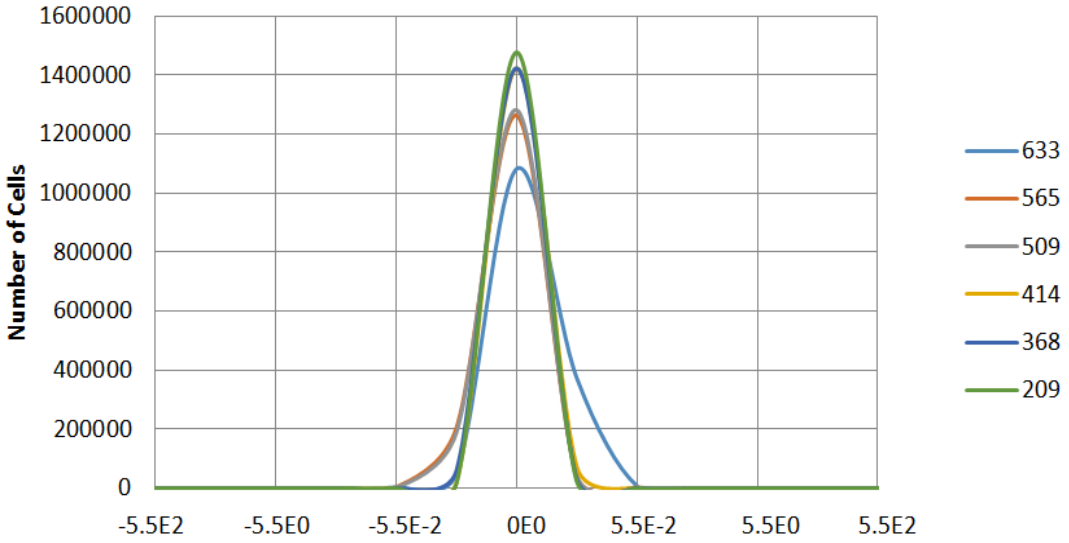

Figure 5.11e: Local Continuity Residual Histogram

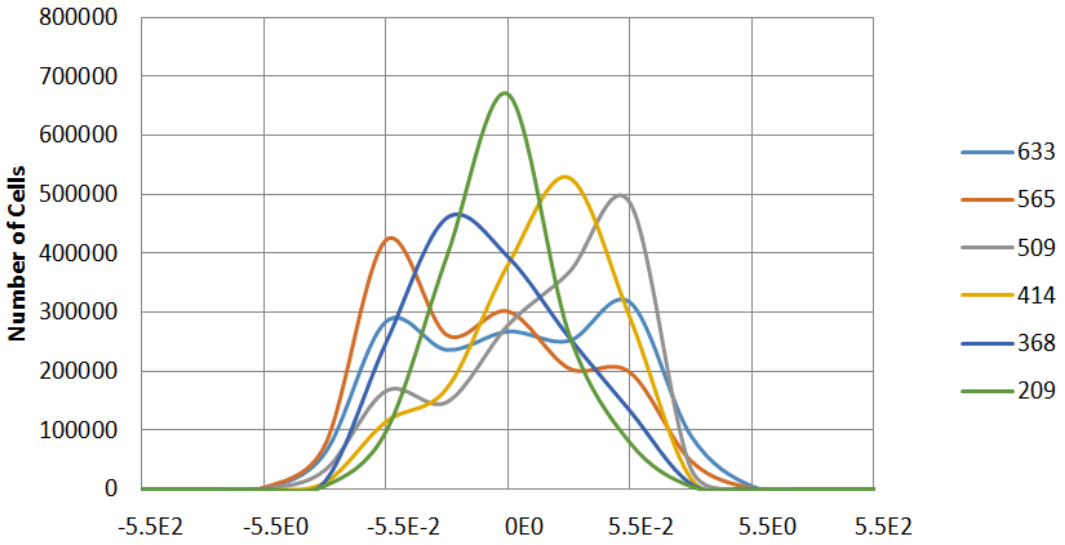

Figure 5.11f: Local TDR Residual Histogram

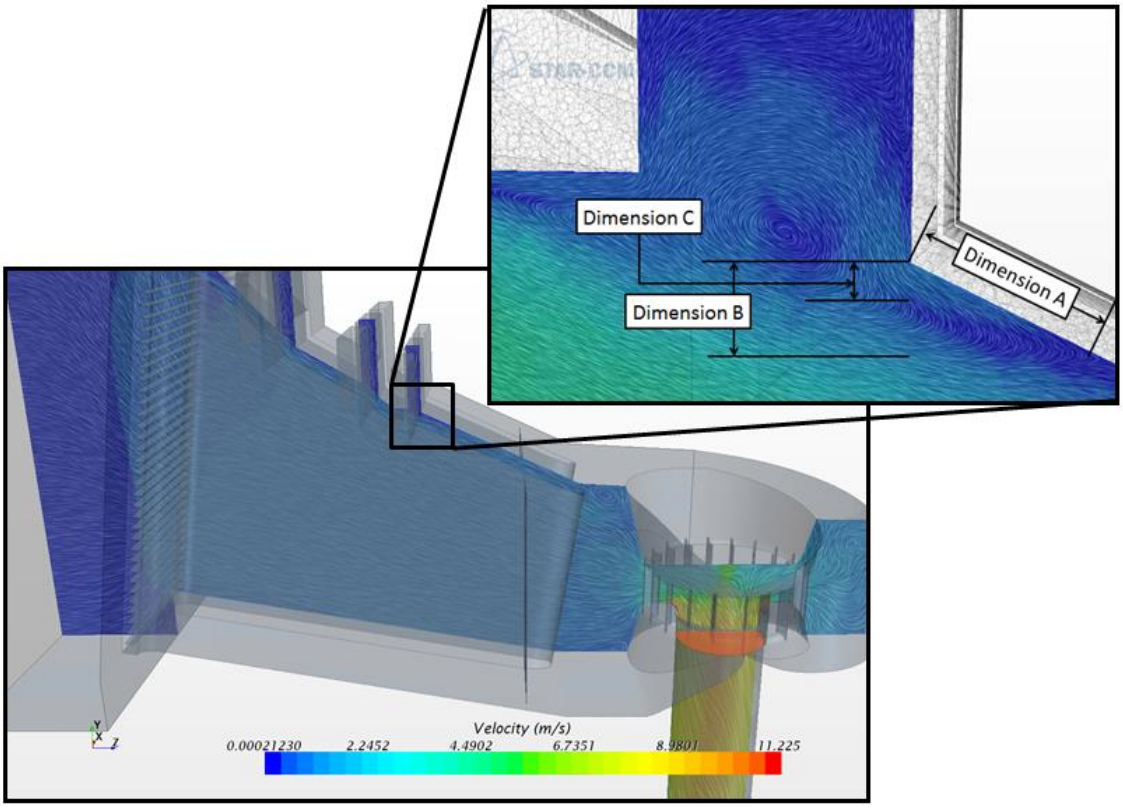

Figure 5.12: Diagram of Flow Recirculation Characteristics

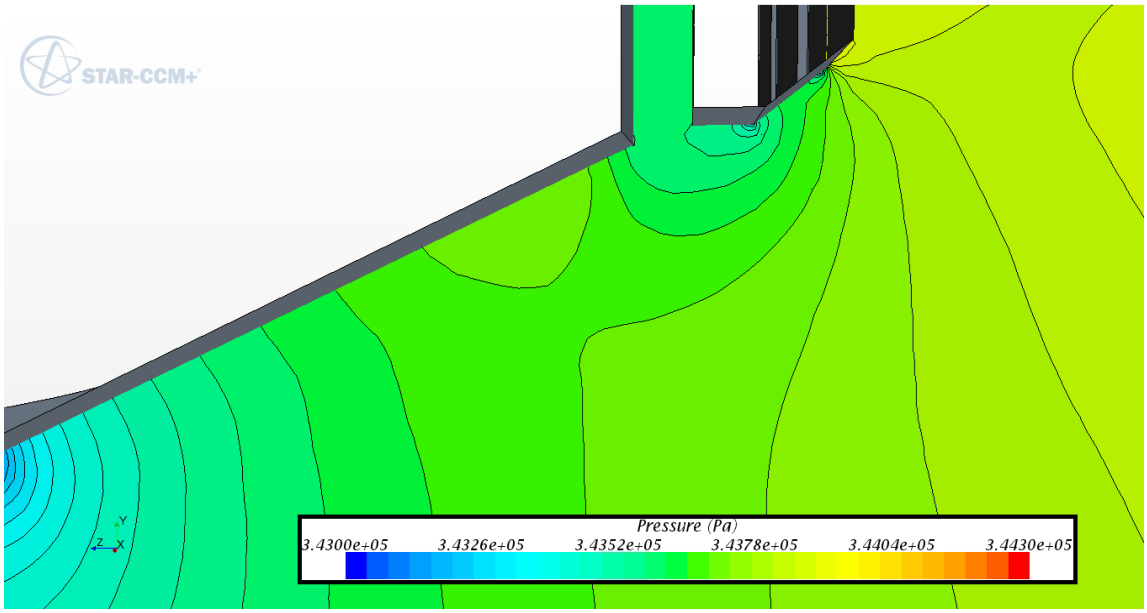

Figure 5.13: Pressure Distribution at the Recirculation Site

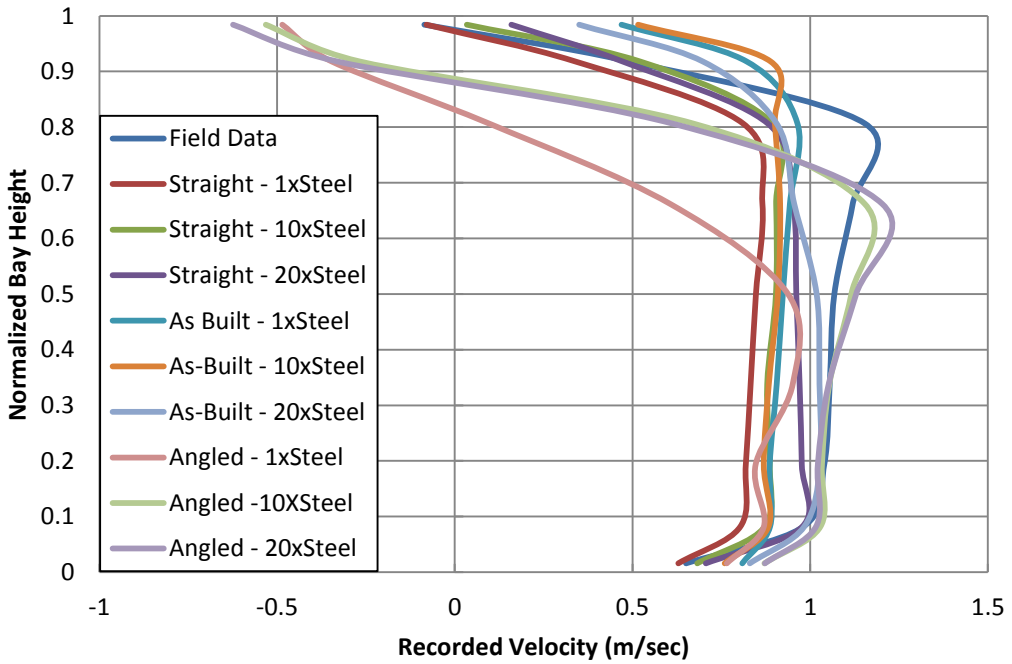

Figure 5.14: Bay A Velocity Distribution Resulting From As-Built Modifications

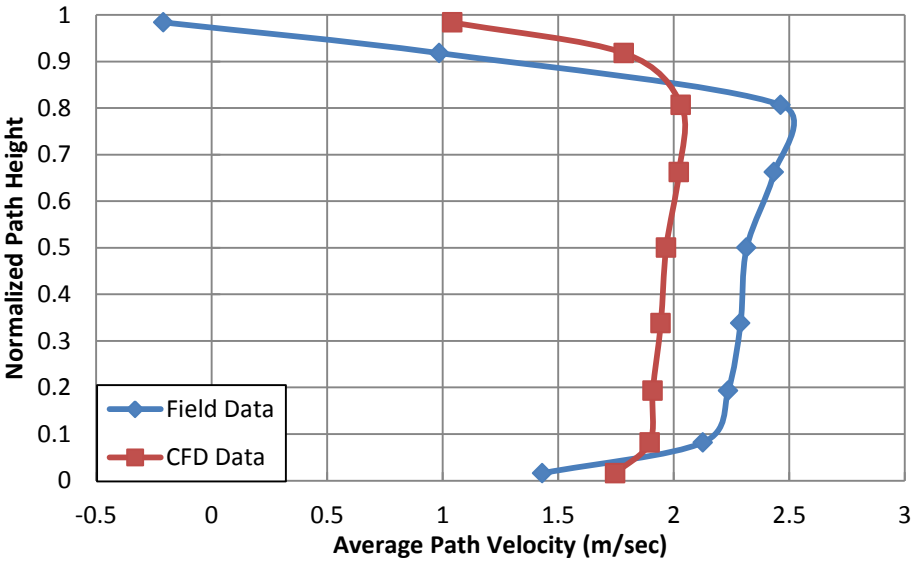

Figure 5.15: Bay A Validation at 634 m^3sec^{-1}

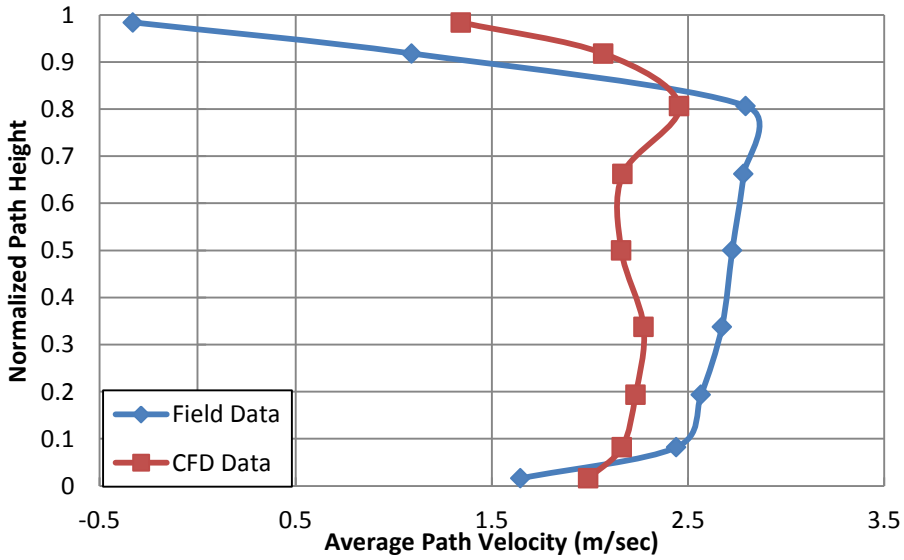

Figure 5.16: Bay B Validation at 634 m^3sec^{-1}

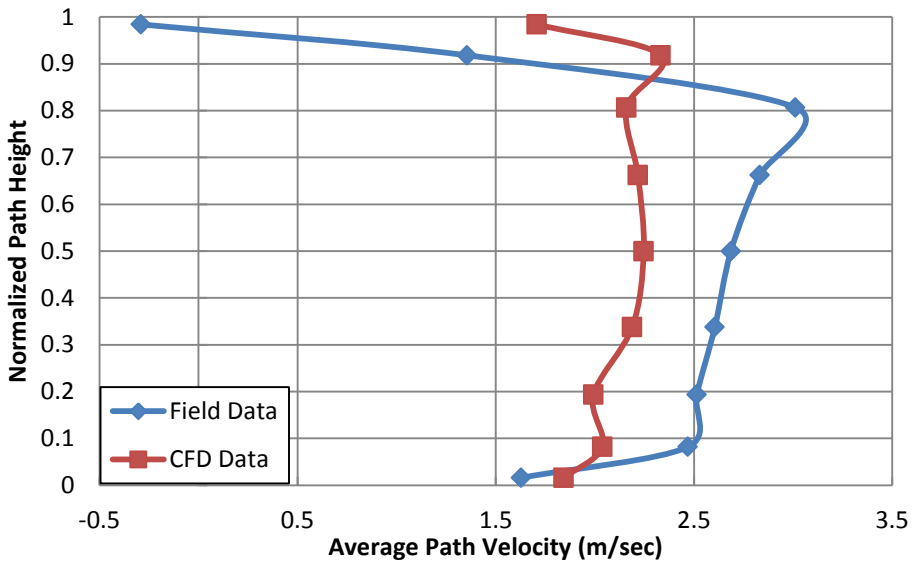

Figure 5.17: Bay C Validation at 634 m^3sec^{-1}

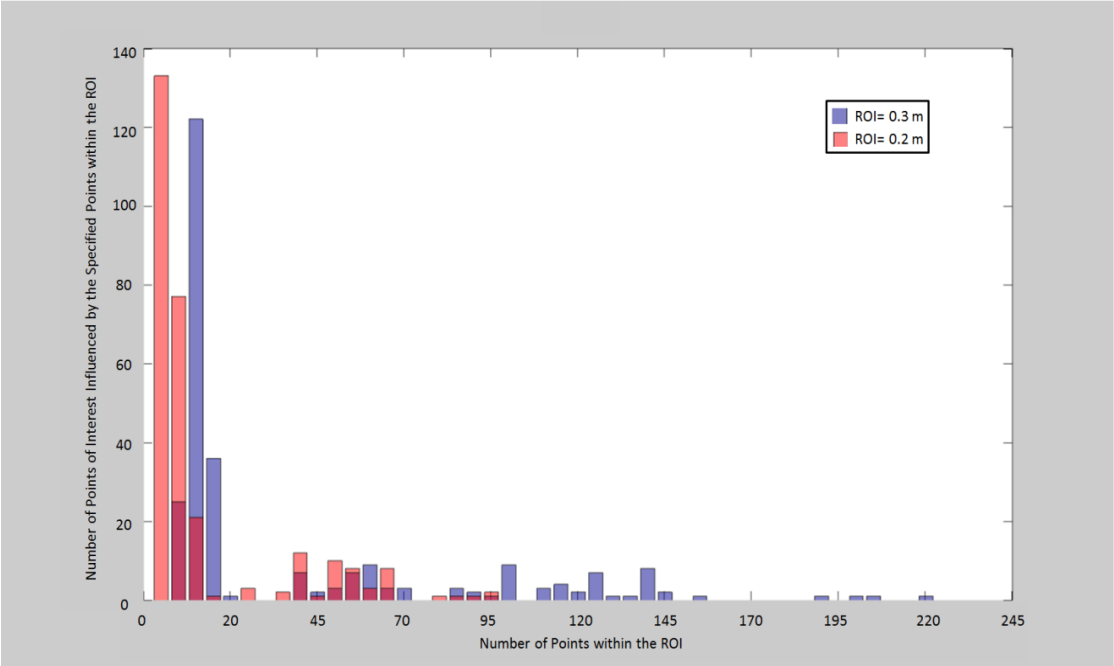

Figure 5.18: Number of Points of Influence Histogram

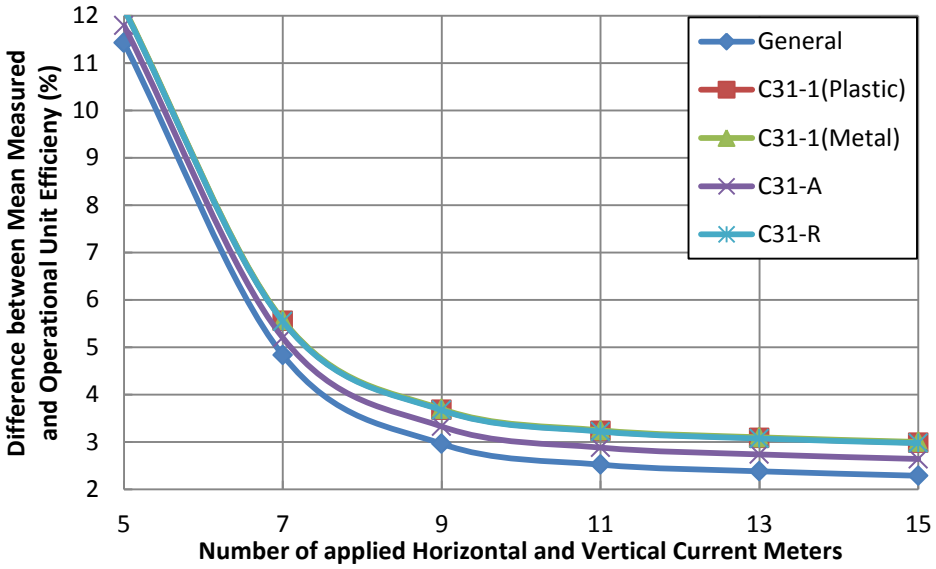

Figure 5.19: As-Built Static Current Meter Accuracy Differential

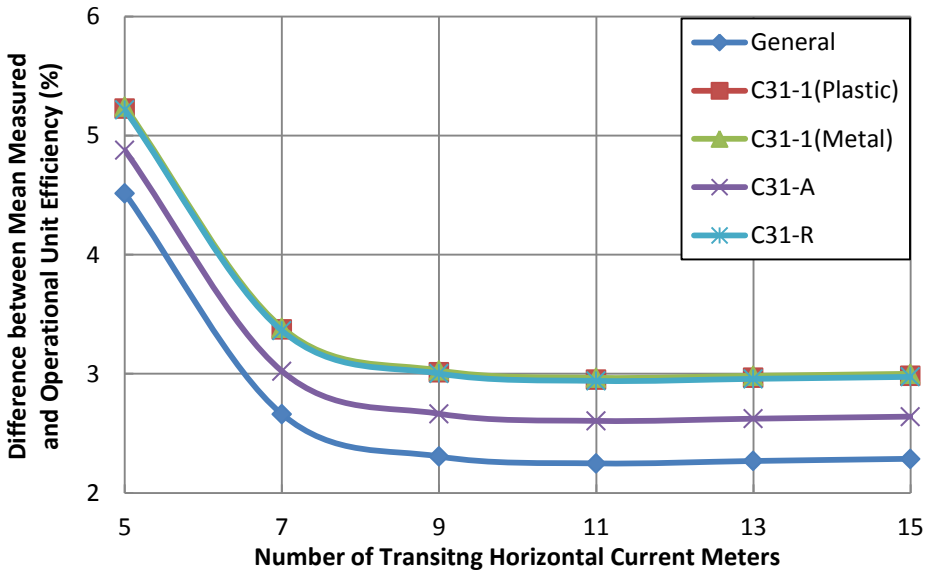

Figure 5.20 As-Built Dynamic Current Meter Accuracy Differential

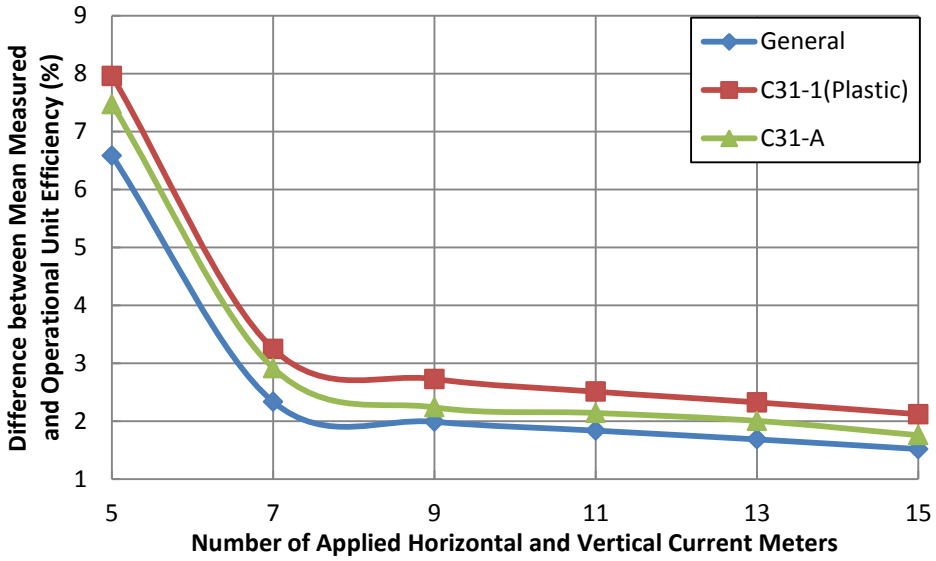

Figure 5.21: Modified As-Built Static Current Meter Accuracy Differential

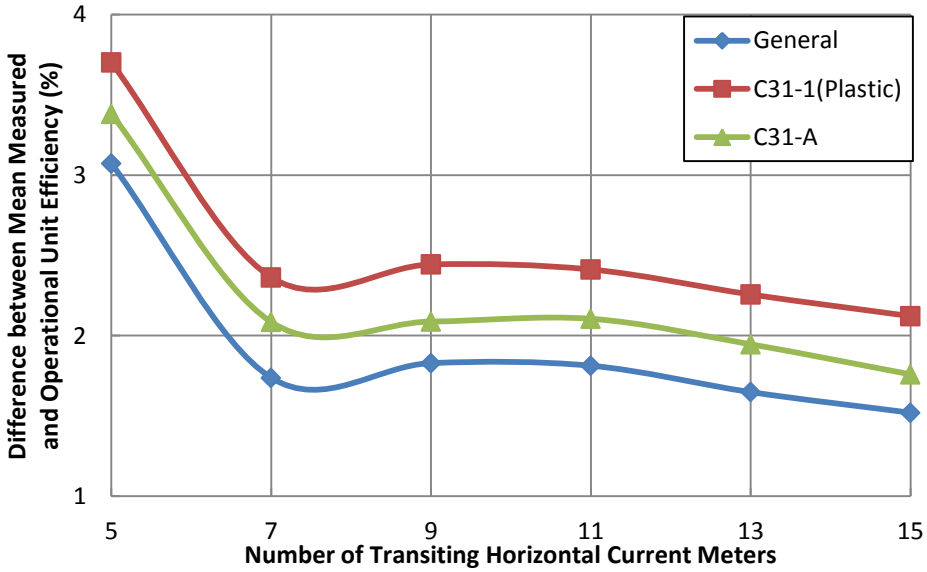

Figure 5.22 Modified As-Built Dynamic Current Meter Accuracy Differential

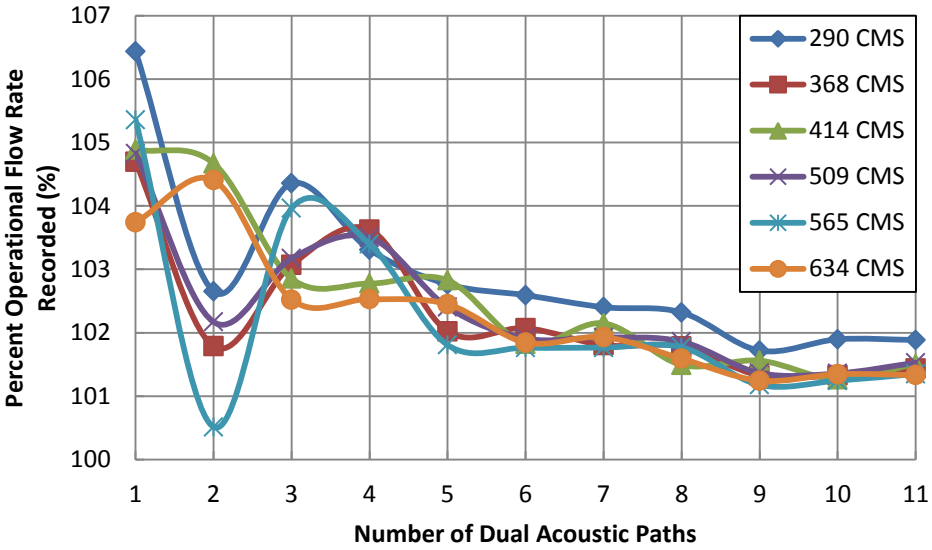

Figure 5.23: Dual Path Recorded Flow Rate Accuracy

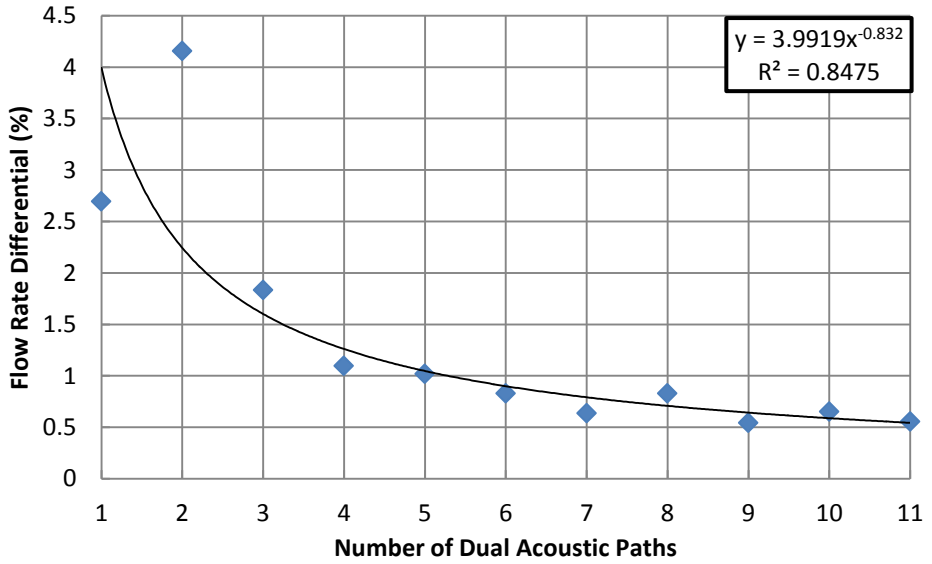

Figure 5.24: Differential between the Maximum and Minimum Percent Recorded Flow Rate

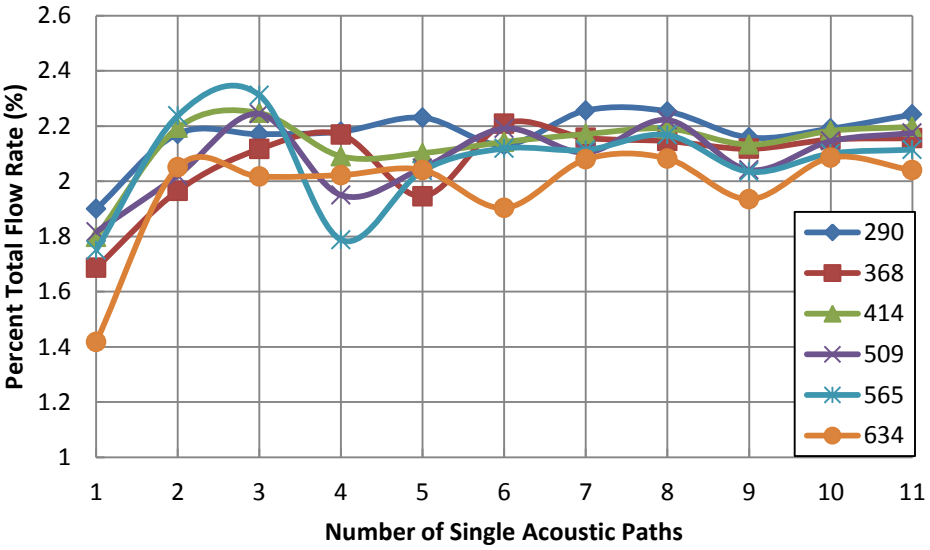

Figure 5.25: Differential in Flow Rates Predicted by Single Acoustic Paths in each direction as a function of the overall Flow Rate

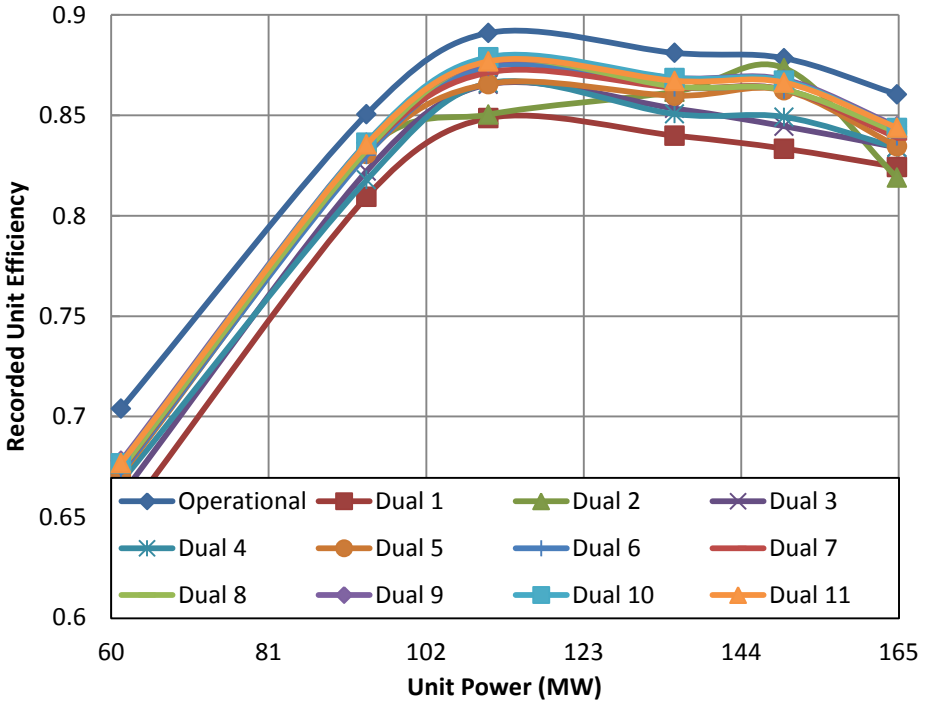

Figure 5.26: Recorded Unit Characteristic Curve as a Function of the Number of Applied Dual Acoustic Paths

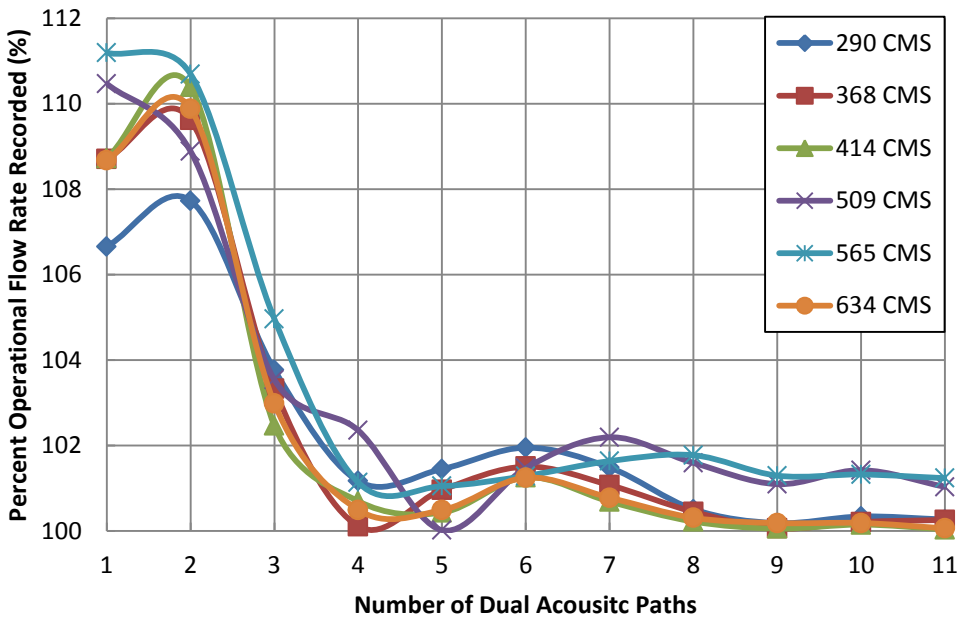

Figure 5.27: Differential in Flow Rates Predicted by Single Acoustic Paths in each direction as a function of the overall Flow Rate

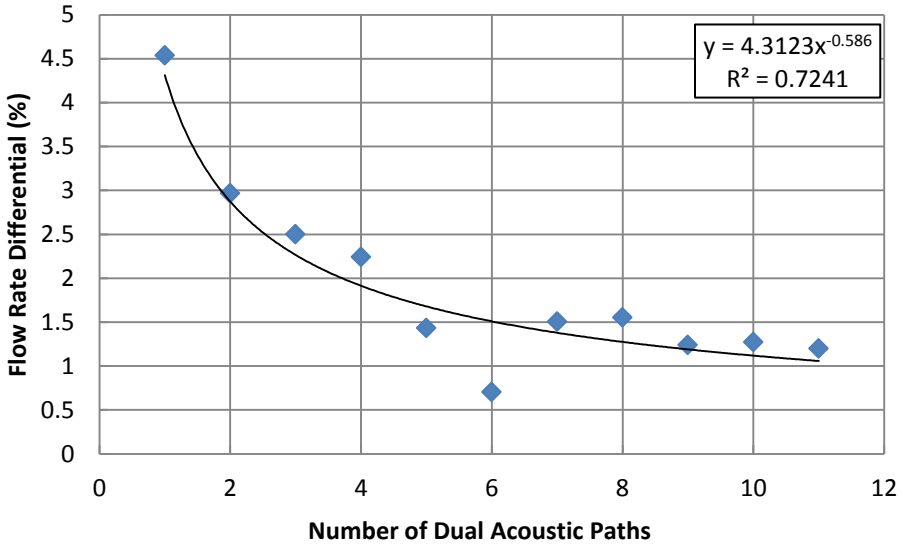

Figure 5.28: Differential in Flow Rates Predicted by Single Acoustic Paths in each direction as a function of the overall Flow Rate

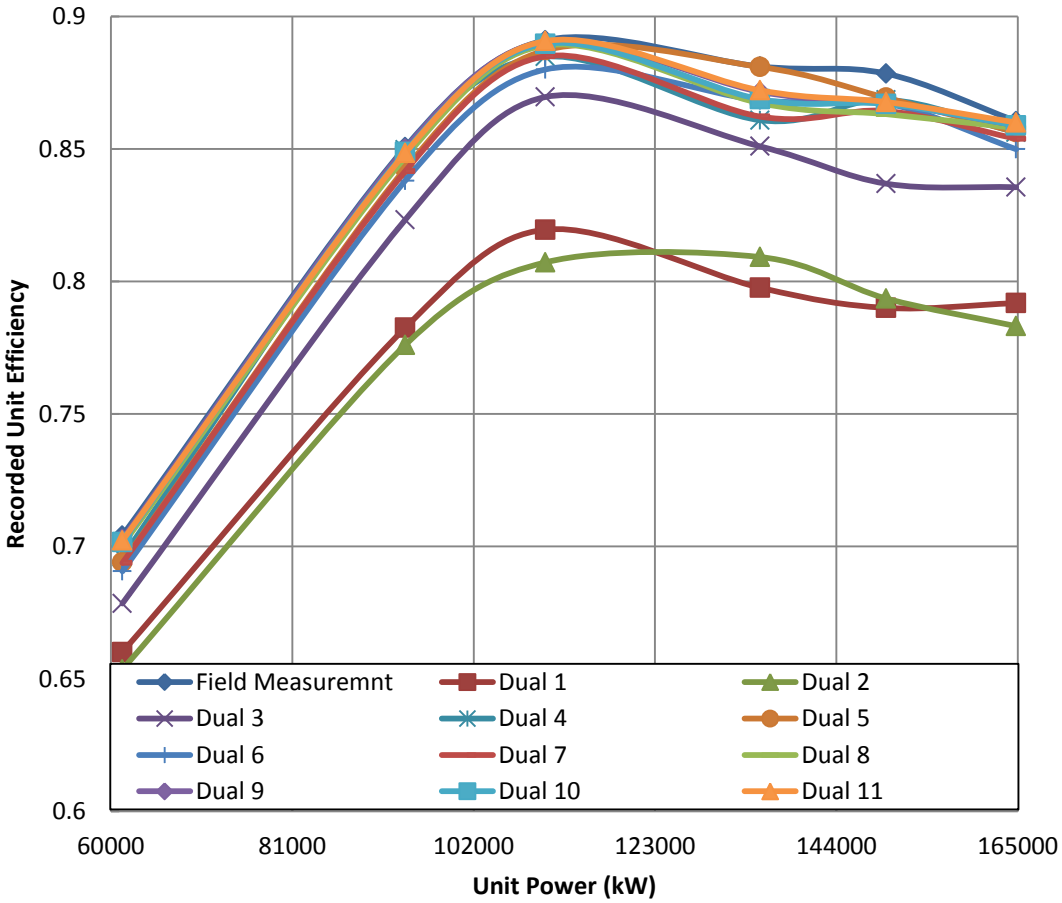

Figure 5.29: Differential in Flow Rates Predicted by Single Acoustic Paths in each direction as a function of the overall Flow Rate

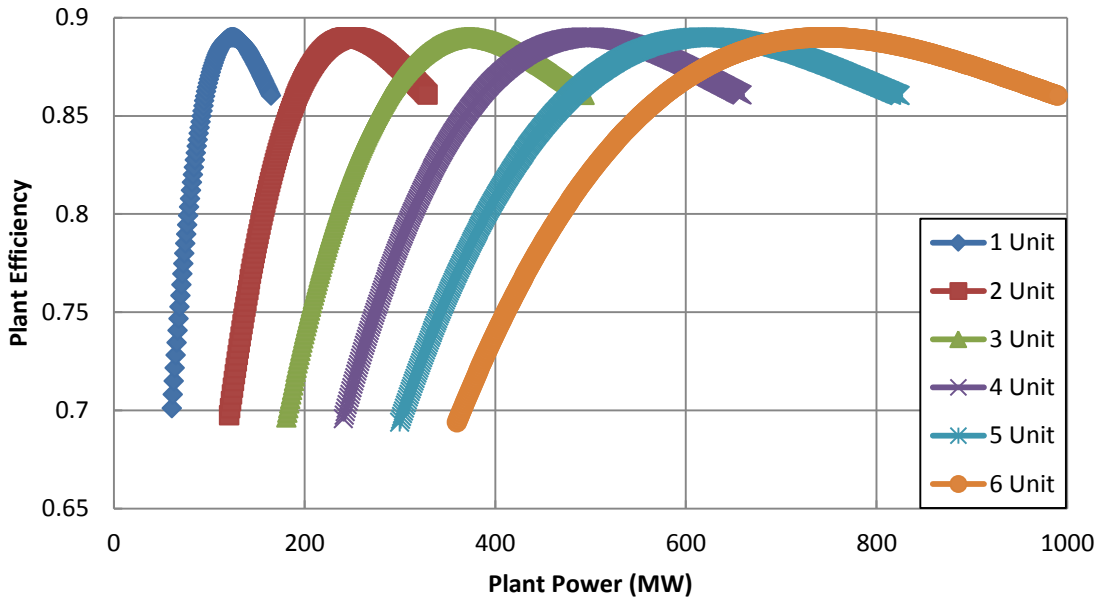

Figure 5.30: Performance of Increasing Number of Units using the Operational Efficiency of the Unit 4

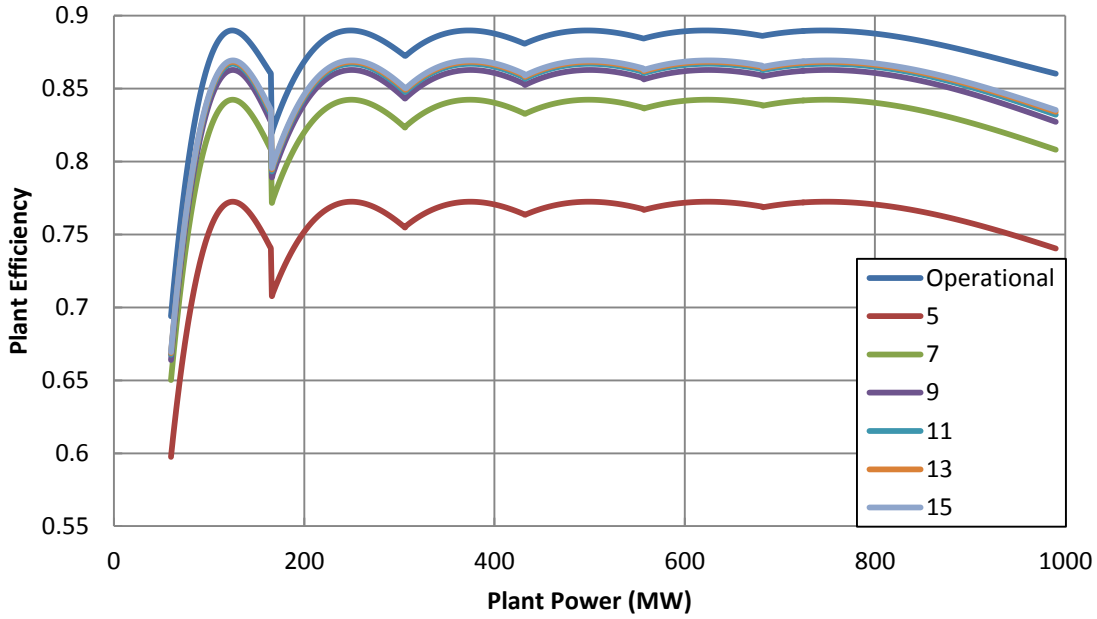

Figure 5.31: Optimal Performance of the Plant informed by Operational Efficiency of the Unit as well as Static Mounted General Current Meter Measured Efficiency

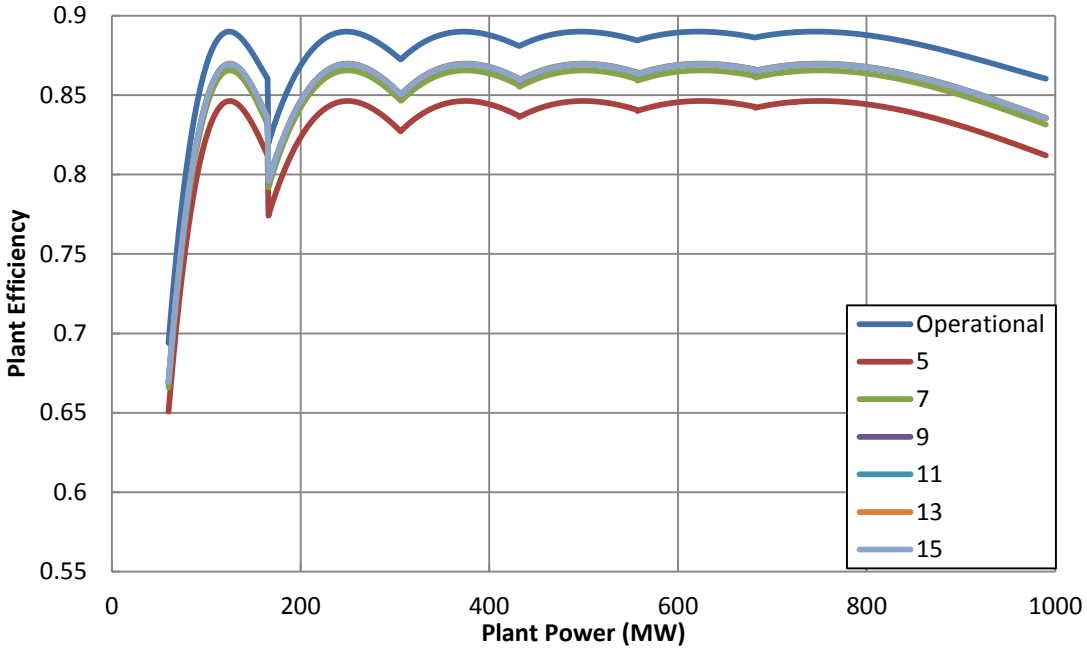

Figure 5.32: Optimal Performance of the Plant informed by Operational Efficiency of the Unit as well as Dynamic Mounted General Current Meter Measured Efficiency

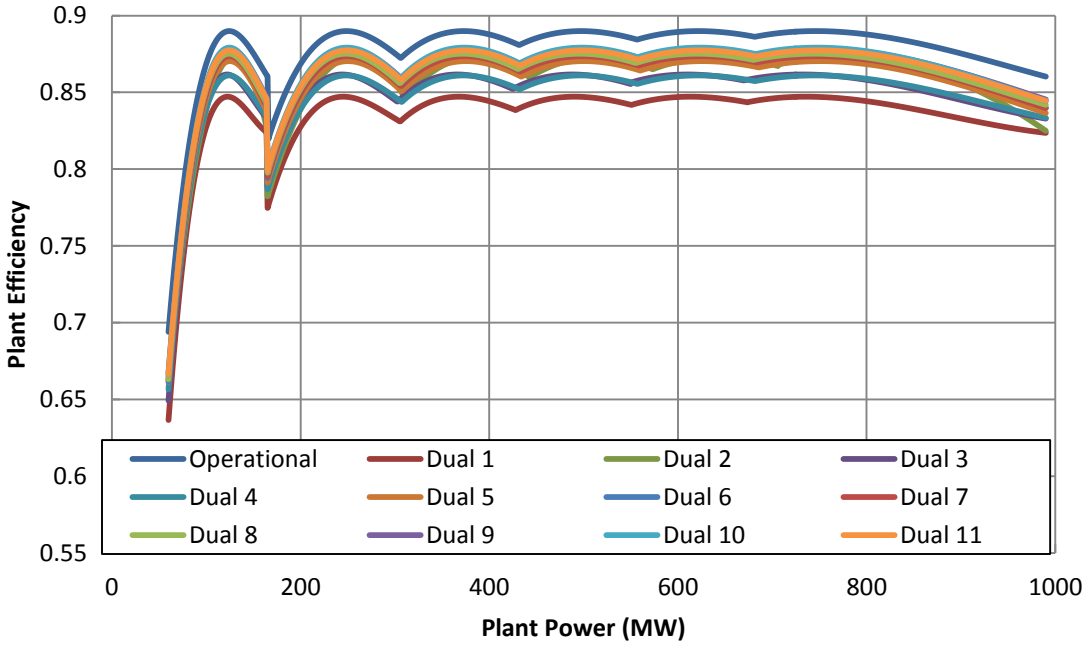

Figure 5.33: Optimal Performance of the Plant informed by Operational Efficiency of the Unit as well as Dual Acoustic Time of Flight Measured Efficiency

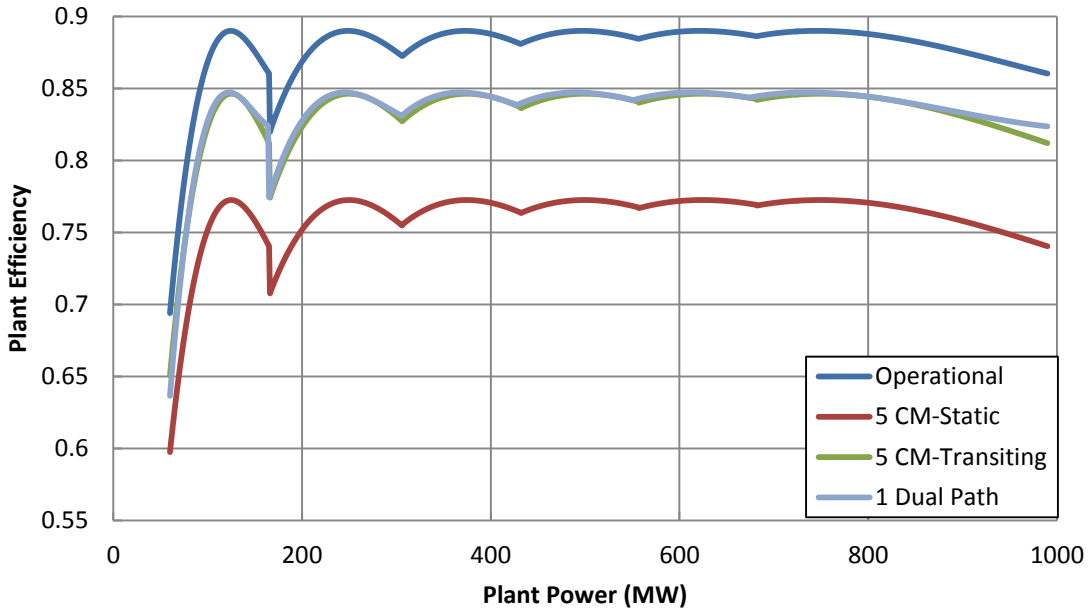

Figure 5.34: Optimal Performance of the Plant informed by Operational Efficiency of the Unit and the lowest levels of investigated Current Meters and Acoustic Paths

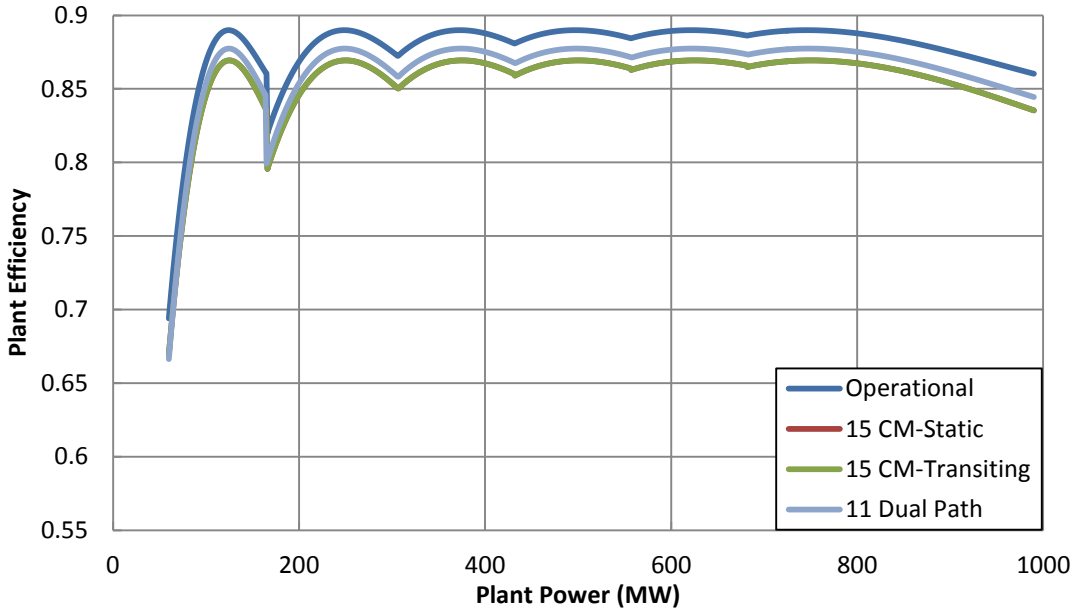

Figure 5.35: Optimal Performance of the Plant informed by Operational Efficiency of the Unit and the highest levels of investigated Current Meters and Acoustic Paths

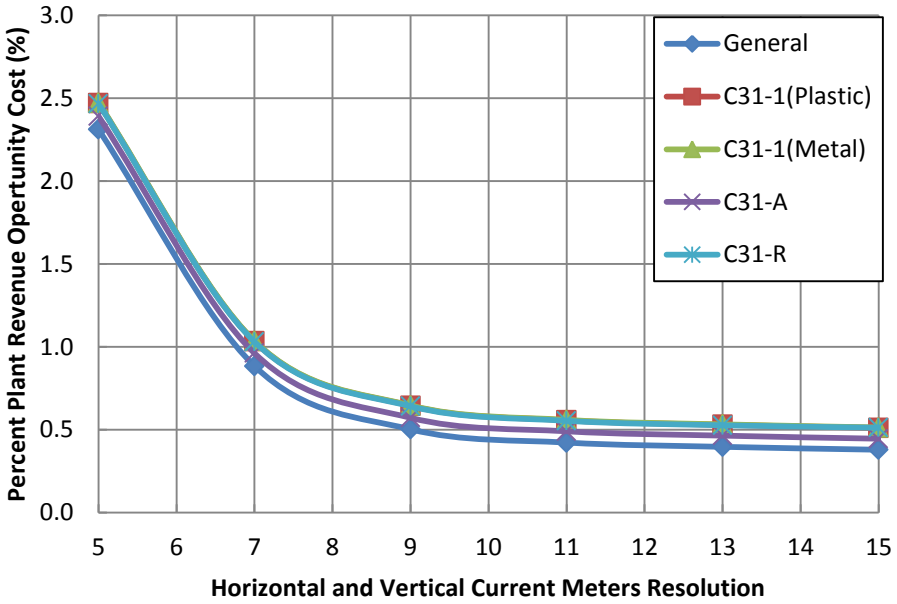

Figure 5.36: As-Built Static Current Meter Opportunity Cost as a Ratio of Annual Plant Revenue

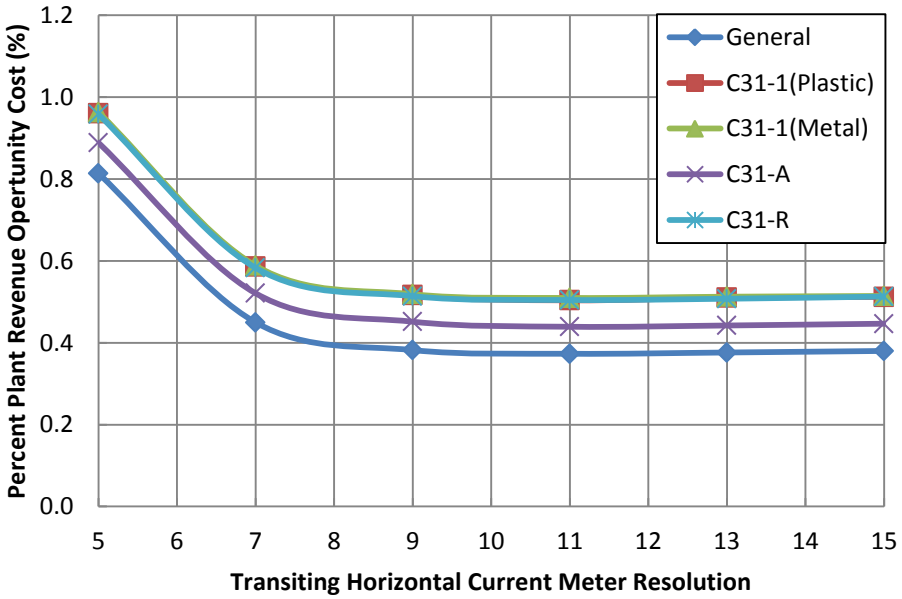

Figure 5.37: As-Built Dynamic Current Meter Opportunity Cost as a Ratio of Annual Plant Revenue

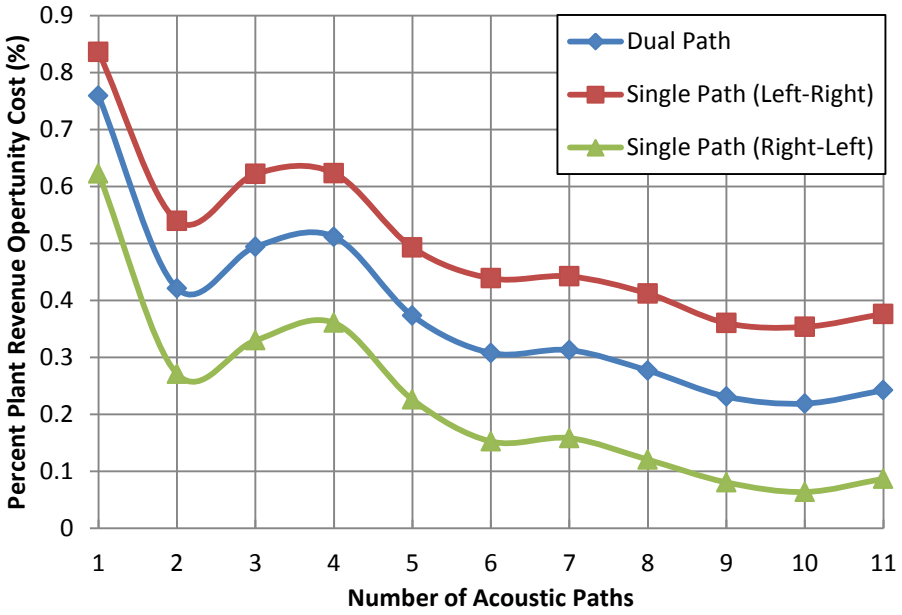

Figure 5.38: As-Built Acoustic Time of Flight Opportunity Cost as a Ratio of Annual Plant Revenue

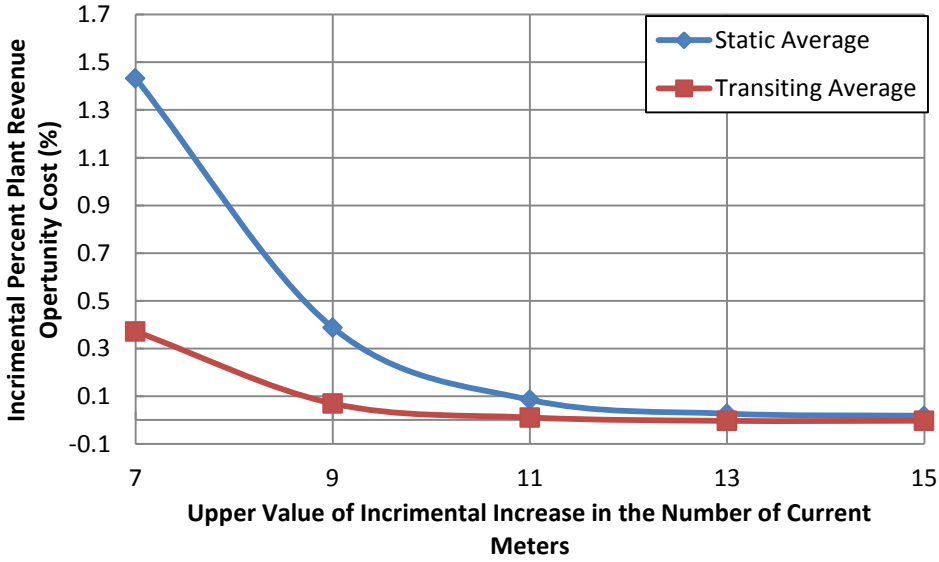

Figure 5.39: As-Built Static and Transiting Current Meter Incremental Opportunity Cost as a Ratio of Annual Plant Revenue

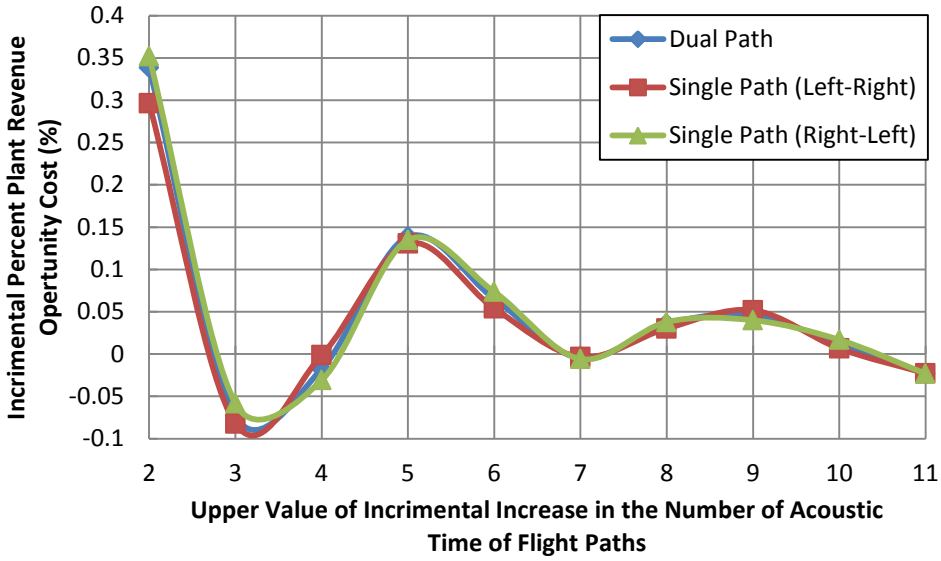

Figure 5.40: As-Built Acoustic Time of Flight Incremental Opportunity Cost as a Ratio of Annual Plant Revenue

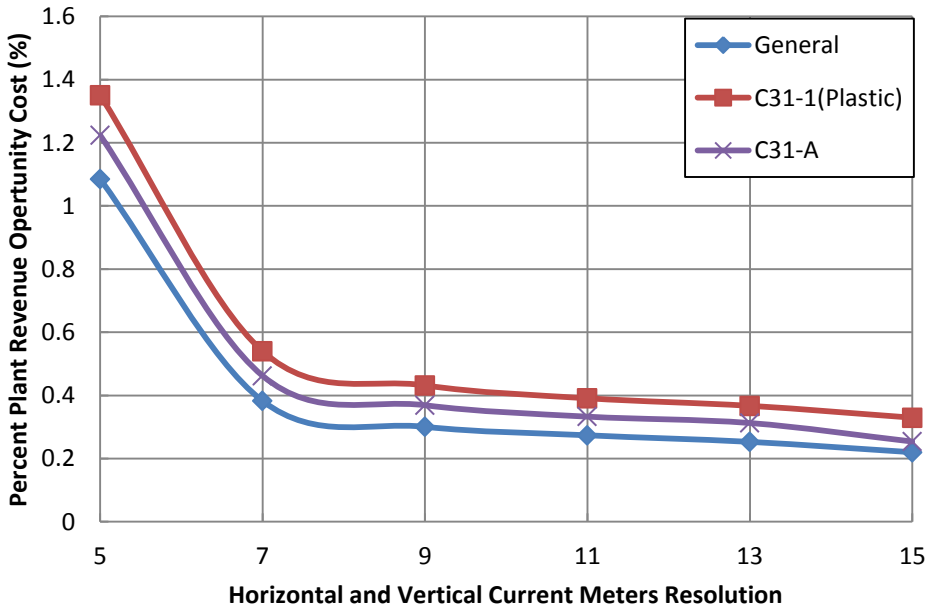

Figure 5.41 Modified As-Built Static Current Meter Opportunity Cost as a Ratio of Annual Plant Revenue

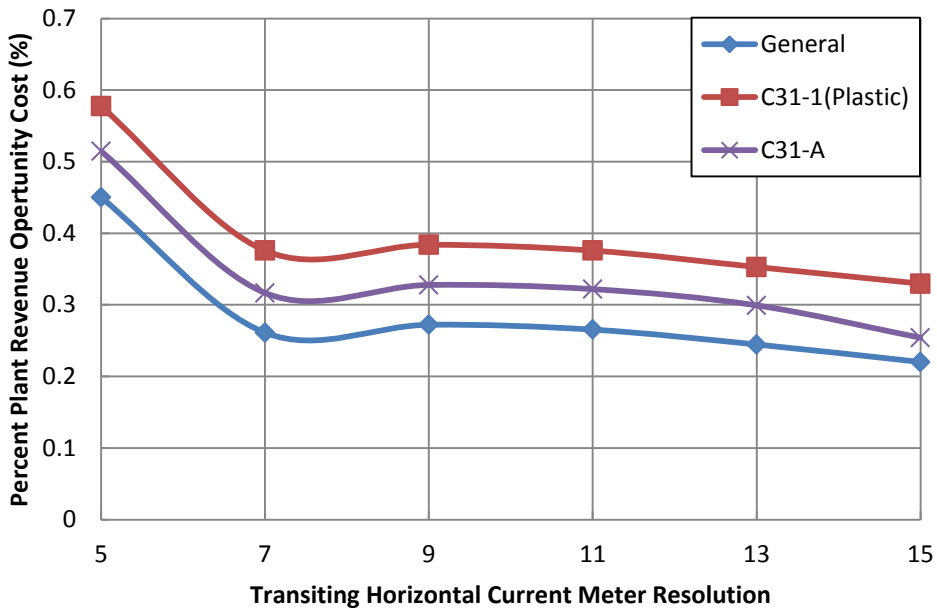

Figure 5.42: Modified As-Built Dynamic Current Meter Opportunity Cost as a Ratio of Annual Plant Revenue

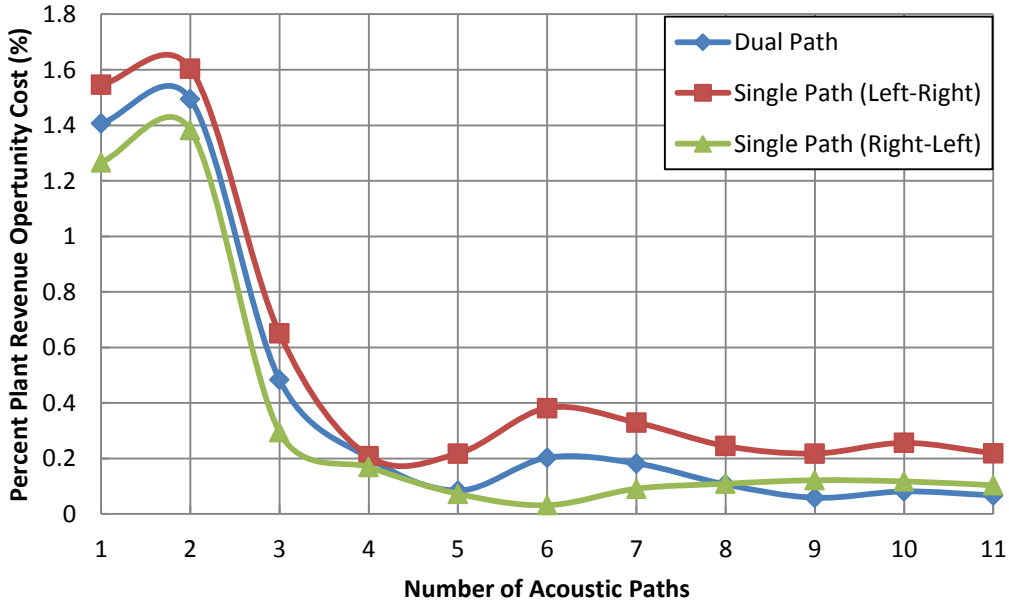

Figure 5.43: Modified As-Built Acoustic Time of Flight Opportunity Cost as a Ratio of Annual Plant Revenue

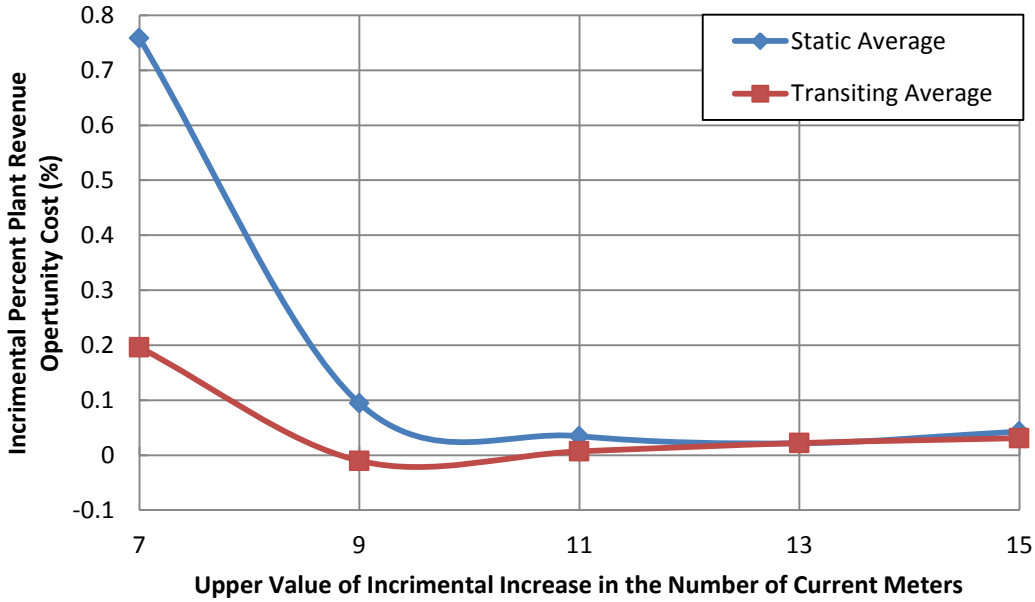

Figure 5.44: Modified As-Built Static and Transiting Current Meter Incremental Opportunity Cost as a Ratio of Annual Plant Revenue

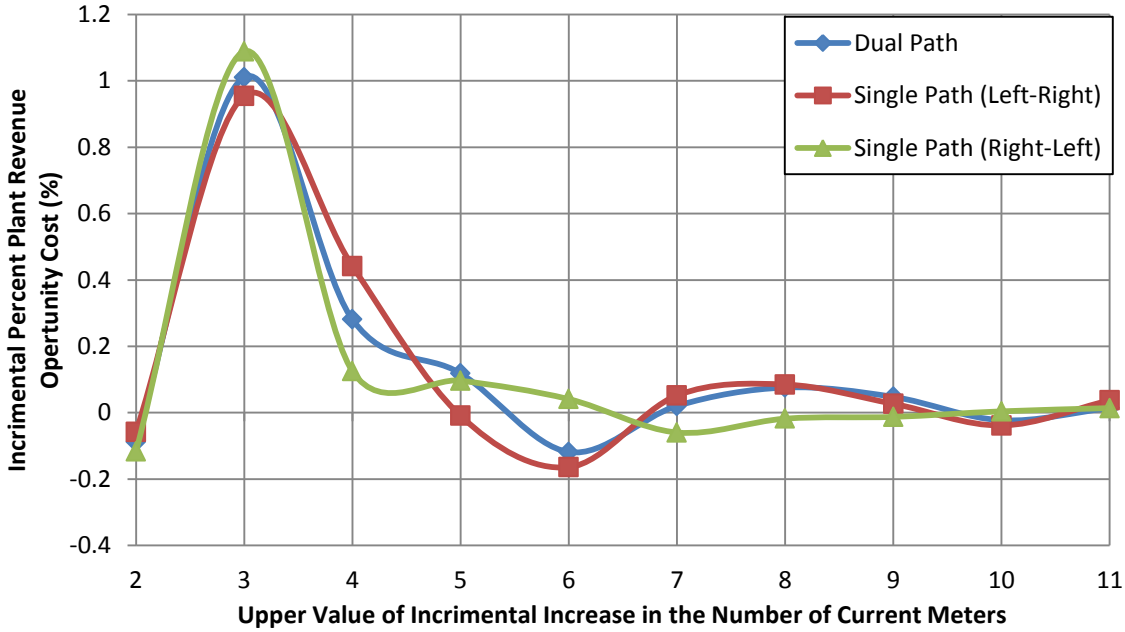

Figure 5.45: Modified As-Built Acoustic Time of Flight Incremental Opportunity Cost as a Ratio of Annual Plant Revenue

Table 5.1. Preliminary Investigation Bay Flow Distribution Percent Distribution

Simulation Number	Closure Model	Right Inlet Percent Flow (%)	Axial Inlet Percent Flow (%)	Left Inlet Percent Flow (%)
1	K-Eps	30.67	34.17	35.16
2		30.15	34.38	35.47
3		30.76	34.23	35.01
4		30.34	34.54	35.12
5	SST	30.97	33.91	35.11
6		30.32	34.45	35.23
7		30.38	34.62	35.00
8		30.18	34.53	35.29
Field Measurement		30.17	34.59	35.23

Table 5.2. Preliminary Investigation Bay Flow Distribution Accuracy

Simulation Number	Closure Model	Right Inlet Percent Flow (%)	Axial Inlet Percent Flow (%)	Left Inlet Percent Flow (%)
1	K-Eps	98.34	98.78	99.80
2		99.93	99.39	99.32
3		98.03	98.96	99.37
4		99.43	99.86	99.68
5	SST	97.33	98.04	99.67
6		99.51	99.60	99.99
7		99.31	99.92	99.36
8		99.98	99.83	99.82

Table 5.3. Preliminary Investigation Bay Flow Distribution Model ANOVA Analysis

		Bay A Model (F Value)	
		Upstream	Downstream
K-Eps	A-L-R	37.56	2.65
	A-L	37.97	4.26
	A-R	33.01	3.36
	A	63.03	3.74
SST	A-L-R	37.75	2.49
	A-L	36.46	3.93
	A-R	38.81	2.00
	A	50.67	2.39

Table 5.4. Preliminary Investigation Bay Flow Distribution Prototype ANOVA Analysis

		Acoustic Time of Flight ANOVA (F Value)		
		Bay A	Bay B	Bay C
K-Eps	A-L-R	1.458	0.097	0.137
	A-L	1.824	0.164	0.066
	A-R	1.475	0.104	0.080
	A	1.720	0.097	0.083
SST	A-L-R	1.252	0.082	0.159
	A-L	1.910	0.140	0.074
	A-R	1.596	0.093	0.090
	A	1.664	0.086	0.142

Table 5.5. Mesh Resolution Goodness of Fit Study

Hydraulic Characteristic	Bay A R^2	Bay B R^2	Bay C R^2
U	0.8996	0.744	0.8571
V	0.9771	0.8179	0.9729
W	0.9928	0.9857	0.9873
TKE	0.9828	0.9563	0.9691

Table 5.6. Recirculation Zone Description

Bay	Permutation Number	Dimension A (m)	Dimension B (m)	Dimension C (m)
A	1	0.79	0.26	0.17
	2	0.80	0.25	0.16
	3	1.34	0.41	0.18
	4	1.29	0.34	0.18
B	1	0.66	0.23	0.14
	2	0.73	0.24	0.13
	3	1.31	0.44	0.23
	4	1.55	0.49	0.36
C	1	0.73	0.24	0.14
	2	0.71	0.25	0.11
	3	1.26	0.41	0.21
	4	1.23	0.51	0.27

Table 5.7. Acoustic Time of Flight Velocities resulting from the Modified As-Built CFD

Bay Floor Roughness (m)	Normalized Height	As-Built (m sec^{-1})	Straight Obstruction (m sec^{-1})	Angled Obstruction (m sec^{-1})
Smooth	0.98	0.47	-0.08	-0.49
	0.92	0.82	0.34	-0.35
	0.81	0.96	0.81	0.10
	0.66	0.94	0.87	0.61
	0.50	0.92	0.85	0.94
	0.34	0.91	0.83	0.95
	0.19	0.89	0.82	0.85
	0.08	0.89	0.80	0.87
	0.02	0.81	0.63	0.77
0.091	0.98	0.52	0.03	-0.53
	0.92	0.89	0.52	-0.27
	0.81	0.90	0.89	0.67
	0.66	0.92	0.90	1.15
	0.50	0.91	0.90	1.12
	0.34	0.88	0.88	1.05
	0.19	0.87	0.89	1.03
	0.08	0.88	0.87	1.03
	0.02	0.76	0.68	0.87
0.182	0.98	0.07	0.16	-0.62
	0.92	0.05	0.47	-0.33
	0.81	0.08	0.88	0.61
	0.66	0.07	0.95	1.20
	0.50	0.05	0.96	1.13
	0.34	0.08	0.97	1.05
	0.19	0.07	0.98	1.02
	0.08	0.05	0.98	1.02
	0.02	0.08	0.71	0.87

Table 5.8. Acoustic Time of Flight Modified As-Built CFD Percent Difference from Field Data

Bay Floor Roughness (m)	Bay Ceiling As-Built Permutation Percent Difference (%)		
	As-Built	Straight Obstruction	Angled Obstruction
Smooth	21.98	20.97	47.23
0.091	24.42	13.83	30.43
0.182	14.34	9.45	33.42

Table 5.9. Bay Flow Distribution Accuracy

Flow Rate (m^3sec^{-1})	Bay A Accuracy (%)	Bay B Accuracy (%)	Bay C Accuracy (%)
290	98.37	98.77	99.81
368	95.45	97.77	98.37
414	95.49	98.01	98.23
509	96.42	97.77	99.16
565	96.09	97.42	99.22
634	97.58	97.83	99.93

Table 5.10. Acoustic Time of Flight Validation F Test

Flow Rate (m^3sec^{-1})	Bay A Accuracy (%)	Bay B Accuracy (%)	Bay C Accuracy (%)
290	1.08E-02	5.65E-02	3.63E-04
368	1.11E-02	1.34E-02	3.91E-02
414	4.65E-06	1.16E-02	1.93E-02
509	1.22E-02	2.60E-02	1.84E-02
565	1.51E-02	7.96E-03	1.23E-02
634	9.14E-03	1.95E-02	6.82E-04

Table 5.11. Acoustic Time of Flight Validation Average Percent Accuracy

Path Number	Bay A Accuracy (%)	Bay B Accuracy (%)	Bay C Accuracy (%)
1	655.19	601.28	787.98
2	17.86	-4.17	37.35
3	80.29	79.56	72.25
4	83.18	78.51	77.47
5	85.02	81.07	82.88
6	84.95	84.22	82.95
7	85.72	86.50	78.69
8	88.61	88.13	82.08
9	79.30	79.79	87.94

Table 5.12. Acoustic Time of Flight Validation Standard Deviation

Path Number	Bay A STD	Bay B STD	Bay C STD
1	51.67	26.67	26.81
2	9.62	10.41	5.98
3	2.30	6.15	1.04
4	0.69	1.13	0.64
5	0.68	1.95	0.95
6	0.64	0.93	1.19
7	0.69	0.90	1.43
8	1.02	0.94	1.95
9	2.14	2.33	0.68

Table 5.13. Interpolation Numerical Method Investigation Results

Radius of Influence (m)	0.2	0.2	0.3	0.3	Nearest Neighbor
Weighing Power	2	3	3	2	
Percent Variability	0.32	0.28	1.12	1.12	2.79

Table 5.14. Average Percent of Operational Flow Rate Recorded As-Built: General Current Meter

		Horizontal Current Meter Resolution					
		5	7	9	11	13	15
Vertical Current Meter Resolution	5	115.04	112.59	111.47	111.47	111.83	111.84
	7	107.91	105.51	104.75	104.67	104.85	104.85
	9	106.11	103.74	103.10	103.05	103.14	103.14
	11	105.53	103.16	102.63	102.54	102.62	102.63
	13	105.26	102.88	102.38	102.33	102.37	102.38
	15	105.11	102.72	102.28	102.21	102.23	102.25

Table 5.15. Average Percent of Operational Flow Rate Recorded As-Built: Ott C31-1(Plastic) Current Meter

		Horizontal Current Meter Resolution					
		5	7	9	11	13	15
Vertical Current Meter Resolution	5	116.20	113.70	112.57	112.56	112.91	112.92
	7	108.95	106.50	105.72	105.64	105.81	105.81
	9	107.10	104.69	104.03	103.98	104.06	104.06
	11	106.51	104.09	103.55	103.46	103.53	103.54
	13	106.22	103.80	103.29	103.24	103.27	103.27
	15	106.07	103.64	103.18	103.10	103.12	103.14

Table 5.16. Average Percent of Operational Flow Rate Recorded As-Built: Ott C31-1(Metal) Current Meter

		Horizontal Current Meter Resolution					
		5	7	9	11	13	15
Vertical Current Meter Resolution	5	116.23	113.72	112.60	112.58	112.93	112.94
	7	108.97	106.52	105.74	105.66	105.83	105.83
	9	107.13	104.71	104.05	104.00	104.09	104.08
	11	106.53	104.11	103.57	103.48	103.55	103.56
	13	106.24	103.82	103.31	103.26	103.29	103.29
	15	106.09	103.66	103.20	103.12	103.14	103.16

Table 5.17. Average Percent of Operational Flow Rate Recorded As-Built: Ott C31-A Current Meter

		Horizontal Current Meter Resolution					
		5	7	9	11	13	15
Vertical Current Meter Resolution	5	115.63	113.15	112.03	112.02	112.37	112.39
	7	108.44	106.01	105.24	105.16	105.33	105.33
	9	106.61	104.22	103.57	103.52	103.61	103.60
	11	106.03	103.63	103.10	103.01	103.08	103.09
	13	105.74	103.35	102.84	102.79	102.82	102.83
	15	105.59	103.19	102.73	102.66	102.68	102.70

Table 5.18. Average Percent of Operational Flow Rate Recorded As-Built: Ott C31-R Current Meter

		Horizontal Current Meter Resolution					
		5	7	9	11	13	15
Vertical Current Meter Resolution	5	116.19	113.68	112.55	112.54	112.89	112.90
	7	108.93	106.48	105.71	105.63	105.79	105.79
	9	107.09	104.67	104.02	103.97	104.05	104.04
	11	106.49	104.08	103.54	103.44	103.52	103.52
	13	106.21	103.79	103.27	103.22	103.26	103.26
	15	106.05	103.63	103.17	103.09	103.11	103.13

Table 5.19. Standard Deviation in Percent of Operational Flow Rate Recorded over all Flow Rates As-Built: General Current Meter

		Horizontal Current Meter Resolution					
		5	7	9	11	13	15
Vertical Current Meter Resolution	5	0.85	1.02	0.87	0.94	1.01	1.09
	7	0.58	0.49	0.50	0.46	0.50	0.56
	9	0.44	0.40	0.39	0.40	0.41	0.45
	11	0.39	0.39	0.37	0.37	0.40	0.41
	13	0.38	0.35	0.35	0.35	0.35	0.38
	15	0.35	0.34	0.34	0.32	0.33	0.35

Table 5.20. Standard Deviation in Percent of Operational Flow Rate Recorded over all Flow Rates As-Built: Ott C31-1(Plastic) Current Meter

		Horizontal Current Meter Resolution					
		5	7	9	11	13	15
Vertical Current Meter Resolution	5	2.16	2.03	2.17	2.08	2.06	2.24
	7	1.95	1.79	1.89	1.78	1.81	1.87
	9	1.76	1.69	1.75	1.72	1.70	1.77
	11	1.74	1.71	1.72	1.69	1.71	1.73
	13	1.59	1.61	1.66	1.63	1.65	1.68
	15	1.63	1.65	1.68	1.65	1.65	1.67

Table 5.21. Standard Deviation in Percent of Operational Flow Rate Recorded over all Flow Rates As-Built: Ott C31-1(Metal) Current Meter

		Horizontal Current Meter Resolution					
		5	7	9	11	13	15
Vertical Current Meter Resolution	5	2.08	2.01	2.13	1.99	2.03	2.17
	7	1.96	1.83	1.93	1.78	1.84	1.88
	9	1.81	1.75	1.80	1.74	1.75	1.80
	11	1.78	1.77	1.78	1.72	1.76	1.76
	13	1.63	1.66	1.71	1.66	1.69	1.72
	15	1.68	1.70	1.73	1.69	1.70	1.72

Table 5.22. Standard Deviation in Percent of Operational Flow Rate Recorded over all Flow Rates As-Built: Ott C31-A Current Meter

		Horizontal Current Meter Resolution					
		5	7	9	11	13	15
Vertical Current Meter Resolution	5	2.11	2.07	2.17	2.04	2.09	2.22
	7	1.96	1.84	1.93	1.79	1.86	1.89
	9	1.80	1.76	1.79	1.75	1.75	1.80
	11	1.78	1.77	1.77	1.72	1.76	1.76
	13	1.62	1.66	1.71	1.66	1.69	1.72
	15	1.68	1.70	1.73	1.69	1.70	1.72

Table 5.23. Standard Deviation in Percent of Operational Flow Rate Recorded over all Flow Rates As-Built: Ott C31-R Current Meter

		Horizontal Current Meter Resolution					
		5	7	9	11	13	15
Vertical Current Meter Resolution	5	0.58	0.73	0.62	0.70	0.78	0.86
	7	0.43	0.24	0.32	0.26	0.27	0.35
	9	0.32	0.20	0.24	0.22	0.22	0.27
	11	0.26	0.21	0.23	0.21	0.22	0.25
	13	0.29	0.21	0.22	0.21	0.20	0.22
	15	0.25	0.20	0.22	0.20	0.19	0.21

Table 5.24. Average Percent of Operational Flow Rate Recorded Modified As-Built: General Current Meter

		Horizontal Current Meter Resolution					
		5	7	9	11	13	15
Vertical Current Meter Resolution	5	106.6	105.2	105.2	105.2	105.2	104.9
	7	103.6	102.3	102.3	102.3	102.2	102.0
	9	103.3	102.0	102.0	102.0	101.9	101.7
	11	103.1	101.8	101.8	101.8	101.7	101.6
	13	103.1	101.8	101.8	101.8	101.7	101.5
	15	103.1	101.7	101.8	101.8	101.6	101.5

Table 5.25. Average Percent of Operational Flow Rate Recorded Modified As-Built: Ott C31-1 (Plastic)

		Horizontal Current Meter Resolution					
		5	7	9	11	13	15
Vertical Current Meter Resolution	5	108.0	106.6	106.6	106.6	106.6	106.3
	7	104.6	103.2	103.2	103.3	103.1	102.9
	9	104.0	102.7	102.7	102.7	102.6	102.5
	11	103.8	102.5	102.5	102.5	102.4	102.2
	13	103.8	102.4	102.5	102.5	102.3	102.2
	15	103.7	102.4	102.4	102.4	102.3	102.1

Table 5.26. Average Percent of Operational Flow Rate Recorded Modified As-Built: Ott C31-Type A Current Meter

		Horizontal Current Meter Resolution					
		5	7	9	11	13	15
Vertical Current Meter Resolution	5	107.5	106.4	105.9	106.3	106.2	105.7
	7	104.1	102.9	102.7	102.8	102.7	102.3
	9	103.6	102.4	102.2	102.3	102.2	102.0
	11	103.4	102.2	102.1	102.1	102.0	101.8
	13	103.4	102.2	102.1	102.2	102.0	101.8
	15	103.4	102.1	102.1	102.1	101.9	101.8

Table 5.27. Standard Deviation in Percent of Operational Flow Rate Recorded over all Flow Rates Modified As-Built: General Current Meter

		Horizontal Current Meter Resolution					
		5	7	9	11	13	15
Vertical Current Meter Resolution	5	1.04	0.99	1.02	0.99	0.99	0.95
	7	1.38	1.12	1.08	1.00	0.99	0.97
	9	1.48	1.21	1.16	1.13	1.10	1.11
	11	1.34	1.11	1.04	1.01	0.97	0.97
	13	1.29	1.02	1.02	0.91	0.90	0.92
	15	1.34	1.06	1.01	0.97	0.94	0.93

Table 5.28. Standard Deviation in Percent of Operational Flow Rate Recorded over all Flow Rates Modified As-Built: Ott C31-1 (Plastic) Current Meter

		Horizontal Current Meter Resolution					
		5	7	9	11	13	15
Vertical Current Meter Resolution	5	2.00	1.93	1.90	1.85	1.86	1.81
	7	1.61	1.38	1.32	1.25	1.23	1.17
	9	1.49	1.25	1.17	1.11	1.08	1.05
	11	1.26	1.04	0.96	0.91	0.87	0.85
	13	1.20	0.94	0.90	0.82	0.75	0.74
	15	1.27	0.88	0.83	0.78	0.76	0.75

Table 5.29. Standard Deviation in Percent of Operational Flow Rate Recorded over all Flow Rates Modified As-Built: Ott C31-Type A Current Meter

		Horizontal Current Meter Resolution					
		5	7	9	11	13	15
Vertical Current Meter Resolution	5	1.33	1.31	1.45	1.24	1.32	2.77
	7	1.28	1.08	1.02	0.93	0.95	1.52
	9	1.39	1.14	1.08	1.04	1.03	1.27
	11	1.31	1.07	1.02	1.00	0.97	1.09
	13	1.31	1.07	1.02	0.97	0.97	1.04
	15	1.33	1.07	1.02	1.00	0.97	0.99

Table 5.30. Incremental Annual Benefit Cost Ratio for As-Built Static Current Meter Application

Meter Type	Incremental Current Meter Resolution				
	5 to 7	7 to 9	9 to 11	11 to 13	13 to 15
General	9.08	1.82	0.31	0.08	0.05
C31-1(Plastic)	13.13	2.66	0.48	0.12	0.07
C31-1(Metal)	9.00	1.83	0.33	0.08	0.05
C31-A	7.64	1.56	0.26	0.07	0.04
C31-R	8.33	1.69	0.30	0.08	0.04

Table 5.31. Incremental Annual Benefit Cost Ratio for As-Built Dynamic Current Meter Application

Meter Type	Incremental Current Meter Resolution				
	5 to 7	7 to 9	9 to 11	11 to 13	13 to 15
General	2.316	0.323	0.034	-0.010	-0.010
C31-1(Plastic)	3.426	0.477	0.069	-0.030	-0.007
C31-1(Metal)	2.348	0.327	0.034	-0.009	-0.005
C31-A	1.963	0.278	0.040	-0.008	-0.010
C31-R	2.174	0.301	0.033	-0.009	-0.013

Table 5.32. Years to Achieve a Benefit Cost Ratio of 1 for As-Built Static Current Meter Application

Meter Type	Incremental Current Meter Resolution				
	5 to 7	7 to 9	9 to 11	11 to 13	13 to 15
General	0.11	0.55	3.28	12.22	20.89
C31-1(Plastic)	0.08	0.38	2.08	8.10	13.74
C31-1(Metal)	0.11	0.55	3.05	11.79	19.80
C31-A	0.13	0.64	3.82	14.35	23.62
C31-R	0.12	0.59	3.28	12.80	26.94

Table 5.33. Years to Achieve a Benefit Cost Ratio of 1 for As-Built Dynamic Current Meter Application

Meter Type	Incremental Current Meter Resolution				
	5 to 7	7 to 9	9 to 11	11 to 13	13 to 15
General	0.43	3.10	29.32	N/A	N/A
C31-1(Plastic)	0.29	2.10	14.50	N/A	N/A
C31-1(Metal)	0.43	3.06	29.36	N/A	N/A
C31-A	0.51	3.60	25.31	N/A	N/A
C31-R	0.46	3.32	30.69	N/A	N/A

Table 5.34. Incremental Annual Benefit-Cost Ratio for the As-Built Acoustic Time of Flight Application

Meter Type	Incremental Acoustic Path Resolution					
	1 to 2	2 to 5	5 to 6	6 to 9	9 to 10	10 to 11
Dual Path	21.59	0.84	6.38	1.15	1.19	-2.26
Single Path (Left-Right)	34.28	2.72	20.31	2.94	0.31	-4.77
Single Path (Right-Left)	38.01	2.45	25.82	2.51	0.73	-4.51

Table 5.35. Incremental Annual Benefit Cost Ratio for Modified As-Built Static Current Meter Application

Meter Type	Incremental Current Meter Resolution				
	5 to 7	7 to 9	9 to 11	11 to 13	13 to 15
General	4.47	0.39	0.10	0.07	0.09
C31-1(Plastic)	7.41	0.74	0.22	0.11	0.15
C31-A	4.07	0.37	0.12	0.05	0.13

Table 5.36. Incremental Annual Benefit Cost Ratio for Modified As-Built Dynamic Current Meter Application

Meter Type	Incremental Current Meter Resolution				
	5 to 7	7 to 9	9 to 11	11 to 13	13 to 15
General	14.43	-0.85	0.52	1.58	1.87
C31-1(Plastic)	22.12	-0.90	0.90	2.52	2.55
C31-A	12.69	-0.71	0.38	1.45	2.90

Table 5.37. Years to Achieve a Benefit Cost Ratio of 1 for Modified As-Built Static Current Meter Application

Meter Type	Incremental Current Meter Resolution				
	5 to 7	7 to 9	9 to 11	11 to 13	13 to 15
General	0.22	2.57	9.71	15.10	11.16
C31-1(Plastic)	0.13	1.35	4.46	9.16	6.79
C31-A	0.25	2.68	8.64	18.53	7.45

Table 5.38. Years to Achieve a Benefit Cost Ratio of 1 for Modified As-Built Dynamic Current Meter Application

Meter Type	Incremental Current Meter Resolution				
	5 to 7	7 to 9	9 to 11	11 to 13	13 to 15
General	0.07	-1.18	1.91	0.63	0.53
C31-1(Plastic)	0.05	-1.11	1.11	0.40	0.39
C31-A	0.08	-1.41	2.66	0.69	0.35

Table 5.39. Incremental Annual Benefit-Cost Ratio for the Modified As-Built Acoustic Time of Flight Application

Meter Type	Incremental Acoustic Path Resolution				
	1 to 3	3 to 6	6 to 7	7 to 10	10 to 11
Dual Path	52.42	4.55	1.99	1.52	1.38
Single Path (Left-Right)	56.89	19.85	18.25	1.51	7.28
Single Path (Right-Left)	43.20	19.43	-20.90	-0.54	2.70

Table 5.40. Reduction in Suboptimally Assigned Water per incremental investment in Static Current Meters As-Built Application

Meter Type	Suboptimally assigned water (m^3) per investment ($)				
	5 to 7	7 to 9	9 to 11	11 to 13	13 to 15
General	897,908	172,686	29,454	7,997	4,748
C31-1(Plastic)	1,311,890	252,837	45,650	12,072	6,966
C31-1(Metal)	899,302	173,306	31,298	8,274	4,775
C31-A	758,946	147,665	25,178	6,888	4,024
C31-R	831,652	160,317	28,941	7,645	3,611

*1,351,784,924 m^3 of water travels through the plant annually

Table 5.41. Reduction in Suboptimally Assigned Water per incremental investment in Transient Current Meters As-Built Application

Meter Type	Suboptimally assigned water (m^3) per investment ($)				
	5 to 7	7 to 9	9 to 11	11 to 13	13 to 15
General	2,646,403	505,956	65,391	-22,512	-26,519
C31-1(Plastic)	3,902,488	736,925	135,326	-68,079	-18,424
C31-1(Metal)	2,674,642	504,986	68,164	-21,879	-12,950
C31-A	2,239,826	427,516	77,375	-18,548	-27,434
C31-R	2,474,526	467,211	63,159	-20,250	-34,344

*1,351,784,924 m^3 of water travels through the plant annually

Table 5.42. Reduction in Suboptimally Assigned Water per incremental investment in Acoustic Time of Flight Paths As-Built Application

Meter Type	Suboptimally assigned water (m^3) per investment ($)					
	1 to 2	2 to 5	5 to 6	6 to 9	9 to 10	10 to 11
Dual Path	2,015,778	89,740	629,596	116,309	115,303	-226,721
Single Path (Left-Right)	3,140,896	298,723	1,943,073	287,738	31,480	-469,114
Single Path (Right-Left)	3,646,784	257,073	2,576,659	252,242	70,827	-438,317

*1,351,784,924 m^3 of water travels through the plant annually

Table 5.43. Reduction in Suboptimally Assigned Water per incremental investment in Static Current Meters Modified As-Built Application

Meter Type	Suboptimally assigned water (m^3) per investment ($)				
	5 to 7	7 to 9	9 to 11	11 to 13	13 to 15
General	433,602	37,544	10,183	6,197	9,119
C31-1(Plastic)	711,065	69,787	21,205	10,411	14,265
C31-A	392,489	35,584	10,941	5,206	12,869

*1,351,784,924 m^3 of water travels through the plant annually

Table 5.44. Reduction in Suboptimally Assigned Water per incremental investment in Transient Current Meters Modified As-Built Application

Meter Type	Suboptimally assigned water (m^3) per investment ($)				
	5 to 7	7 to 9	9 to 11	11 to 13	13 to 15
General	1,392,447	-82,267	49,639	152,262	189,875
C31-1(Plastic)	2,086,901	-80293	80572	238872	247,867
C31-A	1,204,909	-65,518	33,941	138,883	278,642

*1,351,784,924 m^3 of water travels through the plant annually

Table 5.45. Reduction in Suboptimally Assigned Water per incremental investment in Acoustic Time of Flight Paths Modified As-Built Application

Meter Type	Suboptimally assigned water (m^3) per investment ($)				
	1 to 3	3 to 6	6 to 7	7 to 10	10 to 11
Dual Path	4,092,366	438,960	203,975	153,076	133,695
Single Path (Left-Right)	4,972,621	1,868,627	1,907,051	151,055	715,193
Single Path (Right-Left)	537,9419	1,928,696	-2,035,478	-53,421	258,341

*1,351,784,924 m^3 of water travels through the plant annually

Appendix 10: Residual Threshold Values

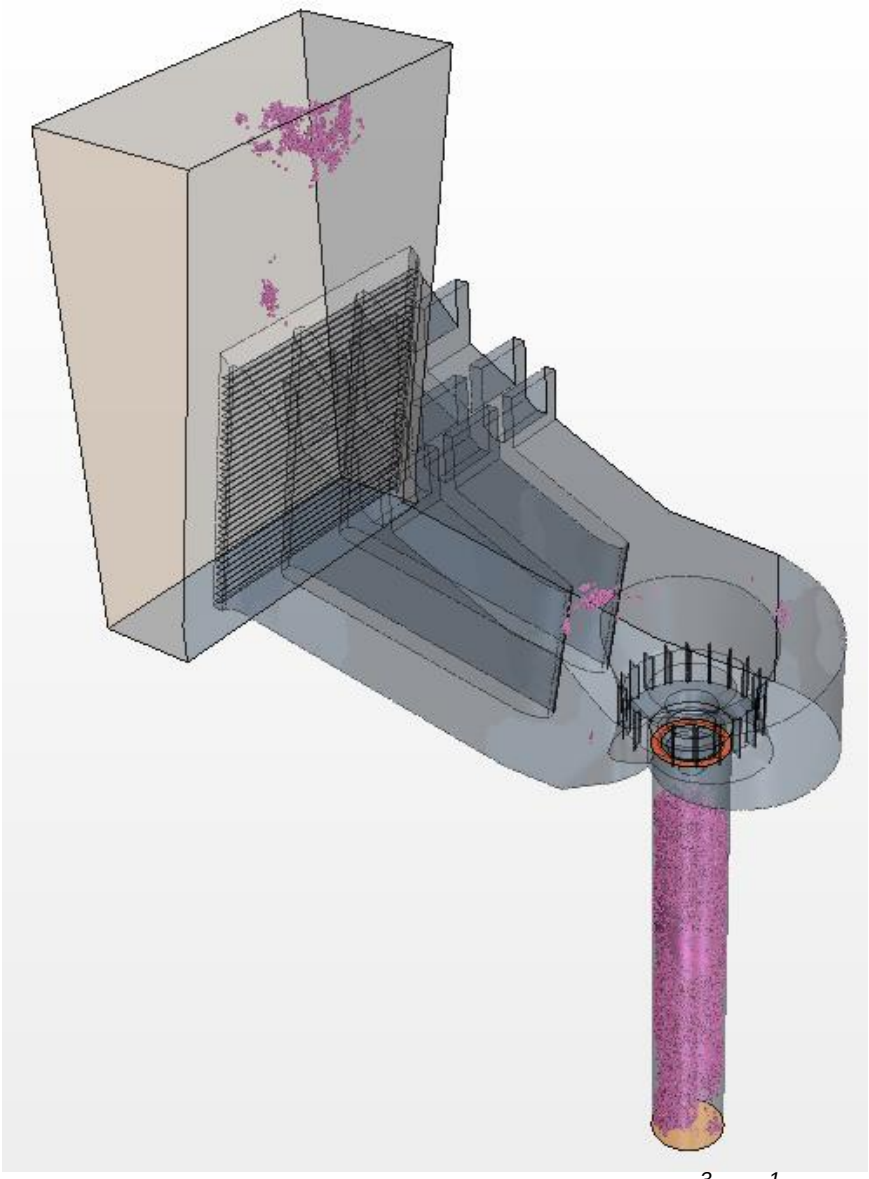

Figure A11.1: Continuity Residual of 290 m^3sec^{-1}

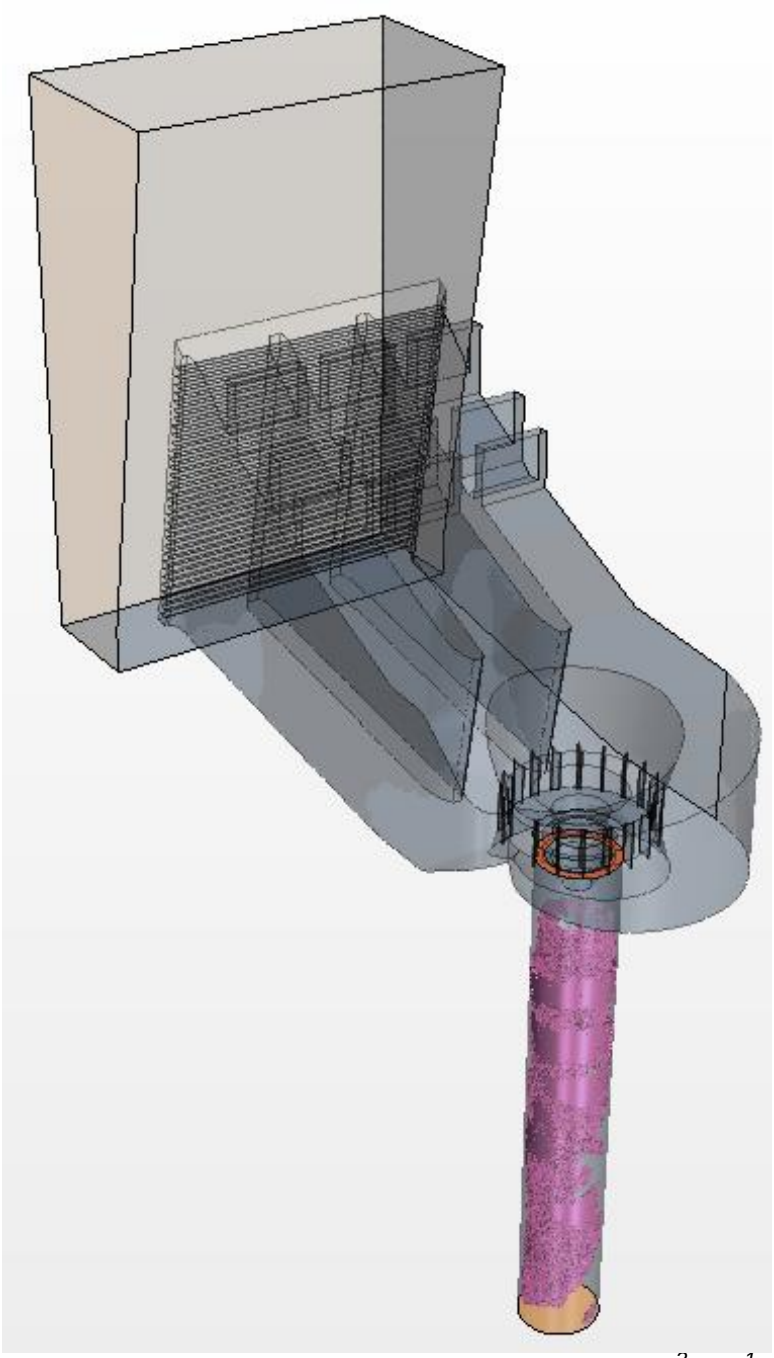

Figure A11.2: Y Momentum Residual of 290 m^3sec^{-1}

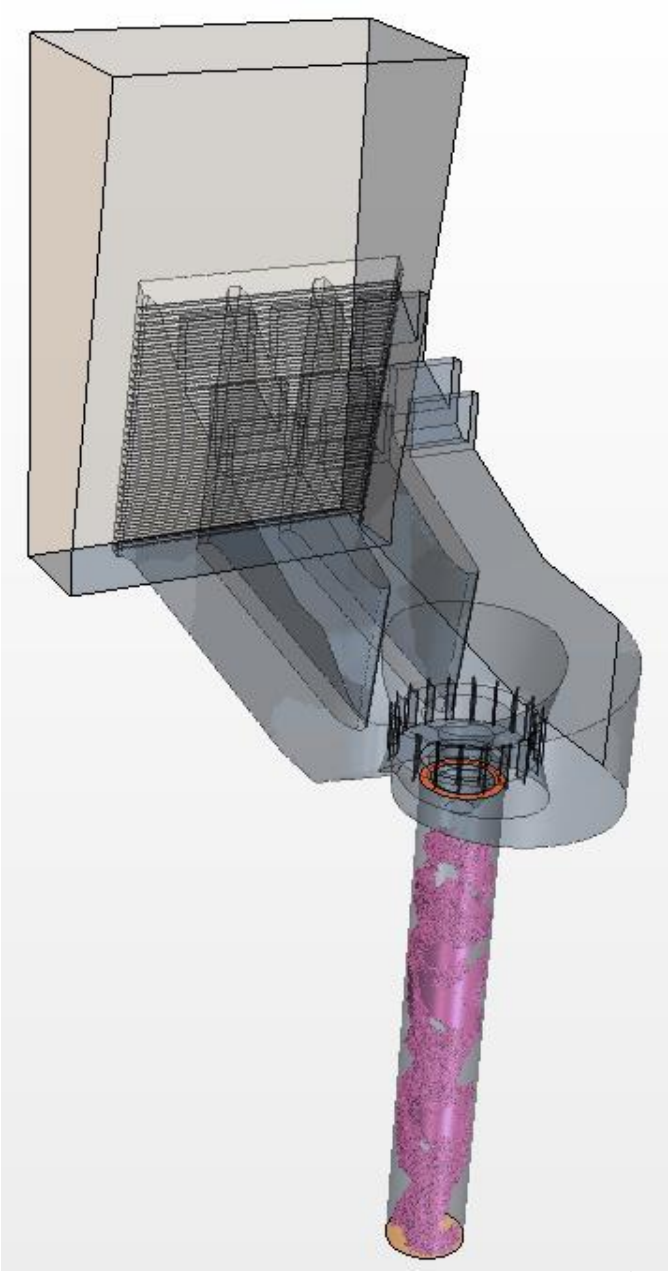

Figure A11.3: X Momentum Residual of 290 m^3sec^{-1}

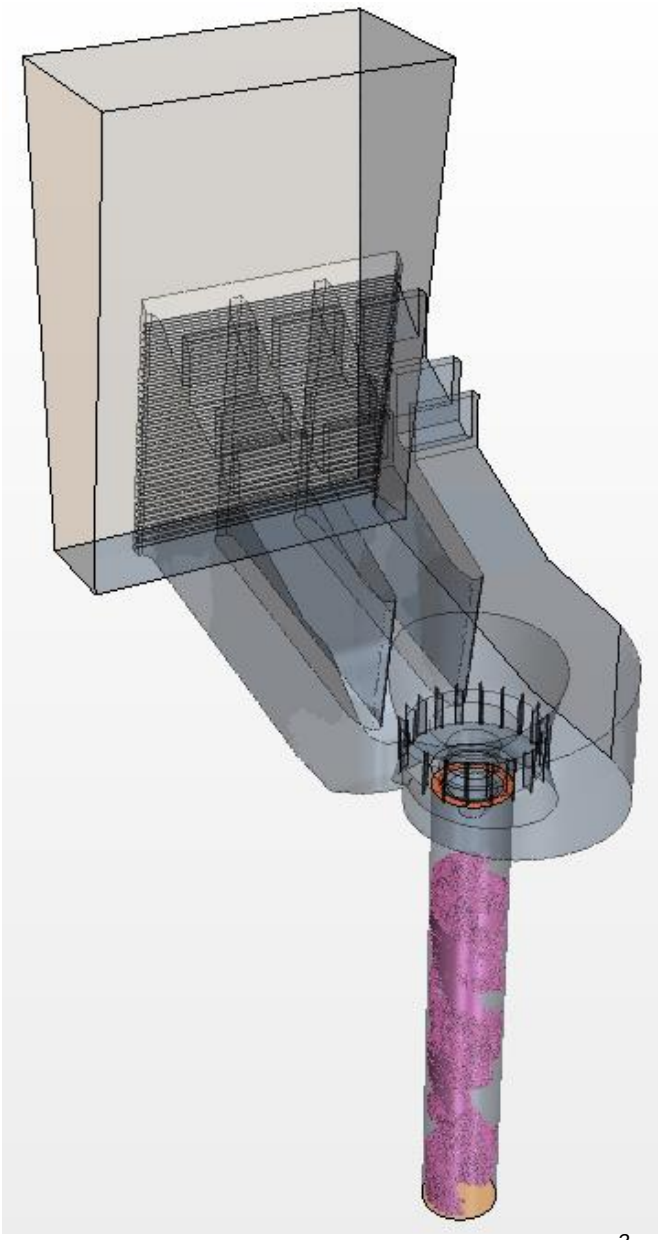

Figure A11.4: Z Momentum Residual of 290 m^3sec^{-1}

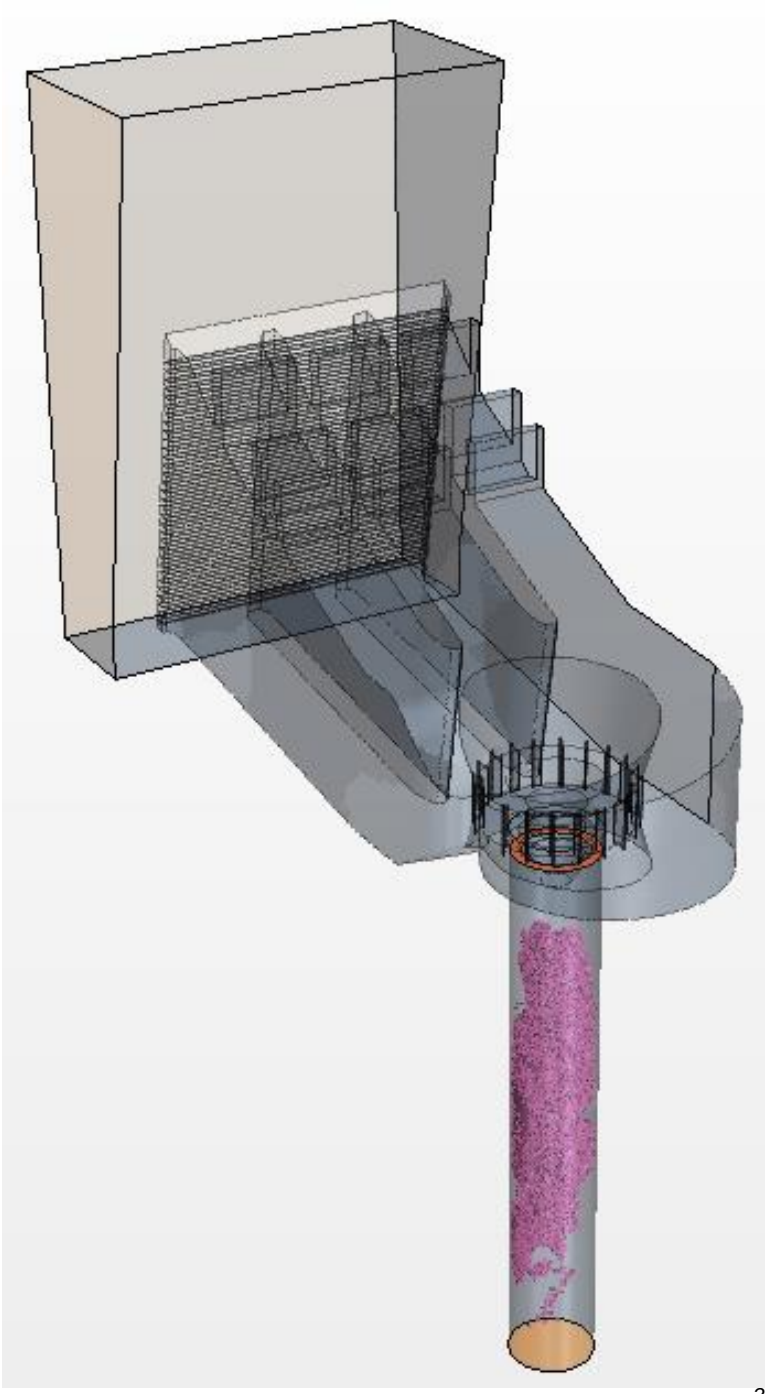

Figure A11.5: Turbulent Kinetic Energy Residual of 290 m^3sec^{-1}

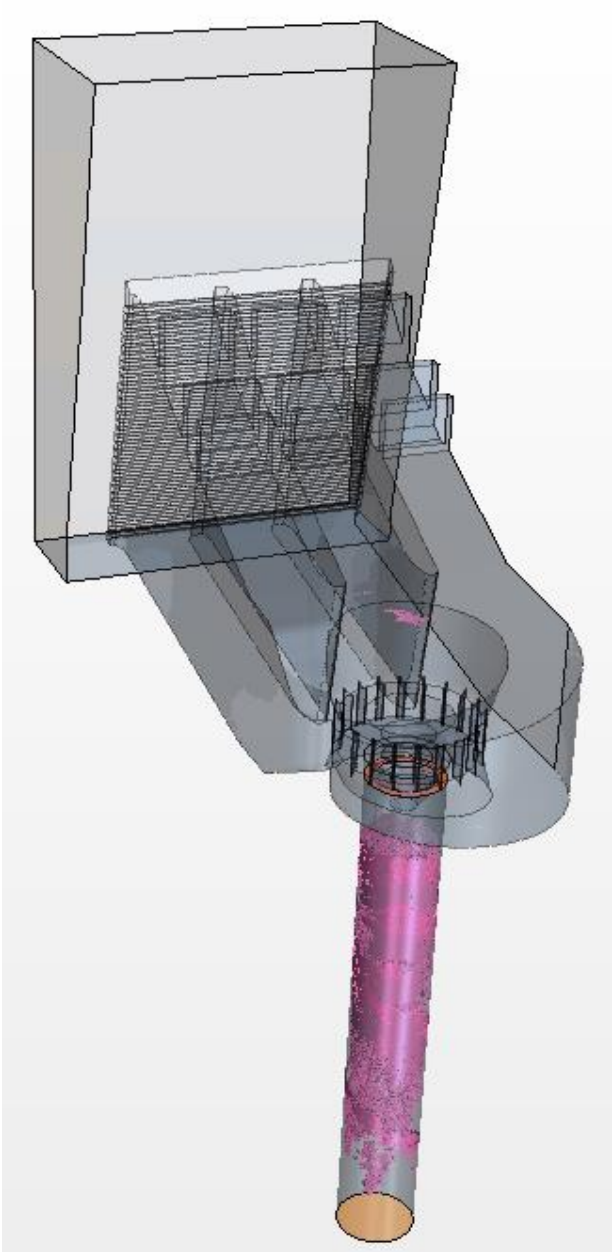

Figure A11.6: Specific Dissipation Rate Residual of 290 m^3sec^{-1}

Appendix 11: Assessed Performance Curves

As-Built Static Current Meter Application Analysis

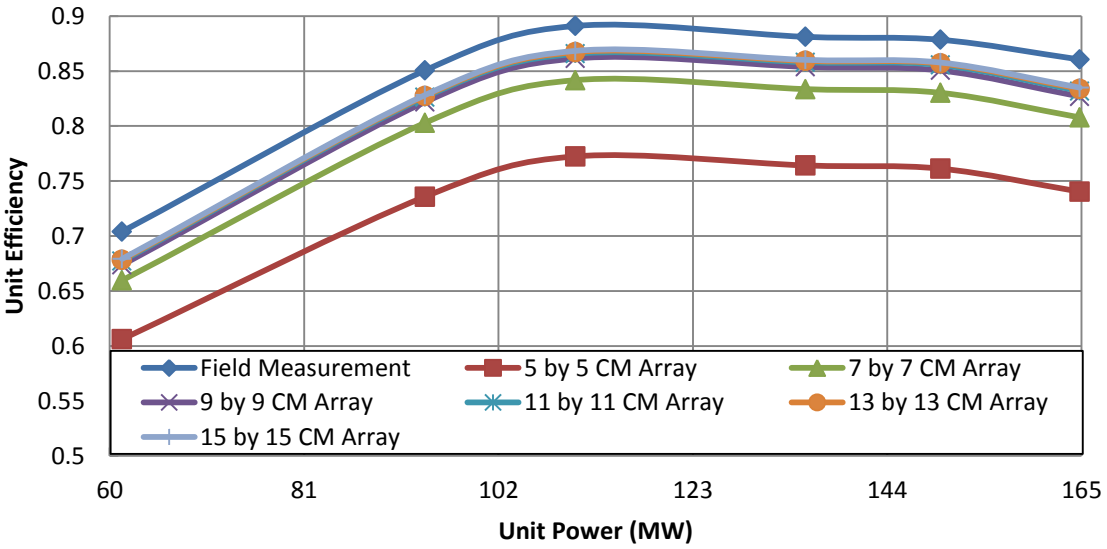

Figure A11.1: Recorded Unit Characteristic Curve as a Function of the Number of Static General Current Meters

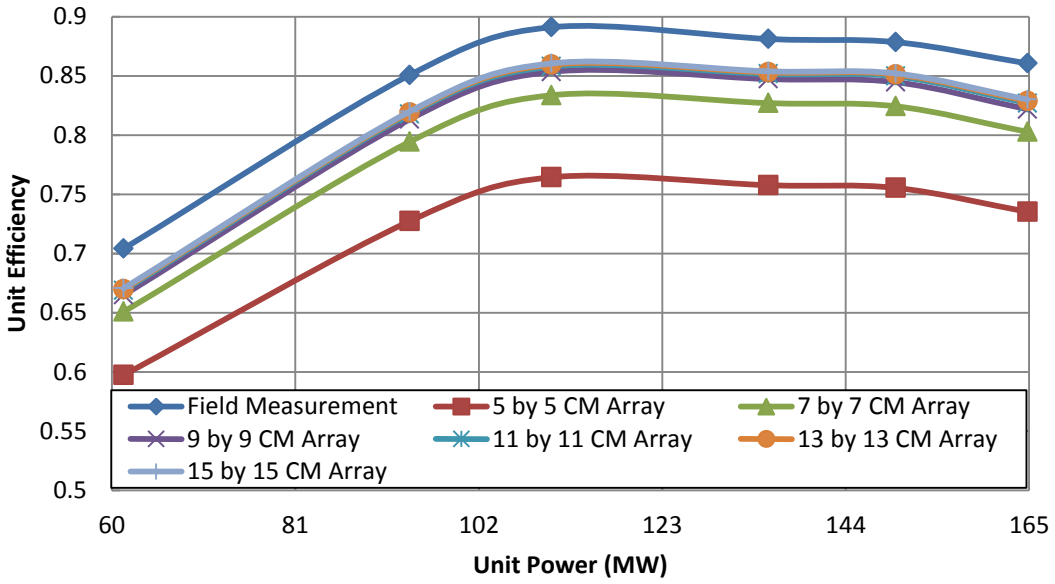

Figure A11.2: Recorded Unit Characteristic Curve as a Function of the Number of Static Ott C31-1(Plastic) Current Meters

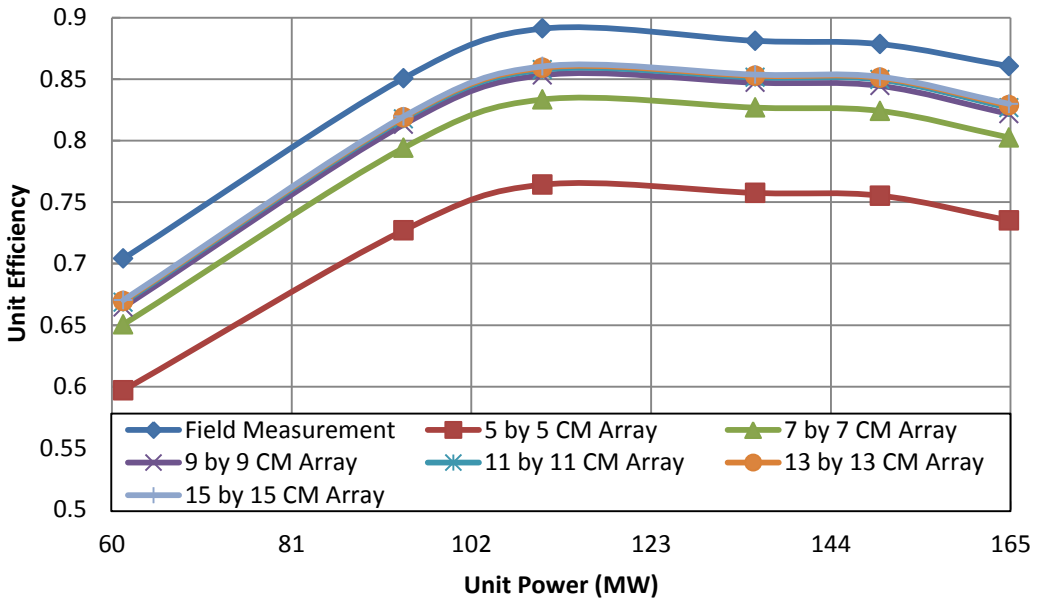

Figure A11.3: Recorded Unit Characteristic Curve as a Function of the Number of Static Ott C31-1(Metal) Current Meters

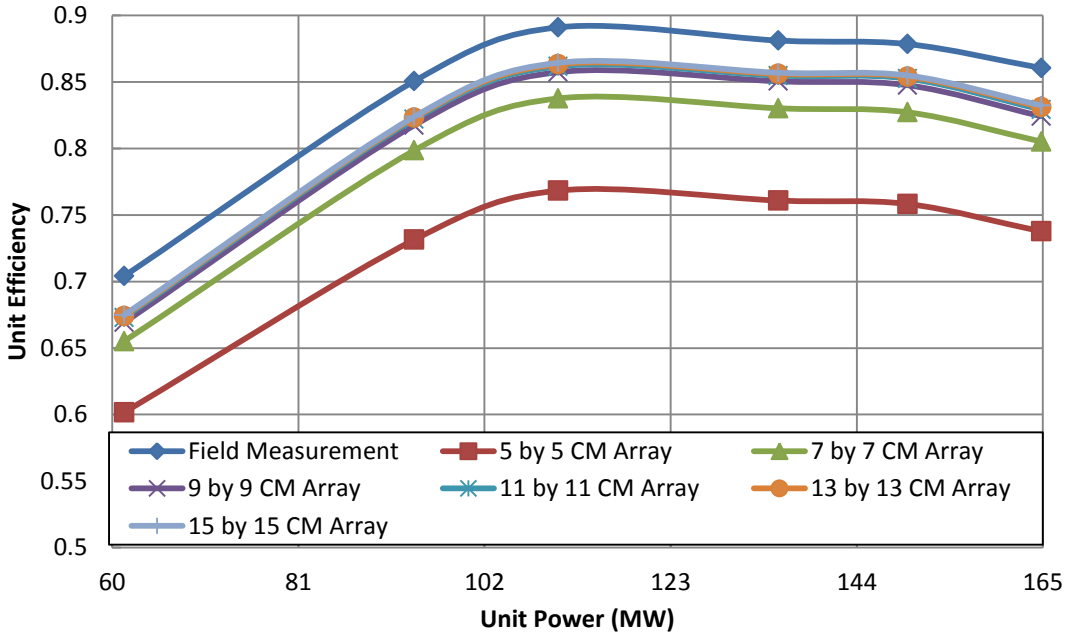

Figure A11.4: Recorded Unit Characteristic Curve as a Function of the Number of Static Ott C31-A Current Meters

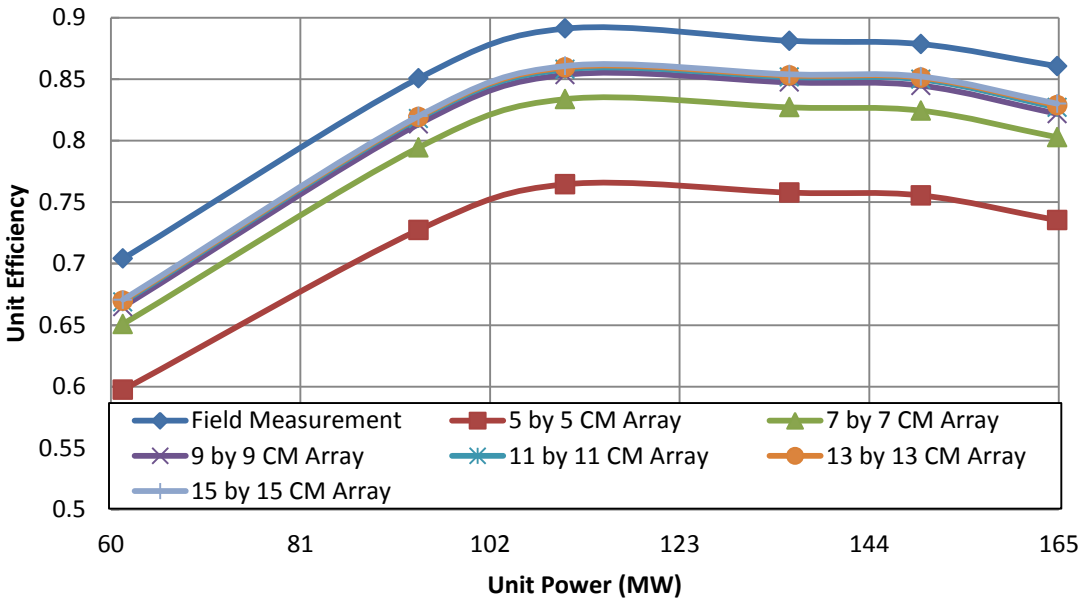

Figure A11.5: Recorded Unit Characteristic Curve as a Function of the Number of Static Ott C31-R Current Meters

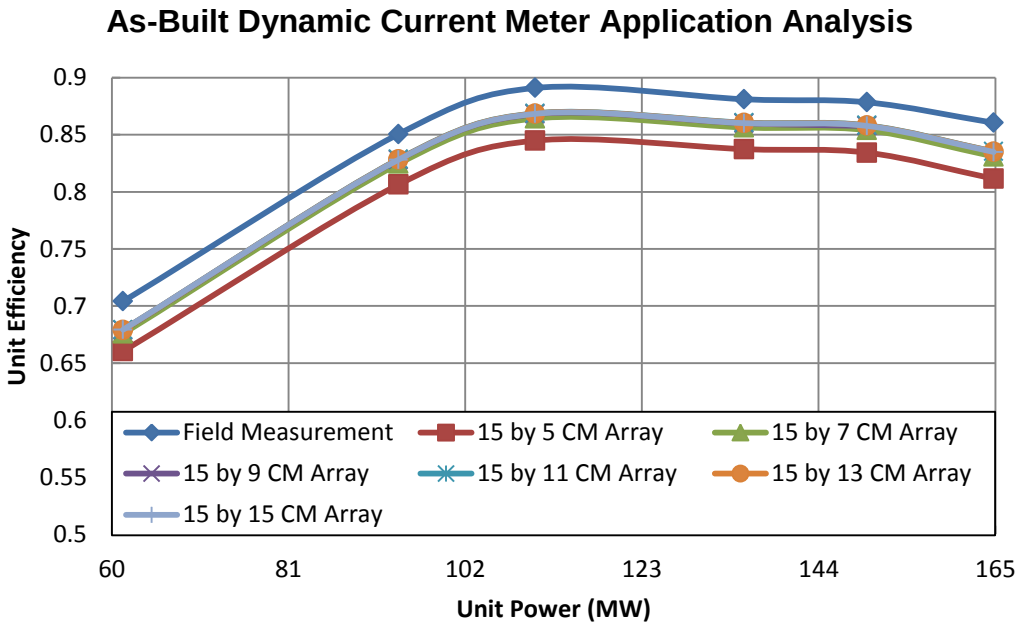

Figure A11.6: Recorded Unit Characteristic Curve as a Function of the Number of Dynamic Applied General Current Meters

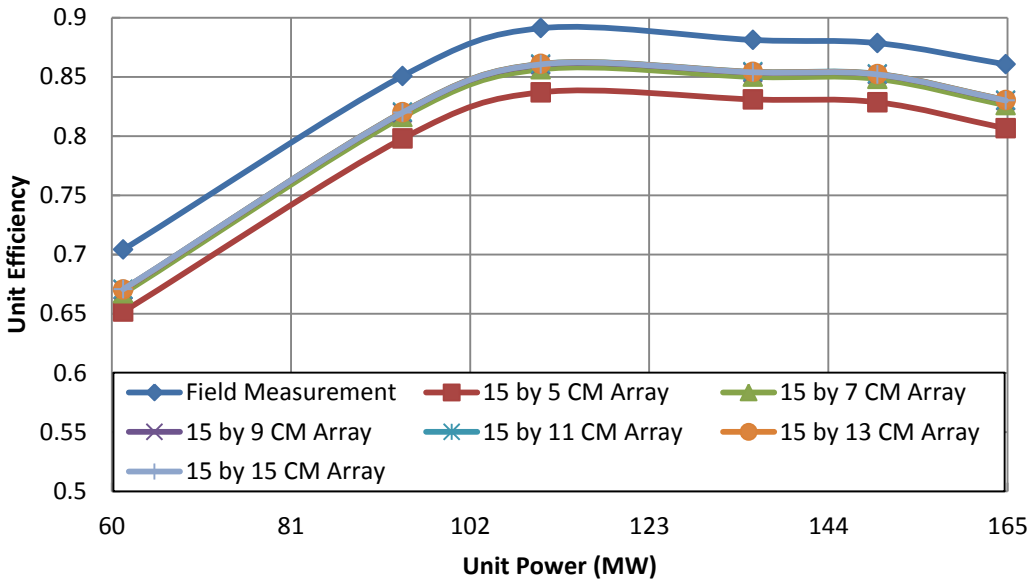

Figure A11.7: Recorded Unit Characteristic Curve as a Function of the Number of Dynamic Ott C31-1(Plastic) Current Meters

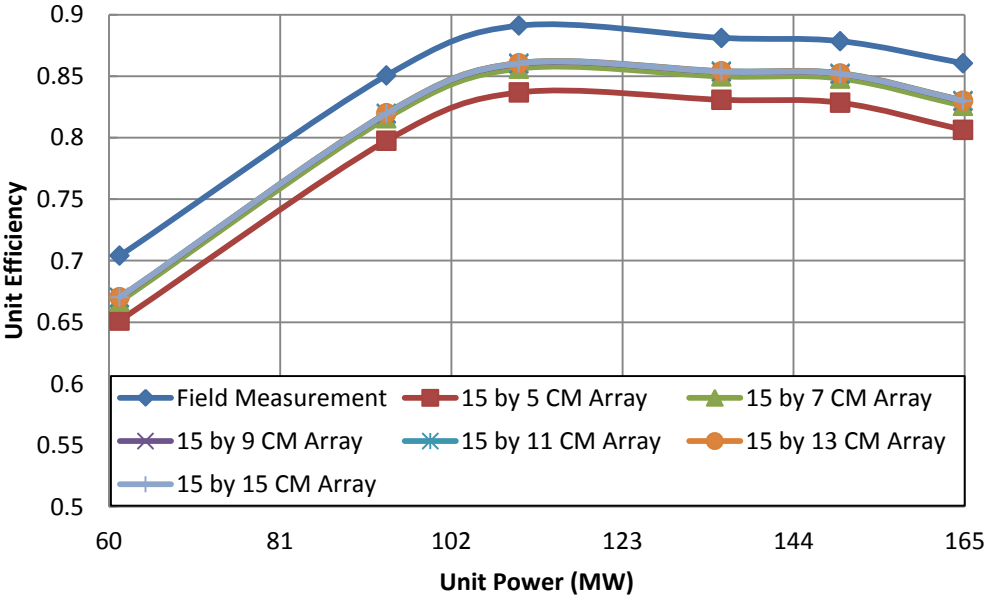

Figure A11.8: Recorded Unit Characteristic Curve as a Function of the Number of Dynamic Ott C31-1(Metal) Current Meters

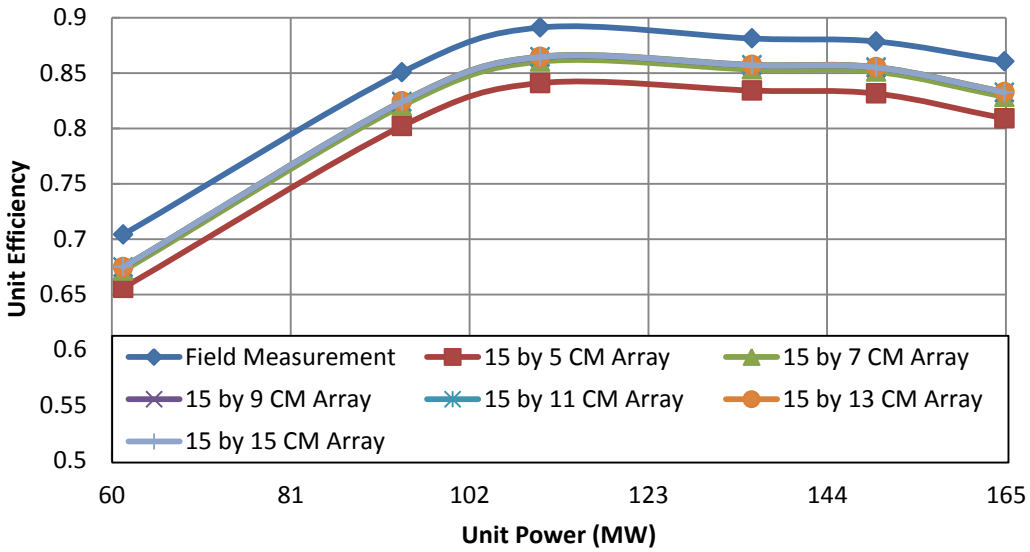

Figure A11.9: Recorded Unit Characteristic Curve as a Function of the Number of Dynamic Ott C31-A Current Meters

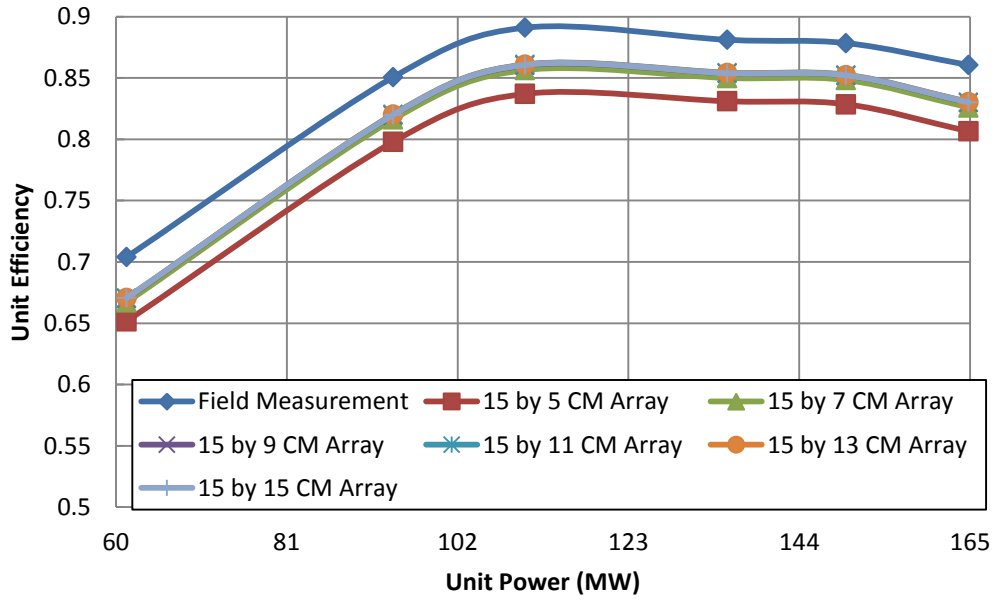

Figure A11.10: Recorded Unit Characteristic Curve as a Function of the Number of Dynamic Ott C31-R Current Meters

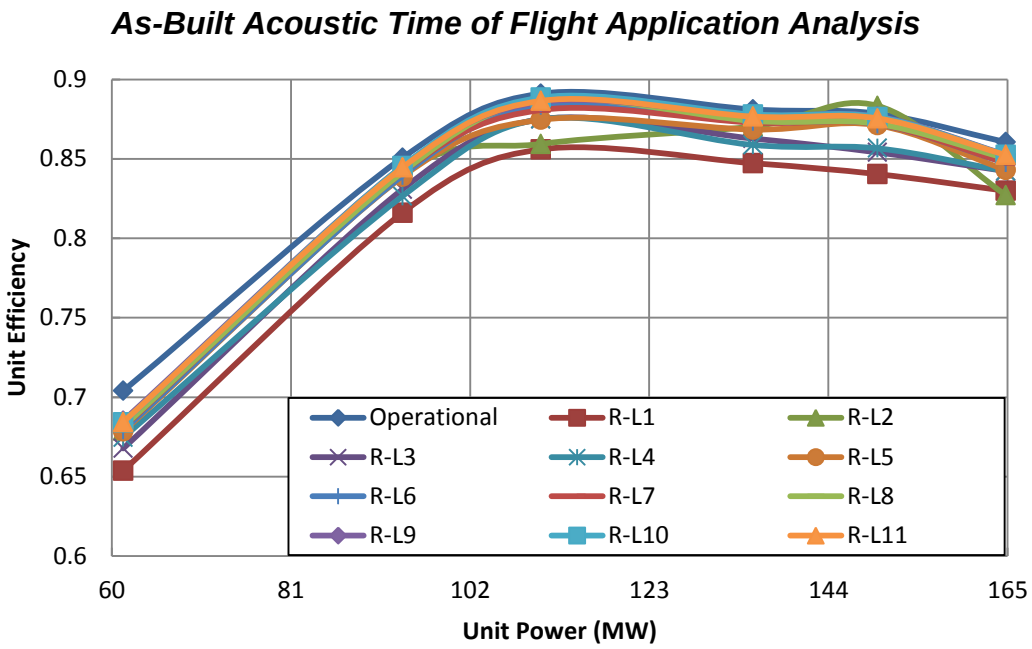

Figure A11.11: Recorded Unit Characteristic Curve as a Function of the Number of Applied Single Acoustic Paths (Right to Left)

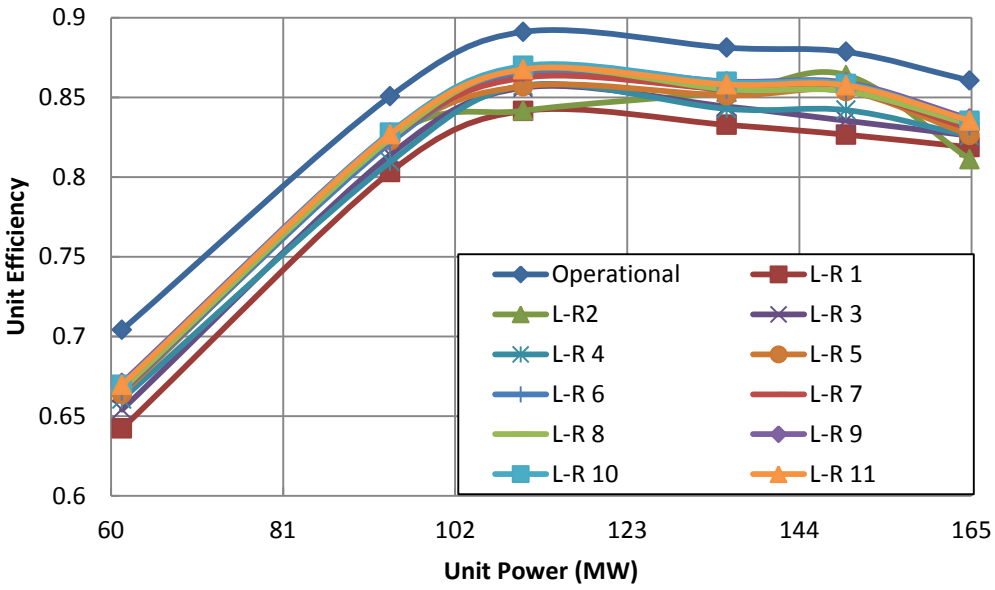

Figure A11.12: Recorded Unit Characteristic Curve as a Function of the Number of Applied Single Acoustic Paths (Left to Right)

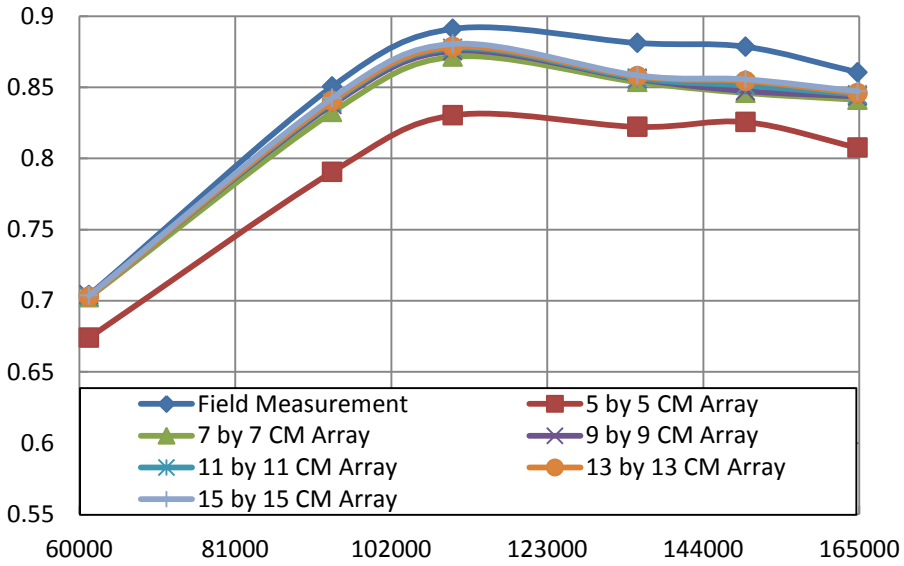

Figure A11.13: Recorded Unit Characteristic Curve as a Function of the Number of Static General Current Meters

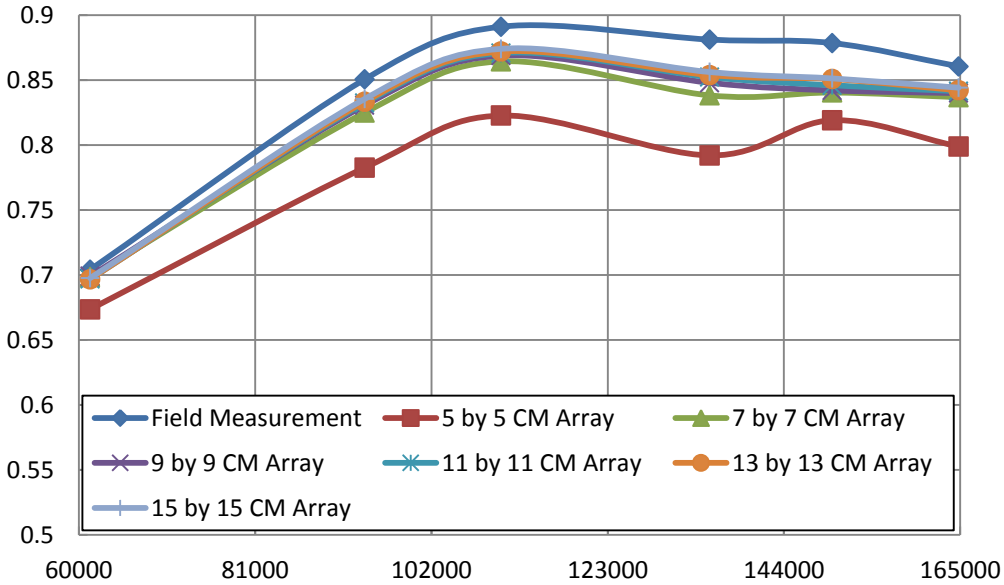

Figure A11.14: Recorded Unit Characteristic Curve as a Function of the Number of Static Ott C31-1(Plastic) Current Meters

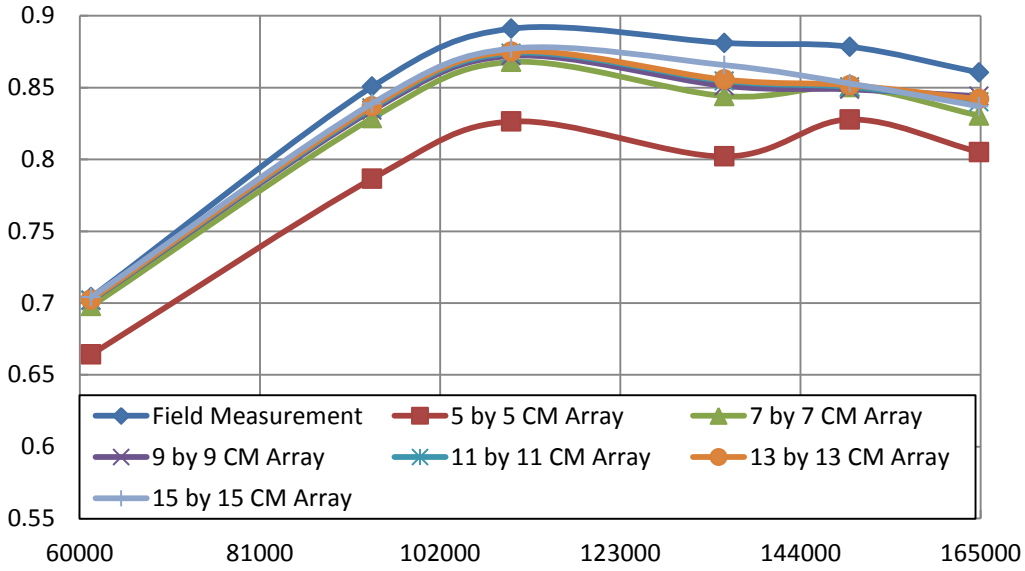

Figure A11.15: Recorded Unit Characteristic Curve as a Function of the Number of Static Ott C31 Type A Current Meters

Modified As-Built Dynamic Current Meter Application Analysis

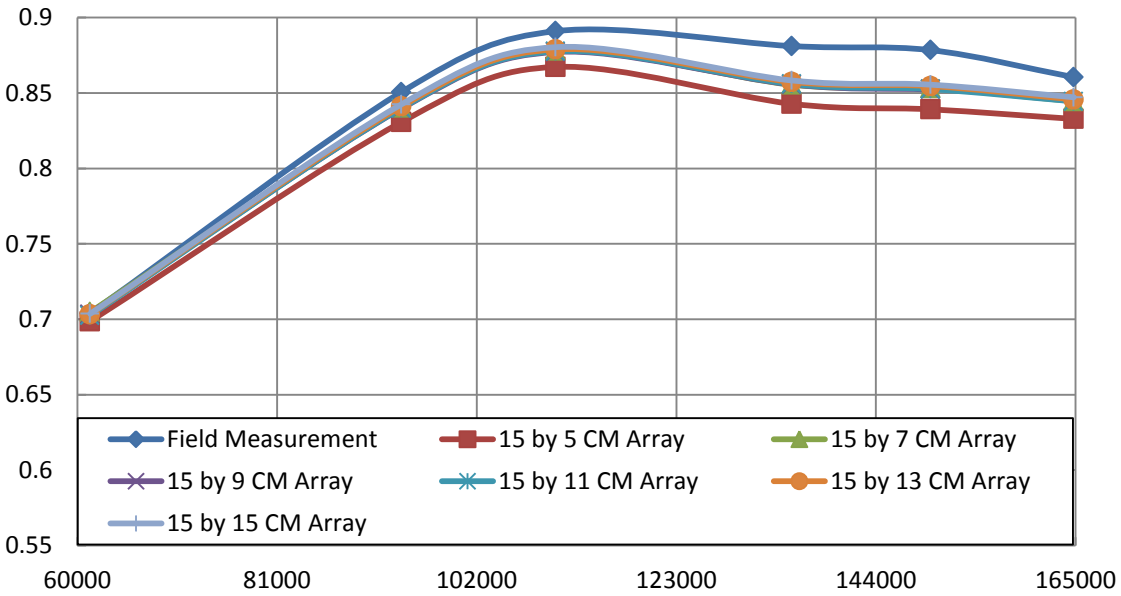

Figure A11.16: Recorded Unit Characteristic Curve as a Function of the Number of Transiting General Current Meters

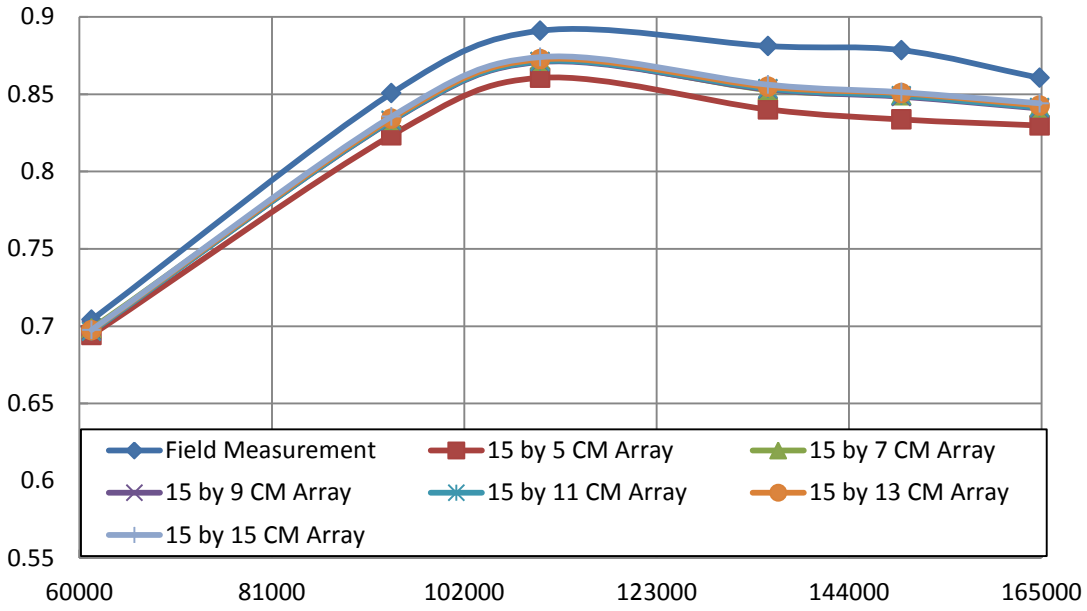

Figure A11.17: Recorded Unit Characteristic Curve as a Function of the Number of Transiting Ott C31-1(Plastic) Current Meters

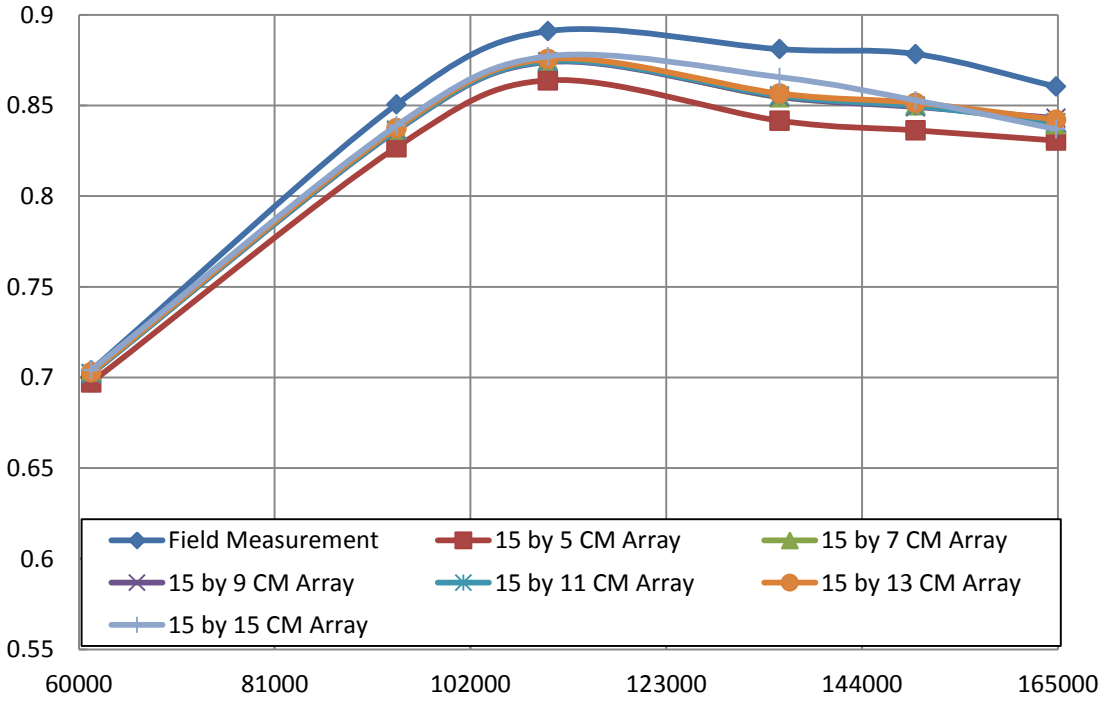

Figure A11.18: Recorded Unit Characteristic Curve as a Function of the Number of Transiting Ott C31 Type A Current Meters

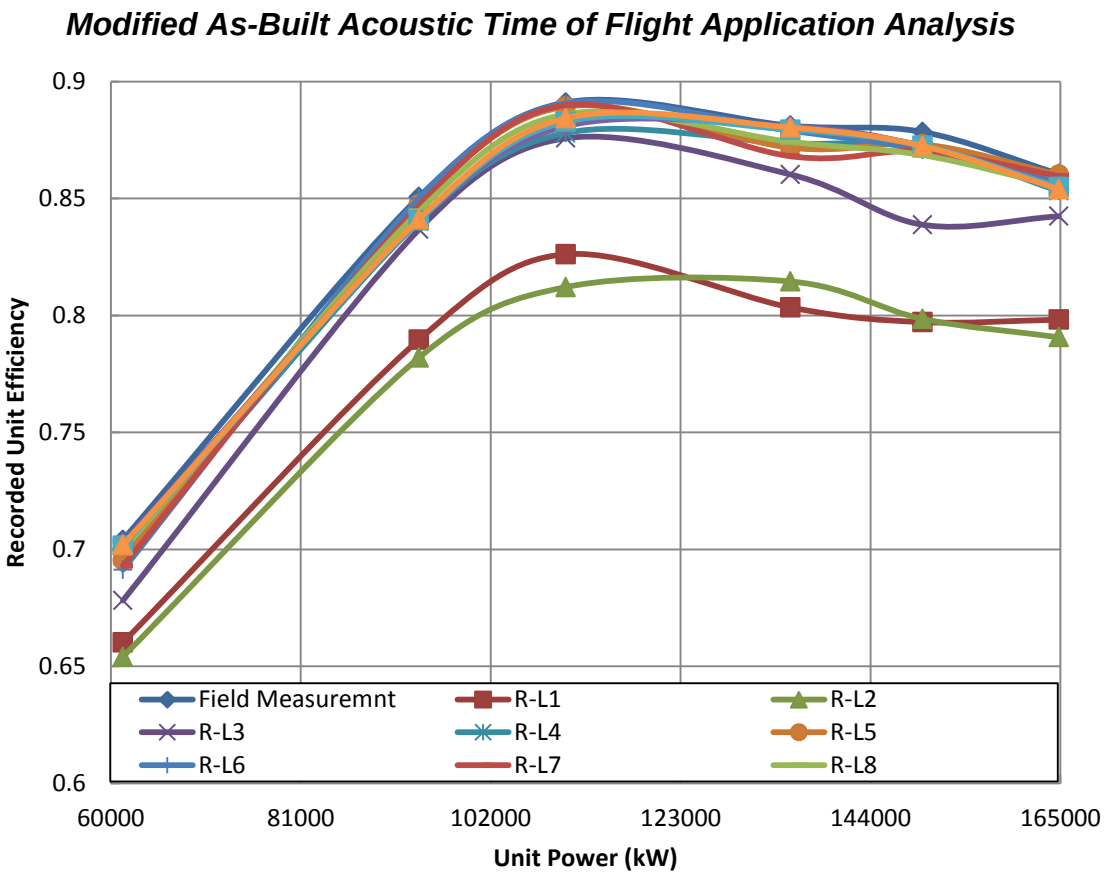

Figure A11.19: Recorded Unit Characteristic Curve as a Function of the Number of Applied Single Acoustic Paths (Right to Left)

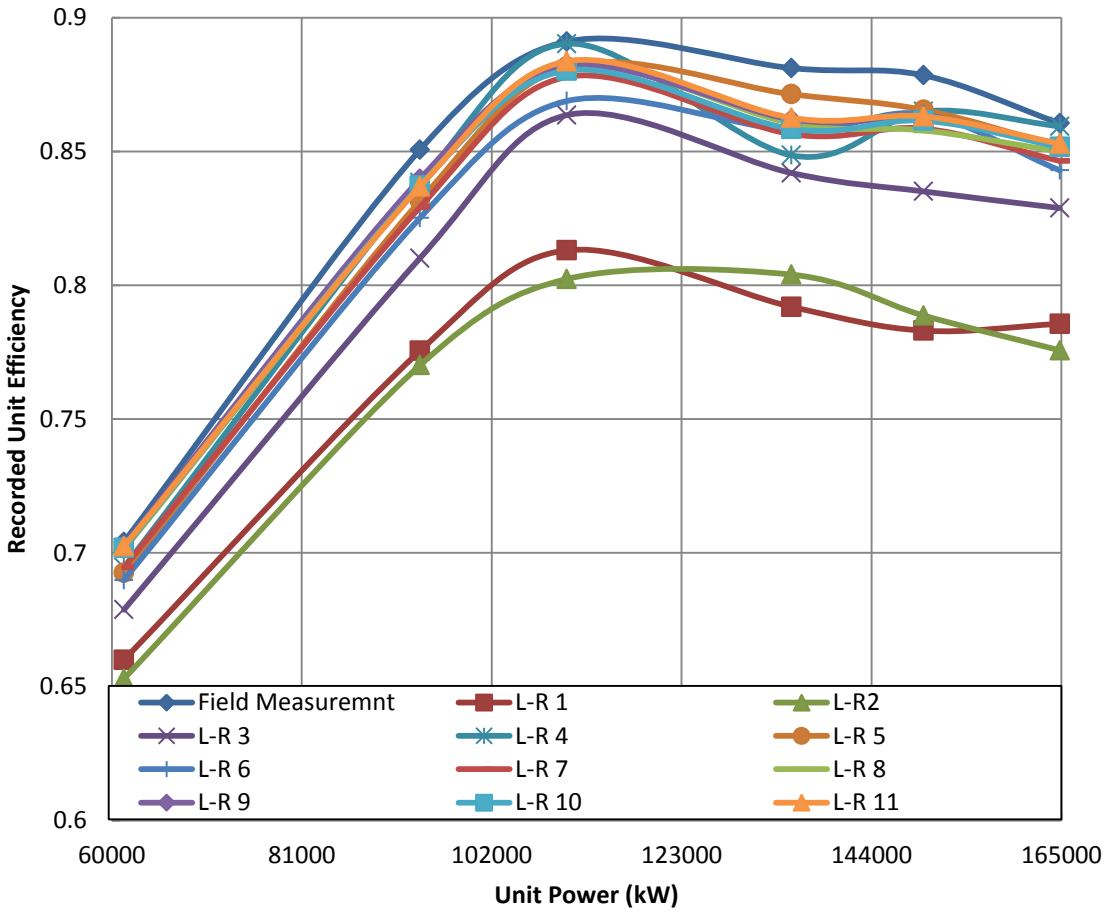

Figure A11.20: Recorded Unit Characteristic Curve as a Function of the Number of Applied Single Acoustic Paths (Left to Right)

VITA

Mark Christian was born in 1990 to Donald and Sara Christian in St. Louis Missouri. As a result of his parent's employment Mark was primarily raised in Europe, spending a period of years in both Alconbury England and Wiesbaden Germany. After moving back stateside, he attended the Florida Institute of Technology where he received his Bachelors of Science in Ocean Engineering. Mark's undergraduate thesis involved the design, construction and deployment of a full scale ocean energy device designed to harvest electricity from ocean waves.

He then moved to Knoxville Tennessee, to pursue his Ph.D. in Energy Science and Engineering with a focus in hydropower asset management best practices. To this end he began working with the Energy-Water Resource Systems Group at Oak Ridge National Laboratory. His primary focus was on quantifying the value of flow measurement through a specific subset of hydropower plants because they represent a significant percentage of the domestic hydropower fleet and there is currently no guidance for the industry. In addition to this the author had the operation to work on several additional projects, primarily discretized into policy and technical work.

Mark's technical efforts involved work with the State Department in Southeast Asia to maximize power production of local hydropower facilities and preserve water for agricultural use. In addition to this he performed research in concert with Apple Inc. to ensure the successful development and operation of a small hydroplant designed to power a local data center. His final technical work outside of his thesis was in the development of preliminary research into the economic viability of developing hydropower facilities near remote Alaskan Villages to mitigate the high cost local electricity. The policy work performed by Mark includes the development of an Official Comment to the proposed EPA Clean Power plan which was heavily leveraged in the development of the American Nuclear Society's comment to the plan. Furthermore Mark has led a team of his fellow graduate students in advocacy efforts for the development creation of an Energy Policy Council within the Tennessee State Legislature. This blend of policy and technical science project reflects the intent of the Bredesen Center for Interdisciplinary Research and Graduate Education to develop the next generation of leaders in the energy industries.

Outside of his professional work, Mark is married to his wife Guinevere and they have two dogs and one cat. In his spare time Mark thoroughly enjoys cooking and running.